Computer Simulation of Laser-Induced Ultrafast Demagnetization and Switching Dynamics of Magnetically Ordered Materials

Dissertation

zur Erlangung des Grades eines Doktors der Naturwissenschaften

vorgelegt von Florian Jakobs

Im Fachbereich Physik
der Freien Universität Berlin
November 2022

Gutachter:

1. Dr. Unai Atxitia (Instituto de Ciencia de Materiales de Madrid)
2. Prof. Dr. Piet Brouwer (Freie Universität Berlin)

Tag der Disputation 15.03.2023

Selbstständigkeitserklärung

Ich erkläre gegenüber der Freien Universität Berlin, dass ich die vorliegende Dissertation selbstständig und ohne Benutzung anderer als der angegebenen Quellen und Hilfsmittel angefertigt habe. Die vorliegende Arbeit ist frei von Plagiaten. Alle Ausführungen, die wörtlich oder inhaltlich aus anderen Schriften entnommen sind, habe ich als solche kenntlich gemacht. Diese Dissertation wurde in gleicher oder ähnlicher Form noch in keinem früheren Promotionsverfahren eingereicht.

Mit einer Prüfung meiner Arbeit durch ein Plagiatsprüfungsprogramm erkläre ich mich einverstanden.

Berlin, 09. November 2022

Kurzzusammenfassung

Im Rahmen dieser Arbeit wurden Laser-induzierte ultraschnelle Entmagnetisierungs- und Schaltungsdynamiken von magnetisch geordneten Materialien mittels atomistischer Spindynamik-Simulationen durchgeführt. Dazu wurde ein semiklassisches Spinmodell verwendet, dessen Dynamik mit Hilfe der stochastischen Landau-Lifshitz-Gilbert-Gleichung berechnet wurde. Die Ergebnisse wurden mit experimentellen Messungen verglichen, die von Mitarbeitern der University of California in Berkeley und des Fritz-Haber-Instituts in Berlin durchgeführt wurden, sowie mit anderen, bereits veröffentlichten Daten.

Zunächst wurden verschiedene ferrimagnetische GdFeCo-Legierungen untersucht. Diese sind von besonderem Interesse, da seit etwa 15 Jahren bekannt ist, dass sich GdFeCo besonders gut für ultraschnelles Schalten eignet. Dabei wird die Magnetisierung innerhalb kürzester Zeit nach Anregung durch einen kurzen Laserpuls (≈ 100 fs) invertiert.

Von großem technischen Interesse ist das Schalten mittels elektrischer Pulse, die jedoch deutlich länger sind (5-6 ps). Deswegen wurde ein breites Spektrum von Pulsdauern auf ihre verursachten Schaltungsdynamiken untersucht und mit experimentellen Ergebnissen verglichen. Es wurde festgestellt, dass das voll-optische Schalten für Pulsdauern über zwei Größenordnungen möglich ist, und dass das verwendete Modell in der Lage ist, das experimentell gemessene Schaltverhalten über größere Zeitskalen quantitativ korrekt zu beschreiben.

Des Weiteren wurde erstmals die Heusler-Legierung $\mathrm{Mn_2Ru}_x\mathrm{Ga}$ mit Hilfe eines atomistischen Spinmodells modelliert. Das erst kürzlich experimentell gefundene Schaltverhalten dieser Legierung konnte in Computersimulationen reproduziert werden. So wurde gezeigt, dass das erarbeitete Modell das von Banerjee *et al.* [1] gemessene Schaltverhalten nach Anregung mit einem einzigen Laserpuls reproduziert.

Nach der Simulation dieser beiden Ferrimagnete wurde eine allgemeine Studie über das Schalten und die Magnetisierungsdynamik in ferrimagnetischen Materialien durchgeführt. Dabei wurde ein allgemeines makroskopisches Modell für die Magnetisierungsdynamik nach Anregung durch einen Femtosekundenlaser hergeleitet. Die Theorie ist in der Lage, alle Phasen des in Experimenten beobachteten Schaltvorgangs in Ferrimagneten zu reproduzieren. Des Weiteren wurde festgestellt, dass die Magnetisierungsdynamik während des Schaltprozesses von einem relativistischen Relaxationspfad zu einem Austausch-dominierten Bereich übergeht, was auf die dominierende Verstärkung der Austauschrelaxation zurückzuführen ist.

Anschließend wurde der Spezialfall eines Antiferromagneten betrachtet. Dazu wurde das zuvor entwickelte makroskopische Modell auf Antiferromagneten angewandt und eine Bewegungsgleichung für die magnetische Ordnung hergeleitet. Mit Hilfe atomistischer Spinsimulationen und des makroskopischen Modells wurde eine bisher nur vermutete schnellere, Austausch-verstärkte Magnetisierungsdynamik von Antiferromagneten festgestellt und systematisch untersucht.

Um das Schalten von magnetischen Materialien besser zu verstehen, sind auch andere Systeme, wie etwa das Elektronen- und das Phononensystem von großer Bedeutung. Deswegen wurden Spindynamik-Simulationen in Nickel, Kobalt und Eisen unter Verwendung von Ab-initio-Berechnungen durchgeführt, mit dem Ziel, experimentell gemessenene Gitterdynamiken besser zu verstehen. Dabei wurde festgestellt, dass der Energiefluss zum und vom Spinsystem von zentraler Bedeutung ist und einen verlangsamenden Effekt auf die Phononendynamik hat. Der Vergleich mit experimentellen Daten zeigt, dass die atomistischen Spindynamik-Simulationen eine konsistente quantitative Beschreibung aller drei Teilsysteme liefern, was eine Verbesserung bekannter Modelle, wie etwa des Drei-Temperaturmodells darstellt.

Short Summary

In this work the laser-induced ultrafast demagnetization and switching dynamics of magnetically ordered materials were simulated by means of atomistic spin-dynamics simulations. The dynamics of the system were calculated numerically using the stochastic Landau-Lifshitz-Gilbert equation. The obtained results were compared with experimental measurements performed by collaborators from the University of California in Berkeley and at the Fritz-Haber Institute in Berlin, as well as with previously published data.

First, various ferrimagnetic GdFeCo alloys were investigated as they are particularly well suited for all-optical switching. During this process, the magnetization is reversed within a few picoseconds of excitation by an ultrashort short laser pulse (≈ 100 fs). Of great technical interest is switching using electrical pulses, which are, however, significantly longer (5-6 ps). Therefore, a wide range of pulse durations were simulated in order to investigate their ability to switch various GdFeCo alloys. It was found that single pulse all-optical switching is possible for pulse durations that span two orders of magnitude. The same underlying physics, based on atomistic spin-dynamics simulations, is able to describe switching within hundreds of femtoseconds as well as tens of picoseconds. Furthermore, element-specific damping was found to be a key parameter for switching using longer pulse durations. The simulation results were compared to experiments, yielding a quantitative agreement when including local Gd-concentration inhomogeneities.

Furthermore, the Heusler alloy $\mathrm{Mn_2Ru}_x\mathrm{Ga}$ was modeled. The derived model was able to reproduce various key material properties, such as the Curie temperature, the magnetization curve or the Ru-concentration dependence of the magnetization-compensation temperature. Moreover. the model was able to quantitatively reproduce the magnetization dynamics of single pulse toggle switching as measured by Banerjee *et al.* [1]. It was also demonstrated that, contrary to previous understanding coming from rare-earth transition metal alloys, toggle switching in $\mathrm{Mn_2Ru}_x\mathrm{Ga}$ is possible even when both Mn sublattices demagnetize at very similar rates.

After simulating these two ferrimagnets a general study of switching and magnetization dynamics in ferrimagnetic materials was carried out. A general macroscopic theory for the magnetization dynamics of ferrimagnetic materials driven by femtosecond laser photo excitation was derived. The theory reproduces all stages of the switching process observed in experiments. It was found that during the switching process the magnetization dynamics transitions from a relativistic relaxation path to an exchange-dominated regime due to the strong enhancement of the exchange relaxation.

Next, the special case of an antiferromagnet was considered. The previously developed macroscopic model was applied to antiferromagnets and an equation of motion for their magnetic order were derived. With the help of atomistic spin simulations, a faster, exchange-enhanced magnetization dynamic of antiferromagnets was found and systematically investigated, which was previously only suspected. Notably, the found exchange enhancement depends strongly on the number of neighboring spins of the other sublattice.

In order to better understand switching of magnetic materials, other systems such as the electron and the phonon system are also of great importance. Therefore, spin dynamics simulations in nickel, cobalt and iron were performed using ab initio calculations with the aim of better understanding experimentally measured lattice dynamics. It was found that the energy flow to and from the spin system is of great importance and has a slowing effect on the phonon dynamics. Comparison with experimental data showed that the atomistic spin dynamics simulations provide a consistent quantitative description of all three subsystems, which is an improvement on previously used models such as the three-temperature model.

Contents

Chapter 1

Introduction

1.1 Motivation

The amount of data processed by the world is increasing exponentially and doubles roughly every three years. We witnessed another huge increase at the start of the pandemic in 2020 [2]. Naturally, this amount of data demands ever larger and faster processing and storage capabilities.
In magnetic hard drives information is stored using small ferromagnetically aligned areas, so-called magnetic domains, that contain the information of a single bit. The main advantages over other types of data storages, such as solid-state drives, are the longevity and price, but magnetic hard drives fall short on reading and writing speed. Typically bits are written by applying a magnetic field in the desired direction, switching the domain to the desired state. However, this process is fairly slow since the reorientation time depends on the strength of the applied field and is limited to approximately 1 ns.
Only small improvements, such as heat-assisted magnetic recordings, have been found in this area [3, 4]. In order to keep up with the ever increasing need for data processing and information storage fundamentally new approaches need to be explored.

Recent developments in magnetism are approaching the limits of spin dynamics on the order of picoseconds. Pioneering works in this field show that even switching of ferrimagnetic domains on these timescales is possible, promising a new fast and energy-efficient way of writing data [5, 6]. However, many fundamental questions in this new research field of *ultrafast magnetization dynamics* are not fully understood yet.

In this work, laser-induced ultrafast demagnetization and switching of magnetically ordered materials are investigated using atomistic spin-dynamics simulations. During the computer simulations the classical Heisenberg model and the stochastic Landau-Lifshitz-Glibert equation are used and solved numerically. The simulation results are compared to experimental measurements from coworkers and a phenomenological analytical model is derived and compared to the numerical results.

In the following chapter an overview of the current state of ultrafast magnetization dynamics will be given and the most relevant findings in this field will be briefly presented.

1.2 Introduction to ultrafast magnetization dynamics

1.2.1 Ultrafast demagnetization

The first pioneering works in the field of ultrafast magnetization dynamics were performed in thin nickel films during the 1980s. At that time experiments found typical demagnetization times between 1 and 40 ns [7]. In the early 1990s Vaterlaus *et al.* measured the spin-lattice relaxation time of gadolinium to be about 100 ± 80 ps [8]. This result was in agreement with the theoretically estimated demagnetization time of 48 ns by Hübner and Bennemann, that was published shortly after [9]. They based their theoretical prediction on spin-lattice-relaxation only, as it was believed, that spins only couple weakly to the light of an incoming laser pulse. This assumption was based on the fact that, in thermodynamic equilibrium the spin-orbit interaction is only a small relativistic correction to the electronic Hamiltonian. In the mid-1990s it was therefore concluded, that demagnetization upon laser heating proceeds on typical timescales of 50 ps up to 1 ns driven by spin-lattice relaxation.

In 1996, due to the development of lasers with pulse durations of only a few fs, Beaurepaire *et al.* were able to measure the magnetization dynamics of face-centered cubic Ni after excitation with a 60 fs laser pulse [5]. Using the magneto-optical Kerr effect (MOKE) they found that the magnetization drops to 55 % of its saturation value within only 100 fs, questioning the previous understanding. The results of their famous experiment are shown in figure 1.2.1. As outlined previously, these results came as a surprise at the time and thus the term *ultrafast demagnetization* was coined. Within the publication of Beaurepaire *et al.* the results could only be explained by introducing a direct, dominant electron-spin coupling alongside the much weaker spin-lattice coupling, forming the so-called three temperature model. The three-temperature model assumes different temperatures for the involved subsystems, namely electrons, spins and phonons and various coupling constants to exchange energy between the subsystems.

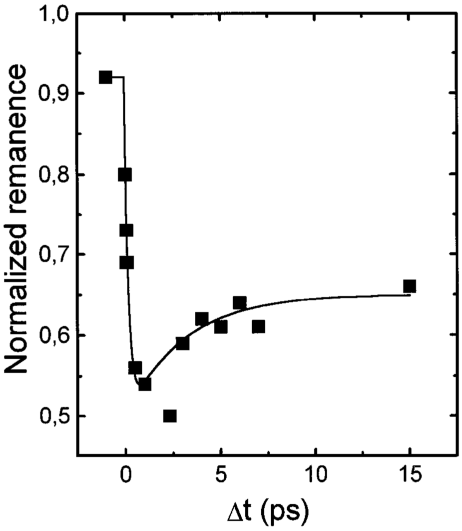

Figure 1.2.1: *The first measured ultrafast magnetization dynamics of face-centered cubic nickel measured by Beaurepaire et al. Figure taken from Ref. [5].*

Upon excitation with an ultrafast laser the electron subsystem absorbs all of the energy, which leads to a rapid increase of the electron temperature. This added energy then gets distributed to the spin and phonon subsystem via the electron-spin coupling and the electron-lattice coupling, until eventually a new equilibrium temperature is reached.

In the following years, the results of Beaurepaire *et al.* were reproduced and confirmed many

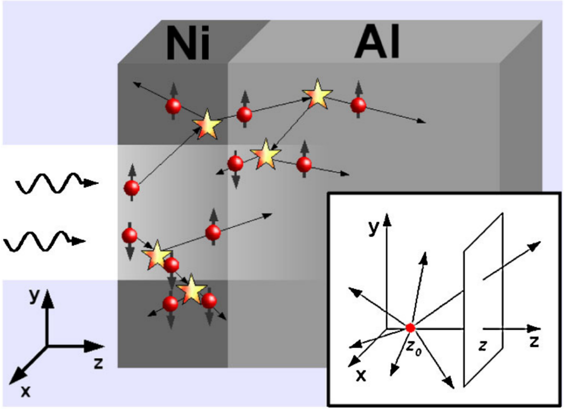

Figure 1.2.2: *Superdiffusive spin transport at a Ni/Al interface. After laser excitation of the nickel layer more majority spin electrons diffuse into the Al-substrate, while minority spin electrons stay within the Ni-layer. This then causes a reduction in the magnetization in the Ni-layer. Figure taken from Ref. [16].*

times [10, 11, 12]. Today it is understood that the pump pulse excites the electron system, and the excited non-thermal hot electron distribution becomes thermalized on time scales of several hundred femtoseconds [13]. During this process the energy of the electron subsystem is transferred to the spin subsystem (a different degree of freedom of the electrons). On longer timescales of up to 10 ps the energy is then transferred to the lattice, until all three subsystems return to equilibrium.

However, the exact mechanisms underlying this rapid demagnetization are still unclear and disputed today. In particular the fast vanishing of angular momentum on these extremely short time scales still remains open. Koopmans *et al.* argued that Elliott-Yafet-type scattering is responsible for the rapid demagnetization [14]. By emitting or absorbing a phonon an electron has a chance to flip its spin and thus the demagnetization process conserves its total angular momentum [15].

An alternative explanation was provided by Battiato *et al.* [16, 17]. They argue that so-called *superdiffusive spin currents* are responsible for the ultrafast demagnetization process. This model relies on different spin-dependent transport properties of hot electrons. This causes more majority spin electrons to diffuse into the substrate, while minority spin electrons stay, due to their larger scattering cross section, within the magnetic layer. This leads to a reduction of the magnetization. The process is illustrated in figure 1.2.2.

The predicted superdiffusive spin currents where measured shortly after by Rudolf *et al.* [18] and Turgut *et al.* [19] in Ni/Fe multilayer samples divided by insulating spacer materials such as Ni/Ru/Fe on a timescale of several hundred femtoseconds. Furthermore, Graves *et al.* looked at ferrimagnetic GdFeCo after laser excitation, finding enhanced demagnetization and switching dynamics driven by a non-local transfer of angular momentum between Gd-rich and Fe-rich regions [20].

On the other hand, there have been a number of works that find no meaningful contribution of superdiffusive spin transport to the demagnetization process. Moisan *et al.* looked at CoPt and CoPd domain patterns finding no change in demagnetization time as function of the domain structure [21]. In contrast to Graves *et al.*, they concluded that inter-domain hot electron spin transfer only contributes negligibly to the demagnetization dynamics in this system. Further joined experimental and theoretical studies by Shokeen *et al.* in Ni and Co films found no significant contribution of superdiffusive spin transport in these materials and instead concluded that spin flips play the most significant role during demagnetization in Ni and Co [22].

However, ultrafast demagnetization has also been found in magnetic samples on insulating substrate materials [23]. Therefore, superdiffusive spin transport should be considered a supporting mechanism and cannot be the only mechanism behind ultrafast demagnetization.

Thus the explanation provided by Koopmans *et al.* based on Elliott-Yafet-type scattering remains the best theory for the observed rapid demagnetization.

1.2.2 Ultrafast magnetization switching

In 2007 Stanciu and coworkers used laser pulses on a femtosecond scale with different polarizations to manipulate the magnetization of ferrimagnetic GdFeCo in the absence of an applied magnetic field [24]. This discovery became known as *helicity-dependent all-optical switching.* When using right-handed circular polarized laser pulses they could write a spin-up domain and when using left-handed circular polarized light, domains in a spin-down state were written. Linear polarized light resulted in thermal demagnetization without deterministic switching. Figure 1.2.3 shows the results of this experiment in two MOKE before- and after pictures of the sample. Besides in GdFeCo alloys, helicity-dependent all-optical switching was found in a broad range of ferrimagnetic rare-earth-transition-metal structures, such as FeTb [25], TbCo multilayers [26] as well as in ferromagnets such as CoPt or FePt nanoparticles [27, 28].

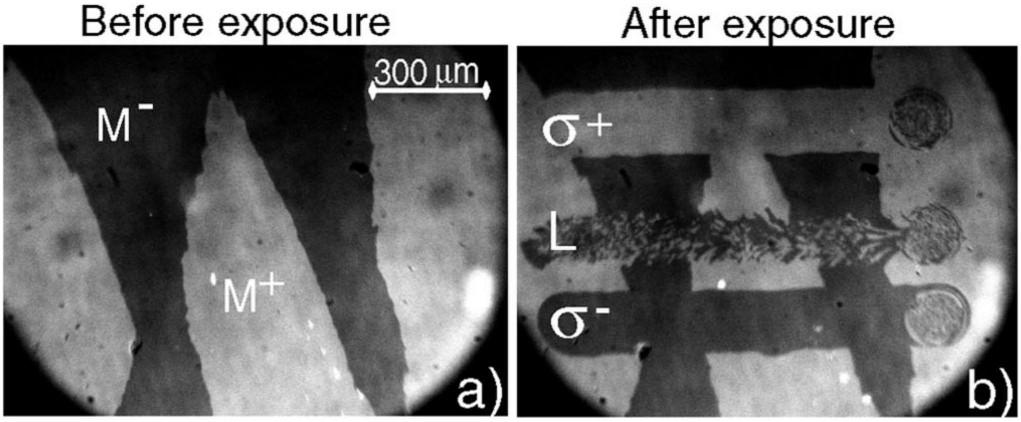

Figure 1.2.3: *MOKE images of the helicity-dependent writing process. Subfigure* ***a)*** *shows the before state with white and black areas corresponding to M^+ and M^- magnetic domains, respectively. Subfigure* ***b)*** *shows the same sample after exposure with a femtosecond laser. The exposure with right-handed circular polarized light caused a domain to be written in a spin-up state (σ^+ top), after exposure with left-handed circular polarized light the domain was imprinted in a spin-down state (σ^- bottom) and for linear polarized light only thermal demagnetization without deterministic switching was observed (L middle). Figure taken from Ref. [24].*

Possible explanations for this phenomena utilize the inverse Faraday effect [29, 30, 31]. The Faraday effect describes a rotation in the polarization that is proportional to the projection of the magnetic field along the propagation direction of the light wave. The inverse Faraday effect describes the opposite effect, whereby magnetization is induced via the electric field of an incoming light wave and the induced magnetization depends on the polarization of the light wave. By demagnetizing the probe with a high-intensity laser pulse and inducing an additional magnetization ΔM via the inverse Faraday effect, single pulse helicity-dependent all-optical switching can be explained.

However, the origin of all-optical helicity-dependent switching is still being debated and

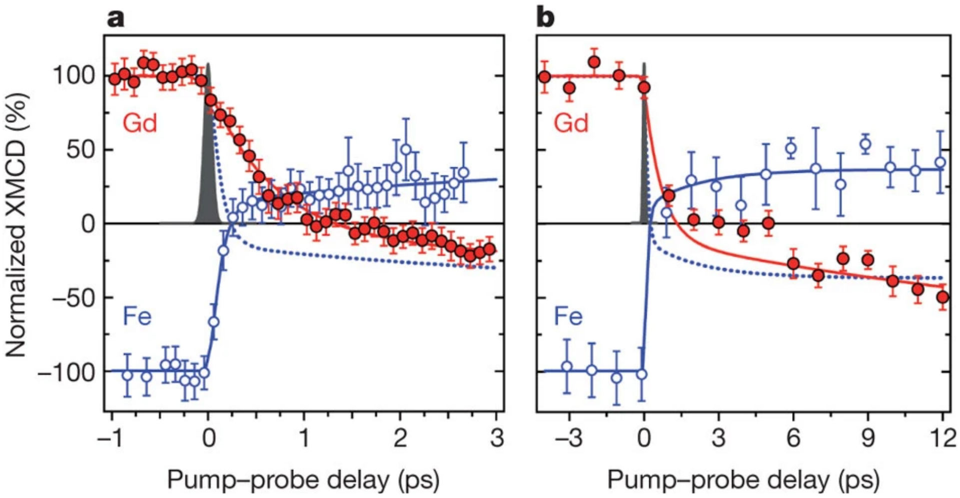

Figure 1.2.4: *Magnetization switching dynamics of $Gd_{25}Fe_{65.6}Co_{9.4}$ after excitation with a 60 fs laser pulse. XMCD measurements of Gd are shown as red points and Fe measurements are shown as blue points. The solid lines are fits according to a double exponential function. Subfigures* ***(a)*** *and* ***(b)*** *show the results of the experiments on different timescales. Figure taken from Ref. [6]*

other mechanisms, such as *magnetic circular dichroism* have been proposed, where the absorption of a light wave depends on its polarization [27]. In the years after the experiments of Stanciu and coworkers [24] it was found that linearly polarized light is also able to toggle switch GdFeCo compounds [6, 32]. Contrary to helicity-dependent all-optical switching the magnetic state was not overwritten, but instead the magnetization was just toggle-switched with a single linearly polarized laser pulse.

Thermally induced all-optical switching

Thermally induced all optical switching was discovered by Radu *et al.* in 2011. They used a 60 fs linear polarized laser pulse on amorphous $Gd_{25}Fe_{65.6}Co_{9.4}$ films and X-ray magnetic circular dichroism (XMCD) to record element-specific magnetization dynamics of both Gd and Fe. Figure 1.2.4 shows the results of these measurements on two different time scales. This breakthrough experiment revealed two key findings. First, the Fe sublattice demagnetizes four times faster than the Gd sublattice and second, the discovery of a *transient ferromagnetic like state*. After approximately 250 fs, while the Gd-sublattice is still demagnetizing, the Fe-sublattice aligns itself in parallel with the Gd-sublattice for a short time, despite the antiferromagnetic coupling between them. This short parallel alignment between the sublattices is not allowed in equilibrium due to the strong antiferromagnetic coupling and it is thus called a transient ferromagnetic-like state. After approximately 1 ps, the system starts to cool down again and the sublattices return to a ferrimagnetic state and remagnetize to a new equilibrium temperature.

Atomistic spin-dynamics simulations provide an excellent theoretical framework for studying experiments like these. Ostler and coworkers used them to show that in fact the thermal stimulus alone is sufficient for switching [32, 33]. Figure 1.2.5, recorded by Ostler *et al.*, displays magneto-optical images of a $Gd_{24}Fe_{66.5}Co_{9.5}$ film of the initial state and after exposure to several consecutive 100 fs-long laser pulses. These experiments show that each linear po-

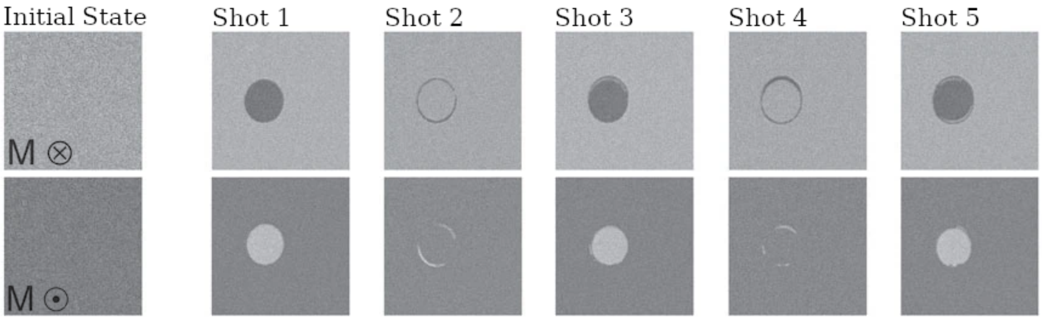

Figure 1.2.5: *Magneto-optical images of a $Gd_{24}Fe_{66.5}Co_{9.5}$ film of the initial state and after several consecutive 100 fs-long laser pulses. The first and second row differ in the initial magnetization direction. Figure adapted from Ref. [32].*

larized pulse toggle-switches the magnetization deterministically. This confirms the results shown in figure 1.2.4 and the switching process is deterministically driven by the thermal energy of the pulse alone.

Contrary to the helicity-dependent experiments by Stanciu *et al.* discussed in Chapter 1.2.2, the current magnetic state of GdFeCo is not overwritten. Instead the magnetization is only toggle-switched.

This type of switching was therefore called *helicity-independent all-optical switching*. These findings motivated research into new excitation mechanisms, away from ultrashort, femtosecond scale laser pulses. Experiments used the thermal stimulus of picosecond scale electric pulses as well as laser pulses of up to 15 ps to switch GdFeCo [34, 35, 36, 37]. This slower, picosecond-scale switching was unexpected, since the commonly accepted driving mechanism is based on faster exchange of angular momentum between sublattices than magnetization relaxation to the medium. Therefore, the efficiency of such a switching mechanism should be drastically reduced on longer time scales. These slower, picosecond-scale mechanisms open the door for electric pulses as stimuli as they are of particular technological interest.

Single pulse toggle-switching in ferrimagnets has also attracted a lot of attention as a promising solution for low-energy, faster-memory applications [38, 39, 40]. For the last decade, all-optical switching was only observed in specific rare-earth-transition-metal ferrimagnetic alloys such as GdFeCo, GdTbCo alloys [41, 42], Tb/Co stacks [43], or multilayered stacks of Pt/Gd/Co [44].

In 2020 a second class of materials showing all-optical switching capabilities was found, Mn_2Ru_xGa Heusler alloys [45, 46]. This raises the question of how much of the understanding of GdFeCo carries over to this new material class, since for Mn_2Ru_xGa so far only a handful of experimental works show ultrafast magnetization dynamics and switching. In particular, switching in rare-earth-transition-metal ferrimagnetic alloys is not fully understood either. For example it is currently unclear why for RE-TM alloys containing Gd switching can be observed, whereas Tb-based alloys without Gd, such as TbFeCo, do not show helicity-independent switching despite the presence of a transient ferromagnetic state [47]. While the ferromagnetic-like state lasts for more than 20 ps, the magnetization reverses back to its initial state. On the other hand, Tb-based alloys featuring a minuscule amount of Gd, such as $Gd_4Tb_{18}Co_{78}$ do switch upon heat excitation [41, 42].

Besides the question about classes of materials fit for switching, other parameters, such as the influence of the initial starting temperature and the impact of the ferrimagnetic compensation temperature, and their impact on switching are also subject of ongoing research [46]. Furthermore, the maximum duration of the switching stimulus and factors impacting this duration are investigated. Also, an understanding of single-pulse switching is missing due to the lack of an established theory accurately describing the transition to the nonequilibrium reversal path induced by femtosecond laser photoexcitation.

1.3 Outline of the thesis

This introductory chapter gives a brief introduction into ultrafast magnetization dynamics, starting from the first experimental discoveries in nickel towards thermally stimulated magnetization switching in GdFeCo. The suggested driving mechanisms behind these ultrafast processes have been presented briefly, such as Elliott-Yafet-type scattering and superdiffusive spin transport.

In Chapter 2 a brief introduction into the experimental methods of investigating ultrafast magnetization dynamics will be presented, namely the magneto-optical Kerr effect and X-ray magnetic circular dichroism to measure the dynamics of the spin subystem. Furthermore, additional methods will be presented to investigate the other involved subsystems, such as electrons and lattice. Angle-resolved photoemission spectroscopy allows the measurement of the band structure and the determination of the electron temperature. Femtosecond electron diffraction makes it possible to observe the evolution of the phonon temperature.
Afterwards a short introduction to the fundamental principles of density functional theory will be given with the goal of motivating the use of a localized electron-spin picture for itinerant ferromagnetic metals and the use of atomistic spin-dynamics simulations.
At last, the fundamentals of atomistic spin-dynamics simulations will be presented, starting with the classical Heisenberg-spin model from which the equilibrium state of the spin system can be derived. The stochastic Landau-Lifshitz-Gilbert equation describes the dynamics of atomistic spins at finite temperatures and will be introduced afterwards.
Since laser induced magnetization dynamics also rely on the simulation of the electron- and phonon temperature dynamics, the modeling of the laser excitation and their connection to the spin system will be discussed.
This work mostly focuses on a numerical simulation of the Landau-Lifshitz-Gilbert equation and thus a short overview of the numerical methods will be presented. At the end, a short overview over commonly used, phenomenological spin models will be given.

In Chapter 3, simulations of femtosecond laser-induced switching of the magnetization in the ferrimagnetic alloy GdFeCo are presented. One of the main questions investigated in this work was the impact of the laser pulse duration on the switching behavior. Phenomenological models suggest a femtosecond scale exchange relaxation between sublattice magnetization as the driving mechanism for switching. However, recent observations of thermally induced switching in GdFeCo by several picosecond optical laser pulses as well as electric current pulses have questioned this assumption. To that end, atomistic spin-dynamics simulations have been performed for a wide range of system parameters, such as composition, laser power and pulse duration. They are compared within this chapter with experimental results by J. Gorchon and coworkers from the University of California at Berkeley (US).

In Chapter 4, a new material showing helicity-independent all optical switching, namely $\mathrm{Mn_2Ru_xGa}$, is simulated using atomistic spin-dynamics simulations. The Heusler alloy $\mathrm{Mn_2Ru_xGa}$ has recently attracted a lot of attention, as in 2020 it was shown by Banerjee and coworkers, that this material can be switched all optically, making it a member of a second class of materials showing this behavior, besides rare-earth-transition-metal-alloys.
In this chapter, the spin Heisenberg Hamiltonian of $\mathrm{Mn_2Ru_xGa}$ is modeled based on experimental measurements and the discovered all-optical switching will be reproduced. Based on many years of experience coming from rare-earth-transition-metal-switching it was believed, that very different element-specific demagnetization dynamics are one of the requirements

for switching. This is fulfilled in alloys such as GdFeCo as they are composed of two different ions with different properties. However, the discovery of all-optical switching in $\mathrm{Mn_2Ru_xGa}$ Heusler alloys questions this understanding since both sublattices consist of Mn. Therefore the necessity for two different materials with different properties will be investigated.

Despite the experimental and theoretical demonstration of all optical switching in GdFeCo and $\mathrm{Mn_2Ru_xGa}$, a complete understanding of single-pulse all-optical switching is still missing. This is due to a lack of an established theory accurately describing the transition to the nonequilibrium reversal path induced by femtosecond laser photoexcitation. In Chapter 5, a general macroscopic theory for the magnetization dynamics of ferrimagnetic materials upon femtosecond laser excitation will be developed.
The model will be tested against atomistic spin-dynamics simulations of GdFeCo and the $\mathrm{Mn_2Ru_xGa}$ model developed in Chapter 4.

Chapter 6 will focus on the different magnetic response of antiferromagnets (AFMs) compared to ferromagnets (FMs). The exact behavior of AFMs under laser excitation is not fully understood due to the missing net magnetization of AFMs. Although scarce, experiments in AFMs suggest a faster response of the magnetic order parameter compared to FMs, such as studies in rare-earth Dy using femtosecond x-ray diffraction measuring FM and AFM-spin-helix states. It is assumed, that the exchange of angular momentum between sublattices in AFMs speeds up their dynamics, a process that is absent in ferromagnets. However, evidence of this exchange-enhancement of the ultrafast magnetization dynamics in AFMs is scarce due to the difficulties of conducting a systematic comparison on the same system with a FM and AFM magnetic order.
In Chapter 6 the exchange-enhancement of the antiferromagnetic order dynamics will be investigated theoretically in a variety of different scenarios. Furthermore, an equation of motion for the magnetic order dynamics will be derived from the developed model of Chapter 5 and validated by computer simulations using atomistic spin-dynamics simulations.

Since the discovery of ultrafast demagnetization in nickel most research focused on the spin and electron systems. However, ultrafast magnetization dynamics are governed by the interplay of electrons, spins and phonons and information on the response of all three subsystems is required. A consistent description of the demagnetization and microscopic energy flow in transition metals is still missing and common phenomenological models, such as the three-temperature model, are used.
Therefore, the last two chapters examine the magnetization dynamics of transition metals and the energy dynamics between electrons, phonons and spins after excitation with a femtosecond laser pulse. To that end, an energy-conserving atomistic spin model is developed that utilizes ab initio calculations of electron-phonon interactions. The modeled dynamics of the phonon system are compared to femtosecond electron-diffraction experiments performed by D. Zahn and coworkers at the Fritz-Haber Institute in Berlin, as well as previously reported electron and magnetization dynamics. Chapter 7 focuses hereby on nickel, whereas Chapter 8 deals with the transition metals iron and cobalt.

In the end, a brief summary of the most important results as well as an outlook will be given.

Chapter 2

Fundamentals

2.1 Experimental techniques

Even though this work focuses primarily on computational methods and theory, a basic understanding of the experimental techniques used in ultrafast magnetization dynamics is required in order to compare the theoretical results with experiments.
To that end, pump-probe experiments are most commonly used to investigate the response of a magnetic sample to a femtosecond laser pulse. In these experiments the magnetization is first taken out of equilibrium via a pump pulse. Afterwards, the response of the different subsystems, namely the magnetic spin system, the electron system or the phonon system is measured with a probe pulse. The spin system can be investigated with the magneto-optical Kerr effect or with the X-ray magnetic circular dichroism. The response of the electron system can be measured with angle-resolved photoemission spectroscopy and the phonon system via femtosecond electron diffraction. These experimental methods will be explained in more detail in the following.

2.1.1 The magneto-optical Kerr effect

The magneto-optical Kerr effect (MOKE) and the Faraday effect describe a change of the polarization state of light interacting with matter. Whereas the Faraday effect describes a polarization change upon transmitting light through a sample, the Kerr effect describes the change of polarization when the light is reflected from the surface of the sample. The polarization change upon reflection can be described by a complex Kerr angle

$$\Theta_K = \theta_K + i\epsilon_K, \tag{2.1.1}$$

where the real part θ_K is the *Kerr rotation* and the imaginary part ϵ_K is the *Kerr ellipticity.* Θ_K describes the difference of the polarization angles of the reflected light Θ_R and the initial incident light Θ_i.
The linear optical response of a material to an electric field $\mathbf{E}$ is described by the first order induced polarization vector $\mathbf{P}$:

$$\mathbf{P} = \int \chi^{(1)}(\mathbf{r}, \mathbf{r}') \cdot \mathbf{E}(\mathbf{r}') d\mathbf{r}'. \tag{2.1.2}$$

Here $\chi^{(1)}$describes the first order optical susceptibility tensor, that itself depends on the dielectric tensor ϵ via

$$\epsilon_{i,j} = \delta_{i,j} + 4\pi\chi^{(1)}_{i,j}. \tag{2.1.3}$$

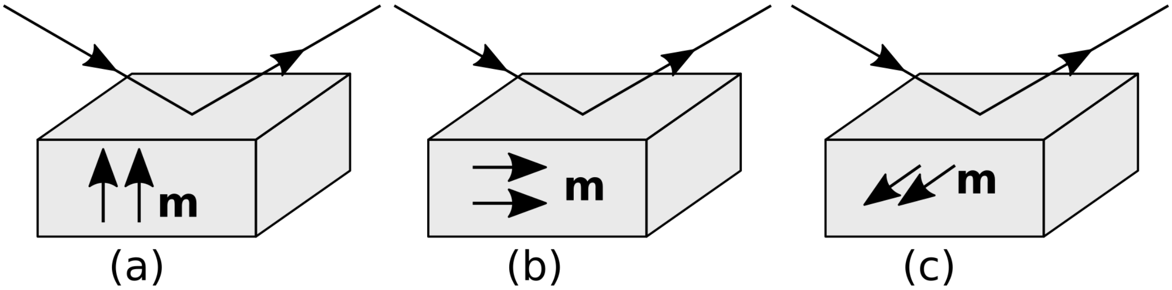

Figure 2.1.1: *Illustration of three possible configurations of the magneto-optical Kerr effect:* ***(a)*** *polar Kerr effect with the magnetization pointing out of the sample (PMOKE),* ***(b)*** *longitudinal Kerr effect with the magnetization in plane and in the plane of incident (LMOKE) and* ***(c)*** *transverse Kerr effect with in plane magnetization but perpendicular to the plane of the incoming light (TMOKE).*

For a non-magnetic material, the dielectric tensor only contains diagonal elements as these elements are independent of the magnetization $\mathbf{m}$. For a magnetic material the dielectric tensor features off-diagonal elements $Q\epsilon^{ijk}m_k$ with a material dependent parameter Q, (more details in Ref. [48]).
From the dielectric tensor ϵ a 2×2 reflectivity matrix $r_{ij}(\mathbf{m})$ can be calculated. This matrix describes how the initial polarization state is transformed onto the reflected one

$$E_{r,i} = r_{ij}(\mathbf{m})E_i^j. \tag{2.1.4}$$

Here $E_{i,j}$ and $E_{r,j}$ are the s- and p-amplitudes of the incoming and reflected light. From this the polarization angles can be calculated via $\Theta_i = \arctan(E_{i,s}/E_{i,p})$ for the incident light and as $\Theta_r = \arctan(E_{r,s}/E_{r,p})$ for the reflected light. Since the Kerr angle Θ_K depends on the magnetization-dependent off-diagonal elements, it becomes possible to calculate the sample's magnetization by measuring θ_K and ϵ_K.
There are three possible Kerr effect configurations, shown in figure 2.1.1. The polar Kerr effect (PMOKE) appears for a magnetization saturated out-of-plane (figure 2.1.1a). This case has the largest Kerr-sensitivity. In case of the longitudinal Kerr effect (LMOKE) the magnetization is aligned in plane while also being in the plane of incident (figure 2.1.1b) and in the transverse Kerr effect (TMOKE) the magnetization points in plane and perpendicular to the plane of incident (figure 2.1.1c).

The time-resolved magneto-optical Kerr effect

The magnetization dynamics induced by a laser can be measured using the time-resolved magneto-optical Kerr effect (TRMOKE). In a typically setup, a pump-probe scheme is used, where a laser pulse is split into a high-power pump pulse and a much weaker probe pulse. The probe pulse gets delayed via an adjustable delay line and linearly polarized [49, 50]. Both pulses are focused on the same spot of the sample and the delayed reflected probe pulse is analyzed to measure the magnetic response induced by the pump pulse. Besides femtosecond laser pulses it is also possible to use other pump mechanisms, such as short magnetic-field pulses [51, 52]. In order to perform time-resolved measurements the delay between the pump and probe pulse is changed step-by-step and the acquired Kerr signal is analyzed for each step. Since the sample reacts to the incoming pump pulse the time-resolved response of the sample can be measured this way.

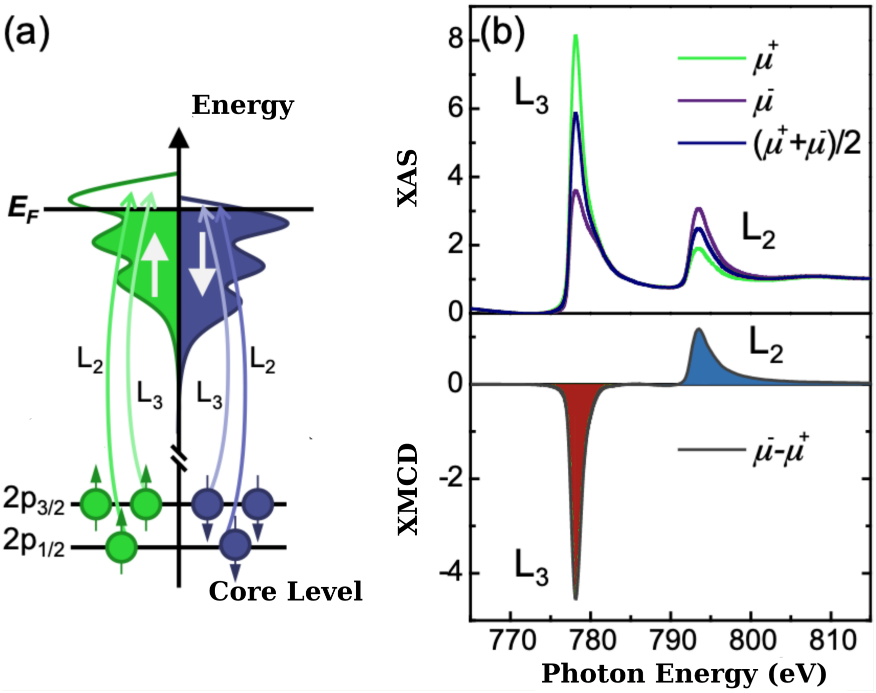

Figure 2.1.2: ***(a)*** *Schematics of the electron transition of XMCD in a transition metal showing the* $2p \rightarrow 3d$ *core-level excitation at the* $L_{2,3}$ *edges. Because of a lack of free d-states at the Fermi level of the majority band (shown in blue), only minority spins photoelectrons (shown in green) can be excited to the valence band.* ***(b)*** *X-ray absorption spectra (XAS) and XMCD spectra for the Co* $L_{2,3}$ *edge, showing the right* (μ_+) *and left* (μ_-) *circular polarization, along with their average (absorption spectrum) and the difference spectrum (XMCD). Figure adapted from Ref. [57].*

An example application of MOKE is shown in figure 1.2.1, where Beaurepaire *et al.* measured the first ultrafast demagnetization of nickel using TRMOKE.

2.1.2 X-ray magnetic circular dichroism (XMCD)

X-ray magnetic circular dichroism (XMCD) is in many ways analogous to the time-resolved magneto-optical Kerr effect. This method uses a shorter wavelength in the X-ray range. It detects the magnetic contrast through X-ray absorption, which depends on the relative orientation of the local magnetization and the light's polarization vector. Both the size and the direction of the magnetic moments can be measured element selectively. A big advantage of this method is the high time resolution of less than 100 fs, which makes it an excellent technique for studying ultrafast spin dynamics. The element-specific probing of materials makes it particularly interesting for the study of ferrimagnetism and it even allows the study of individual spin-, orbital- and dipolar moments and the magnetocrystalline anisotropy [53]. It is therefore an extremely versatile and often used experimental technique in the field of magnetic materials research [6, 54, 55, 56]. However, the major downside of this technique is its high effort as it requires X-rays with specific frequencies. These can only be achieved at electron synchrotron facilities. Figure 2.1.2 shows the basic process of XMCD for a transition metal. In the illustrated case the $2p$ core states are filled while the $3d$ states are only

half filled, which creates the net magnetic moment for transition metals. Spin-orbit coupling causes the $2p$ core states to split in a $j = 3/2$ level (L3 edge) and a $j = 1/2$ level (L2 edge) with a small energy difference between them ($l + s$ and $l - s$, respectively). In order to describe XMCD, it is easiest to follow the two-step picture presented by Stöhr [53, 58].
In a first non-magnetic step right- or left-circularly polarized photons transfer their angular momentum to the excited electrons. Since right- or left-circularly polarized photons transfer different angular momenta, $+\hbar$ and $-\hbar$, respectively, the excited electrons have opposite spins depending on the absorbed photon. Since the core states $p_{3/2}(\mathrm{L}_3)$ and $p_{1/2}(\mathrm{L}_2)$ have opposite spin-orbit couplings, the spin polarization will be different depending on the edges.
In a second step the excited electron scatters to an available unoccupied valence $3d$ states. Owing to the spin polarization of the valence states, there is a different number of spin-up and spin-down holes available, as indicated in figure 2.1.2 a). Therefore, the absorption cross section of the two polarizations is different, resulting in the magnetic dichroism effect. Stöhr refers to the spin-split valence shell as a 'detector' for the spin of the excited photoelectrons [58]. The results of such a measurement can be seen in figure 2.1.2 b) where the XMCD spectra for the Co L_2, L_3 edge is shown for right (μ_+) and left (μ_-) handed polarization, along with their average (top) and difference (bottom). If there are less spin-up than spin-down holes available, the XMCD spectrum has a net negative L_3 peak, and a positive L_2 peak. However, this simplified picture only describes s-shell excitations accurately. For $2p$ core states some spin-flip transitions are allowed. Thus contrary to the picture above, polarized X-rays are allowed to excite some spins of the opposite polarization. For example, for the L_2 edge left circular polarized light excites 25% spin-up and 75% spin-down electrons [53].
For rare-earth metals, the equivalent to the L_2, L_3 edges are the M_4 and M_5 edges, yielding excitations of $3\mathrm{d}_{3/2}$ and $3\mathrm{d}_{5/2}$ core states to unoccupied 4f-states [59]. One of the most prominent applications of XMCD in the field of ultrafast magnetism has been shown previously in figure 1.2.4 by Radu *et al.* [6], where XMCD was used to record element-specific magnetization switching in $\mathrm{Gd}_{25}\mathrm{Fe}_{65.6}\mathrm{Co}_{9.4}$.

X-ray magnetic linear dichroism (XMLD)

Besides using circular polarized light for X-ray absorption spectroscopy, it is possible to use linear polarized light. In this case, the effect is called *X-ray magnetic linear dichroism* (XMLD) and it is based on the different X-ray absorption cross sections of the **E**-vector of linear polarized X-rays, depending on its orientation in comparison to the magnetic moments. It is a second order effect, that depends on the magnetization $\langle M^2 \rangle$ and on the magneto-crystalline anisotropy. The XMLD signal is therefore much smaller than XMCD and it is thus less commonly used for the investigation of transition metals [60, 61]. However, it still finds application in the investigation of antiferromagnets, such as NiO [62, 63], or in the measurement of magneto-crystalline anisotropy [64, 65].

2.1.3 Other experimental techniques

In order to fully understand the dynamics of the magnetic spin system, other subsystems and their interactions, such as the electron and the phonon system, need to be considered too. In Chapter 1.2.1 the experiments by Beaurepaire *et al.* were presented that measured for the first time ultrafast demagnetization of nickel [5]. In order to explain their measurements they used the three-temperature model, that assumes different temperatures for the involved subsystems, namely electrons, spins and phonons and various coupling constants to exchange energy between the subsystems. Theoretical models like the Koopmans' model, that explain rapid spin relaxation via Elliott-Yafet-like processes, also model the involved electron and phonon subsystems [14]. In order to understand ultrafast spin dynamics, it is therefore essential to also understand the electron and phonon subsystems.

Angle-resolved photoemission spectroscopy (ARPES)

The electron subsystem can be measured with methods such as angle-resolved photoemission spectroscopy (ARPES) [66, 67]. This method allows for the measurement of the band structure of a solid and is based on the photoelectric effect. During the experiment, a monochromatic laser beam, typically in the ultraviolet or higher spectral range is used. If the incoming photon provides sufficient energy to overcome the necessary work ϕ, electrons are emitted from the sample. The kinetic energy ϵ_{kin} of such an electron can be written as

$$\epsilon_{\text{kin}} = \hbar\omega - \phi - |\epsilon_{\mathbf{k}}|. \tag{2.1.5}$$

Here ω describes the angular frequency of the incoming photon and $\epsilon_{\mathbf{k}}$ stands for the binding energy in regard to the Fermi level ϵ_F. Equation 2.1.5 makes it possible to relate the kinetic energy of the emitted electron to its initial binding energy. The amount of detected electrons is furthermore proportional to their emission probability, which is related to their density of states. By measuring the emission angle of the emitted electrons it is possible to calculate their in-plane momentum and thus obtain an understanding of the band structure.

Femtosecond electron diffraction (FED)

In order to measure the phonon system, *femtosecond electron diffraction* (FED) (or sometimes *ultrafast electron diffraction*) can be used. FED combines a temporal resolution of hundreds of femtoseconds with real-space structural information of the lattice on the atomic scale and it is therefore an excellent tool for measuring the lattice and phonon response to an incoming short laser or heat pulse.

Similar to other methods in the field of ultrafast magnetization dynamics it uses a pump-probe scheme. However, in order to probe the lattice an electron- instead of a laser pulse is used. An in-depth explanation of this experimental setup and details can be found in Ref. [68] and is here summarized briefly.

After exciting the sample with a laser pump pulse the lattice response is measured with an electron probe pulse. This causes the electron pulse to diffract and the resulting diffraction patterns are detected with an electron camera. The recorded diffraction pattern contains structural information of the sample. By tracking the relative change of the intensity of selected Bragg peaks, as well as the change of the integrated background intensity for different pump-probe delays, the temporal response of the lattice can be measured. Figure 2.1.3 shows an example of a radial average obtained by angularly integrating the diffraction image shown in the insert. Immediately after photoexcitation, energy is transferred from the

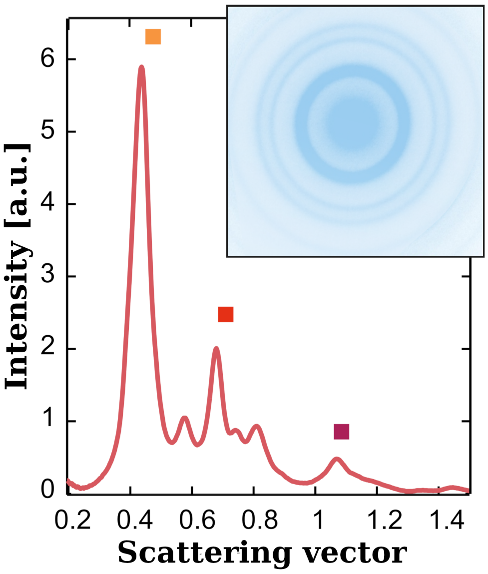

Figure 2.1.3: *The radial average obtained by angularly integrating the diffraction image of titanium shown in the insert. The image was averaged from over 2500 electron pulses with an energy of 100 keV. Three Bragg peaks are marked with a square. Figure adapted from Ref. [68] and Ref. [69].*

electron subsystem to the phonon system, which moves towards a new higher thermal equilibrium temperature. This causes the Debye-Waller factor and therefore the relative height of the Bragg-peaks to decrease, which is caused by an increase of the mean square displacement $\langle u^2 \rangle$ of the atoms around their equilibrium positions. The background also increases due to inelastically scattered electrons. The tracked change in mean square displacement can then be correlated with the phonon temperature (see Chapter 7).

2.2 Atomistic spin dynamics from ab initio theory

In this chapter a brief introduction of density functional theory (DFT) is presented following Refs. [70] and [71]. The goal of this section is to shortly introduce fundamental principles of density functional theory in order to motivate and justify the use of atomistic spin-dynamics simulations for ultrafast magnetization dynamics.
For example, as spin systems are inherently quantum systems, it is not intuitively clear, why the semiclassical approach made by atomistic spin-dynamics simulations compare well to experimental measurements [72]. Furthermore, it requires some explaining, why the Heisenberg model that assumes localized spins or insulators can be used for transition metals that feature an electron gas with itinerant electrons. Thus, the goal of this chapter is to establish the groundwork for atomistic spin-dynamics simulations from first-principle calculations.

The tremendous complexity of solving the Schrödinger equation for many interacting electrons is the core problem that DFT is trying to solve. The non relativistic Hamiltonian $\hat{H}$ for such a case can be written as:

$$\hat{H} = -\frac{\hbar^2}{2}\sum_I \frac{\nabla_I^2}{M_I} + \frac{1}{2}\sum_{I\neq J}\frac{1}{4\pi\epsilon_0}\frac{Z_I Z_J e^2}{|\mathbf{R}_I - \mathbf{R}_J|} - \frac{\hbar^2}{2m}\sum_i \nabla_i^2 + \frac{1}{2}\sum_{i\neq j}\frac{1}{4\pi\epsilon_0}\frac{e^2}{|\mathbf{r}_i - \mathbf{r}_j|} - \sum_{i,I}\frac{1}{4\pi\epsilon_0}\frac{Z_I e^2}{|\mathbf{r}_i - \mathbf{R}_I|}, \tag{2.2.1}$$

where the indices i, j describe electrons with mass m and charge e, I, J indicate atomic nuclei with their masses M_I. $\mathbf{R_I}$ and $\mathbf{r_I}$ describe nuclei and electron coordinates, respectively, and Z_I is the atomic number. Since the nuclei are much heavier than electrons, the Born-Oppenheimer approximation can be used, assuming fixed nuclei while treating the electrons as dynamic objects. This simplifies the Hamiltonian to:

$$\hat{H} = -\frac{\hbar^2}{2m}\sum_i \nabla_i^2 + \frac{1}{2}\sum_{i\neq j}\frac{1}{4\pi\epsilon_0}\frac{e^2}{|\mathbf{r}_i - \mathbf{r}_j|} - \sum_{i,I}\frac{1}{4\pi\epsilon_0}\frac{Z_I e^2}{|\mathbf{r}_i - \mathbf{R}_I|} = \hat{T} + \hat{W} + \hat{V}_{\text{ext}}. \tag{2.2.2}$$

Here, $\hat{T}$ is the kinetic energy operator of the electrons, $\hat{W}$ is the operator determining the Coulomb energy of electron-electron interactions and $\hat{V}_{\text{ext}}$ is the external potential accounting for the Coulomb interaction between electrons and nuclei. The total energy is the expectation value of $\hat{H}$

$$E = \langle\Psi|\hat{H}|\Psi\rangle = T + W + \int d^3r V_{\text{ext}}(\mathbf{r})n(\mathbf{r}), \tag{2.2.3}$$

with T and W describing the expectation values of $\hat{T}$ and $\hat{W}$ and $n(\mathbf{r})$ being the electron charge density. Hohneberg and Kohn showed, that the total energy of a system is a unique functional of the ground-state electron density [73]. The expressions for the kinetic energy and the electron-electron interaction are the same for any system, it is thus the external potential that makes the Hamiltonian unique and hence specifies it [70]. Therefore, DFT assumes that knowing $n_{gs}(\mathbf{r})$, the ground state electron density,

$$n_{gs}(\mathbf{r}) = \sum_{i=1}^{N}\int d^3r_i |\Psi_{gs}(\mathbf{r}_1, \mathbf{r}_2, ...\mathbf{r}_N)|^2 \delta(\mathbf{r} - \mathbf{r}_i) \tag{2.2.4}$$

implies that the potential used in the Hamiltonian is known. The full Hamiltonian and all of its states including the excited ones are specified. This makes the charge density $n(\mathbf{r})$ a key quantity in describing the ground state of the system and replacing the need for a many-electron wave function. The energy of the ground state can be expressed via the ground-state electron-charge density

$$E[n(\mathbf{r})] = T[n(\mathbf{r})] + W[n(\mathbf{r})] + V_{\text{ext}}[n(\mathbf{r})]. \tag{2.2.5}$$

and finding the exact ground-state density minimizes this energy. For an explicit form of $E[n(\mathbf{r})]$ one could minimize the expression in equation 2.2.5 with respect to $n(\mathbf{r})$. In practice this is challenging, especially for $T[n(\mathbf{r})]$ and $W[n(\mathbf{r})]$. The solution of this problem was attempted by Kohn and Sham [74].

2.2.1 The Kohn-Sham approach

For the Kohn-Sham approach it is first assumed that W, the electron-electron interaction part of equation 2.2.5, is absent. In that case electrons moving in the field of an external potential V_{eff} can be described by the one-electron Schrödinger equation:

$$\left(-\frac{1}{2}\nabla^2 + V_{\text{eff}}(\mathbf{r})\right)\Psi_i(\mathbf{r}) = \epsilon_i \Psi_i(\mathbf{r}). \tag{2.2.6}$$

This equation is also referred to as the *Kohn-Sham equation* in the context of density-functional theory calculations. The solutions of this equation can be used to calculate a one-particle density by summing over all occupied states:

$$n_{op}(\mathbf{r}) = \sum_{occ} |\Psi(\mathbf{r})|^2. \tag{2.2.7}$$

The basic principle of the Kohn-Sham approach is the assumption, that one can find an effective potential V_{eff}, such that the density n_{op} is the same as the ground-state density of the fully interacting system, n_{gs}. It can be proven that this is true for a homogeneous electron gas, but not in general. However, this is an efficient way to get an approximation of the ground state electron density of a fully interacting system by carefully selecting an effective potential, even if it results from a one-particle system.

The challenge is to find V_{eff} so that $n_{op}(\mathbf{r})$ becomes equal to $n_{gs}(\mathbf{r})$. This can be done by using the Hartree electrostatic interaction instead of the full electron-electron interaction. To account for the error made by this approximation, one introduces the exchange-correlation energy density $\epsilon_{\text{xc}}[n_{op}(\mathbf{r})]$ and one can deduct an expression for V_{eff} (more details on this in Refs. [70, 75, 76]):

$$V_{\text{eff}}(\mathbf{r}) = V_{\text{ext}}(\mathbf{r}) + \int \frac{n_{op}(\mathbf{r}')}{|\mathbf{r}-\mathbf{r}'|} d^3r' + \epsilon_{\text{xc}}[n_{op}(\mathbf{r})] + n_{op}(\mathbf{r}) \frac{\partial\{\epsilon_{\text{xc}}[n_{op}(\mathbf{r})]\}}{\partial n_{op}(\mathbf{r})}. \tag{2.2.8}$$

The Kohn-Sham equation (equation 2.2.6) can now be solved with the effective potential introduced in equation 2.2.8. Since the effective potential of equation 2.2.8 depends on the electron density, which is the property one is trying to derive, a self-consistent calculation has to be performed, where an initial electron density is first guessed and then used to calculate V_{eff}. This V_{eff} is then used to solve the Kohn-Sham equation which in return yields a new electron density via equation 2.2.7, which is then used to calculate a new effective potential V_{eff} in equation 2.2.8. This is repeated until convergence is obtained. Since the electron density is a key quantity in the DFT approach, other properties, such as the energy of the ground state, can be calculated from it.

2.2.2 Deducting magnetic properties

For magnetic materials, spin-up and spin-down electrons experience different effective potentials $V_{\text{eff}}^{\uparrow}$ and $V_{\text{eff}}^{\downarrow}$ and therefore, one must treat the Kohn-Sham equation (equation 2.2.6) separately for spin-up and spin-down states. That difference amounts to a constant shift between the electron states of the two spin channels, which is referred to as exchange splitting. With this, important parameters of magnetic materials can be calculated, such as the magnetic moment. Furthermore, it is possible to calculate the band structure or band dispersion and the energy-resolved density of states, as well as atomic magnetic moments and the interatomic exchange interactions. Therefore DFT calculations are performed for **k**-points in the irreducible part of the first Brillouin zone. To that end, the Kohn-Sham equation must be solved for the selected **k**-point.

One commonly used approach is to expand the unknown wave function $\Psi_{\mathbf{k}}(\mathbf{r})$ in a set of basis functions $\chi_{l\mathbf{k}}$:

$$\Psi_{\mathbf{k}}(\mathbf{r}) = \sum_{l}^{l_{\max}} c_{l\mathbf{k}} \chi_{l\mathbf{k}}(\mathbf{r}). \tag{2.2.9}$$

In this sum, l is referring to an index that involves the principle quantum number, the orbital quantum number, and the magnetic quantum number. There are different choices for a set of basis functions $\chi_{l\mathbf{k}}$, giving rise to different electronic structure methods, such as LCAO (linear combination of atomic orbitals), LAPW (linearized augmented plane waves) or LMTO (linear muffin tin orbitals).

Based on equation 2.2.9, a system of equations can be deducted whose eigenstates $\Psi_{\alpha,\mathbf{k}}$ can be used to calculate the one-electron density (see Ref. [71] and Ref. [70] for more details). This is done by summing over all possible **k**-vectors and occupied eigenstates for each spin channel separately:

$$n^{\uparrow}(\mathbf{r}) = \sum_{i}^{occupied} \sum_{k} \left| \Psi_{i\mathbf{k}}^{\uparrow}(\mathbf{r}) \right|^2 \tag{2.2.10}$$

$$n^{\downarrow}(\mathbf{r}) = \sum_{i}^{occupied} \sum_{k} \left| \Psi_{i\mathbf{k}}^{\downarrow}(\mathbf{r}) \right|^2 \tag{2.2.11}$$

from which the electron and the magnetization densities ($m(\mathbf{r})$) are obtained through

$$n(\mathbf{r}) = n^{\uparrow}(\mathbf{r}) + n^{\downarrow}(\mathbf{r}) \tag{2.2.12}$$

$$m(\mathbf{r}) = n^{\uparrow}(\mathbf{r}) - n^{\downarrow}(\mathbf{r}). \tag{2.2.13}$$

Plotting the eigenvalues of the Kohn-Sham equation as function of **k** yields a band structure plot. Figure 2.2.1 shows the band structure of bcc Fe for spin-up electrons on the left and spin-down electrons on the right. The figure shows, that the eigenvalues strongly depend on **k**, known as band dispersion. Furthermore, the exchange splitting is clearly visible, meaning the spin-down states are shifted up in energy compared to the lower spin-up states. Therefore, a higher number of spin-up states is occupied than spin-down states, yielding a net magnetization. The exchange splitting is particularly noticeable around the Fermi level, as these energy bands are dominated by the Fe 3d orbitals, which experience the largest effect of the exchange interaction and hence have the largest exchange splitting. The magnetic spin moment, based on the data shown in figure 2.2.1, coincides almost perfectly with the experimentally measured magnetic moment.

Density functional theory can also be used to calculate the density of states of an electronic

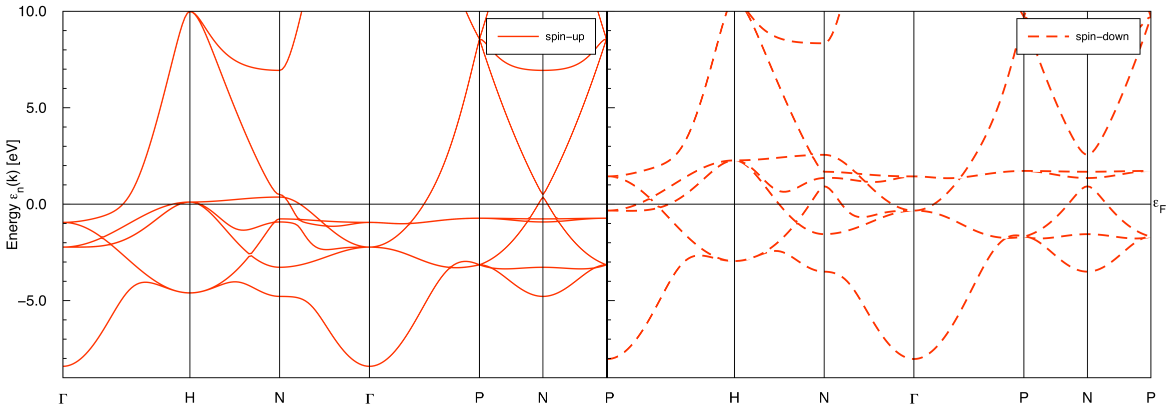

Figure 2.2.1: *Band structure of bcc Fe. The band structure of spin-up electrons is shown on the left and of spin-down electrons on the right-hand side (dashed). The Fermi energy is marked as a line at 0 eV. Figure adapted from Ref. [77].*

structure as well as to calculate the spin anisotropy coming from spin-orbit coupling. This anisotropy locks the magnetization direction on specific crystalline orientations. More on this will be discussed in Chapter 2.3.1.

2.2.3 From density functional theory to atomistic spin-dynamics simulations

One of the most interesting results coming from DFT calculations for atomistic spin-dynamics simulations is the magnetization density $m(\mathbf{r})$. Figure 2.2.2 a) shows the magnetization density of bcc Fe. Darker areas indicate an increase in magnetization density, lighter areas an absence of magnetization. The nuclei of the system, positioned at the corners of the image, have most of the magnetization in their vicinity since the $3d$ orbitals are centered on these atoms. Figure 2.2.2 b) shows the same magnetization density calculation for a larger area. This magnetization localization is not unique to bcc Fe, but is found in most magnetic materials. This is caused by the mentioned exchange splitting of the delocalized electron states with significant band dispersion, as shown in figure 2.2.1.

Since the areas of high magnetization density are located around the nuclei, and the interstitial regions only contribute negligibly, the quantum mechanical description can be replaced by an atomistic description of magnetism. Instead of using densities of spin-up and spin-down electrons, the relevant information is replaced by an integrated property, such as a magnetic moment. The magnetic moment of a single atom can therefore be treated as a single spin in the Heisenberg model, as illustrated in the insert of figure 2.2.2 b).

The magnetization density shown in figure 2.2.2 is generated by electrons moving through the material. If the time-dependent DFT (not discussed here) had been used to calculate this, fluctuations around the time-independent densities would be visible in figure 2.2.2. Without an external driving stimulus, such as a laser, the frequency of such fluctuations must come from the electrons traveling through the lattice. They spend some time at one atomic site before jumping over to the next one. The exact frequency of this is material dependent. They can be estimated to be between 10-100 fs for most materials, based on an estimation on drift velocity and average atomic distance. Therefore, the description of the magnetization dynamics of atomic spins using averaged atomistic moments is valid on time scales larger

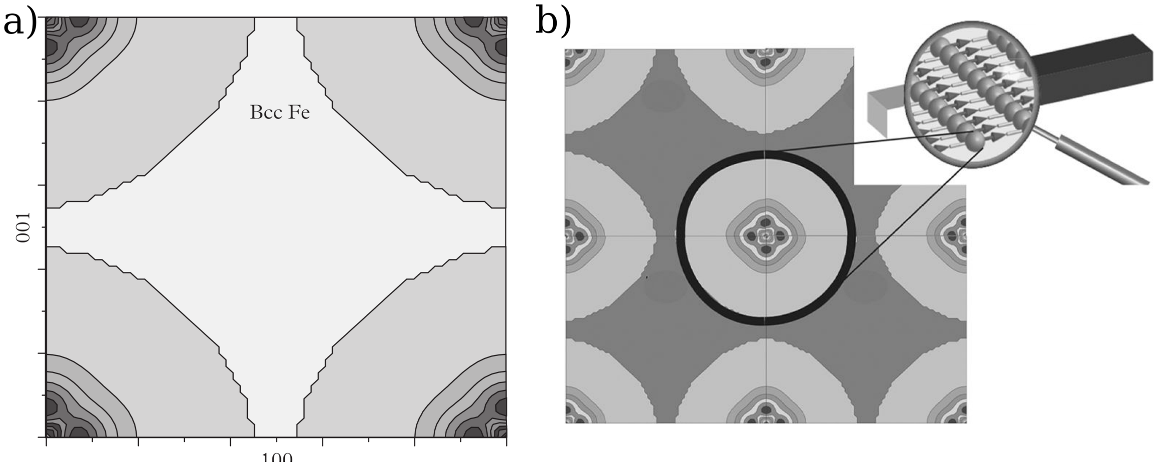

Figure 2.2.2: ***(a)*** *Magnetization density of bcc Fe in real space. Darker areas indicate an increase in magnetization density, lighter areas indicate a lower magnetization density. The nuclei of the system are located at the corners of the image.*
(b) *Schematic illustration of multiscale spin modeling. Like in subfigure* ***(a)*** *darker areas indicate an increase in magnetization density with subfigure* ***(a)*** *on a larger scale. Since the areas of high magnetization density are located around the nuclei, they can be treated as a single spin in the Heisenberg model and in atomistic spin-dynamics simulations. This step is indicated in the top right. Image adapted from Ref. [70].*

than 10–100 fs. In this case, the smaller, faster fluctuations of the magnetization density can be ignored and a Born–Oppenheimer-like (adiabatic) approximation can be adopted for the magnitude and direction of the atomic spins.

The new atomistic description of magnetism uses a Heisenberg Hamiltonian that takes the form

$$\mathcal{H} = -\sum_{i \neq j} \mathcal{J}_{i,j} \mathbf{S}_i \cdot \mathbf{S}_j, \tag{2.2.14}$$

where $\mathcal{J}_{i,j}$ is the exchange interaction between the magnetic moments $\mathbf{S}_i$ and $\mathbf{S}_j$ at sites i and j (more on this in Chapter 2.3.1).

The connection between DFT and the atomistic Heisenberg model was made by Liechtenstein *et al.* [78, 79]. They mapped the electronic structure onto a Heisenberg pair interaction potential $\mathcal{J}_{i,j}$ using the magnetic force theorem. They found that for any two spins, for a small angle deviation from the ground state θ, the total energy changes proportional to θ^2. Using multiple scattering theory, an expression was found for $\mathcal{J}_{i,j}$

$$\mathcal{J}_{ij} = \frac{\mathrm{Im}}{4\pi} \int_{-\infty}^{E_F} \mathrm{Tr}\left[\delta_i(E) G_{ij}^{\uparrow}(E) \delta_j(E) G_{ji}^{\downarrow}(E)\right] dE, \tag{2.2.15}$$

where the trace is over orbital indices. E_F is the Fermi energy, $\delta_i(E)$ yields the local exchange splitting between spin-up and spin-down states at site i and $G_{ij}^{\sigma}(E)$ is the Green function that connects site i and j for electrons with spin σ. An in depth explanation and derivation of this result is found in Refs. [78] and [79] and it is just introduced here for completeness.

It is worth noting, that equation 2.2.15 was derived for a collinear spin alignment, it is thus in principle not relevant at finit temperatures. Despite this, equation 2.2.15 can still be treated as a good approximation for the Heisenberg exchange at finite temperature [70].

2.3 Modeling ultrafast magnetization dynamics with atomistic spin-dynamics simulations

This chapter presents the basic model used in this thesis, atomistic spin-dynamics (ASD) simulations. It relies on the Heisenberg model, that uses classical spins whose dynamics is described by the stochastic-Landau–Lifshitz–Gilbert equation.
The connection between DFT-based methods to ASD was already presented in the previous chapter. Even though spin systems are quantum systems, the semiclassical approach made by ASD yields good agreement with experimental measurements for the description of magnetic systems at elevated temperatures [72]. The simplifications made by the atomistic model are necessities for a numerical approach, since even simulating only few atoms over short times using a full quantum-mechanical picture and the time-dependent DFT requires enormous computational resources [80].
The choice of an atomistic description of magnetization dynamics over a continuous vector field, as is done in micromagnetic simulations, has several advantages. First, the building block of materials is the atom, and hence a description of magnetism in an atomistic way is very natural and allows for an interpretation of experimental results in a deeper and clearer way. The stochastic Landau–Lifshitz–Gilbert equation is able to simulate magnetic materials at elevated temperatures. This makes it an excellent tool to simulate many ultrafast effects and phenomena such as ultrafast demagnetization of transition metals or magnetization switching, as introduced in Chapter 1.2. As shown in Chapter 2.2, many parameters such as the Heisenberg exchange can be derived from first principles using density-functional theory, without the need of using experimental results as input for simulations. Furthermore, atomistic spin-dynamics simulations are able to reproduce a wide range of magnetic phenomena, from ferro-, antiferro- and ferrimagnets to domain walls and skyrmions.

2.3.1 The Heisenberg model

The Heisenberg model was originally proposed by Werner Heisenberg in 1928 [81]. It assumes classical spins $\mathbf{S}$ normalized via the atomic spin moment μ_s. The spin moment μ_s is related to the saturation magnetization via

$$\mu_s = \frac{M_s a^3}{n}, \tag{2.3.1}$$

where M_s is the saturation magnetization at 0 K, a is the size of the unit cell, and n is the number of atoms per unit cell. μ_s is typically given in multiples of the Bohr magneton μ_B owing to its electronic origin.
Each spin interacts with its neighbouring spins via the Heisenberg exchange interaction J and the Heisenberg Hamiltonian becomes:

$$\mathcal{H}_\mathrm{exc} = -\sum_{i \neq j} J_{ij} \mathbf{S}_i \cdot \mathbf{S}_j. \tag{2.3.2}$$

Here $\mathbf{S}_i = \boldsymbol{\mu}_i / \mu_{s,i}$ represents a classical, normalized spin vector at site i. $\mathbf{S}_i$, couples to its neighboring spin $\mathbf{S}_j$ via the coupling constant J_{ij} with $J_{ij} > 0$ for ferromagnetic coupling and $J_{ij} < 0$ for antiferromagnetic coupling.
Heisenberg assumed that the exchange between two spins comes from the overlapping of

the atomic orbitals and thus only includes nearest-neighbour interactions. However, this is only true for insulators or localized spins. In metals electrons have itinerant character and the Heisenberg exchange in these materials is caused by Coulomb interaction and Pauli's exclusion principle for fermions [82].

As described in Chapter 2.2, it is possible to calculate the Heisenberg exchange J from first principles using density functional theory. A second possibility for calculating the exchange interaction J is using experimental parameters such as the Curie temperature T_c. For a generic atomistic model with z nearest neighbour interactions, the exchange constant can be derived from the mean-field expression [83]:

$$J = \frac{3k_\mathrm{B}T_c}{z \cdot \epsilon}. \tag{2.3.3}$$

Here k_B is the Boltzmann constant and ϵ is a correction factor which arises from magnon-magnon interaction in the 3D Heisenberg model [84].

Even though the original model by Heisenberg only considered nearest-neighbour exchange, more complex spin structures can be modeled using frustrated exchange interactions over many neighbours, such as spin spirals or Skyrmions [85].

Additional contributions

The Heisenberg exchange alone is fully isotropic and yields magnetic ordering on an atomic level. The magnetic anisotropy is a second important contribution to the Hamiltonian. It is responsible for the alignment along a preferred spatial direction. There are several effects which give rise to anisotropy, but the most important one is the magnetocrystalline anisotropy coming from spin-orbit coupling which connects the spin degrees of freedom with the electronic orbitals, i.e. the crystal lattice.

The contribution of the anisotropy reads as:

$$\mathcal{H}_\mathrm{ani} = -d_z \sum_i S_{i,z}^2. \tag{2.3.4}$$

Depending on the sign of the anisotropy constant d_z, the term denotes either an easy axis, which lowers the internal energy if the magnetization aligns itself in this direction, or a hard axis, which causes an energy increase.

Like the Heisenberg exchange, the magnetocrystalline anisotropy can be calculated from first principles using DFT [70]. The anisotropy only plays a minor role in ultrafast magnetization dynamics since its contribution to the total energy of the Hamiltonian is typically just around 1% of the exchange contribution. However, it can play an important role during the remagnetization after the initial excitation, as it causes the magnetization to realign itself with the easy axis of the system. This process typically happens on timescales of several picoseconds up to the nanosecond range.

At last the energy of an external field must be considered in the Hamiltonian. This is done via the Zeeman energy term that can be written as

$$\mathcal{H}_\mathrm{Zee} = -\mu_\mathrm{s} \sum_i S_i \cdot \mathbf{B}. \tag{2.3.5}$$

This term makes it energetically more favourable for the spins to align themselves parallel to the applied external magnetic field $\mathbf{B}$.

The total energy of the system is therefore the sum of all contributions introduced:

$$\mathcal{H} = \mathcal{H}_\mathrm{exc} + \mathcal{H}_\mathrm{ani} + \mathcal{H}_\mathrm{Zee}. \tag{2.3.6}$$

Furthermore, additional effects such as long ranging dipole-dipole interaction or Dzyaloshinskii–Moriya interaction, can be added to the Hamiltonian. However, dipole-dipole interaction is not included here, as it is of limited importance for ultrafast spin dynamics and including it comes with a large computational cost.

2.3.2 Magnetic ordering phenomena

Ferromagnetism

The simplest magnetically ordered state is a ferromagnet (FM). Typical examples are the transition metals iron, nickel and cobalt as well as some of the lanthanide metals [82]. In a ferromagnet, the magnetic moments of individual atoms are aligned in parallel to each other in small regions, so-called domains. This parallel ordering of magnetic moments is illustrated in figure 2.3.1 a). In an unmagnetized state adjacent domains are statistically distributed and have different magnetic net moments (the sum of all individual magnetic moments) pointing in different directions. If a magnetic field is applied the individual domains can align themselves with the external field becoming a permanent magnet. Above the Curie temperature T_c a ferromagnet looses its magnetic ordering and becomes paramagnetic.

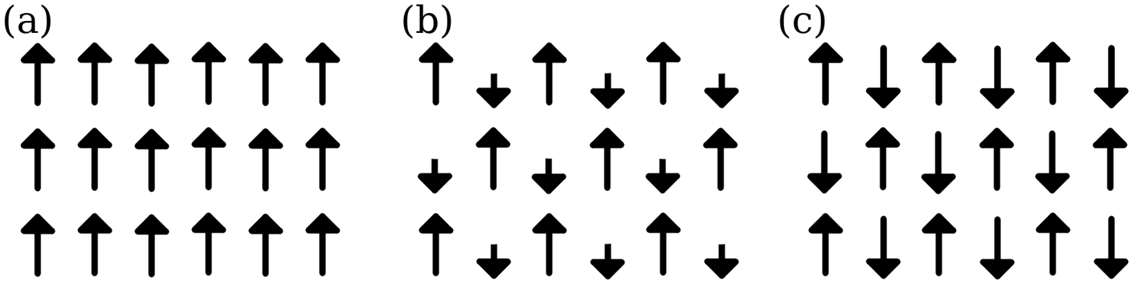

Figure 2.3.1: *Illustrations of typical magnetically ordered states.* ***(a)*** *Ferromagnetism,* ***(b)*** *Ferrimagnetism,* ***(c)*** *Antiferromagnetism.*

Ferrimagnetism

In ferrimagnets the magnetic moments of adjacent spins μ_A and μ_B are of different size and point in opposite directions since they couple antiferromagnetically. This means the Heisenberg exchange in equation 2.3.2 is negative.

Figure 2.3.1 b) shows an illustration of a ferrimagnetic ordering of spins. In general the magnetic moments of both sublattices do not fully cancel each other, however, depending on the two sublattices and their respective material parameters, ferrimagnets can feature a so-called magnetization compensation temperature T_M. $T_\mathrm{M} < T_c$ is referring to the temperature at which the magnetization of both sublattice cancels each other, so that the total magnetization becomes zero. For temperatures different to T_M a net-magnetization can be measured. Depending on the exact ratio of magnetic moments, ferrimagnets can feature ferromagnetic like behaviour $\mu_A \ll \mu_B$ or an antiferromagnetic like behaviour $\mu_A \approx \mu_B$. Typical examples of ferrimagnets are GdFeCo or $\mathrm{Mn_2Ru_xGa}$.

Antiferromagnetism

An antiferromagnet is a ferrimagnet where the magnetic moments of both sublattices are of equal size $\mu_A = \mu_B$. They therefore compensate each other completely and no net magnetization can be measured. An illustration of an antiferromagnetic alignment of spins is shown in figure 2.3.1 c). The equivalent to the Curie temperature of a ferromagnet, is called Néel temperature, T_N for antiferromagnets. It describes the temperature at which an antiferromagnet becomes paramagnetic and no magnetic order can be found. An example of an antiferromagnetic material is MnO [82].

Paramagnet

Due to the finite Heisenberg exchange strength between magnetic moments, the magnetic order will eventually undergo a second order phase transition from an ordered state to an unordered paramagnetic state. This critical temperature is called Curie temperature T_c for ferro- and ferrimagnets and Néel temperature, T_N for antiferromagnets.

2.3.3 The stochastic Landau-Lifshitz-Gilbert equation

In the previous section the classic Heisenberg Hamiltonian was introduced. It describes the equilibrium state of the spin system and its magnetic properties. In order to simulate non-equilibrium scenarios the equation of motion of each spin, the Landau-Lifshitz-Gilbert equation

$$\frac{\partial \mathbf{S}}{\partial t} = -\frac{\gamma}{(1+\alpha^2)\mu_s}\mathbf{S}_i \times \mathbf{H}_i - \frac{\gamma\alpha}{(1+\alpha^2)\mu_s}\mathbf{S}_i \times (\mathbf{S}_i \times \mathbf{H}_i)\,, \tag{2.3.7}$$

needs to be solved. In this work this is done numerically for millions of spins which yields the non-equilibirum dynamics of the entire spin ensemble.

Spin dynamics

The equation of motion of an electron can be derived using the quantum-mechanical Heisenberg equation of motion:

$$i\hbar\frac{\partial\langle\tilde{\mathbf{s}}(t)\rangle}{\partial t} = \langle[\tilde{\mathbf{s}}(t), \tilde{\mathcal{H}}]\rangle \tag{2.3.8}$$

Here $\tilde{\mathbf{s}}(t)$ denotes the quantum-mechanical angular momentum operator and $\tilde{\mathcal{H}}$ the Hamiltonian. Assuming that $\tilde{\mathcal{H}}$ is composed of a polynomial of angular momentum operators $\tilde{\mathbf{s}}$, the commutator $[\tilde{\mathbf{s}}(t), \tilde{\mathcal{H}}(\tilde{\mathbf{s}}(t))]$ can be developed in $\hbar$:

$$[\tilde{\mathbf{s}}(t), \tilde{\mathcal{H}}(\tilde{\mathbf{s}}(t))] = -i\hbar\left(\tilde{\mathbf{s}}(t) \times \frac{\partial}{\partial\tilde{\mathbf{s}}}\right)\tilde{\mathcal{H}}(\tilde{\mathbf{s}}(t)) + \mathcal{O}(\hbar^2). \tag{2.3.9}$$

Therefore, the equation of motion can be written as:

$$i\hbar\frac{\partial\langle\tilde{\mathbf{s}}(t)\rangle}{\partial t} = -i\hbar\langle\left(\tilde{\mathbf{s}}(t) \times \frac{\partial}{\partial\tilde{\mathbf{s}}}\right)\tilde{\mathcal{H}}(\tilde{\mathbf{s}}(t))\rangle + \mathcal{O}(\hbar^2). \tag{2.3.10}$$

For $\hbar \to 0$ this quantum-mechanical equation of motion transitions into the classical limit case

$$\frac{\partial \mathbf{s}_i}{\partial t} = -\left(\mathbf{s}_i \times \frac{\partial}{\partial \mathbf{s}_i}\right) \mathcal{H}(\mathbf{s}_i) \tag{2.3.11}$$

The quantum-mechanical expectation values $\langle \tilde{\mathbf{s}} \rangle$ and $\langle \tilde{\mathbf{H}} \rangle$ become the 'classical' quantities $\mathbf{s}$ and $\mathcal{H}$ according to the Ehrenfest theorem [86]. The spin $\mathbf{s}_i$ of an atom i is related to the magnetic moment by means of the gyromagnetic ratio $\gamma = g\mu_\mathrm{B}/\hbar$:

$$\mathbf{s}_i = \frac{\boldsymbol{\mu}_i}{\gamma} = \frac{\mu_s}{\gamma}\frac{\boldsymbol{\mu}_i}{\mu_s} = \frac{\mu_s}{\gamma}\mathbf{S}_i. \tag{2.3.12}$$

The factor μ_s was introduced in equation 2.3.1 and $\mathbf{S}_i = \frac{\boldsymbol{\mu}_i}{\mu_s}$ is a normalized spin vector.
The derivative of the Hamiltonian

$$-\frac{\partial \mathcal{H}(\mathbf{s}_i)}{\partial \mathbf{s}_i} =: \mathbf{H}_i \tag{2.3.13}$$

is referred to as the effective field $\mathbf{H}_i$, which can be used to write equation 2.3.11 as

$$\frac{\partial \mathbf{S}_i}{\partial t} = -\frac{\gamma}{\mu_s}\mathbf{S}_i \times \mathbf{H}_i. \tag{2.3.14}$$

This equation is the dissipationless Landau-Lifshitz equation [87] and it describes the precessional motion of a normalized, magnetic moment in an effective field. However, this equation is fully energy conserving and an excited spin described by this equation would precess forever due to a missing damping term. Therefore Landau and Lifshitz introduced a phenomenological damping parameter α_{LL} yielding the *Landau-Lifshitz* (LL) equation [87]:

$$\frac{\partial \mathbf{S}_i}{\partial t} = -\frac{\gamma}{\mu_s}\mathbf{S}_i \times \mathbf{H}_i - \frac{\alpha_{LL}}{\mu_s}\mathbf{S}_i \times (\mathbf{S}_i \times \mathbf{H}_i). \tag{2.3.15}$$

It is a differential equation describing the temporal behavior of spins under the action of an effective magnetic field. The first summand on the right-hand side of equation (2.3.15) describes the precession of the spin around $\mathbf{H}_i$, while the second part of the right-hand side accounts for the dissipation, eventually leading to a parallel alignment with $\mathbf{H}_i$. Figure 2.3.2 illustrates the motion of a spin around the field $\mathbf{H}_i$. The propagation motion is shown in red and the relaxation movement in green.

However, the Landau-Lifshitz equation leads to an unphysical behavior for the limiting case of a large damping, $\alpha_{LL} \to \infty$. Therefore, in 1955, T. L. Gilbert proposed an alternative damping term yielding the *Landau-Lifshitz-Gilbert* (LLG) equation [88]:

$$\frac{\partial \mathbf{S}_i}{\partial t} = -\frac{\gamma}{\mu_s}\mathbf{S}_i \times \mathbf{H}_i + \alpha \mathbf{S}_i \times \frac{\partial \mathbf{S}_i}{\partial t}. \tag{2.3.16}$$

Similar to the Landau-Lifshitz equation α denotes a phenomenological damping constant, but it is not identical to α_{LL}. For practical reasons it is easier to write equation (2.3.16) in an explicit form. This is done by applying it once to itself and making use of $|\mathbf{S}_i| = 1$ which yields

$$\frac{\partial \mathbf{S}}{\partial t} = -\frac{\gamma}{(1+\alpha^2)\mu_s}\mathbf{S}_i \times \mathbf{H}_i - \frac{\gamma\alpha}{(1+\alpha^2)\mu_s}\mathbf{S}_i \times (\mathbf{S}_i \times \mathbf{H}_i). \tag{2.3.17}$$

In the explicit form of the LLG equation the gyromagnetic ratio γ is renormalized via

$$\gamma_L = \frac{\gamma}{(1+\alpha^2)\mu_s} \tag{2.3.18}$$

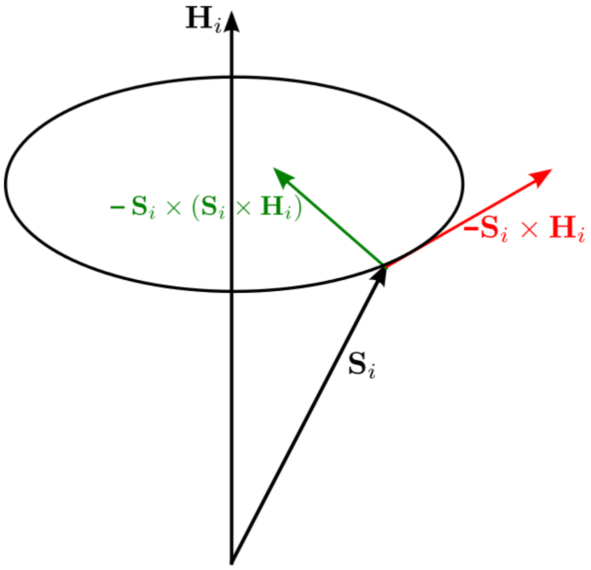

Figure 2.3.2: *Illustration of the motion of a spin in an effective field* $\mathbf{H}_i$*. The motion is composed of a propagation motion (red) and a relaxation motion (green).*

with the scalar isotropic Gilbert damping α. This renormalization of the gyromagnetic ratio is a consequence of expressing the Landau–Lifshitz–Gilbert equation in the same form as the Landau–Lifshitz equation. In the case of small damping, $\alpha \ll 1$, it becomes clear, that the two equations are equivalent [89].

In the context of magnetization dynamics, and in particular ASD simulations, any effects that dissipate energy and angular momentum out of the spin system to the environment are denoted as 'damping' and are part of the Gilbert damping α. The most important damping mechanism is magnon-phonon scattering at elevated temperature, with associated spin-flip scattering. First-principle calculations of damping typically only deal with this dominant mechanism [70].
This is the basic mechanism behind the spin-transfer torque, which can lead to damping or anti-damping in the LLG. In addition to that, a dynamic magnetic system radiates electromagnetic waves as described by Maxwell's equations, which also can involve angular momentum transfer [70]. In a more general form of the LLG the isotropic Gilbert damping α is replaced by a 3×3 damping tensor $\tilde{\alpha}(\mathbf{m})$.
In this general form, the damping also depends on the magnetization direction $\mathbf{m}$. Like with other parameters of atomistic spin-dynamics simulations the Gilbert damping can be calculated from first principles. It is either possible to calculate it using the breathing Fermi surface model and the torque correlation model [90, 91, 92] or using scattering theory from linear response [93, 94, 95].
However, most of the time, the damping tensor is assumed to be isotropic and scalar, replacing the full tensor with a scalar parameter α. This is mostly done for simplicity and ease of use. Especially in atomistic spin-dynamics simulation the Gilbert damping is often treated as the only free parameter, after using *ab initio* values and/or experimental values to fix all other simulation parameters.

Langevin dynamics

Since the Gilbert damping dissipates energy and angular momentum, in this context it is understood as the coupling strength between the spin-system and the lattice heat bath.
Yet the LLG in the form of equation (2.3.17) only describes the behavior of spins without thermal fluctuations at $T = 0$ K. Thermal effects cause thermodynamic fluctuations of the spin moments. For high enough temperatures, they can be stronger than the Heisenberg exchange interaction giving rise to a ferromagnetic-paramagnetic transition.
These effects can be taken into account using Langevin dynamics. This approach was developed in 1963 by William F. Brown. The basic idea is to assume that the thermal fluctuations on each atomic site can be represented by a Gaussian white noise term [96]. This is done by adding a stochasic field $\boldsymbol{\zeta}_i(t)$ to the effective field $\mathbf{H}_i$ so that

$$\mathbf{H}_i' = \boldsymbol{\zeta}_i(t) - \frac{\partial \mathcal{H}}{\partial \mathbf{S}_i}. \tag{2.3.19}$$

The thermal noise ζ is characterized by white noise distributed according to a Gaussian with

$$\langle \boldsymbol{\zeta}_i(t) \rangle = 0 \qquad \text{and} \qquad \langle \zeta_i^\nu(t) \zeta_j^\theta(t') \rangle = 2\frac{\alpha \mu_s}{\gamma} k_\mathrm{B} T \delta_{i,j} \delta_{\nu,\theta} \delta(t - t'). \tag{2.3.20}$$

Here the indices i and j represent grid locations and ν, θ Cartesian coordinates. T is the electron temperature and the coefficient in front of the delta function in equation 2.3.20 is determined by the fluctuation dissipation theorem.
It is important to note, that the noise scaling in equation 2.3.20 directly depends on the Gilbert damping α. At first, this is unsurprising since the Gilbert damping dissipates energy out of the spin system and thus, in order to maintain an equilibrium more energy needs to be introduced via $\boldsymbol{\zeta}_i(t)$. On the other hand the noise scaling with α also means a direct coupling to the electron heat bath governed by α, since equation 2.3.20 also scales with the electron temperature T. The reaction speed of the spin system to a rapid electron temperature change, therefore directly scales with α and thus the Gilbert damping also represents the coupling strength between the electron and the spin subsystem.

The used Langevin dynamics fall short on very short timescales. On one hand they require a well-defined electron temperature, which is typically not the case in the first 100 fs after excitation with a femtosecond scale laser pulse. On the other hand $\boldsymbol{\zeta}_i(t)$ describes white noise uncorrelated in time and space for short timescales, however, the thermal fluctuations are correlated in time, coming from the dynamic interactions between the atoms and lattice/electron system and thus the noise is coloured [97].
For very large systems and/or long timescales, numerical feasibility limits the use of ASD simulations and the Landau-Lifshitz-Gilbert equation. In many cases it is simply too time consuming to solve the LLG for millions of spins over several hundred picoseconds. Instead it is easier to use a different model such as the Landau-Lifshitz-Bloch equation or micromagnetic simulations. Atomistic spin-dynamics simulations bridge the gap between *ab initio* methods and micromagnetic simulations on the nanometer and picosecond scale.
The Landau–Lifshitz equations for interacting spin systems are coupled non-linear differential equations. There are only a few special cases for which analytical solutions exist, such as for a two-spin system or for a coherent rotation of coupled spins in an external magnetic field.
There are a number of conservation relations that can be derived analytically, that also apply for general numerical simulations [70].

In the simplest case with $T = 0$ K and $\alpha = 0$ the total energy of the spin system is conserved as there is no channel through which energy is able to leave or be added to the system. In this case the total angular momentum is also conserved for an isotropic Heisenberg exchange, as no external torque acts on the system.
However, as soon as $\alpha > 0$ the Landau-Lifshitz-Gilbert equation is no longer energy or angular momentum conserving. Regardless of this, the length of individual spins is always conserved independent of other parameters such as damping or temperature. In the typical case for atomistic spin-dynamics simulations $T > 0$ and $\alpha > 0$ the length of individual spins is in fact the only preserved quantity. In this case, all other quantities are derived by averaging over the entire spin bath after solving the Landau-Lifshitz-Gilbert equation numerically.

2.3.4 A basic overview over the numerical methods

The atomistic spin-dynamics simulation of this work are largely performed on *graphics processing units* (GPUs) working in tandem with a *central processing unit* (CPU). The simulation of the complete spin system, especially the numerical solution of the Landau-Lifshitz-Gilbert equation is done on the GPUs while the CPU controls all parameters of the simulation. This is done since GPUs are designed to compute the same instructions with different data sets simultaneously [98]. The code was in large parts developed by A. Donges in the group of U. Nowak at the University of Konstanz. More details on the numerics and the program can be found in Ref. [99].
The spin simulations are performed on a 3-dimensional grid, where each grid site is occupied by a spin of one of the sublattices. The grid is extended in each direction by a halo, in which the boundary conditions are applied (such as open- or periodic boundary conditions) [99]. The time evolution of the spin system is simulated on the GPUs and only the temperature evolution of the electron and phonon systems are computed on the CPU. Thermal noise for the electron and phonon heat baths is generated using the host-API of the CuRAND library routines [99, 100].
The Landau-Lifshitz-Gilbert equation belongs to the class of ordinary differential equations of first order and can thus be solved numerically with the help of a one-step method for given initial conditions.
The Heun method [101] uses a predictor-corrector method which matches the Stratonovich interpretation of the stochastic process. This algorithm first calculates a predictor value as an approximation, which is then used to calculate the final approximation in a second step. In addition, discrete time steps Δt are used for the temporal evolution in the method, so that $t_n = n \cdot \Delta t$. In the following, the shorthand notation $S_n = S(t_n)$ is used. For a one-dimensional differential equation of the form

$$\frac{\partial S(t)}{\partial t} = f\left(S(t), H(t), t\right) + g\left(S(t), t\right) \cdot \zeta(t) \tag{2.3.21}$$

the predictor $\overline{S}_{n+1}$ is first determined starting from the value S_n using an Euler integration method:

$$\bar{S}_{n+1} = S_n + f(S_n, H_n, t_n)\Delta t + g(S_n, t_n) \cdot \bar{\zeta}_n \tag{2.3.22}$$

$\zeta(t)$ represents the white noise introduced in section 2.3.3. Afterwards, in a second step, the value S_{n+1} after (n+1) time steps is derived as

$$\begin{aligned} S_{n+1} = S_n &+ \frac{1}{2}\left(f(S_n, H_n, t_n) + f(\bar{S}_{n+1}, \bar{H}_{n+1}, t_{n+1})\right)\Delta t \\ &+ \frac{1}{2}\left(g(S_n, t_n) + g(\bar{S}_{n+1}, t_{n+1})\right)\cdot\bar{\zeta}_n \end{aligned} \tag{2.3.23}$$

The deterministic error convergence of this method is 2, which means that the error goes to zero with the square of the step size.

2.3.5 Modeling laser excitations of magnetic materials

The equilibrium state of an electron system in a metal can be described by an electron temperature T_{el} and a corresponding Fermi-Dirac distribution of the electron energy.

When the metal is excited by a laser, almost all of the energy is absorbed by the electron system by exciting electrons to higher energy levels, whereas the lattice system remains mostly unaffected. On a timescale of a few hundred femtoseconds electron-electron scattering leads to a thermalization back to a Fermi-Dirac distribution of a new, higher electron temperature. Due to the small specific heat of the electrons this temperature can reach up to several thousand Kelvin. So far the phonon system remained unaffected by the laser and its temperature T_{ph} remains similar to its initial temperature. However, electron-phonon scattering slowly leads to an equilibration of the two heat baths over the next picoseconds.

All of these processes can be described in a simple way by the two-temperature model (TTM). It was first proposed by Kaganov *et al.* [102] and is commonly used in atomistic spin-dynamics simulations. At its core it is a simple version of the three-temperature model used by Beaurepaire *et al.* to describe ultrafast demagnetization in nickel [5] without the spin system, which is simulated separately using ASD.

The two-temperature model

The two-temperature model can be expressed as two coupled differential equations:

$$C_{\mathrm{el}}\frac{\partial T_{\mathrm{el}}}{\partial t} = -g_{\mathrm{ep}}\left(T_{\mathrm{el}} - T_{\mathrm{ph}}\right) + P_l(t) \tag{2.3.24}$$

$$C_{\mathrm{ph}}\frac{\partial T_{\mathrm{el}}}{\partial t} = +g_{\mathrm{ph}}\left(T_{\mathrm{el}} - T_{\mathrm{ph}}\right), \tag{2.3.25}$$

where C_{el} is the electron specific heat, C_{ph} describes the specific heat of the phonons and $P_l(t)$ characterizes the energy coming from the laser. In ultrafast magnetism $P_l(t)$ is typically assumed to be Gaussian shaped with a full width at half maximum between $\approx 50 - 500$ fs. C_{el}, C_{ph} and g_{ep} are highly material-dependent and can be calculated from *ab initio* calculations or determined in experiments.

The electron specific heat $C_{\mathrm{el}}(T)$ can be derived via the internal energy density u using $C_{\mathrm{el}}(T) = \frac{\mathrm{d}u}{\mathrm{d}T}$. Using the Sommerfeld expansion of Drude's free electron gas yields [82]:

$$C_{\mathrm{el}}(T) = \frac{\mathrm{d}u}{\mathrm{d}T} \approx \frac{\pi^2 k_{\mathrm{B}}^2}{3} T g(\varepsilon_F) = \gamma T. \tag{2.3.26}$$

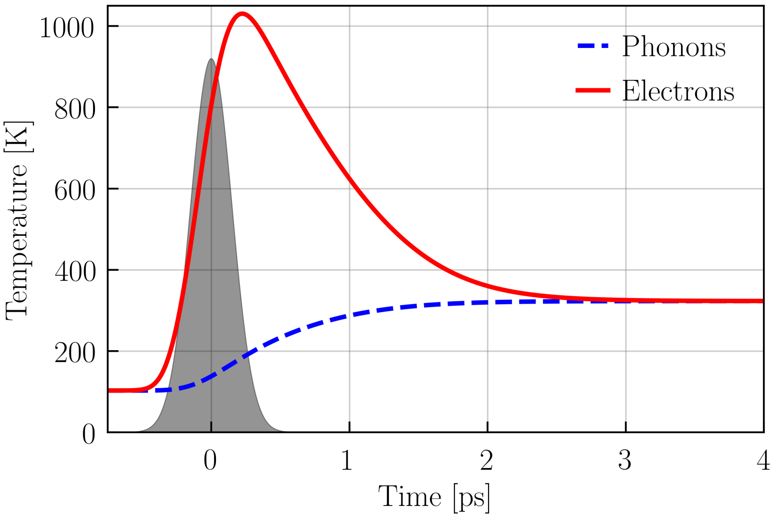

Figure 2.3.3: *An example of the electron temperature evolution (red) and the phonon temperature (blue, dashed) after excitation with a laser at* $t = 0$ *(grey a.u.) following the two-temperature model.*

Here k_B is the Boltzmann constant and $g(\varepsilon_F)$ describes the density of states. γ is defined as $\gamma = \frac{\pi^2 k_\mathrm{B}^2}{3} g(\varepsilon_F)$ and thus the electronic specific heat increases linearly with the temperature.

The phonon specific heat C_ph can be calculated in the same way, using the internal energy via $C_\mathrm{ph}(T) = \frac{\mathrm{d}u_\mathrm{ph}}{\mathrm{d}T}$. This energy term itself can be modeled using the Debye- or the Einstein model [103, 104]. For elevated temperatures both models yield very similar results and the Einstein model only falls short for very low temperatures. However, unlike for the Debye model, an explicit analytically solvable expression can be given for the Einstein model:

$$C_\mathrm{ph}(T_\mathrm{ph}) \approx 3nk_\mathrm{B}\left(\frac{T_\mathrm{E}}{T_\mathrm{ph}}\right)^2 \frac{e^{T_\mathrm{E}/T_\mathrm{ph}}}{(e^{T_\mathrm{E}/T_\mathrm{ph}}-1)^2}, \tag{2.3.27}$$

with T_E being the Einstein temperature and n the atom density.

The electron phonon coupling g_ep describes the energy transfer rate between the electron and phonon systems and can be calculated via [105]:

$$g_\mathrm{ep}(T_\mathrm{el}) = \frac{-\pi k_\mathrm{B}^3 \lambda_\mathrm{ep} T_\mathrm{D}^2}{2\hbar D(\varepsilon_F)} \int_{-\infty}^{\infty} D^2(\varepsilon) \frac{\partial f}{\partial \varepsilon} d\varepsilon, \tag{2.3.28}$$

with T_D being the Debye temperature and λ_ep being a dimensionless coupling constant. Figure 2.3.3 shows an example simulation of the two-temperature model. The dynamics of the electron temperature T_el is shown in red and the phonon temperature T_ph in blue, after excitation with a 100 fs laser pulse at $t = 0$. Figure 2.3.3 shows a rapid increase of the electron temperature during the laser excitation. After ≈ 300 fs T_el reaches its maximum and equilibrates with the phonons over the next 2-3 ps until a new common equilibrium temperature is reached.

Linking the two-temperature model and the spin system

Atomistic spin-dynamics simulations are not energy conserving except in some special cases, such as in the absence of damping. However, it is possible to link the electron-phonon subsystems, modeled via the two-temperature model, with the spin subsystem, modeled using atomistic spin-dynamics simulations, and thus make the whole system, consisting of these three subsystems, energy conserving.
This is done by monitoring the energy change ΔE_s of the spin system between two timesteps following Ref. [106] via:

$$\Delta E_s = \frac{s^2}{s \cdot (s+1)} \left(\mathcal{H}\{\mathbf{S}_i(t+\Delta t)\} - \mathcal{H}\{\mathbf{S}_i(t)\} \right) \tag{2.3.29}$$

$\mathcal{H}$ is referring to the Heisenberg Hamiltonian (equation 2.3.6), Δt is the numerical timestep and s the spin quantum number s. The factor $\frac{s^2}{s \cdot (s+1)}$ accounts for the fact that the spins are quantized (for example $s \approx 1/2$ for nickel), but the classical Heisenberg Hamiltonian assumes $s = \infty$ which, if uncorrected, yields a false spin energy.
For nickel with $s \approx 1/2$ this yields a correction factor of $\frac{s^2}{s \cdot (s+1)} = 1/3$, for cobalt with $s \approx 3/2$ the correction factor is 0.6 and for iron with $s \approx 2$ the correction factor becomes 2/3.
In order to couple the energy change of the spin system to the two-temperature model, ΔE_s is subtracted from the energy subsystem via a modified TTM:

$$C_{\text{el}} \frac{\Delta T_{\text{el}}}{\Delta t} = -g_{\text{ep}} \left(T_{\text{el}} - T_{\text{ph}} \right) + P_l(t) - \frac{\Delta E_s}{\Delta t}. \tag{2.3.30}$$

This assumes, that the spin system receives all of its energy from the electron subsystem. Furthermore, when the spin system remagnetizes, which corresponds to a decrease in energy, the energy of the spin system is transfered back to the electron system.
Direct spin-phonon coupling is not considered here, which, is a reasonable approximation in transition metals, due to the fast time scales of the demagnetization dynamics [14, 107] and the low magnetocrystalline anisotropy of transition metals, such as nickel [108]. However, in rare-earth elements such as terbium, a direct spin-phonon coupling might be necessary to be included [109].

The two-temperature model and its shortcomings

Due to its simplicity, the TTM has several severe shortcomings that will be addressed briefly. First, while the electron system only takes a couple of hundred femtoseconds to thermalize and follows a Fermi-Dirac distribution, it is in a non-equilibrium state during this time and assigning an electron temperature T_{el} during this time is not possible. It remains challenging to model this non-equilibrium state, but there have been different additions proposed to address this problem, for example by delaying the electron heating via a phenomenological thermalization time [110]. Another proposed idea is to divide the electronic system in a thermal bath that contains the majority of thermal electrons at temperature T_{el} and a second non-thermal electron bath, that contains a laser-excited distribution, which relaxes, driving energy into the thermal distribution through electron-electron and electron-phonon interactions [111].
Similar to the electron system, the phonon system also remains in a non-thermal state for several tens of picoseconds after laser excitation, which also makes assigning a temperature during this time problematic.

To address this problem a division of the lattice in N independent phonon subsystems has been proposed, that interact with one another through phonon-phonon scattering and with the electrons via electron-phonon scattering. Therefore, these phonon subsystems evolve independently and a separate "lattice temperature" for each of them can be defined [112, 113]. Furthermore, without any additions, the spin degree of freedom is not addressed in the TTM model. A way to directly tie the spin system to the TTM model was presented in Chapter 2.3.5 or can be found in Ref. [114, 109].

The TTM assumes the electron-phonon coupling g_{ep} to be constant and the electronic specific heat to increase linearly via $C_{\mathrm{el}}(T) = \gamma T$. In many cases this is a valid approximation, but many parameters of the TTM itself are temperature dependent [115, 105]. It is possible to include these temperature dependencies into the model, however, they are highly material-dependent and require extensive *ab initio* calculations or experimental measurements of the simulated material. At last, additional temperature effects such as surfaces or heat diffusion are not considered, but can be included if necessary within the general TTM framework.

For ASD it is in most cases sufficient to simply calculate the presented simple version of the TTM. Most corrections are either still under development, rely heavily on *ab initio* calculations or experimental measurements, and are often just small corrections to the existing model. These additions have often only limited impact on the spin-dynamics simulations itself, and thus do not justify the effort it takes to adapt them. The two-temperature model therefore remains the most commonly used model to describe electron and phonon temperature dynamics for ASD and ultrafast demagnetization dynamics and corrections or additions are only included if they are needed for a specific problem.

2.3.6 Phenomenological spin models

Since atomistic spin dynamic models typically require large numerical efforts, it is of great interest to find phenomenological models that compare well to ASD simulations with as little loss of accuracy as possible. These models should be well suited to describe typical ultrafast phenomena, such as rapid demagnetization and switching of ferrimagnets. This is typically done by using micromagnetic simulations and macrospin models. The idea is to combine a large number of atomistic spins into a single large macrospin and find new equations of motion for these macrospins.

To that end, two models are briefly presented here, at first a short introduction to mean-field-spin models as they often are building blocks for other, more sophisticated phenomenological models and second, the Baryakhtar model proposed by Mentink and co-workers [116].

Mean-field-spin model

The mean-field approximation (MFA) assumes that all spins are statistically equivalent and each spin interacts with a similar effective field surrounding it. This effective field is based on an averaged equilibrium distribution surrounding the spin and by doing this all interactions of individual spins like in the Heisenberg model are replaced with a single spin coupled to an effective field.

$$\mathbf{S}_i \cdot \mathbf{S}_j \rightarrow \mathbf{S}_i \cdot \langle \mathbf{S} \rangle \tag{2.3.31}$$

This reduces the many-body problem to an effective one-body problem which can be solved at much lower computational cost. Thus the mean-field Hamiltonian can be written as [82]:

$$\mathcal{H}_{\mathrm{MF}} = -\sum_i \mathbf{S}_i \cdot (zJ\langle\mathbf{S}\rangle)\,. \tag{2.3.32}$$

Here z is the number of nearest neighbor sites of spin i and J is the Heisenberg exchange coupling. The expression in the brackets on the right-hand side does not depend on any lattice site and can thus can be written as a magnetic field:

$$\mu_s \mathbf{H}_{\mathrm{MF}} = zJ\mathbf{m}. \tag{2.3.33}$$

Here the average magnetization $\mathbf{m} = \sum_i \frac{\mathbf{S_i}}{N}$ was used, with N being the number of spins. For a ferrimagnet with sublattices a and b with exchange constants J_{aa} between sublattice a spins, J_{bb} between sublattice b spins and J_{ab} as coupling between sublattice a and b spins, the mean field becomes

$$\mu_a \mathbf{H}_a^{\mathrm{MFA}} = z_a J_{aa} \mathbf{m}_a + z_{ab} J_{ab} \mathbf{m}_b. \tag{2.3.34}$$

Here z_a and z_{ab} are the numbers of first nearest neighbours of type a and b, respectively, μ_a is the magnetic moment of spin a. The element-specific equilibrium magnetization can be calculated via the self-consistent solution of $m_a = L(\beta\mu_a H_a^{\mathrm{MFA}})$ and $m_b = L(\beta\mu_b H_b^{\mathrm{MFA}})$. Where $L(x)$ is the Langevin function and $\beta = 1/k_B T$ and T is the electron temperature.

Baryakhtar model

A simple model for describing element-specific magnetization dynamics and switching in ferrimagnets with sublattices a and b was proposed by Mentink and co-workers [116]. Longitudinal spin dynamics, describing the change along the initial magnetization direction or an applied field (typically defined as the z-axis), were derived from the Onsager relations [117]

$$\frac{\mu_a}{\gamma_a}\frac{dm_a}{dt} = \alpha_a^{\mathrm{B}} \mu_a H_a + \alpha_{\mathrm{exc}}(\mu_a H_a - \mu_b H_b) \tag{2.3.35}$$

$$\frac{\mu_b}{\gamma_b}\frac{dm_b}{dt} = \alpha_b^{\mathrm{B}} \mu_b H_b + \alpha_{\mathrm{exc}}(\mu_b H_b - \mu_a H_a). \tag{2.3.36}$$

Here, $\alpha_{a,b}^{\mathrm{B}}$ are relativistic relaxation parameter, which dissipate angular momentum out of the spin system, and α_{exc} is the exchange relaxation parameter describing the rate of dissipation of angular momentum between the sublattices. $H_{a(b)}$ is an internal effective field described later. Equations 2.3.35 and 2.3.36 are set up so that the total angular momentum is conserved. Within this model, the values for $\alpha_{a,b}^{\mathrm{B}}$ and α_{exc} are not further specified, but used as fitting parameters when comparing to experiments. They are typically assumed to be constant. The internal effective field $H_{a(b)}$, acting on sublattice $a(b)$, are derived from a non-equilibrium mean-field approximation,

$$\mu_a H_a = -\beta^{-1} L^{-1}(m_a) + \mu_a H_a^{\mathrm{MFA}}, \tag{2.3.37}$$

where, $L^{-1}(x)$ is the inverse Langevin function, $\beta = 1/k_B T$ and T is the electron temperature. At equilibrium, the effective field is $H_a = 0$, as $m_a = L(\beta\mu_a H_a^{\mathrm{MFA}})$ and thus the right-hand side of equation 2.3.37 vanishes. By solving equations (2.3.35) and (2.3.36) together with the two-temperature model, describing the electron and phonon temperature dynamics and explained in more detail in Chapter 2.3.5, ultrafast magnetization dynamics similar to atomistic spin-dynamics simulations can be obtained. It is furthermore possible to use this approach to discuss element-specific demagnetization and switching dynamics [118, 119].

Chapter 3

Unifying femtosecond and picosecond single-pulse magnetic switching in GdFeCo

The results of this chapter have been published in

- F. Jakobs, T. A. Ostler, C.-H. Lambert, Y. Yang, S. Salahuddin, R. B. Wilson, J. Gorchon, J. Bokor, and U. Atxitia, Unifying femtosecond and picosecond single-pulse magnetic switching in Gd-Fe-Co, *Physical Review B* **103** p. 104422, (Mar 2021).

and the content of this chapter is in large parts identical with the published work. All experiments have been performed by J. Gorchon and coworkers from the University of California in Berkeley.

The published version can be found at `https://doi.org/10.1103/PhysRevB.103.104422`

3.1 Introduction

The speed of switching between two stable magnetic states has become a major bottleneck for future advancement of magnetic-based information technologies. The use of femtosecond laser pulses emerged as a promising solution for the ultrafast control of magnetism by the demonstration of subpicosecond spin dynamics in nickel [5, 14]. The number of potential applications of this ultrafast spin dynamics quickly increased after the discovery of single pulse switching of the magnetic polarity in ferrimagnetic GdFeCo alloys [24, 6, 32, 26]. Further development of devices based on single-pulse switching, e.g. magnetic tunnel junctions, needs of not only a complete understanding of the switching mechanisms but also providing computational means for realistic design of, for example, spintronics operations using ferrimagnets, such as the energy efficient spin-orbit switching [120, 121, 122] and high velocity domain wall motion driven by fields [123], electric currents [124] and thermal gradients [125]. It was shown that the heat provided by the femtosecond optical pulse alone is already a sufficient stimulus to switch the magnetization [32, 33, 126]. Since the commonly accepted driving mechanism is based on faster exchange of angular momentum between sublattices (~ 100 fs) than magnetization relaxation to the medium, the efficiency of such a mechanism should be drastically reduced at longer time scales [126]. This picture was contested by the observation of both thermal single-pulse AOS in GdFeCo alloys using laser pulse durations ranging from 50 fs up to 15 ps [37, 36] and by the heat produced by picosecond electric pulses [35]. Despite intense research to establish a robust theoretical framework for the quantitative description of thermal single-pulse (optical or electrical origin) AOS in GdFeCo, a unified picture is missing[126, 127, 128, 129, 127, 130, 38]. It is furthermore unclear, whether the proven theoretical models for fs-pulse switching are able to describe the (up to two orders of magnitude larger) picosecond scale pulse switching. Recent experimental/theoretical work using phenomenological models suggested distinguished different relaxation pathways for femtosecond- and picosecond pulses [131].

One of the most promising techniques for achieving a unified picture are atomistic spin dynamics (ASD) methods. They have demonstrated the ability to adequately describe the equilibrium properties of GdFeCo alloys [132] and to describe the non-equilibrium dynamics upon femtosecond laser excitation qualitatively, such as a transient ferromagnetic-like state [6], thermal single-pulse AOS [32], rapid magnon localization and coalescence [133]. Furthermore, ASD methods have provided a range of predictions about the behaviours of the switching as a function of Gd concentration, ambient (or initial) temperature, and laser fluence [134, 135]. In the present work we provide a unified picture of the single-pulse all-optical switching induced by pulses with durations spanning three orders of magnitude, from femtoseconds to picoseconds. To do so, we use atomistic spin dynamics methods and pump-probe experiments of single-pulse all optical switching in GdFeCo alloys. We show that quantitative agreement between theory and experiment is achieved when element specific damping parameters are considered in the model. These combined studies allow us to uncover the underlying physics behind magnetic switching using heat pulses up to several picoseconds in duration. Further, based on our model, we find optimal conditions for laser and material to allow switching of pulse durations up to 15 picoseconds.

3.2 Experimental Setup and Model

3.2.1 Experimental set up

The experiments were carried out on a series of $\mathrm{Gd}_x(\mathrm{Fe}_{90}\mathrm{Co}_{10})_{100-x}$ films of concentrations from $x = 24\%$ to 32% grown by co-sputtering of the following stacks (in nm): $\mathrm{Si/SiO_2(100)/Ta(5)/GdFeCo(20)/Pt(5)}$. The sample is not crystallized and instead has an amorphous structure. Hysteresis loops were measured using magneto-optic Kerr effect (MOKE) at room temperature (Fig. 3.2.1 a)). All samples exhibited perpendicular magnetic anisotropy, and the coercivity H_c are extracted from the hysteresis loops (Fig. 3.2.1 a)). The coercive field H_c increases and the polarity of the hysteresis loops reverse in sign at concentration values of around $x = 28\%$ and 29% Gd, which indicates the existence of a magnetization compensation point at those concentrations at 300 K (Fig. 3.2.1 b)).

An amplified 250 kHz Ti:sapphire laser with 810 nm center wavelength was used for generating the high energy pulses and as a time-resolved probe (Coherent RegA). The laser pulse duration FWHM was tunable from $\Delta t = 55$ fs to $\Delta t = 15$ ps by adjusting the final pulse compressor in the chirped pulse amplifier. Individual single-shot laser pulses could be obtained from our laser system. A MOKE microscope was used for imaging the sample magnetization after each single laser pulse shot and check for the reversal at various pulse

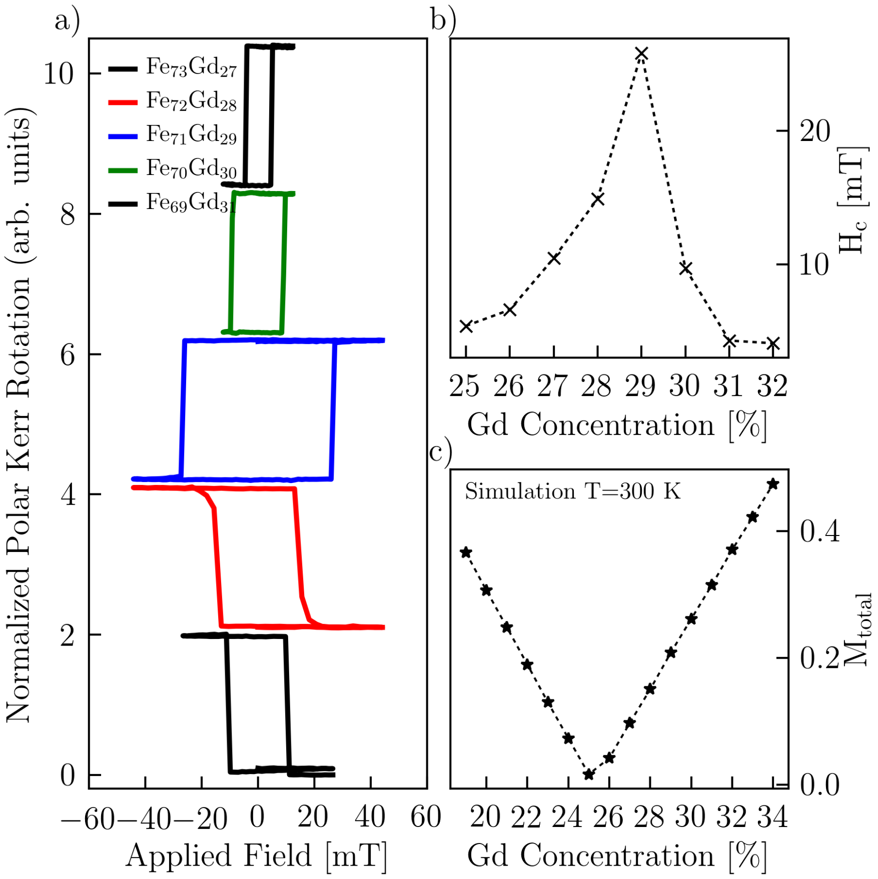

Figure 3.2.1: *a) Magnetic hysteresis of different FeGd-alloys between 27-31 % Gadolinium probed by the magneto optical Kerr rotation at 300 K. The use of an objective lens that is close to the electromagnet's gap induces an additional slope on the Kerr hysteresis data, due to a Faraday effect in the lenses' glass. This slope, which is independent of the sample, was numerically removed from this figure. The polarity of the hysteresis changes as the system crosses the compensation. The coercivity diverges as the Gd-concentration approach the compensation point. b) The experimentally measured coercive field H_c of subfigure a) as function of the Gd concentration. The line is guidance to the eye. c) The simulated total magnetization of the FeGd-alloy at 300 K as function of the Gd concentration. The simulated magnetization compensation temperature is slightly lower (between 25 % -26 %) than the experimental one with the drawn line being guidance to the eye.*

energies. The system also allows one to obtain time-resolved MOKE data in a pump/probe fashion. However, when stretching the pulse duration for the pump, the probe stretches equally, reducing the experimental time-resolution. The probe was focused through a $50x$ objective down to a size of about $1 - 2\mu$m. The pump was focused via a 15 cm lens. We note that pump/probe experiments demonstrating switching dynamics require an external applied out-of-plane magnetic field of around 10 mT in order to reset the magnetization after each pulse event. Details of the pump-probe and microscope setup can be found in Ref. [136].

3.2.2 Model

We use an atomistic spin model based on the classical Heisenberg spin Hamiltonian:

$$\mathcal{H} = -\sum_{i\neq j} J_{ij}\mathbf{S}_i \cdot \mathbf{S}_j - \sum_i d_z S_z^2. \tag{3.2.1}$$

$\mathbf{S}_i = \boldsymbol{\mu}_i/\mu_{s,i}$ represents a classical, normalized spin vector at site i with $\mu_{s,i}$ being the atomic magnetic moment of each sublattice. The spin at site i, $\mathbf{S}_i$, couples to the neighboring spin, $\mathbf{S}_j$ via the coupling constant J_{ij}. The second term of the Hamiltonian describes the on-site anisotropy with easy-axis along the z axis with constant anisotropy energy, d_z. The lattice structure of GdFeCo is amorphous and thus difficult to fully characterize [6]. Similar to previous works, we model GdFeCo alloys as a two sub-lattice system with FeCo being represented by a generic transition metal (TM) sublattice and Gd as a second sublattice that is randomly scattered throughout the TM. The simulation of FeCo as one sublattice is justified by the parallel alignment of Fe and Co up to the Curie temperature and the delocalized nature of their spins. The spin dynamics are described by the atomistic stochastic-Landau-Lifshitz-Gilbert equation (sLLG) [72]

$$\frac{(1+\alpha_i^2)\mu_{s,i}}{\gamma}\frac{\partial \mathbf{S}_i}{\partial t} = -\left(\mathbf{S}_i \times \mathbf{H}_i\right) - \alpha_i\left(\mathbf{S}_i \times \left(\mathbf{S}_i \times \mathbf{H}_i\right)\right). \tag{3.2.2}$$

where γ is the Gyromagnetic ratio and $\mu_{s,i}$ represents the magnetic moment of sublattice i. The phenomenological, material-dependent parameter α_i determines the rate of transfer of energy and angular momentum in and out of the magnetic system and gives rise to a damping of the spin dynamics. The damping parameter is included phenomenologically and is strongly material dependent [72]. By including a Langevin thermostat, statistical - equilibrium and non-equilibrium thermodynamic properties can be obtained. This is achieved by adding an effective field-like stochastic term $\boldsymbol{\zeta}_i$ to the effective field $\mathbf{H}_i = \boldsymbol{\zeta}_i(t) - \frac{\partial\mathcal{H}}{\partial\mathbf{S}_i}$, with white noise properties [97]:

$$\langle\boldsymbol{\zeta}_i(t)\rangle = 0 \quad \text{and} \quad \langle\boldsymbol{\zeta}_i(0)\boldsymbol{\zeta}_j(t)\rangle = 2\alpha_i k_{\mathrm{B}} T_{\mathrm{el}}\mu_{s,i}\delta_{ij}\delta(t)/\gamma. \tag{3.2.3}$$

The noise represents the effect of the hot itinerant electrons onto the two sub-lattices of localized spins. The electron temperature T_{el} is therefore used to scale the noise and has an indirect impact on the spin dynamics via the stochastic field $\boldsymbol{\zeta}(t)$ entering the sLLG. Throughout all simulations no external magnetic field was applied. It is a fair approximation to neglect the applied magnetic fields in our model as the energy scale of the Zeeman interaction is much smaller than the exchange interaction which drives the demagnetization and switching processes. Only on longer much longer timescales does the magnetic field become important.

In our computational model, we consider a spin simple cubic lattice composed of two spin sublattices, Fe and Gd with dimensions of $N = 160 \times 160 \times 160 \approx 4\,000\,000$ spins. This system size yields minimal boundary effects and provides a large enough number of spins for calculating and averaging macroscopic parameters. To handle the computational effort of solving the sLLG for over four million spins, the simulations were performed on GPUs making use of the Nvidia CUDA C-API [137].

We use the so-called two temperature model (TTM) to describe the temporal changes in the

Table 3.1: *Table of the Heisenberg spin Hamiltonian parameters (left) and the two temperature model (TTM) (right). Values are taken from Ref. [135].*

$\mathcal{H}$	Value		Units	TTM		Units
$J_{\text{Fe-Fe}}$	3.46	$\times 10^{-21}$	[J]	C$_{\text{ph}}$	3×10^6	[J/Km^3]
$J_{\text{Gd-Gd}}$	1.389	$\times 10^{-21}$	[J]	C$_{\text{el}}$	$\gamma_{\text{el}} \cdot T_{\text{e}}$	
$J_{\text{Fe-Gd}}$	$-$ 1.205	$\times 10^{-21}$	[J]	γ_{el}	700	[J/Km^3]
$\gamma_{\text{Fe/Gd}}$	1.76	$\times 10^{-21}$	$[\frac{1}{\text{Ts}}]$	g$_{\text{ep}}$	6×10^{17}	[J/sKm^3]
d_z	8.072	$\times 10^{-22}$	[J]			
$\mu_{\text{s,Fe}}$	1.92		[μ_{B}]			
$\mu_{\text{s,Gd}}$	7.63		[μ_{B}]			
α_{Gd}	0.01					
α_{Fe}	varied					

electron- and phonon temperature (T_{ph}) [102, 110],

$$C_{\text{el}} \frac{\partial T_{\text{el}}}{\partial t} = -g_{\text{ep}} \left(T_{\text{el}} - T_{\text{ph}} \right) + P_l(t) \tag{3.2.4}$$

$$C_{\text{ph}} \frac{\partial T_{\text{ph}}}{\partial t} = +g_{\text{ep}} \left(T_{\text{el}} - T_{\text{ph}} \right). \tag{3.2.5}$$

C_{el} and C_{ph} represent the specific heat of the electron- and phonon system. Here, $P_l(t)$ represents the absorbed energy by the electron system, coming from the laser. All of the material parameters used in this study are listed in table 3.1 and are taken from Ref. [135].

Fig. 3.2.2 b) shows an example of the resulting T_{el} and T_{ph} dynamics upon application of a 100 fs laser pulse. Due to the low heat capacity of the electrons, the T_{el} increases within the same time scale of the laser pulse (shaded area) and can reach up to several thousand Kelvin. When T_{el} and T_{ph} are out of equilibrium, the electron-phonon coupling drives a transfer of energy from the electrons to the phonons, cooling the hot electron system and heating the lattice within a couple of picoseconds. As the pulse duration increases, the situation slowly changes until the time scales of the laser excitation and electron-phonon relaxation processes become similar. Fig. 3.2.2 a) shows, as an example, the T_{el} and T_{ph} dynamics for a laser pulse duration of 1 ps. In this case, the energy transfer from the electrons and phonons acts on almost the same time-scale as the energy load from the laser to the electrons. The direct consequence is that for the same absorbed energy, the maximum temperature reached by the electron system is reduced as the pulse duration increases. Ultimately, for very long pulses the dynamics of the electron and phonon temperature becomes the same and the steep T_{el} increase disappears.

Fig. 3.2.3 shows the corresponding magnetic response of the Fe and the Gd sublattices to the discussed 1 ps pulse for different fluences (a-c). We note that in the simulations a new equilibrium state is reached fairly quickly after about 7-8 ps after the initial excitation. At that point T_{el} and T_{ph} are equilibrated and both sublattices have adjusted to the new electron temperature. Additional effects that slow down the reordering process, such as domain formation, or heat transport are not considered.

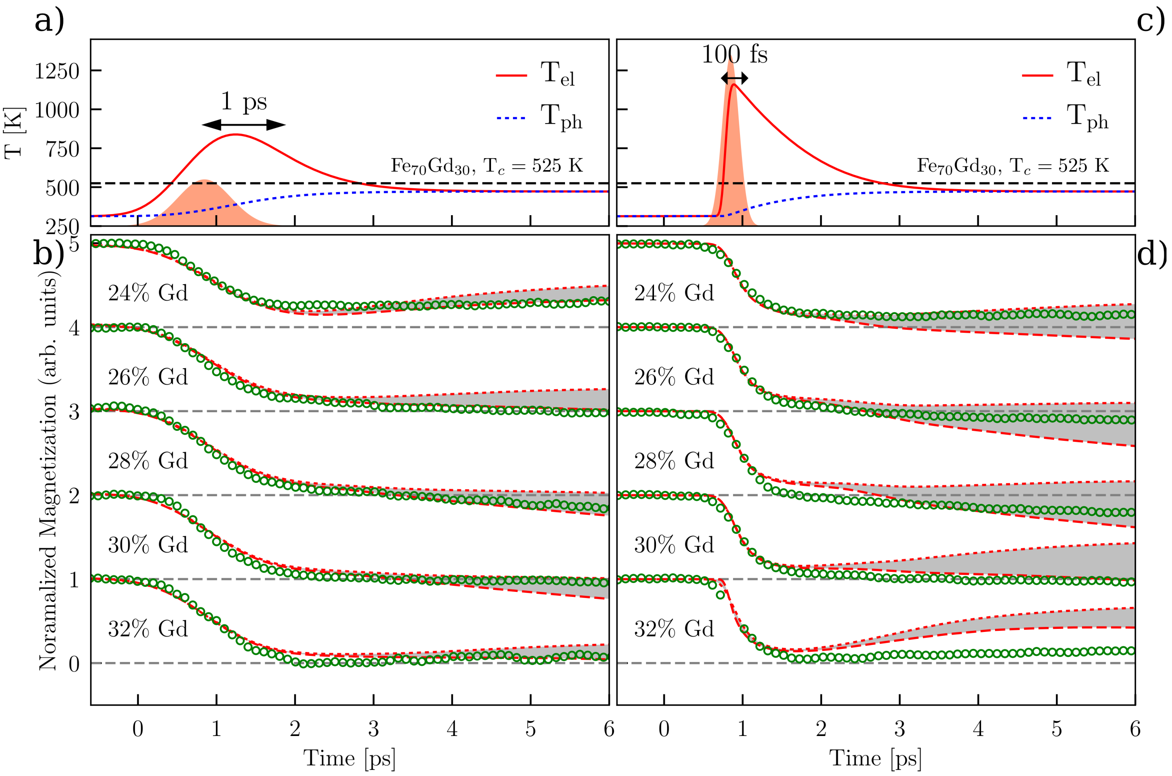

Figure 3.2.2: *The temperature dynamics of the T_{el} (solid red) and T_{ph} (blue dotted) for a pulse duration of a) 1 ps and b) 100 fs. The total energy of the pulse is the same for both pulse durations. c) and d) atomistic spin dynamics simulations (red dotted lines) and experimental measurements (large green dots) of the magnetization dynamics of the Fe-sublattice for a range of Gd-concentrations at 300 K. The experimental normalized magnetization is obtained through a shifting and normalization of the measured pump-induced change in magnetization $(M_s + \Delta M_z)/M_s$, where M_s is the saturation magnetization. The simulated normalized magnetization is obtained by dividing the averaged magnetic moment by the average magnetization at 300 K of each sublattice. The plots for each Gd-concentration are shifted by an offset of 1 among each other. The simulations correspond to a Gaussian weighted average of multiple simulations of different Gd concentrations with a variance of $\sigma^2 = 5.76$ %. The grey area between the dotted red lines indicate a variation in the laser fluence of ≈ ±0.5 % of a chosen mean fluence. Due to the overlapping of pump and probe pulse in the experiment and for direct comparison, the dynamics coming out from the simulations are convoluted with a 800 fs probe pulse, and the simulations for the 100 fs pulse are convoluted using a 250 fs probe pulse.*

3.3 Quantitative comparison between experiments and simulations

Fig. 3.2.2 c) shows a direct, quantitative description of the dynamics of thermal single-pulse magnetic switching of GdFeCo alloys using femtosecond- and picosecond pulse durations. The figure depicts the z component of the normalized magnetization m of the Fe sublattice for a pulse duration of 1 ps (left) and 100 fs (right) with experimental measurements being

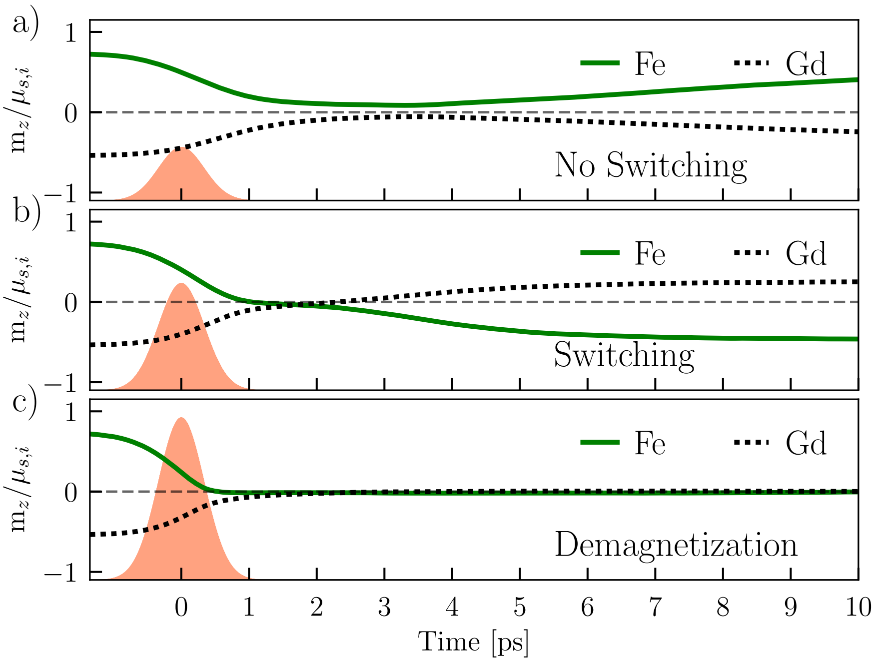

Figure 3.2.3: *The (normalized) magnetization dynamics for Fe (green) and Gd (black) after excitation by different fluences of a 1 ps laser pulse. a) the magnetization dynamics for a weak 1 ps pulse that does not switch the alloy. b) the dynamics for an increased fluence that does switch GdFe. c) the dynamics for a high fluence that demagnetizes the alloy. The dynamics of the two temperature model for a similar laser excitation is shown in Fig. 3.2.2 a).*

shown as green points and computer simulations in red [1]. The laser fluence used is sufficient to achieve AOS for the Gd concentrations between 26 % and 30 % (Fig. 3.2.2 c),d)) for both pulse durations. We estimate the absorbed fluence to be around 1.5mJ/cm^2 (assuming a 30% absorption, Ref. [36]), which corresponds to about $5 \cdot 10^8$ J/m^3 for our 30 nm-thick metallic film. We note that an important distinction between the experiments' and simulations' energy absorption scenarios, is that in the experiments we find an exponentially decaying absorption profile, whereas in the simulations the full magnetic layer can be set to absorb a homogeneous energy density. To account for potential fluctuations of the laser fluence during data acquisition, two different results from simulations for laser fluences with a variation of 0.5% are shown as red dotted- and dashed lines in Fig. 3.2.2 c) and d). Importantly laser and material parameters in this section were kept constant throughout all simulations. The intrinsic damping parameters α_{Fe} and α_{Gd} for the Fe and Gd sublattices were set to $\alpha_{\mathrm{Fe}} = 0.06$ and $\alpha_{\mathrm{Gd}} = 0.01$. The inclusion of the element specific nature of the damping in our model is one of the key factors that allowed us to quantitatively describe our experimental measurements. In a recent work on single-pulse AOS in TbGdFeCo alloys, similar conclusions have been drawn about the role of distinct damping parameters in AOS [138]. These damping parameters are in agreement with the ultrafast spin dynamics measured in the respective pure materials [139, 140]. While Fe and Co demagnetize on time scales of

---

[1] In our setup it is not possible to measure the pulse duration after the objective (because we need a collimated beam for the autocorrelator), so we do not have a measure of the probe pulse duration after the objective. We estimate the pulse to stretch by about 160fs to 240fs after the objective based on the 50nm bandwidth of the laser and assuming 3 to 4.5cm of UV fused silica glass for the optics. Based on this we estimate the probe pulse to 100 fs + 200 fs = 300fs and 1 ps - 200 fs = 800 fs in the two experimental conditions of Fig. 3.2.2

hundreds of femtoseconds, the rare-earth Gd responds much slower to optical excitation [6]. It has been argued that the reason behind these slow dynamics is the localized character of the $4f$ spins and the absence of orbital angular momentum [114]. In previous works the same damping value is consistently used for both sublattices. However, the good quantitative agreement between our experiments and the model suggests, that the damping parameter for RE-metals used in sLLG models should be lower than the one used in transition metals. This picture of larger damping for FeCo than for Gd aligns with recent observations on magnetic domain wall mobility in GdFeCo [141]. Our choice of larger damping value for FeCo than for Gd, is in agreement with those observations. We note that since the laser probes areas of tens of micrometres, it is important to consider the chemically inhomogeneous nature of the experimental samples with locally varied Gd-concentrations [20]. The switching behavior within these chemical inhomogenities strongly depends on local system parameters, especially the Curie temperature T_c, which varies with the Gd-concentration. For example a $Fe_{75}Gd_{25}$ alloy shows a $T_c \approx 560$ K while a $Fe_{66}Gd_{34}$ alloy only has a $T_c \approx 500$ K. The influence of such chemical inhomogenities is especially relevant when working close to the critical laser fluence, which marks the energy threshold for switching and non-switching behavior. Close to this fluence level one region with a Gd-concentration might switch for a given fluence while another Gd-concentration does not switch for the same fluence (see Fig. 3.2.3). Therefore we take a weighted (Gaussian) average of independent simulations of different Gd concentrations with a variance of $\sigma^2 = 5.76\%$ Gd, which yielded the best agreement with our experiments. The expectation value μ of the distribution was set to the experimentally indicated one ($\mu = x$ for an $Fe_{1-x}Gd_x$ alloy). The actual distribution variance in our experiments is unknown, however we explored values around the experimentally measured ones by Graves and co-workers[20]. This agreement is robust, varying σ by 10% - 20% yielded similarly good agreement. As discussed in the previous section and shown in Fig. 3.2.2 c) and d), the magnetization dynamics in the simulations reach an equilibrium state after a couple of picoseconds. Additional effects, relevant on longer timescales such as domain formation, heat transport or small applied magnetic fields used in the experiments are not considered in this model. Therefore, a comparison to experimental results on time scales of several hundred picoseconds is beyond the scope of the present work. To conclude this section we found, that atomistic spin models are sufficient for a quantitative description of our experiments for a wide range of pulse durations and Gd-concentrations with only a single set of parameters for all of them.

3.4 Optimal conditions for picosecond pulse switching

In this section we investigate the robustness of our findings and explore the ideal material and laser conditions necessary for energy-efficient switching in GdFeCo. Previous models have suggested, that a distinct demagnetization time τ is necessary to achieve switching. The damping α_i at site i is one of the key parameters for controlling τ_i as previous works in ferrimagnets suggest a $\tau_i \propto \mu_i/\alpha_i$ scaling [118]. Based on the same arguments, one could imagine that the maximum pulse duration within the used model also depends on the intrinsic demagnetization time scales. Indeed, a detailed understanding about the role of damping parameters on switching efficiency could be used to tailor optimized dissipative paths in engineered heterostructures. Thus, in the following we study the dependence of the critical fluence and the maximal pulse duration on the intrinsic damping.

In the previous section we used $\alpha_{\mathrm{Fe}} = 0.06$ and $\alpha_{\mathrm{Gd}} = 0.01$. However these values are

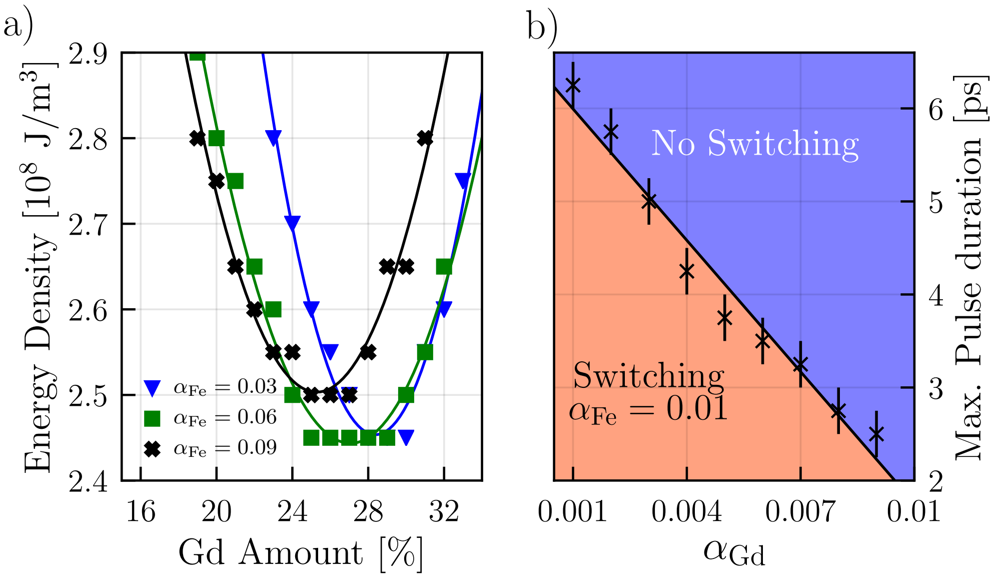

Figure 3.4.1: *Simulation results for a) critical laser fluence of a 350 fs pulse as function of the Gd concentration ($\alpha_{Gd} = 0.01$ constant) for $\alpha_{Fe} = 0.03$ (blue triangles), 0.06 (green boxes), 0.09 (black crosses). The lines represent an x^2 fitting and serve only as a guide to the eye. b) Maximum pulse duration achieved in the model as function of the Gd-damping α_{Gd} ($\alpha_{Fe} = 0.01$ constant) for an $Fe_{75}Gd_{25}$ alloy.*

of phenomenological origin, chosen to match our experiments. In the following we explore switching behavior for damping values of higher and lower α_{Fe} while keeping α_{Gd} constant. Furthermore, the data gained from computer simulations that we show in the following correspond to a fixed Gd concentration. In comparison, when we compare the results of the model and those of the experiment, we accounted for the chemical inhomogeneity of the samples by averaging the magnetization dynamics data over a range of concentrations. Consequently, their dynamics are not directly comparable.
Fig. 3.4.1 a) shows the critical fluence found in simulations as function of the Gd-concentration for different α_{Fe} in the range of $\alpha_{Fe} = 0.03 - 0.09$ while keeping a fixed $\alpha_{Gd} = 0.01$. With an increasing damping α_{Fe} from 0.03 to 0.09 which speeds up the Fe-spin dynamics, we observe a shift of the critical fluence minimum towards lower Gd-concentrations from 29% ($\alpha_{Fe} = 0.03$) to 25% ($\alpha_{Fe} = 0.09$). Furthermore Fig. 3.4.1 shows a x^2-fit as a guide to the eye of the shift of the critical fluence for each Gd-concentration. We observe not just a shift of the critical fluence minimum from 29 % Gd to 25 % Gd, but also a shift of the general switching window in the same direction.

Impact of the pulse duration.– Magnetic switching driven by electric pulses is of interest for future technological applications. However, generating electrical pulses shorter than a few picoseconds is extremely difficult. Therefore finding switching conditions to achieve single-pulse AOS with the longest possible pulses becomes a challenge. Previous experimental results estimated that laser pulses with durations of up to 10 ps were able to switch the magnetization for a very especific Gd-concentration, $Gd_{27}FeCo$ alloys [36]. For different Gd-concentrations the maximum pulse duration within the model decreases notably, such as for $x_{Gd} = 24$ % the maximum pulse duration reduces to 1 ps [36]. Here we show that in order

to describe single-pulse AOS, ASD simulations and the physics described by them, remain valid on timescales of up to 15 ps. Fig. 3.4.1 b) shows the maximum pulse duration of an $\text{Fe}_{75}\text{Gd}_{25}$ alloy as function of the Gd-damping α_{Gd} while keeping $\alpha_{\text{Fe}} = 0.01$ constant. We find a linear increase of the maximum possible pulse duration that is able to switch the alloy with a decreasing Gd-damping α_{Gd}. Decreasing α_{Gd} slows down the Gd dynamics compared to the Fe-sublattice which seems to increase the maximum pulse duration. For $\alpha_{\text{Fe}} = 0.01$ and $\alpha_{\text{Gd}} = 0.001$ we were able to switch an $\text{Fe}_{75}\text{Gd}_{25}$ alloy in our simulations with a pulse of more than 6 ps. This is far longer than what we found in our own experiments (see Fig. 3.4.3) but is only slightly longer than the maximum pulse duration for that alloy found in Ref. [131]. Since the maximum pulse duration is highly susceptible to the ratio between dampings, $\alpha_{\text{Fe}}/\alpha_{\text{Gd}}$, the difference between our experiments and those in Ref. [131] could be related to a somewhat smaller damping ratio in our experiments, owning for instance to slight differences in the growing conditions. We performed further simulations with different absolute values of α_{Fe} and α_{Gd}, while keeping a constant ratio $\alpha_{\text{Fe}}/\alpha_{\text{Gd}}$. These simulations have shown that the position of the critical fluence minimum with respect to the Gd-concentration varies much with the ratio $\alpha_{\text{Fe}}/\alpha_{\text{Gd}}$, but only slightly with the absolute values of α_{Fe} and α_{Gd}.
This seems to indicate that switching with ps-pulses works best when the damping difference between the sublattices is as large as possible.
To gain further insight into this process, we conduct computer simulations on a large set of Gd-concentrations, laser fluences and pulse durations. The goal here was to find the maximum pulse duration that switches the alloy for a given set of Gd-concentrations and pulse energies. In order to do so, we first define a switching criteria: Starting from $m_{z,\text{Fe}} > 0$ every simulation could end up in one of the three possible states: *i*) recovery ($m_{z,\text{Fe}} \geq 0.12$) (see Fig. 3.2.3 a)), *ii*) switching ($m_{z,\text{Fe}} \leq -0.12$) (Fig. 3.2.3 b)) and *iii*) thermal demagnetization ($0.12 > m_{z,\text{Fe}} > -0.12$) (Fig. 3.2.3 c)). The state of the system is evaluated 20 ps after the laser excitation in order to give the spin system time to equilibrate to the final temperature. This duration should be sufficient as the system size is relatively small compared to larger domain-size features, which are important on much longer time-scales. Before we present the full result as a 2D color map we first focus on two subsets of the full result.
Fig. 3.4.2 a) shows the maximum possible pulse duration for a fixed total absorbed energy density of $5 \cdot 10^8$ J/m^3 that still switches the system with $\alpha_{\text{Fe}} = 0.03$ and $\alpha_{\text{Gd}} = 0.01$.

Increasing the Gd-concentration allows for longer pulses to switch the system up to approximately 31.0 % Gd when the fixed total energy density of $5 \cdot 10^8$ J/m^3 causes the system to completely demagnetize. This is due to the decreasing Curie temperature of the sample as the Gd concentration increases. In Fig. 3.4.2 b) the Gd concentration is set to 28% and the total absorbed energy density is varied. In order to switch this $\text{Fe}_{72}\text{Gd}_{28}$ alloy with longer pulses one needs to linearly provide more energy via the laser. This is related to the electron-phonon coupling, which is already significately acting for longer pulses while the laser pulse is still pumping energy into the electron system. This cools down the electron system temperature at a faster rate than for femtosecond laser pulses. Thus more energy input from the laser is needed, as more energy is translated to the phonon system during the laser pulse.

Fig. 3.4.3 shows the full result by combining all simulations with the color representing the maximum pulse duration as a function of the Gd-concentration (x-axis) and total absorbed

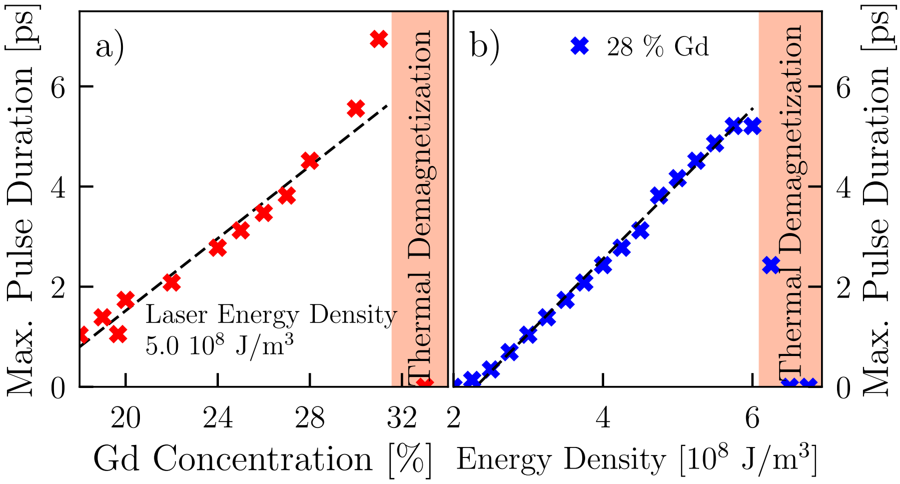

Figure 3.4.2: *a) Maximum possible pulse duration gained from simulations as a function of the Gd-concentration for a fixed laser energy. b) Simulated maximum pulse duration as a function of the absorbed energy for a fixed Gd-concentration of 28%.*

energy density (y-axis). Red colors refer to the possibility of switching the system with longer pulses (up to 6 ps for the chosen damping parameters), while areas with blue colors only allow for switching with short pulses. The top right corner with high absorbed energy densities and high Gd-concentrations completely demagnetizes once a certain threshold is crossed. This area increases linearly as the Gd-concentration increases, due to the linearly decreasing Curie temperature. For longer pulse durations the allowed set of parameters that switches the FeGd alloy reduces to a much narrower set (or switching window). For example, only Gd-concentrations between $\approx$ 26% Gd and 32% Gd are able to be switched with 5 ps pulses and require a precise laser energy. Otherwise the alloy either demagnetizes completely or recovers without switching. The experimental measurements of the maximal achievable pulse duration are shown as white circled points with the color indicating their maximum pulse duration. The overall agreement between our experiments and our model is good. However for the 31% and the 25% Gd concentration the maximum measured pulse duration was only about 220 fs and disagrees with the results of our model (31% Gd-measurement not shown). The experimental results of Ref. [131] with ps-scale switching even up to 23% Gd agree quite well with our simulations. Ref. [131] also finds a similar linear increase of the switching duration as the Gd-concentration increases. In our analysis we used a threshold of $m_{z,\mathrm{Fe}} < -0.12$, that divides switching from demagnetization. This chosen threshold value affects the maximum pulse duration. Reducing this threshold, increases the maximum pulse duration for switching. However, the shape of the different areas in Fig. 3.4.3 are not affected by the chosen threshold value. For simplicity, in our model we neglected any heat dissipation of the GdFeCo alloy towards the substrate. The heat dissipation in the first couple of picoseconds barely affects the overall behaviour of the magnetization dynamics, and, consequently the switching behavior. Considering $m_{z,\mathrm{Fe}} < 0$ as the switching criteria in the absence of cooling is problematic as this state can also be considered as a pure thermal demagnetized state. Further studies could include the effect of the substrate.

Furthermore, as found in the previous section, the maximum switching duration depends on the damping ratio $\alpha_{\mathrm{Fe}}/\alpha_{\mathrm{Gd}}$ (compare fig. 3.4.1 b)). In the simulations for Fig. 3.4.3

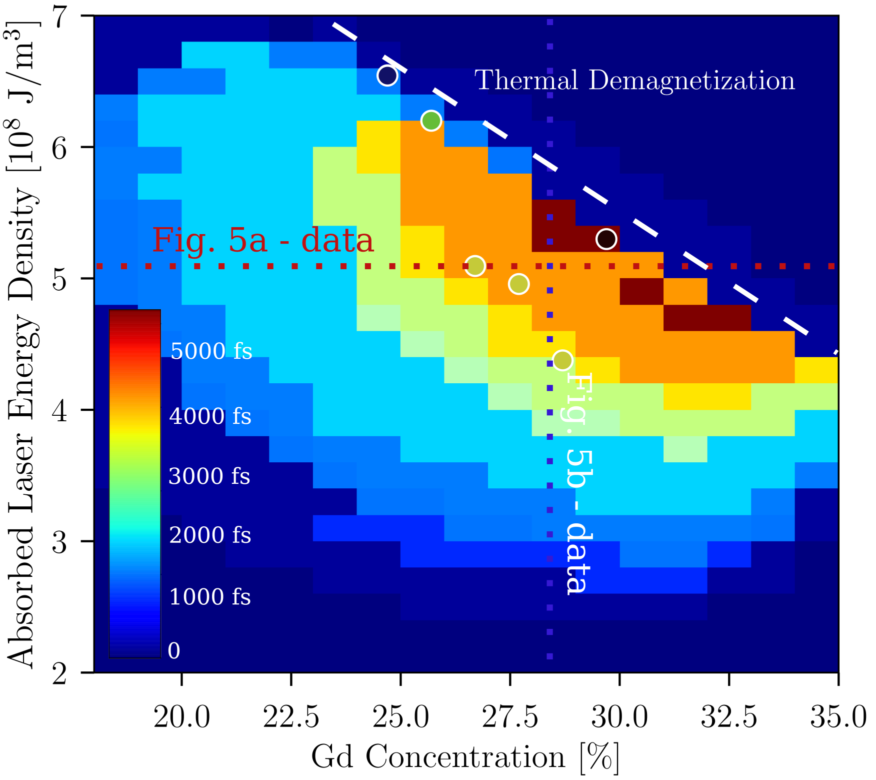

Figure 3.4.3: *Maximum laser pulse duration (as color) as function of the Gd concentration (x-axis) and absorbed power density (y-axis). Red color areas correspond to longer laser pulses, while blue areas only switch for short pulse durations. The damping parameters for this set of simulations were set to* $\alpha_{\text{Fe}} = 0.03$ *and* $\alpha_{\text{Gd}} = 0.01$*. For high laser fluences and high Gd-concentrations the system gets completely demagnetized (top right). The experimental measurements of the maximal achievable pulse duration are shown as white circled points with the color indicating their maximum pulse duration.*

we used moderate values of $\alpha_{\text{Fe}} = 0.03$ and $\alpha_{\text{Gd}} = 0.01$. Using a higher ratio of $\alpha_{\text{Fe}}/\alpha_{\text{Gd}}$ would most likely result in longer switching durations than those seen in Fig. 3.4.3. Notably, previous experimental measurements have shown switching for pulse durations up to 15 ps for compositions close to the magnetic compensation. Our model is also capable of reproducing such a switching duration with up to 15 ps by combining the results of this section. By selecting a high ratio between the element specific damping parameters $\alpha_{\text{Fe}} = 0.01$ and $\alpha_{\text{Gd}} = 0.001$ and choosing optimal parameters from Fig. 3.4.3 for the pulse energy, we were able to switch a $\text{Gd}_{29}\text{Fe}_{71}$-alloy using a 14 ps pulse with an absorbed laser energy density of $5.95 \cdot 10^8$ J/m^3.

3.5 Conclusions

To summarize, we have conducted a joint theoretical and experimental study of single pulse switching of various GdFeCo-alloys using a wide range of pulse durations, from a few femtoseconds up to 15 picoseconds. Our results show that switching is possible for this wide range of pulse durations of two orders of magnitude, however the available material param-

eters that allow for switching reduce as the pulse duration increases. We demonstrate, that the same, underlying physics utilized by atomistic spin dynamics simulations is able to describe switching within hundreds of femtoseconds, as well as tens of picoseconds.
In our experiments, the magnetization dynamics are measured using time resolved magneto-optical Kerr measurements, which provide information on the Fe-spin sublattice dynamics. We were able to quantitatively reproduce those measurements using atomistic spin dynamics simulations (ASD) for all pulse durations used in our experiments, and a wide range of Gd-concentrations between 24% Gd up to 32%. We have kept the same set of material parameters throughout all simulations, e.g. atomic magnetic moments, exchange and anisotropy constants, which demonstrates the robustness of our model. The results of this approach demonstrate that atomistic spin dynamics methods and the physics described by them in the context of single laser pulse all-optical switching still remain valid on timescales of up to 15 ps. One consequence of our study, based on the quantitative agreement between theory and experiment, is the necessity to consider distinct element-specific damping constants. This is in striking contrast to previous works, where only qualitative comparisons were performed. In order to achieve this quantitative agreement, we also needed to consider material inhomogeneities with respect to the Gd-concentration in the model.
As for technological applications of single pulse switching, establishing conditions for steering pulse duration able to switch magnetization in GdFeCo alloy could foster picosecond electric pulse as switching stimulus for spintronic applications. The first works utilizing picosecond electic pulses have already shown promising results [35], but quantitative computational modelling is still missing. Therefore, we believe, that the insights provided by the modeling work presented here will help to better understand the conditions necessary for electric pulse switching. To explore this possibility, we have investigated computationally the optimal system parameters to achieve the longest possible pulse duration able to switch GdFeCo. In agreement with recent works on single-pulse AOS in TbGdFeCo alloys, we found a large discrepancy between the distinct element specific damping parameters to be a key parameter for longer pulse duration switching [138]. Furthermore our results show, that for long pulse durations the set of available parameters of Gd-concentrations and laser fluences, – the so-called switching window – reduces continuously as the pulse duration increases. Using a well defined, ideal set of parameters by combining various results of our work, allowed us to switch a $Gd_{29}Fe_{71}$-alloy in an ASD-simulation using a 14 ps pulse. Ref. [142] showed that single pulse AOS is not limited to alloys but it is also possible in ferrimagnetic multilayers. These kind of heterostructures are better suited for technological applications as they allow for each layer to be tailored individually. Atomistic spin dynamics methods have been used in previous works to model ferrimagnetic multilayers and investigate the conditions for AOS using femtosecond laser pulses [143, 144, 33]. Our results provide a first quantitative prediction of how composition affects single-shot switching for different material properties through varying the composition. By varying the composition, the effective exchange between antiferromagnetically coupled species is varied. One should be able to draw equivalences between this and, for example, a multilayer structure of Gd/Fe with different thicknesses and/or number of repeats of theses layers. However, this task goes beyond the aim of the present work. Our results can furthermore help to understand AOS in other material such as the recently observed switching in Mn_2Ru_xGa Heusler alloys [45].

Chapter 4

Atomistic spin model of single pulse toggle switching in Mn_2Ru_xGa Heusler alloys

The results of this chapter have been published in

- F. Jakobs, and U. Atxitia, Atomistic spin model of single pulse toggle switching in Mn_2Ru_xGa Heusler alloys, *Applied Physics Letters* **120** p. 172401, (Apr 2022).

and the content of this chapter is in large parts identical with the published work.

This chapter is not printed in the online version.
The published version can be found at `https://doi.org/10.1063/5.0084846`

Chapter 5

Universal Criteria for Single Femtosecond Pulse Ultrafast Magnetization Switching in Ferrimagnets

The results of this chapter have been published in

- F. Jakobs, and U. Atxitia, Universal Criteria for Single Femtosecond Pulse Ultrafast Magnetization Switching in Ferrimagnets, *Physical Review Letters* **129**, p. 037203, (Jul 2022).

and the content of this chapter is in large parts identical with the published work. Large parts of the macroscopic model presented in this chapter were developed by U. Atxitia with the numerical simulations for GdFeCo and MnRuGa developed and performed as part of this thesis.

The published version can be found at `https://doi.org/10.1103/PhysRevLett.129.037203`

Ultrafast magnetization switching induced by a single femtosecond laser pulse has attracted a lot of attention as a promising solution for low energy, faster memory applications [24, 6, 32, 158, 20, 145, 159, 44, 160, 142, 133, 38, 161, 162, 46]. Until recently only GdFeCo alloys and synthetic ferrimagnets [44], presented the ability to switch under either optical femtosecond laser- [32, 158, 44] or electric picosecond current-pulses [35, 39]. Although several micro- and macroscopic models have reproduced single-pulse switching in GdFeCo ferrimagnets [163, 126, 135, 128, 127, 116, 164, 165, 129, 166, 167, 33, 130, 168, 169, 131], complete understanding of the role of electrons, lattice and spin sublattices and their mutual interactions remains a challenge [170]. The existing criteria for switching rely on the existence of two antiferromagnetically coupled magnetic sublattices showing distinct dynamical response to femtosecond laser photo-excitation. While in single species ferromagnets such as 3d transition metals, relaxation of angular momentum occurs via dissipation into other degrees of freedom – relativistic relaxation – in two-sublattice magnets, additionally, relaxation can occur via angular momentum exchange between sublattices – exchange relaxation. By driving the spin system into a non-equilibrium state where exchange relaxation dominates, a non-equilibrium ultrafast reversal path opens. One of the most outstanding, open questions is about the conditions or criteria for the onset of the exchange dominated relaxation regime. Crucially, it is unclear how previous understanding gained from observation in GdFeCo translates into the recent discovery of single-pulse switching in the ferrimagnetic Heusler alloy Mn_2Ru_xGa [45], where the two antiferromagnetically coupled Mn atoms are of the same kind in comparison to Gd and FeCo.

In this work we present a general theoretical framework for the description of single pulse switching of ferrimagnets. We provide explicit expressions for the relativistic and exchange relaxation parameters as a function of microscopic material parameters, including their dependence on temperature and non-equilibrium sublattice magnetization. This allows us to uncover the criteria for the onset of the exchange-dominated relaxation regime and switching. We verify the validity of the model by direct comparison to atomistic spin model simulations of both GdFeCo and Mn_2Ru_xGa alloys.

We shall describe each magnetic atom at site i as a classical spin vector $\mathbf{s}$ of a unit length. The magnetic and mechanical moments of each atom/element are given by $\boldsymbol{\mu} = \mu_s \mathbf{s}$ and $\mathbf{S} = \mu_s \mathbf{s}/\gamma$ where μ_s is the magnetic moment and γ is the gyromagnetic ratio. We consider a classical Heisenberg spin Hamiltonian[72]:

$$\mathcal{H} = -\sum_{i \neq j \langle ij \rangle} J_{ij} \mathbf{s}_i \cdot \mathbf{s}_j - \sum_i d_i^z (s_i^z)^2. \tag{5.0.1}$$

To model a ferrimagnet, one needs to consider two sublattices with different and antiparallel magnetic moments μ_a and μ_b, with three different exchange coupling constants. Two ferromagnetic couplings for each sublattice coupling with itself (J_a and $J_b > 0$) and a third for the antiferromagnetic interaction between them, $J_{ab} < 0$ [132]. The second term in Eq. (5.0.1) describes the contribution to the energy of on-site uniaxial anisotropy with easy-axis in z-direction and anisotropy constant, d_i^z.

The macroscopic model we propose is derived from a microscopic spin model, where the equation of motion for the spin dynamics of each atomic spin is the stochastic Landau-Lifshitz-Gilbert (LLG) equation [72]:

$$\frac{\partial \mathbf{s}_i}{\partial t} = -\frac{|\gamma|}{(1+\lambda^2)\mu_i} \left[(\mathbf{s}_i \times \mathbf{H}_i) - \lambda \left(\mathbf{s}_i \times (\mathbf{s}_i \times \mathbf{H}_i) \right) \right]. \tag{5.0.2}$$

λ is the local intrinsic atomic damping, the effective field $\mathbf{H}_i = \boldsymbol{\zeta}_i - \frac{\partial \mathcal{H}}{\partial \mathbf{s}_i}$, where thermal fluctuations are represented by the stochastic field $\boldsymbol{\zeta}_i$.

The non-equilibrium macroscopic magnetization dynamics of the element-specific angular momentum $S_a = \mu_a \langle s_a \rangle / \gamma$, where $m_a = \langle s_a \rangle$ is the first moment of the non-equilibrium distribution function, can be described by [126]:

$$\frac{dS_a}{dt} = \alpha_a \mu_a H_a + \alpha_{\mathrm{ex}} (\mu_a H_a - \mu_b H_b) \tag{5.0.3}$$

where $a \neq b$. The macroscopic relativistic damping parameter in Eq. (5.0.3) reads [171]

$$\alpha_a = 2\lambda_a \frac{L(\xi_a)}{\xi_a}. \tag{5.0.4}$$

Here, $L(\xi)$ stands for the Langevin function. The relaxation parameter strongly depends on temperature and non-equilibrium magnetization state through the thermal field $\xi_a = \beta \mu_a H_a^{\mathrm{MFA}}$. In the exchange approximation, the MFA field acting on sublattice a is:

$$\mu_a H_a^{\mathrm{MFA}} = z_a J_{aa} m_a + z_{ab} J_{ab} m_b. \tag{5.0.5}$$

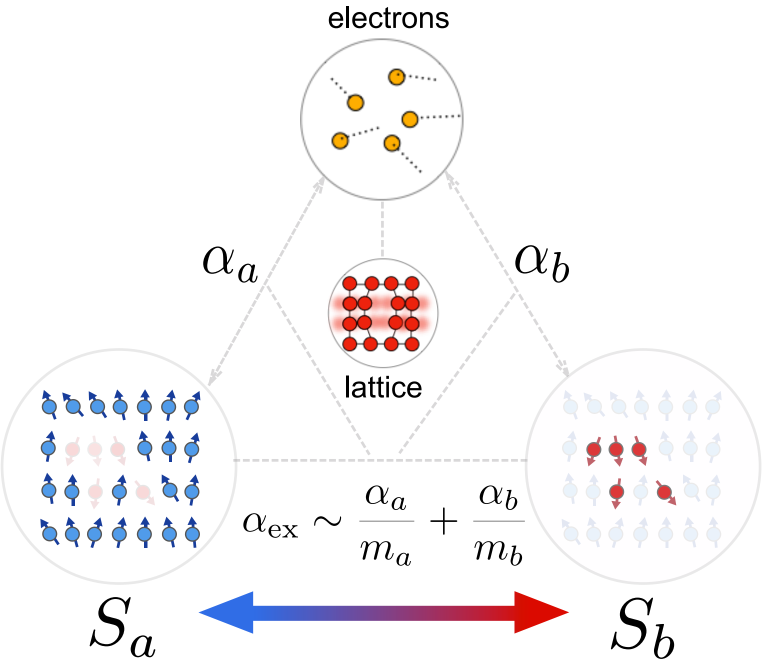

Figure 5.0.1: *Degrees of freedom involved in single-pulse switching; electrons, lattice and element-specific spin systems. Electrons act as heat-bath to the spin system with an element-specific coupling strength given by $\alpha_{a(b)}$. Exchange relaxation rate $\alpha_{\rm ex} \sim \alpha_a/m_a + \alpha_b/m_b$, where $m_{a(b)}$ are the normalized sublattice magnetization magnitude.*

Here, z_a is the number of nearest neighbours (n.n.) of spins of type a, and z_{ab} is the amount of n.n. of type b. The macroscopic damping increases with temperature up to a value $\alpha_a = 2/3$ at the critical temperature [171]. The exchange relaxation parameter $\alpha_{\rm ex}$ is given by

$$\alpha_{\rm ex} = \frac{1}{2}\left(\frac{\alpha_a}{z_{ab} m_a} + \frac{\alpha_b}{z_{ab} m_b}\right). \tag{5.0.6}$$

This expression is the extension of the non-local exchange relaxation in ferromagnets to local exchange relaxation in ferrimagnets. The role of $\alpha_{\rm ex}$, α_a and α_b as the coupling between the sublattices and heat baths is visualized in Fig. 5.0.1. In single species ferromagnets, sublattices a and b represent the same spin lattice, hence $\alpha_a = \alpha_b$. Therefore, $\alpha_{\rm ex} = \alpha_a/(z m_a)$, and $\mu_a H_a - \mu_b H_b = \mu_a H_{\rm ex} a_0^2 \Delta m_a$, with a_0 representing the lattice constant. Hence, $\Gamma_{\rm ex}^{\rm non-loc.} = \alpha_{\rm ex}(\mu_a H_a - \mu_b H_b) = \alpha_a (A/M_a(T))\Delta m_a$, where A is the so-called micromagnetic exchange stiffness [172]. $M_a(T) = (\mu_a/v_a) m_a$ is the magnetization density at temperature T, where v_a is the unit cell volume. Non-local exchange relaxation plays a minimal role in the field of ultrafast magnetization dynamics since $\Delta m_a \ll 1$.
The non-equilibrium fields ($\mu_a H_a = 0$ at equilibrium) are given by

$$\mu_a H_a = \frac{(m_a - L(\xi_a))}{\beta L'(\xi_a)}. \tag{5.0.7}$$

where, $L'(\xi) = dL/d\xi$. Note that they are different to the MFA fields in Eq. (5.0.5), and have been derived previously [173, 171]. As the magnetic system approaches thermal equilibrium, the non-equilibrium fields can be cast into Landau-like expressions [126, 171]. Equation (5.0.3) has been proposed before based on symmetry arguments [126, 116] as a direct generalization of the Landau-Lifshitz equation with longitudinal relaxation terms. These models

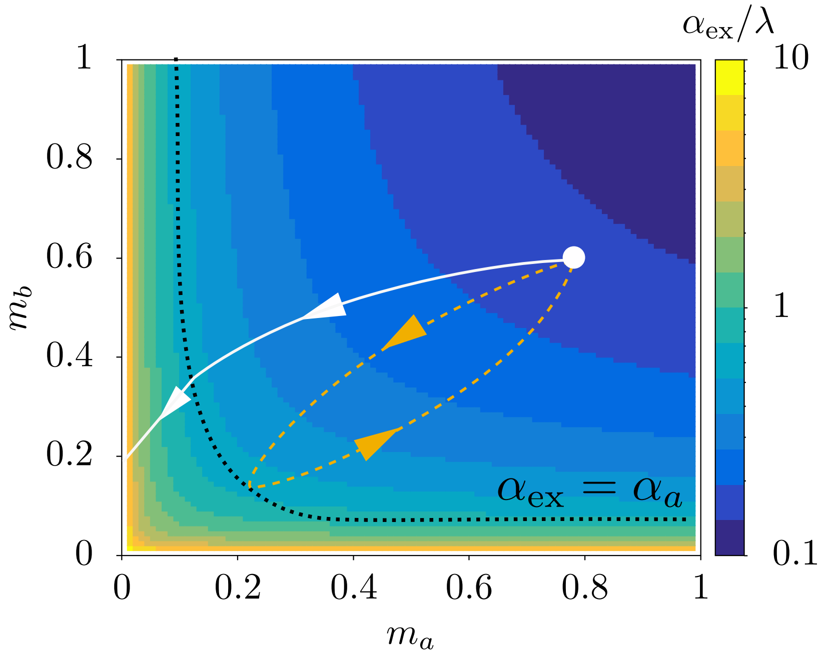

Figure 5.0.2: *Normalized exchange relaxation parameter* $\alpha_{\mathrm{ex}}/\lambda$ *as function of the sublattice magnetization* m_a *and* m_b*, at* $T = 600$ *K. System parameters correspond to GdFeCo.* $\lambda_a = \lambda_b = \lambda = 0.01$*. The dotted black line corresponds to* $\alpha_{\mathrm{ex}} = \alpha_a$*. The white dot represents the starting sublattice magnetization* (m_a, m_b)*. The closed dashed orange line describes a trajectory meeting a no-switching criteria. The open solid white line describes a trajectory meeting a switching criteria.*

have introduced the relaxation parameters at a purely phenomenological level and to some extent their values are arbitrary. Moreover, since they were taken as constant values, most of the non-equilibrium spin physics was not taken into account. Our model overcomes these assumptions by providing expressions for the relativistic and exchange relaxation parameters as a function of the sublattice specific atomic relaxation parameter, $\lambda_{a(b)}$, and normalized magnetization $m_{a(b)}$.

This insight is paramount to find the criteria for the onset of a exchange relaxation dominated state. In Fig. 5.0.2 we present a diagram of the normalized exchange relaxation parameter $\alpha_{\mathrm{ex}}/\lambda$ for GdFeCo alloy parameters as a function of m_a and m_b at a fixed temperature, $T = 600$ K, which corresponds to the Curie temperature of the alloy. We observe that the exchange relaxation parameter strongly depends on the magnitude of sub-lattice magnetization and its value ranges over three orders of magnitude, $\alpha_{\mathrm{ex}}/\lambda = 0.1 - 10$. Importantly, only when magnetic states reduce significantly, does the exchange relaxation dominates over relativistic relaxation.

So far only two classes of ferrimagnets have shown single-pulse switching, $\mathrm{Gd}_x(\mathrm{FeCo})_{1-x}$ alloys and $\mathrm{Mn_2Ru}_x\mathrm{Ga}$. Switching in GdFeCo has been thoroughly studied both experimentally [24, 6, 32, 158, 20] and theoretically [32, 135, 127, 128, 116, 168, 133, 169], whereas in $\mathrm{Mn_2Ru}_x\mathrm{Ga}$ has been only recently demonstrated for a range of Ru concentrations ($x \geq 0.9$) [45]. In GdFeCo alloy, switching is characterised by a fast response of the Fe sublattice and slower response of the Gd sublattice to femtosecond laser photo-excitation. This difference roots to their distinct magnetic moment, $\mu_{\mathrm{Gd}} = 7.6\mu_{\mathrm{B}}$ and $\mu_{\mathrm{Fe}} = 1.92\mu_{\mathrm{B}}$. Differently to GdFeCo, antiferromagnetically coupled Mn spins in $\mathrm{Mn_2Ru}_x\mathrm{Ga}$ have similar atomic magnetic moments. We demonstrate the universality of our theory by direct comparison of the photo-

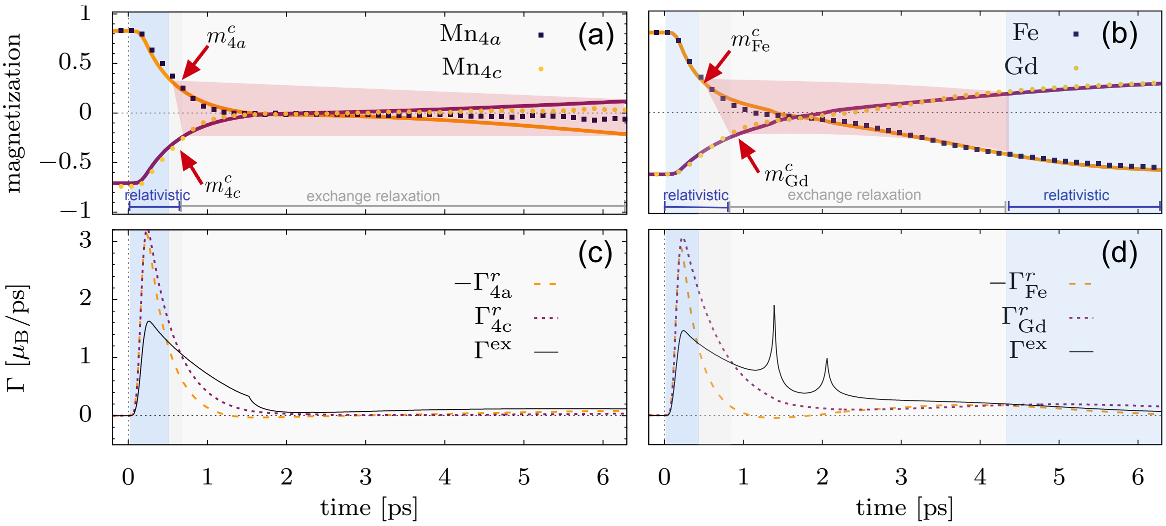

Figure 5.0.3: *Element-specific magnetization dynamics of single-pulse switching in ferrimagnets using an atomistic spin dynamics model (symbols) and a macroscopic model (solid lines) for* $\mathrm{Mn_2Ru_{0.86}Ga}$ *(a) and* $\mathrm{Gd_{25}FeCo}$ *(b). The red area corresponds to the critical values* (m^c_a, m^c_b) *to enter exchange relaxation regime. The blue area corresponds to the time lapse where relativistic relaxation dominates. Different contributions to the element-specific magnetization relaxation for the single-pulse switching dynamics in* $\mathrm{Mn_2Ru_{0.86}Ga}$ *(c) and* $\mathrm{Gd_{25}FeCo}$ *(d).* $\Gamma^r_{a(b)}$ *stands for the relativistic relaxation rate of sublattice* $a = 4a$ *(c) and* $a =$*Fe (d), and* $b = 4c$ *(c) and* $b =$*Gd (d).* Γ^{ex} *is the exchange relaxation rate, which is the same for both sublattices.* $\lambda_a = \lambda_b = \lambda = 0.01$.

induced magnetization switching to computer simulations based on atomistic spin dynamics (Eq. (5.0.2)) for GdFeCo (disordered spin structure) and $\mathrm{Mn_2Ru}_x\mathrm{Ga}$ (ordered spin structure). Their magnetic properties such as magnetic moments and exchange interactions differ substantially. We consider two typical compositions, that show switching, $\mathrm{Gd_{25}(FeCo)_{75}}$ alloys and $\mathrm{Mn_2Ru_{0.86}Ga}$. It is noteworthy; that while for GdFeCo atomistic spin models have been used thoroughly, in $\mathrm{Mn_2Ru_{0.86}Ga}$ similar simulations are missing. We derive the necessary material parameters based on experimental measurements [149, 150, 156, 152, 148]. We find that for $\mathrm{Mn_2Ru_{0.86}Ga}$ the atomic magnetic moments, $\mu_{4a} = 2.88\ \mu_\mathrm{B}$ and $\mu_{4c} = 4.05\ \mu_\mathrm{B}$, and the exchange parameters, $J_a = 1.28 \times 10^{21}$ J, $J_b = 4.0 \times 10^{22}$ J and $J_{ab} = -4.85 \times 10^{22}$ J describe the equilibrium magnetization well as function of temperature. Using these parameters the Curie temperature becomes $T_c = 600$ K and the compensation temperature $T_\mathrm{M} \approx 300$ K. We note that in the experimental samples, those temperatures are sensitive to the growth conditions as well as material composition. However our temperatures are within the reported range of experimentally found temperatures [149, 150, 156, 152, 148]. We use the so-called two-temperature model (TTM) to describe the dynamics of the electron and phonon systems[102, 110]. For both materials we use the same parameters in the TTM and thus the electron and phonon temperatures are the same for the same fluence in both materials [148]. In the TTM, we use the values $c_e = \gamma_e T_e (\gamma_e = 600\ \mathrm{J/Km})^3$ for the electron specific heat, $c_{ph} = 3.8 \times 10^6\ \mathrm{J/Km^3}$ for the phonon specific heat, and $g_{e-ph} = 7 \times 10^{17}\ \mathrm{J/sKm^3}$ for the electron-phonon coupling. The heat-bath to which the spins are coupled is represented by the electron system. Figures 5.0.3 (a) and (b) show excellent agreement between our macroscopic model and atomistic spin dynamics simulations for both alloys for all stages of the magnetization dynamics leading to switching, from fast demagnetization, transient ferromagnetic-like state, to magnetization recovery. Interestingly, the switching dynamics in $\mathrm{Mn_2Ru_{0.86}Ga}$ (Fig. 5.0.3 (a)) differs to GdFeCo (Fig. 5.0.3 (b)), both Mn sublattices demagnetize at similar rate and switch almost simultaneously. Although demagnetization timescales are similar in $\mathrm{Mn_2Ru_{0.86}Ga}$ and GdFeCo, the recovery of the magnetization in $\mathrm{Mn_2Ru_{0.86}Ga}$ is significantly slower. The relaxation of the sublattice magnetization (Eq. 5.0.3) can be split into two contributions, the relativistic relaxation: $\Gamma_a^r = \alpha_a \mu_a H_a$, and exchange relaxation $\Gamma^{\mathrm{ex}} = \alpha_{\mathrm{ex}}(\mu_a H_a - \mu_b H_b)$ (see Fig. 5.0.3(c) and (d)). For both ferrimagnetic alloys, Γ_a^r drives the dynamics in the first hundreds of femtoseconds, until sublattice magnetization reduces sufficiently to enter the exchange relaxation dominated region $\Gamma^{\mathrm{ex}} > \Gamma_a^r$ (Fig. 5.0.2). In this regime, the exchange relaxation steers the systems towards an intermediate metastable state defined by the condition $\mu_a H_a = \mu_b H_b$. Under some conditions this intermediate state precede switching. It is cumbersome however to directly analyse Eqs. (5.0.7) due to its highly non-linear character. Therefore in the following we investigate some limiting scenarios.

In the high temperature limit, $\xi_a = \beta \mu_a H_a^{\mathrm{MFA}} \to 0$, $\Gamma_a^r = 2\lambda_a k_B T m_a$, which is the so-called thermal fluctuation field. The corresponding relaxation time, $\tau_a = \mu_a/(\gamma 2\lambda_a k_B T)$, associated to relativistic relaxation, has been discussed before [126, 118]. Similarly, we can estimate the high-temperature limit of the exchange relaxation rate

$$\Gamma_\infty^{\mathrm{ex}}(m_a, m_b) = \lambda \frac{k_B T}{z} \frac{(m_a + m_b)(m_a^z - m_b^z)}{m_a m_b}. \tag{5.0.8}$$

High temperature limits are valid when the temperature is larger than the exchange energy acting on the spins. Otherwise, intermediate-to-high temperature limit are necessary. This limit adds corrections to previous estimations. For instance, $\mu_a H_a - \mu_b H_b = 3k_B((T - T_c^a)m_a + (T - T_c^b)m_b)$, where $J_{0,a} + J_{0,ab} = 3k_B T_c^a$. The exchange relaxation rate is

$$\Gamma_T^{\mathrm{ex}}(m_a, m_b) = \Gamma_\infty^{\mathrm{ex}} \left(1 - \frac{1}{T} \frac{T_c^a m_a + T_c^b m_b}{m_a + m_b}\right) \tag{5.0.9}$$

For element-specific critical temperature $T_c^a \approx T_c^b$, the correction can be cast as $\Gamma_T^{\mathrm{ex}} = \Gamma_\infty^{\mathrm{ex}}(T - T_c^a)/T$.Since the relativistic relaxation rate is also modified as $\Gamma_a^r = \Gamma_{a,\infty}^r (T - T_c^a)/T$, we can fairly investigate the crossover from relativistic to exchange dominated regime by comparing $\Gamma_\infty^{\mathrm{ex}}$ and $\Gamma_{a,\infty}^r$. Two cases of interest exist, i) one sublattice is faster than the other, and ii) both sublattices demagnetize at the same rate.

In the first case, $\tau_a \ll \tau_b$, sublattice a demagnetizes faster than sublattice b. This corresponds to GdFeCo (Fig. (5.0.3)(b)). Soon after the application of a fs laser pulse, $m_a \ll m_b$, and consequently, $\Gamma^{\mathrm{ex}} \approx \lambda k_B T m_b/(z m_a)$ (cf. Eq.(5.0.8)). We estimate the conditions for the transition from relativistic to exchange-dominated regimes (see Fig. (5.0.3)(d)): From $\Gamma^{\mathrm{ex}} > \Gamma_a^r$, $m_a < \sqrt{m_b/2z_{ab}} \approx 0.288\sqrt{m_b}$, and from $\Gamma^{\mathrm{ex}} > \Gamma_b^r$ and $m_a \leq 1/2z = 0.0833$ (red colored area in Fig. 5.0.3 (b)). A second case, $\tau_a \approx \tau_b$, might also arise when demagnetization times of both sublattices are similar. This is the case of $\mathrm{Mn_2Ru_{0.86}Ga}$ alloys (Fig. (5.0.3)(c)). One can estimate the conditions for the transition $\Gamma^{\mathrm{ex}} = \Gamma_a^r$. This happens for both sublattices when $m_{a,b} = (m_a(0) + m_b(0))^2/(m_a(0)m_b(0))/2z_{ab}$. Assuming a realistic value of $m_b(0)/m_a(0) = 0.9$, the exchange-dominate regime is reached when $m_{a,b} = 0.334$ (red colored area in Fig. 5.0.3 (c)). Notably, this condition only depends on the initial values of the magnetization, $m_{a(b)}(0)$. These results are simple and general, and one of the main result of the present work. One can interpret the transition from relativistic to exchange-dominated regime as follows: as the magnetization of one sublattice decreases, the phase space of available states for the spins of the other sublattice to switch by exchange of angular momentum dramatically increases. While switching spin via coupling to an external bath becomes increasingly difficult as the magnetization reduces.

Once the system has entered the exchange dominated regime the dynamics follows a path where total angular momentum is conserved towards a magnetic state where $\mu_a H_a = \mu_b H_b$. In the high temperature limit, this condition reduces to $m_a^z = m_b^z$, meaning that the exchange relaxation drives the magnetization of both sublattices into the same polarity, i.e. a ferromagnetic-like state [6]. From this condition arises, that in order to have a final $m_a^z < 0$ the following condition is necessary: $S_a^{\text{ex}} + S_b^{\text{ex}} < 0$. Here $S_{a(b)}^{\text{ex}}$ stands for the angular magnetic moment when the system enters the exchange dominated regime. For example, in $\text{Mn}_2\text{Ru}_x\text{Ga}$, since Mn spins are assumed to demagnetize at the same rate, this condition reduces to $S_a^{\text{ex}} + S_b^{\text{ex}} \approx (S_a(0) + S_b(0)) \exp(-t/\tau_a) < 0$. Namely, only for a starting temperature below the compensation temperature, $S_a(0) + S_b(0) < 0$, conditions for switching are fulfilled, in complete agreement to experimental observations [45]. Yet, the exchange relaxation regime needs to be active for a significant time in order for the magnetization to switch. We compare the time scales associated to both the relativistic and exchange relaxation. Relativistic relaxation rate follows $\Gamma_a^r = 2\lambda_a k_B (T - T_c^a) m_a^z$, which is strongly reduced by the ultrafast dynamics of m_a^z, in only a few hundred of femtoseconds $\Gamma_a^r \to 0$. Whereas Γ^{ex} rather follows the dynamics of the temperature T, and therefore decays slower than Γ_a^r (Fig. (5.0.3)(c) and (d)).

The characteristic time scale of the electron and lattice temperature is described by the TTM and for common parameter values in the range of $2 - 3$ ps. As the temperature reduces, the exchange relaxation drives the system towards $(T - T_c^a) m_a^z = (T - T_c^b) m_b^z$. For $T_c^b < T < T_c^a$, the exchange relaxation drives the system back into an antiferromagnetic, but switched sate. As the magnetization builds up in the opposite direction, Γ^{ex}, decreases and the relativistic relaxation takes over. Interestingly, our theory predicts that for systems where $T_c^a \approx T_c^b$ switching would be unlikely, which has been recently demonstrated in rare-earth free synthetic ferrimagnets [174]. Further, one can accelerate the transition from exchange relaxation dominated to the relativistic regime, and speed up complete switching by increasing difference between T_c^a and T_c^b, an effect which has been observed by the substitution of Fe by Co, namely, GdFe by GdCo [41]. While GdFe recovers in tens of picoseconds, GdCo alloys only need of a couple of picoseconds.

To summarize, in this work we have proposed a general macroscopic theory for the magnetization dynamics of ferrimagnetic materials driven by femtosecond laser photo-excitation. Our theory reproduces quantitatively all stages of the switching process observed in experiments. Notably, we have directly compared our theory to computer simulations using atomistic spin dynamics methods for both GdFeCo and $\text{Mn}_2\text{Ru}_x\text{Ga}$ alloys. The magnetization dynamics transits from a relativistic relaxation path to an exchange dominated regime due to the strong enhancement of the exchange relaxation. We demonstrate that switching occurs when the sublattice magnetization reaches a threshold value. These criteria substitute previous ones and pave the way for the discovery of new class of ferrimagnets showing switching.

Chapter 6

Exchange-enhancement of the ultrafast magnetic order dynamics in antiferromagnets

The results of this chapter have been submitted to Physical Review Letters and is currently being reviewed. A preprint has been uploaded to arXiv.org

- F. Jakobs, and U. Atxitia, Exchange-enhancement of the ultrafast magnetic order dynamics in antiferromagnets, arXiv:2206.05783, (Jun 2022).

and the content of this chapter is in large parts identical with the published work.

6.1 Introduction

Ultrafast optical control of the magnetization promises faster data processing and storage [5, 175, 14, 6, 32, 176]. Antiferromagnets (AFMs) show advantages over ferromagnets (FMs), such as faster magnetization dynamics [177, 178, 179, 180, 181, 182, 183]. In AFMs, the frequency of the magnetic oscillations around the anisotropy field in FMs ($\omega_{\mathrm{fm}} \sim H_{\mathrm{A}}$) are exchange-enhanced by the antiferromagnetic coupling (H_{E}) between the spins at different sublattices, leading to a higher oscillation frequency in AFMs, ($\omega_{\mathrm{afm}} \sim \sqrt{H_{\mathrm{E}} H_{\mathrm{A}}}$), orders of magnitude higher than in FMs [184, 185]. Femtosecond laser photo-excitation can induce subpicosecond magnetic order quenching in both FMs and AFMs [5, 186, 187]. The speed of ultrafast quenching of the magnetic order is determined by the strength of the exchange interaction ($1/\tau_{\mathrm{fm}} \sim \alpha_{\mathrm{fm}} H_{\mathrm{E}}$), and the FM damping, α_{fm} [188]. This raises the fundamental question of whether the ultrafast magnetic order dynamics in AFMs is exchange-enhanced with respect to its FM counterpart. We find that the AFM magnetic order responds faster than the FM one to a sudden temperature change due to the exchange-enhancement of the effective AFM damping, $1/\tau_{\mathrm{afm}} \sim \alpha_{\mathrm{afm}} H_{\mathrm{E}}$. We show that, contrary to FMs, the effective AFM damping depends on the number of neighbours to which spins are exchange coupled. Thus, low dimension magnets, such as 2D magnets [189], show a more pronounced speed up. As the system approaches the critical temperature, both the FM and AFM present a critical slow down of the relaxation process, however, the AFM critical exponent is smaller

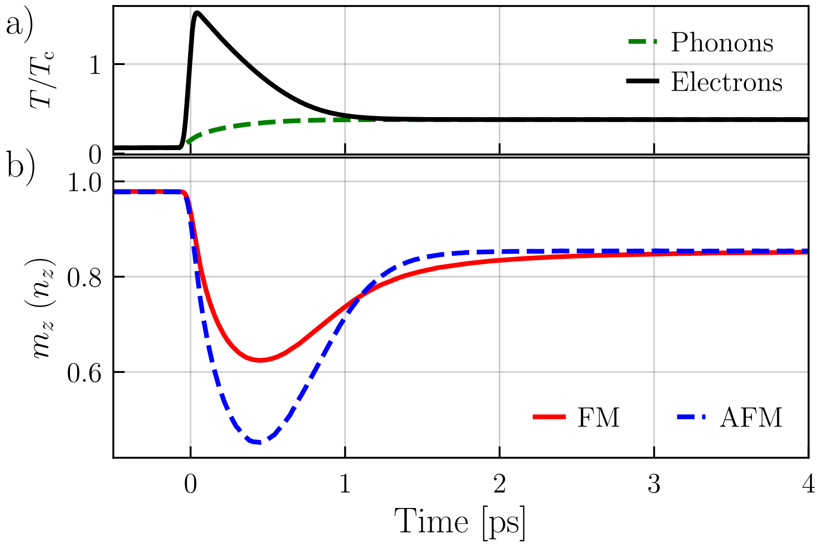

Figure 6.1.1: *(a) Electron and phonon temperature dynamics after an excitation by a 50 fs laser at $t = 0$. (b) The magnetic order dynamics of a FM, m_z (red solid line), and an AFM, n_z (blue dashed line) as a response to the electron temperature dynamics in (a).*

than the FM one. In the temperature dominated regime $T \gg T_c$, our model predicts intrinsically different relaxation dynamics for AFMs and FMs. This scenario corresponds to experiments using powerful femtosecond laser pulses. For FMs, magnetic order quenching slows down as the magnetization reduces, while for AFMs speeds up. We demonstrate the validity of our model by direct comparison to computer simulations using atomistic spin dynamics within an atomistic spin dynamics (ASD) model. Evidence of exchange-enhancement of the ultrafast magnetization dynamics in AFMs is scarce due to the difficulties to conduct a systematic comparison on the same system presenting FM and AFM magnetic order. Studies in rare-earth Dy using femtosecond time-resolved resonant magnetic x-ray diffraction have measured the dynamics of its FM and AFM-spin-helix states. These investigations have shown that the dynamics of the order parameter in the AFM phase is faster than in the FM phase [187]. Laser induced ultrafast magnetization dynamics in FMs have been modeled using computer simulations based on different approaches, from ASD models to macroscopic phenomenological approaches [5, 14, 188]. Within these approaches magnetization dynamics are explained on thermodynamic grounds. When the temperature of the heat-bath is rapidly modified, the magnetic order changes according to $\dot{M} \sim \alpha_{\mathrm{fm}} H$, driven by an effective field $H = -\partial F/\partial M$ at a rate α_{fm}, towards minimal free energy values, $F(M)$ [116]. The thermodynamic argument explains demagnetization and magnetization recovery when the system temperature increases and decreases, respectively. It can be expected to hold for other magnetic structures, such as antiferromagnets, as well. In AFMs however, an additional channel for angular momentum dissipation opens, by direct exchange of angular momentum between sublattices. For a two sublattice AFM, the dynamics of sublattice a can be expressed as : $\dot{M}_a \sim \alpha_a H_a + \alpha_{\mathrm{ex}}(H_a - H_b)$, where α_{ex} represents the rate of inter-atomic transfer of angular momentum between sublattices a and b. In the simplest AFM case, both sublattices are equivalent, such that $H_a = -H_b$ is a valid approximation, leading to $\dot{M}_a \sim (\alpha_a + 2\alpha_{\mathrm{ex}})H_a = \alpha_{\mathrm{afm}} H_a$, where α_a and α_{ex} are the Onsager coefficients describing exchange and relativistic relaxations. For FM and AFM systems defined by the same parameters, $\alpha_{\mathrm{afm}} > \alpha_{\mathrm{fm}}$, and consequently the AFM is faster than the FM.

6.2 Exchange-enhancement of the magnetic order dynamics in antiferromagnets

By using ASD simulations, we first demonstrate the existence of exchange-enhancement on the AFM dynamics in conditions similar to experiments (see appendix). A high temperature regime, $T \gg T_\mathrm{c}$ can be accessed by suddenly heating the electron system using a femtosecond laser pulse (Fig. 6.1.1 (a)). Using the two temperature model (TTM) the electron temperature will rise far above T_c on a timescale of 100 fs (see appendix). The magnetic system responds to this temperature change by reducing its magnetic order on similar time scales. The electron-phonon coupling allows energy transfer from the hot electrons to the lattice in the time scale of only a couple of picoseconds. This allows for the investigation not only of the magnetic order quenching but also its recovery. Figure 6.1.1 (b) shows that the demagnetization in the AFM is larger than in FM, owning to a faster response when excited by the same temperature profile (Fig. 6.1.1 (a)). The magnetic order recovery of the AFM is on the same time scale as the electron-phonon temperature relaxation time, while it takes the FM more time to relax. The exchange-enhancement of the AFM magnetic damping is at the origin of this speed up as we shall demonstrate. The non-equilibrium macroscopic magnetization dynamics of the sublattice can be described by [126]:

$$\frac{1}{\gamma}\frac{dm_a}{dt} = \alpha_a H_a + \alpha_\mathrm{ex}(H_a - H_b) \tag{6.2.1}$$

where $a \neq b$. The macroscopic damping parameter in Eq. (6.2.1) is defined as, $\alpha_a = 2\lambda L(\xi_a)/\xi_a$, here, λ is the atomic damping parameter. Here, $L(\xi_a)$ stands for the Langevin function, with the argument $\xi_a = \beta\mu_a H_a^\mathrm{MFA}$ and $\beta = 1/k_\mathrm{B}T$ [173]. In the mean field approximation (MFA), the field acting on sublattice a is $\mu_a H_a^\mathrm{MFA} = J_0 m_b$, where $J_0 = zJ$ and z is the number of nearest neighbours of spins of type b and J is the exchange interaction energy. Moreover, in the exchange approximation, one can fairly assume that $m_a = m_b = m$, and therefore $\alpha_a = \alpha_b$. Under these assumptions, the exchange relaxation parameter can be written as $\alpha_\mathrm{ex} = 4\alpha_a/(zm)$ (see Chapter 5). One can recover the equation of motion for the FM case for $\alpha_\mathrm{ex} = 0$ (Eq. (6.2.1)), in that case, $\alpha_\mathrm{fm} = \alpha_a$. The non-equilibrium effective fields are given by

$$H_a = \frac{(m_a - m_{0,a})}{\mu_a \beta L'(\xi_a)}. \tag{6.2.2}$$

where, $L'(\xi) = dL/d\xi$ and $m_{0,a} = L(\xi_a)$ [173, 171]. For the two sublattice AFM considered here, $H_a = -H_b = H_n$, where $H_n = (n - n_0)/\mu_a\beta L'(\xi)$. It follows that the dynamics of the Néel order parameter is given by

$$\frac{1}{\gamma}\frac{dn}{dt} = \alpha_\mathrm{afm} H_n. \tag{6.2.3}$$

This demonstrates that the origin of exchange-enhancement of the AFM dynamics can be traced back to the effective AFM damping parameter,

$$\alpha_\mathrm{afm} = \alpha_\mathrm{fm}\left(1 + \frac{4}{z|n|}\right). \tag{6.2.4}$$

We first address the differences and similarities between AFM and FM near thermal equilibrium, where the non-equilibrium fields can be cast into Landau-like expressions [126, 171], $H_n = (\mu_\mathrm{at}/2\widetilde{\chi}_\parallel)\delta n^2/n_e^2$. Here $\widetilde{\chi}_\parallel$ is the longitudinal susceptibility of the Néel vector at zero field

$$\widetilde{\chi}_\parallel = \frac{\mu_\mathrm{at}}{J_0}\frac{\beta J_0 L'}{1 - \beta|J_0|L'}. \tag{6.2.5}$$

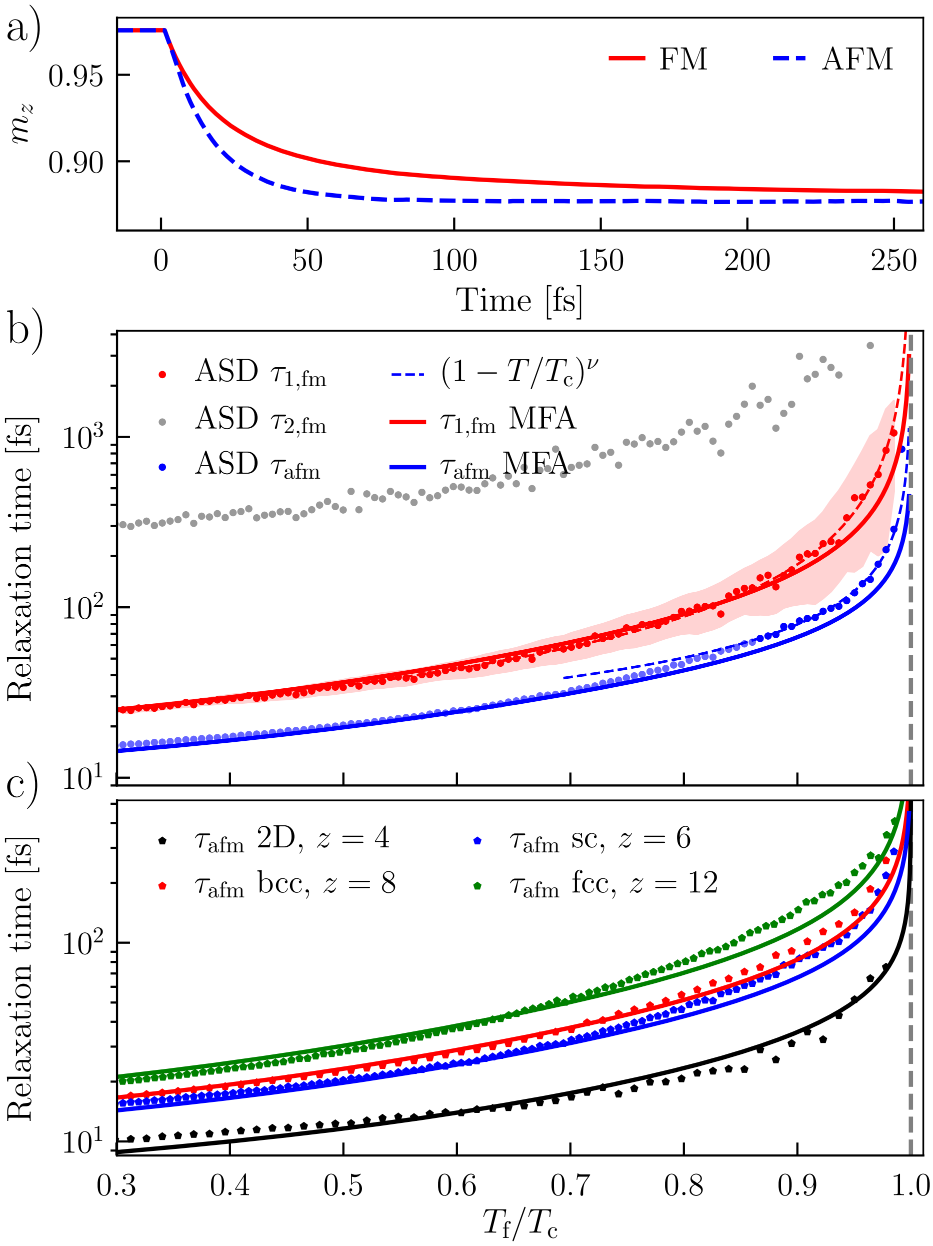

Figure 6.2.1: *(a) Magnetic order dynamics of a FM and an AFM after a step-like temperature increase, $T_\mathrm{i}/T_\mathrm{c} = 0.07$ and final temperature $T_\mathrm{f}/T_\mathrm{c} = 0.33$. (b) Magnetic order relaxation time in FMs and AFMs as a function of $T_\mathrm{f}/T_\mathrm{c}$. Symbols correspond to ASD simulations, solid lines to MFA, and dashed lines are a fit of the scaling law, $(1 - T/T_\mathrm{N})^\nu$ with $\nu = -1.017(7)$ for $\tau_{1,\mathrm{fm}}$ and $\nu = -0.64(2)$ for τ_{afm}. The light red area around the FM data indicates the statistical uncertainty coming from over 50 simulations. For AFMs is not shown since it is around 2-4% at maximum close to T_N. (c) The relaxation time for different lattice structures (sc, bcc, fcc and a 2D square). Symbols correspond to ASD simulations and lines to MFA.*

For small deviations δn_e of the order parameter n, from equilibrium ($\delta n_e \ll n_e$), Eq. (6.2.3) can be expanded around the equilibrium state n_e. The resulting first order linear differential equation in n can be easily solved analytically as an exponential decay, with relaxation time given by $\tau_{\mathrm{afm}} = \widetilde{\chi}_{\|}/\gamma\alpha^{e}_{\mathrm{afm}}$, where $\alpha^{e}_{\mathrm{afm}}$ is calculated for $n = n_e$. At low temperature, where $n_e \approx 1$ the ratio between AFM and FM relaxation time is just given by $\alpha_{\mathrm{afm}}/\alpha_{\mathrm{fm}} = 1{+}4/zn_e$, which equals to $1 + 4/z$ (5/3 for simple cubic) at strictly $T = 0$ K. In striking contrast to the FMs, the effective AFM damping depends on the number of nearest neighbours z. For the MFA limit, $z \to \infty$, the exchange-enhancement vanishes ($\alpha_{\mathrm{afm}} = \alpha_{\mathrm{fm}}$) whereas for systems with low coordination number increases, for example a spin chain with $z = 2$, $\alpha_{\mathrm{afm}} = 3\alpha_{\mathrm{fm}}$. Another relevant example would be the metallic antiferromagnet $\mathrm{Mn_2Au}$ [190, 191, 192], the most promising candidate for future spintronic and memory applications, in which each Mn spin is antiferromagnetically exchange coupled to five neighbours, and thus a speed up of a factor $1 + 4/5 = 1.8$ is expected. At temperatures approaching $T_{\mathrm{c(N)}}$, the order parameter reduces, $n_e \approx 0$, and consequently, $\alpha_{\mathrm{afm}}/\alpha_{\mathrm{fm}} \sim 1/n_e$ diverges. In the MFA, close to $T_{\mathrm{c(N)}}$, the order parameter at equilibrium scales with temperature as $n_e \sim (1 - T/T_{\mathrm{c(N)}})^{1/2}$. Hence the critical behaviour of the AFM damping parameter is $\alpha_{\mathrm{afm}} \sim (1 - T/T_{\mathrm{N}})^{-1/2}$. While the longitudinal susceptibility increases with temperature up to the critical temperature where it diverges, $\widetilde{\chi}_{\|} \approx (1 - T/T_{\mathrm{c(N)}})^{-1}$. Thus, the relaxation time in AFMs scales as $\tau_{\mathrm{afm}} \sim (1 - T/T_{\mathrm{N}})^{-1/2}$, which differs from the scaling for FMs $\tau_{\mathrm{fm}} \sim (1 - T/T_{\mathrm{c}})^{-1}$. Although both AFMs and FMs show the so-called critical slow down near $T_{\mathrm{c(N)}}$, the effect of the exchange-enhancement of the AFM dynamics is to lower the critical exponent. In general, the MFA scaling laws are known to differ from the actual critical scaling exponents, $\tau \sim (1 - T/T_{\mathrm{c}})^{-\nu}$. We conduct ASD computer simulations to verify qualitatively these theoretical predictions, i) to find different critical exponents, ν, for AFMs and FMs, and ii) to demonstrate the dependence on the number of exchange links between spins of the relaxation time in AFMs. To do so, we compute the relaxation time under the same conditions, namely, for small deviations from equilibrium, $\delta n_e/n_e \ll 1$. This is achieved by applying a step-like temperature increase, $\Delta T = T_{\mathrm{f}} - T_{\mathrm{i}}$, such that $\delta n = n_e(T_{\mathrm{i}}) - n_e(T_{\mathrm{f}}) = 0.1 n_e(T_{\mathrm{i}})$ for all initial/final temperatures $T_{\mathrm{i}}/T_{\mathrm{f}}$. An example of such magnetization dynamics for the $z-$component of the order parameter for FM and AFM orderings for a simple cubic lattice ($z = 6$) are shown in Fig. 6.2.1 (a). We find that for FMs the relaxation dynamics is defined by two characteristic times, $\tau_{1,\mathrm{fm}}$ and $\tau_{2,\mathrm{fm}}$, associated to a fast and a slow relaxation process, respectively and for the AFM a single τ_{afm} is enough to describe the demagnetization process. Fig. 6.2.1 (b) shows the relaxation times $\tau_{1,\mathrm{fm}}$, $\tau_{2,\mathrm{fm}}$ and τ_{afm} as function of the reduced temperature $T_{\mathrm{f}}/T_{\mathrm{c}}$ in comparison to the MFA analytical expression derived from Eq. (6.2.3). Interestingly, we find that for all temperatures the slow relaxation time $\tau_{2,\mathrm{fm}}$ is related to fast one $\tau_{1,\mathrm{fm}}$ as $\tau_{2,\mathrm{fm}} = 12\tau_{1,\mathrm{fm}}$. The faster time decay is related to the relaxation of the magnetic order, while the slower one with the relaxation of short-wavelength spin waves[116]. Differently to this characteristic bi-exponential relaxation decay in the FMs, the relaxation process in AFMs is defined by only one, fast characteristic time, τ_{afm}. The relaxation time of the AFM order parameter τ_{afm} is faster than $\tau_{1,\mathrm{fm}}$, for the same microscopic magnetic parameters. In particular, at low temperatures, the ratio between the relaxation times, $\tau_{1,\mathrm{fm}}/\tau_{\mathrm{afm}}$ is close to 5/3, like our predicted theory value for a sc lattice. The absence of a second, slow relaxation process makes that the AFMs reach the final, equilibrium state much faster than in FMs, indeed the characteristic times, in FMs and AFMs, are related as $\tau_{2,\mathrm{fm}} \approx 12(1 + 4/z)\tau_{\mathrm{afm}}$, which ranges from 12 for $z \to \infty$ to 36 for $z = 2$. As the final system temperature T_{f} approaches the critical temperature, T_N, the magnetization dynamics slows down both for AFMs and FMs. Figure (6.2.1)(b) shows the good agreement between our model (MFA-solid lines) and ASD (symbols) for both the AFMs and FMs. The critical behaviour of the relaxation time can be also captured by a temperature scaling function, $\tau_{\|} \sim (1 - T/T_{\mathrm{N}})^{-\nu}$ (dashed lines in Fig. 6.2.1(b)). By fitting our ASD simulation results, we find that for the FM system, $\nu_{\mathrm{fm}} = 1.017(7)$, whereas for the AFM system, $\nu_{\mathrm{afm}} = 0.64(2)$, in qualitative agreement with the prediction of our theory, the critical exponent in AFMs is smaller than in FMs. We note that for the AFM fit, the critical exponent is obtained by taking only the data close to T_{N} into account, where the second term in Eq. (6.2.4) dominates and therefore it coincides with our theoretical analysis. Another fundamental difference between FMs and AFMs is the dependence of the relaxation time on the number of neighbours z to which each spin is coupled. Figure 6.2.1(c) shows the temperature dependence of the τ_{afm} for three different lattice structures in 3D, sc ($z = 6$), bcc ($z = 8$), and fcc ($z = 12$), and in 2D, a square lattice ($z = 4$). Lines in Fig. 6.2.1(c) correspond to the analytical estimation based in our model and symbols to the ASD simulations. We stress that the lattice structure dependence of τ_{afm} only exists for AFMs. Relaxation time in FMs is independent of the lattice structure. One question remains, how could signatures of these exchange-enhanced dynamics in AFMs be found in experiments? To address this problem, we first validate our model by comparing directly the dynamics of an AFM calculated via ASD simulations and Eq. (6.2.3) for three different temperature profiles (see Fig. 6.2.2(a)). One temperature profile corresponds to a step function and the others to the TTM with two sets of parameters. The agreement between ASD simulations and our model is very good. We note that for quantitative comparison between ASD simulations and MFA models, one needs to slightly rescale the exchange parameter, J (for more detail we refer to the appendix sec. A6.4.2). We find that Eq. (6.2.3) describes ASD simulations as far as the microscopic spin configurations are homogeneous, as expected from the MFA grounds of our model (see details in appendix, Sec. A6.4.3). By directly comparing the dynamics of FMs and AFMs under laser pulses, for instance see Figs. 6.1.1 and 6.2.2, one can barely discern the effect of the exchange-enhancement in AFM dynamics. However, our model predicts striking differences between FMs and AFMs in the magnetic order dynamics in the limit of high-temperatures, $T \gg T_{\mathrm{c}}$, and small magnetic order parameter ($\xi = \beta J_0 m \to 0$). This scenario corresponds to experiments using powerful femtosecond laser pulses. For FMs, Eq. (6.2.1) approximates to a linear equation: $(\mu_{\mathrm{at}}/\gamma)\dot{m} = 2\lambda k_B T m$. Thus, the dynamics is described by an exponential decay, namely, it slows down as the magnetization m reduces. In contrast, in the same limit, for AFMs, Eq. (6.2.1) approximates to $(\mu_{\mathrm{at}}/\gamma)\dot{n} \approx 4(4/z)\lambda k_B T$, independent of n, which speeds up the AFM dynamics. This different dynamic directly emerges by increasing the laser fluence so that the electron temperature reaches very high temperatures and the magnetic reduces. In Fig. 6.2.3(a) one can observe the diverse behaviour of the maximum demagnetization ($\Delta_{\max} m(n)$) as a function of the reduced maximum electron temperature $T_{\mathrm{el}}/T_{\mathrm{c}}$ for both AFMs and FMs. We note that since the results depend on the chosen TTM parameters, the results are drawn as a function of $T_{\mathrm{el}}/T_{\mathrm{c}}$ instead of laser intensity. Figure 6.2.3(a) shows that for FMs the shape of $\Delta_{\max} m(T_{\mathrm{el}})$ is convex, while for the AFM, $\Delta_{\max} n(T_{\mathrm{el}})$ is concave. These findings align with an experimental work comparing the magnetic order dynamics of the AFM and FM phases in Dy [187], where for comparable laser powers, the maximum demagnetization in AFMs was larger than in FMs [187]. It was also found that by increasing the laser intensity, the maximum demagnetization rate $\Gamma_{\max}$ increased in AFMs is much stronger than in FMs. Figure 6.2.3 (b) shows how the maximum demagnetization rate increases faster for AFMs than for FMs, in qualitative agreement with experiments conducted in Dy. The different slope of $\Gamma_{\max}$ is directly related to the exchange-enhancement of the effective AFM damping (Eq. (6.2.4)), $1 + 4/z$, for sc used here, $\Gamma_{\max}^{\mathrm{afm}} = (5/3)\Gamma_{\max}^{\mathrm{fm}}$.

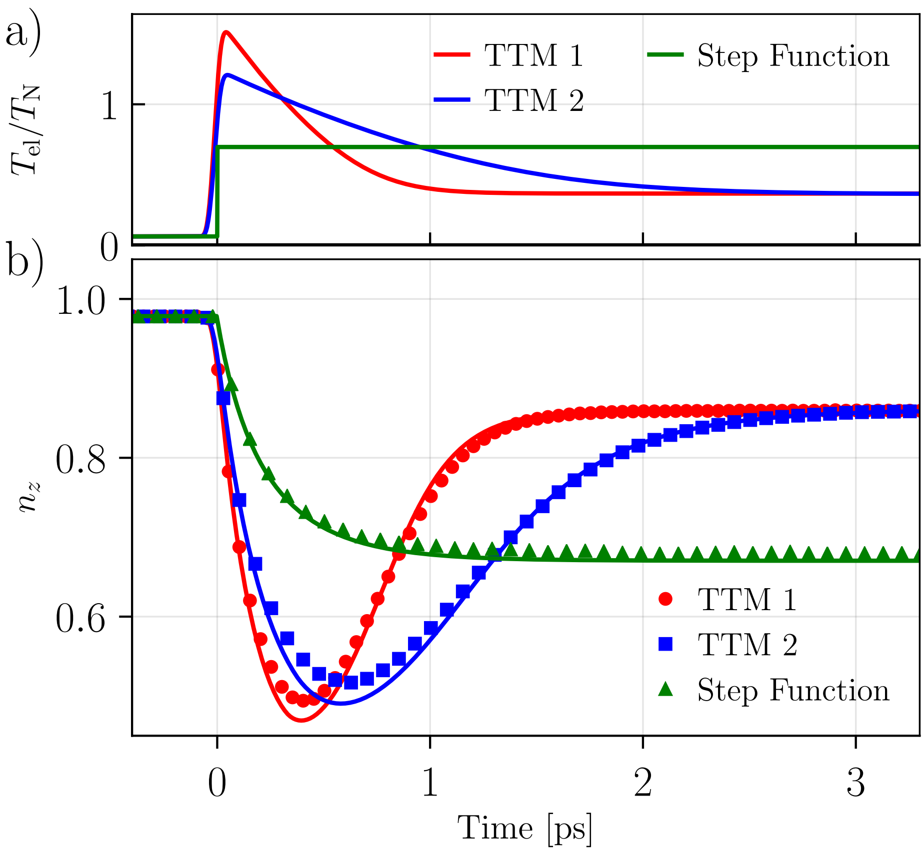

Figure 6.2.2: *(a) Temperature step function ($T_{\mathrm{i}} = 0.06T_N$ and $T_{\mathrm{f}} = 0.7T_N$) and two different T_{el} profiles for the same laser fluence and $g_{\mathrm{ep}} = 6 \times 10^{17} J/sKm^3$ for two sets of parameters (TTM1: $\gamma = 700$ J/K^2m^3, $c_{ph} = 3 \times 10^6$ J/Km^3, and TTM2: $\gamma = 2000$ J/K^2m^3, $c_{ph} = 5 \times 10^5$ J/Km^3). (b) The magnetic order dynamics as a response to the temperature profiles in panel (a). The symbols correspond to ASD simulations and the lines to the numerical solution of Eq.* (6.2.3)*,* ($\lambda = 0.01$)*.*

6.3 Summary

To summarize, we have shown that the ultrafast magnetic order dynamics in antiferromagnets is exchange-enhanced in comparison to ferromagnets with the same system parameters. The origin is the exchange-enhancement of the effective AFM damping. We have provided an equation of motion for the AFM magnetic order and predicted that AFMs have intrinsic faster dynamics and distinct critical dynamics than FMs. Notably, we have found that the exchange-enhancement strongly depends on the number of neighbours to which spins are exchange coupled, for instance in 2D magnets, the speed up of the dynamics is larger. In the very high temperature regime, we have predicted a transition from exponential to linear decay when the magnetic order reduces. We propose a method to discern this effect in experiments using powerful femtosecond laser pulses. We have demonstrate the validity of our model by direct comparison to atomistic spin dynamics simulations.

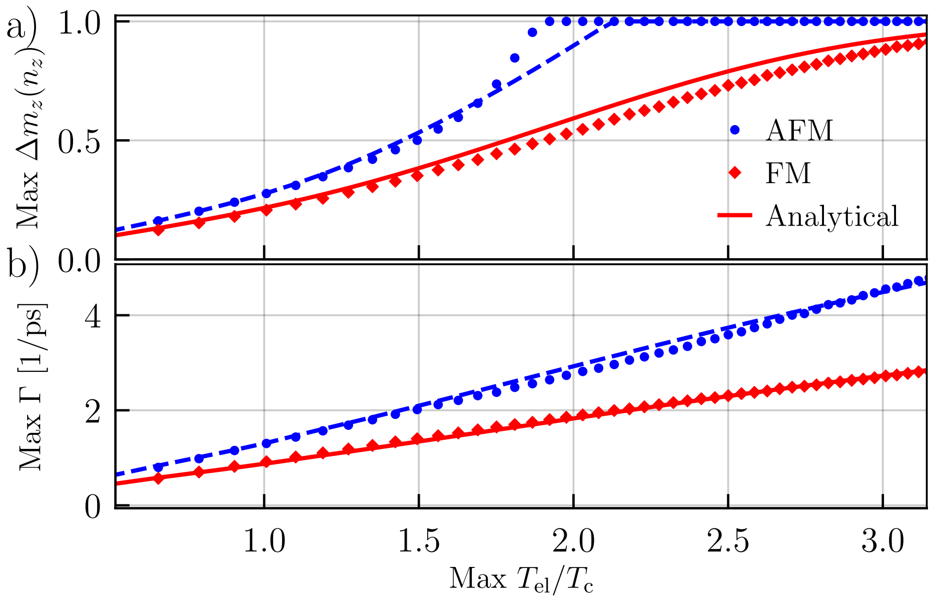

Figure 6.2.3: *(a) Maximum magnetic order quenching Max* $\Delta m_z = \mathrm{Max}|m_0 - m_z(t)|$ *(*$\Delta n_z = \mathrm{Max}|n_0 - n_z(t)|$ *for AFM) as function of the reduced peak electron temperature Max* $T_{\mathrm{el}}/T_{\mathrm{c}}$. *(b) Maximum demagnetization rate as function of the peak electron temperature. Dots, AFM (blue) and FM (red), represent ASD simulations and dashed lines the numerical solution of Eq.* (6.2.3). *Results for a laser pulse of 50 fs duration and* $\lambda = 0.01$ *in the ASD simulations.*

A6.4 Appendix to "Exchange-enhancement of the ultrafast magnetic order dynamics in antiferromagnets"

A6.4.1 Methods

The dynamics of the magnetic order parameter (in FMs and AFMs) are calculated within the framework of a classical, atomistic spin model. The Hamiltonian reads

$$\mathcal{H} = -\frac{J}{2}\sum_{\langle i,j\rangle} \mathbf{s}_i \mathbf{s}_j - d_z \sum_i \left(s_i^z\right)^2 . \tag{A6.4.1}$$

The unit vectors, $\mathbf{s}_i = \boldsymbol{\mu}_i/\mu_{\mathrm{at}}$, represent the normalized magnetic moment of the lattice site i with magnetic moment $\mu_{\mathrm{at}} = \mu_{\mathrm{B}}$. The first term describes nearest neighbors exchange coupling, with $J = \pm 3.450 \times 10^{-21}$ J for the FM (+) and AFM(-). The second term represents the uniaxial anisotropy, with $d_z = 1 \times 10^{-22}$ J for both AFM and FM. The dynamics at finite temperatures are described by the stochastic Landau-Lifshitz-Gilbert (s-LLG) equation,

$$\frac{d\mathbf{s}_i}{dt} = -\frac{|\gamma|}{(1+\lambda^2)}\mathbf{s}_i \times \left[\mathbf{H}_i - \lambda\ (\mathbf{s}_i \times \mathbf{H}_i)\right] . \tag{A6.4.2}$$

Here, γ is the gyromagnetic ratio. The first term represents a precession of the magnetic moments around an effective field $\mathbf{H}_i = -(1/\mu_{\mathrm{at}})(\partial\mathcal{H}/\partial\mathbf{s}_i)$, while the second term represents the transverse relaxation. A phenomenological damping constant λ defines the rate of the relaxation. In order to include the effects of finite temperature, we couple the spin system to a Langevin thermostat which adds an effective field-like stochastic term $\boldsymbol{\zeta}_i$ to the effective

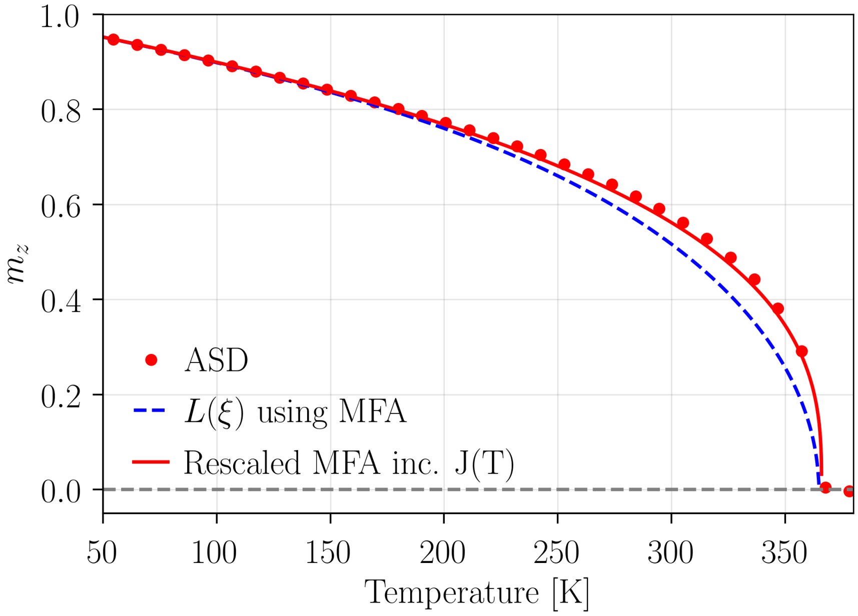

Figure A6.4.1: *Equilibrium magnetization of a sc-lattice as a function of temperature from ASD simulations (red dots), mean field approximation (blue dashed line) and from the MFA model including a temperature dependent rescaled Heisenberg exchange constant* $J(T)$ *(Eq.* (A6.4.6)*), (red line).*

field with white noise properties [97]. The dynamics of the electron temperature T_{el} and the phonon temperature T_{ph} can described via the two-temperature model (TTM) [102, 110],

$$C_{\text{el}}\frac{\partial T_{\text{el}}}{\partial t} = -g_{\text{ep}}\left(T_{\text{el}} - T_{\text{ph}}\right) + P_l(t) \tag{A6.4.3}$$

$$C_{\text{ph}}\frac{\partial T_{\text{ph}}}{\partial t} = +g_{\text{ep}}\left(T_{\text{el}} - T_{\text{ph}}\right). \tag{A6.4.4}$$

where $g_{\text{ep}} = 6 \times 10^{17}$ J/sKm^3 is the electron-phonon coupling constant, $C_{\text{ph}} = 3 \times 10^6$ J/Km^3 and $C_{\text{el}} = \gamma_e T_{\text{el}}$ ($\gamma_e = 700$ J/K^{2}m^3) represent the respective specific heats of the electron- and phonon system. Although we use standard values for metals, these values are material-dependent. $P_l(t)$ is Gaussian shaped and represents the absorbed energy of the electron system coming from the laser.

A6.4.2 Rescaling of the exchange constant for quantitative comparison between MFA and ASD simulations

In the main text, our analytical model for the magnetic order dynamics is based in the mean field approximation (MFA). The equilibrium magnetization as a function of temperature calculated using the MFA slightly differs from the ASD simulations. Fig. A6.4.1 shows the MFA results as a blue dashed line and the ASD simulations as red points for a sc-lattice using $J = 3.450 \times 10^{-21}$ J. For the MFA case, we have rescaled the exchange constant, $J_{\text{mfa}} = 0.73 J_{\text{asd}}$, to obtain $T_N^{\text{MFA}} = T_N^{\text{ASD}}$. We have estimated the ASD critical temperature by calculating the temperature at which the magnetic specific heat diverge. The equilibrium magnetization as a function of temperature using the MFA start to deviate from ASD simulations in the intermediate-to-high temperature region, $T_N/2 < T < T_N$. In order to quantitatively compare our model to ASD simulations we resolve this discrepancy by introducing a temperature dependent Heisenberg exchange modulation $J(T) = J_0 + J'(T)$, where J_0 describes the original MFA Heisenberg exchange constant, $J_{\text{mfa}} = 0.73 J_{\text{asd}}$, $J'(T) > 0$ is a temperature dependent modulation that needs to be determined. We determine it by forcing the equality the equilibrium magnetization calculated through ASD, $m_e = (1 - T/T_N)^{1/3}$ (1/3 for a sc-lattice), and the MFA, $m_e = L(\beta J(T) m_e)$. Thus, the temperature dependent Heisenberg exchange $J(T)$ can be calculated from

$$(1 - T/T_{\text{c}})^{1/3} = L\left(\frac{(J_0 + J'(T))m}{k_{\text{B}}T}\right) \tag{A6.4.5}$$

which can be solves as

$$J'(T) = \frac{1}{\beta m} L^{-1}((1 - T/T_{\text{c}})^{1/3}) - J_0. \tag{A6.4.6}$$

L^{-1} describes the inverse Langevin function for which no analytical expression is known. However there have been numerous attempts at finding a simple and accurate approximation [193, 194]. In this work we have used the equation proposed by Nguessong et al. [194] to approximate the inverse Langevin function numerically.

We note, that by using Eq. A6.4.6 $J(T)$ becomes independent of the numerical value of J_0 and is instead directly calculated from the magnetization curve $m(T)$ via the inverse Langevin function. For a sc-lattice $m_e(T) = (1 - T/T_c)^{1/3}$ agrees well with the atomistic results. However for other lattices (fcc, 2D or bcc), a different analytical expression for $m_e(T)$ is needed to describe $m_e(T)$.

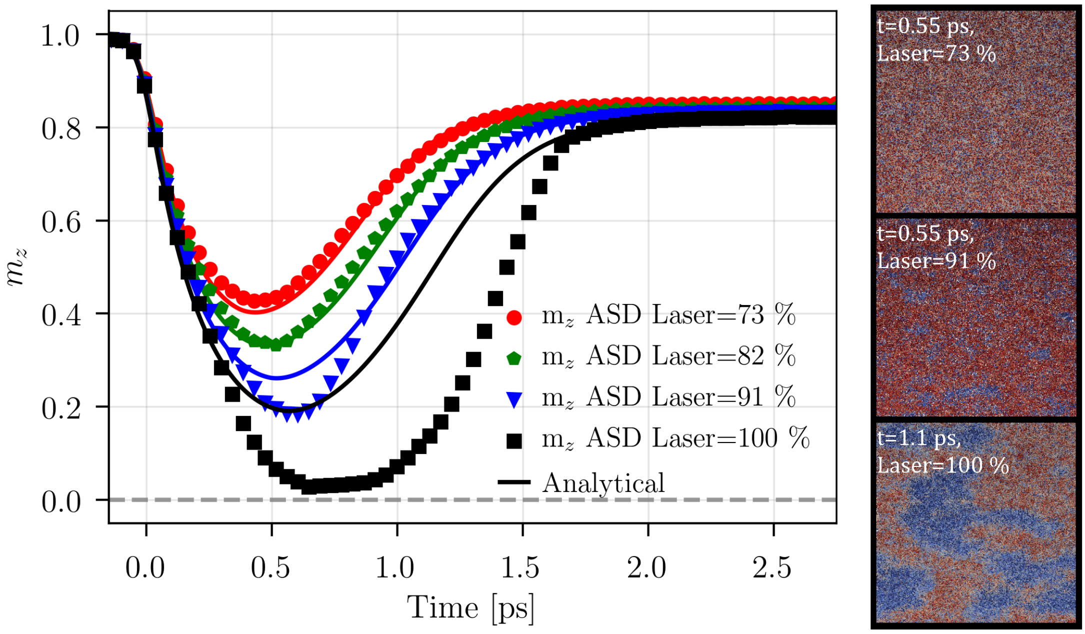

Figure A6.4.2: *ASD simulations of AFM magnetic order dynamics for different laser powers* ($\lambda = 0.01$) *(dots) in comparison to our analytical model (Eq.* (6.2.3)*) (lines). Higher laser powers yields larger demagnetization and the underlying MFA assumptions of Eq.* (6.2.3) *stops being a valid approximation. On the right different states of the spin system are shown, shortly after the excitation with a laser pulse.*

A6.4.3 Breakdown of the MFA model for high fluence laser excitation

As discussed in the main text, our model is based in the MFA. This means that better agreement between ASD and MFA would be expected when the microscopic spin configurations remain close to the MFA assumptions, when each atomic spin sees the same interactions from the neighbouring ones. When magnetic domains are be nucleated, our MFA macroscpin model no longer describes the spin state correctly. Figure A6.4.2. shows the magnetic order dynamics for a range of laser fluences, where symbols correspond to ASD simulations and lines to the macrospin model. For higher fluences the agreement between the two models diminishes. The right side shows snapshots of the microscopic spin configuration at different time delays corresponding to the a time range where maximum demagnetization is achieved. When the laser fluence is only the 73 % of the maximum fluence simulated, the microscopic spin configuration is homogeneous. In that case, the agreement between theory and simulations is very good. As the laser fluence increases, magnetic domains start to nucleate and the theory and simulations to deviate. For the maximum laser fluence that we simulate 100 %, large magnetic domains are nucleated and the MFA breaks down. The theory is not able to describe this situation. For those cases, a micromagnetic model should be developed.

Chapter 7

Lattice dynamics and ultrafast energy flow between electrons, spins, and phonons in a $3d$ ferromagnet

The results of this chapter have been published in

- D. Zahn, F. Jakobs, Y. W. Windsor, H. Seiler, T. Vasileiadis, T. A. Butcher, Y. Qi, D. Engel, U. Atxitia, J. Vorberger, and R. Ernstorfer, Lattice dynamics and ultrafast energy flow between electrons, spins, and phonons in a 3d ferromagnet, *Physical Review Research* **3** p. 023032, (Apr 2021).

and the content of this chapter is in large parts identical with the published work.
Large parts of the theory and in particular all atomistic spin dynamics simulations have been performed as part of this thesis. All experiments were done by D. Zahn and coworkers from the Fritz-Haber-Institut. The density functional theory calculations have been performed by T. A. Butcher and J. Vorberger.

The published version can be found at `https://doi.org/10.1103/PhysRevResearch.3.023032`

7.1 Introduction

The discovery of ultrafast demagnetization in ferromagnetic nickel in 1996 by Beaurepaire et al. [5] induced a paradigm shift in the field of magnetism. The experiment proved that magnetic order can be manipulated on femtosecond time scales, therefore offering new perspectives in data storage. Since then, researchers have worked towards a microscopic understanding of the phenomenon [5, 175, 14, 16, 195, 196, 197, 198, 199, 200, 201, 202, 203, 204]. To acquire microscopic insights into the processes governing the ultrafast demagnetization in itinerant $3d$ ferromagnets, knowledge about the response of electronic, magnetic and lattice degrees of freedom to laser excitation is required. Most of the experimental work in literature focuses either on the magnetization dynamics using the time-resolved magneto-optical Kerr effect (tr-MOKE) [5, 205, 206, 207, 14, 208, 209, 127, 23, 107] or time-resolved X-ray magnetic circular dichroism (tr-XMCD) [210, 211, 55], or on the electronic response using time-resolved photoemission methods [205, 203, 66, 212]. In contrast, the lattice response has received only limited attention [213, 214, 215, 216, 115]. Knowledge of the lattice dynamics is essential, as it plays several important roles in the dynamics of the system: First of all, it serves as a sink for angular momentum [213]. Second, in addition to receiving angular momentum, the lattice is also an energy sink: it drains energy from the electronic system on ultrafast timescales via the creation of phonons. Hence, the electron-phonon coupling strength strongly influences the energy content of the electronic system and consequently also the magnetization dynamics. Finally, the lattice response is in turn also influenced by the magnetization dynamics, both during the demagnetization and the magnetization recovery (remagnetization). The demagnetization of an isolated sample requires spin excitations, e.g. spin flips and/or magnons, which cost energy. This is also visible in the equilibrium heat capacity, which shows a divergence at the Curie temperature [217]. Due to this energy cost, ultrafast demagnetization reduces the energy content in the electronic system and thus indirectly influences the lattice dynamics as well.

Several models have been developed and used to describe the magnetization dynamics of $3d$ ferromagnets following laser excitation [5, 14, 16, 196, 197, 218, 219]. In addition to the magnetization dynamics, however, a consistent model should also describe the electronic and lattice responses correctly. In particular, due to the relatively large heat capacity of the lattice, an accurate description of electron-lattice equilibration is important. Nonetheless, literature values for the electron-phonon coupling parameter G_{ep} of nickel vary by more than an order of magnitude [220, 5, 221, 222, 223, 105, 14, 224, 225, 226, 66, 215]. So far, experimental studies of ultrafast lattice heating in nickel have mostly employed optical techniques [227, 222, 223], which are sensitive to both the electronic and the lattice responses. The most direct technique to study the lattice is diffraction, but there are only few studies that measured the lattice heating directly with time-resolved diffraction [216, 115]. In addition, the electron-phonon coupling was often deduced from observables without considering the energy cost of demagnetization [220, 222, 223, 14, 226]. The large spread in literature values for G_{ep} can manifest itself in an imprecise description of the electron-lattice equilibration and makes different models less comparable. To obtain a consistent model for the microscopic energy flow and the magnetization dynamics, it is paramount to compare theoretical results to the response of all three subsystems, including the lattice. At the same time, the energy flow dynamics between the subsystems need to be described consistently. In particular, energy flow to and from magnetic degrees of freedom needs to be considered. Regarding the existing demagnetization models, the microscopic three-temperature model (M3TM) introduced by Koopmans et al. [14] as well as conventional micromagnetic and atomistic spin dynamics simulations [228, 229, 230, 201] disregard the energy flow associated to the magnetization dynamics. In contrast, the three-temperature model (3TM) introduced by Beaurepaire et al. takes energy flow to and from the spin system into account [5, 231]. However, to deduce the three different coupling constants of the 3TM reliably from experimental data, information on the response of more than one subsystem is required. In addition, the 3TM describes the spin system based on its properties in thermal equilibrium, which is a questionable assumption on short time scales after laser excitation [197, 66]. Similarly, a modified version of the M3TM includes energy flow to and from the spin system, but also assumes a thermalized spin system [208]. Dvornik et al. introduced an energy-conserving model that goes beyond a thermal description of the spin system by employing micromagnetic simulations [225], but no direct comparison with experimentally measured lattice dynamics has been made yet. In this work, we fill this gap by providing a comprehensive experimental and theoretical description of the lattice dynamics in ferromagnetic nickel. We use femtosecond electron diffraction (FED) to directly measure the lattice response to laser excitation. In Section

II we provide an overview of the electron diffraction experiment and the experimental results. The excellent time resolution of our electron diffraction setup allows us to resolve the lattice heating in nickel on femtosecond time scales. Section III discusses the comparison between the experimental results and energy flow models of increasing complexity. For this comparison, we perform spin-resolved density functional theory (DFT) calculations to obtain the electron-phonon coupling parameter G_{ep} as well as the electronic and lattice heat capacities. In Section III.A, we compare the experimental results to the commonly used two-temperature model (TTM) and a modified TTM with strong electron-spin coupling (s-TTM). The latter is the minimal extension of the TTM that considers magnetic degrees of freedom. This comparison reveals that energy transfer to and from magnetic degrees of freedom has a strong impact on the lattice dynamics. In Section III.B, we go a step further and aim for a quantitative description not only of the lattice dynamics, but of all three subsystems using energy-conserving atomistic spin dynamics (ASD) simulations. This hybrid approach of spin dynamics simulations and energy flow model is shown to provide a consistent description of both the non-equilibrium dynamics of the spin system as well as the energy flow between the different subsystems. Section IV provides a summary of the key findings.

7.2 Experiment

The samples were freestanding, polycrystalline nickel films with a thickness of 20 nm sandwiched between 5 nm layers of Si_3N_4 on both sides to avoid oxidation. They were prepared on NaCl crystals by magnetron sputter deposition at room temperature. To obtain freestanding samples, the thin films were transferred onto standard TEM grids using the floating technique [232]. The samples were not exposed to a magnetic field before the measurements. To study the ultrafast structural dynamics of nickel, we used the compact femtosecond electron diffractometer described in Ref. [68]. The samples were excited using ultrashort (ca. 50-80 fs FWHM) laser pulses with different wavelengths (2300 nm, 770 nm and 480 nm), at 4 kHz repetition rate. The measurements were conducted at room temperature (295 K). The structural response of the sample was probed in transmission using short electron pulses. The kinetic energy of the electrons was 65-77 keV, depending on the experiment. In total, the temporal resolution achieved in the experiments was around 170 fs. Figure 7.2.1(a) illustrates the measurement principle and shows a diffraction pattern of our polycrystalline nickel sample. To analyze the changes in the diffraction pattern after laser excitation, the recorded images were radially averaged. A typical radial average of our nickel samples is displayed in Fig. 7.2.1(b) (solid blue line). Next, we performed a fit to the radial averages. Here we apply a global fitting approach [233], which extracts the lattice dynamics based on the full diffraction pattern instead of individual Bragg reflections as conventionally done [234, 235]. In the first step of the fitting routine (static fit), we fitted the average of all radial averages before laser excitation to a function consisting of Lorentzian peaks plus a background function, all convolved with a Gaussian. The peak amplitudes of the Lorentzians were adjustable but the peak positions were fixed in the fit, except for a parameter for the conversion of pixels to scattering vector, a parameter accounting for aberrations of the electron lens and small correction factors for the individual peaks ($\leq 5\%$ deviation). The peak width was one fit parameter, i.e. it was the same for all peaks. The fit result is displayed in Fig. 7.2.1(b) (dashed black line). We used the range from the Bragg reflections (111) to (511), as shown. From the Bragg reflection intensities, we deduce that the sample has a preferred orientation, but this does not affect our analysis of the lattice dynamics. In the second step of the fitting

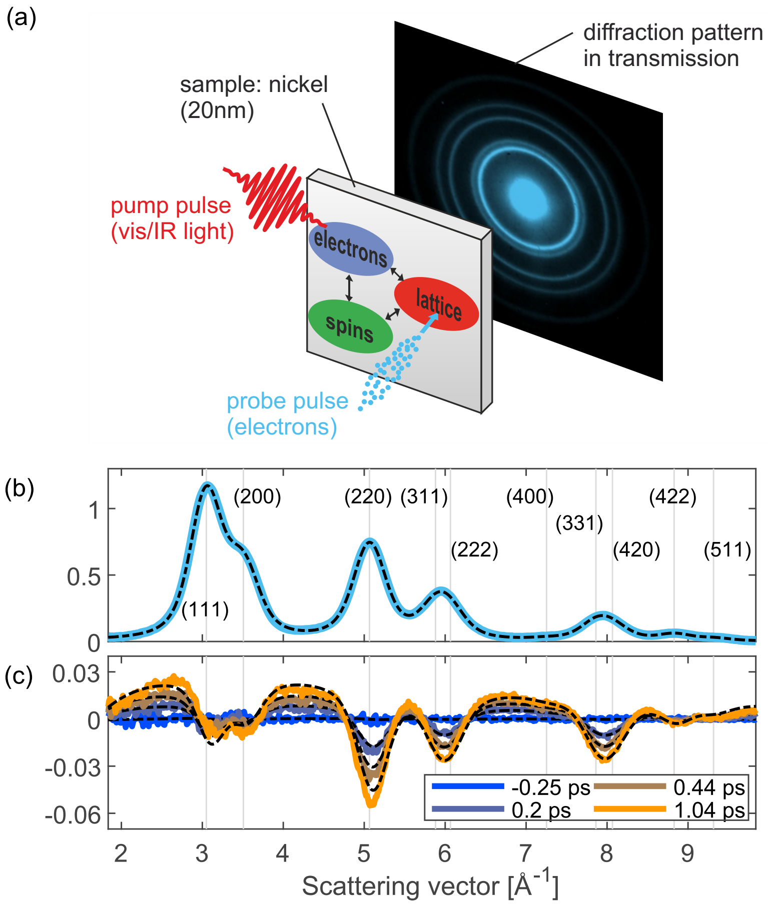

Figure 7.2.1: *Details of the femtosecond electron diffraction experiment. (a) Schematic diagram of the experiment. The electrons in the sample are excited using a visible or infrared laser pulse. The excited electrons transfer energy to the spins as well as to the lattice, depending on the respective coupling strengths (black arrows). The lattice response is probed using an ultrashort electron pulse, which diffracts off the sample. Diffraction patterns are recorded in transmission. b) Radial average of the diffraction pattern (solid blue line) before laser excitation. The dashed black line is a fit to the data (static fit). The background contribution obtained from the static fit was subtracted. c) Differences of the radial averages at several pump-probe delays (solid lines) compared to the radial average before laser excitation. The dashed black line shows the fits to the data (dynamic fit). The details of the fits are described in the text.*

routine, which yields the lattice dynamics after laser excitation (dynamic fit), we fixed all parameters of the fit function at the values obtained from the static fit, except the change in atomic mean-squared displacement (MSD), the lattice expansion and the background parameters, and fitted all the radial averages of the measurement. The MSD is related to the peak intensities as follows [236]:

$$\frac{I(t)}{I_0} = \exp\{-\frac{1}{3}\, q^2 \, \langle u^2 \rangle \, \} \tag{7.2.1}$$

Here, q is the scattering vector, $\langle u^2 \rangle$ is the MSD and I_0 is the intensity before laser excitation. Figure 7.2.1(c) shows changes of the radial averages after laser excitation for several pump-

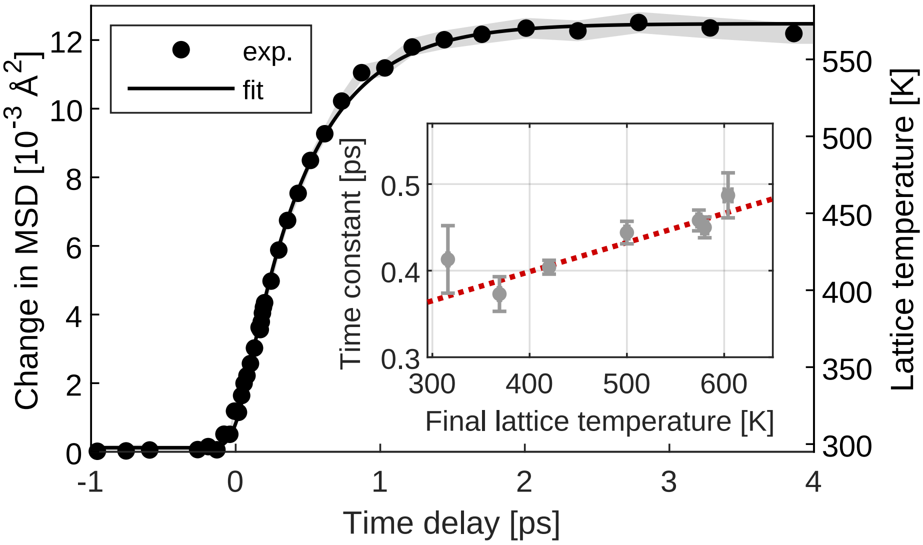

Figure 7.2.2: *Time evolution of the mean squared displacement (MSD) and the lattice temperature after laser excitation with 2300 nm light. In this measurement, the absorbed energy density was 1230*$\frac{\mathrm{J}}{\mathrm{cm}^3}$*. The black dots show the experimental data and the black line is a fit with a single exponential function, convolved with a Gaussian (FWHM: 170 fs) to account for the time resolution. The grey shaded area represents the standard errors of the data points, obtained from the fit of the radial averages. The inset shows the time constants (fit result) for different excitation densities. The error bars represent the standard errors of the single exponential fits. The dotted red line is a linear fit to the data (*$\tau = a \cdot (T_{\mathrm{final}} - 295\ \mathrm{K}) + b$*), with* $a = 0.336 \pm 0.06 \frac{\mathrm{fs}}{\mathrm{K}}$ *and* $b = 360 \pm 20\mathrm{fs}$*. The errors of* a *and* b *are the standard errors from the fit.*

probe delays together with the fit results of the dynamic fit (dashed black lines). The fit yields the evolution of the MSD as a function of pump-probe delay, which is then converted into lattice temperature using the tabulated Debye-Waller factor of Ref. [236]. The deviations of the fit results from the experimental data are caused by secondary scattering effects and the limitations of the phenomenological background function. They do not influence the timescales of the extracted lattice dynamics. The precision of the lattice dynamics is determined using the standard error from the fit. The corresponding error bars are shown as grey shaded areas in all figures. Further details about the global fitting routine are described in Ref. [233]. Figure 7.2.2 shows the evolution of the MSD and the lattice temperature as a function of pump-probe delay for a pump wavelength of 2300 nm (0.54 eV). The temperature rise can be well described by a single exponential function, convolved with the instrument response of ~170fs. The inset of Fig. 7.2.2 shows the time constants of the single exponential function (fit results) for different fluences. The time constant is found to increase linearly with excitation density (dotted red line). Our time resolution of around 170 fs enables us to resolve the lattice heating. We observe time constants that are significantly faster than previous electron diffraction reports [115, 216]. The experimental data as well as the results for the MSD and lattice temperature dynamics are available on a data repository [237]. The TTM and s-TTM results discussed in the next section are also available there.

7.3 Results and energy flow models

7.3.1 Two-temperature models

To go beyond a phenomenological description of the lattice dynamics and connect our observations to microscopic quantities, a model is required. For non-magnetic materials, a frequently used model is the TTM [238, 239], which describes the time evolution of the system by considering the lattice and the electrons as two coupled heat baths. In magnetic materials, such an approach neglects the magnetic degrees of freedom. However, they have a non-negligible contribution to the total heat capacity, as shown in Fig. 7.3.1(a). Several approaches have been introduced to take into account energy flow to and from magnetic degrees of freedom [5, 115, 225]. Here, we follow the approach of Refs. [115, 66] and consider electronic and magnetic degrees of freedom as one heat bath with a common temperature. In the following, we refer to the magnetic contribution as "spins" for simplicity. Note that this includes the orbital magnetic moment. The TTM equations are modified in the following way:

$$
\begin{aligned}
c_\mathrm{l}(T_\mathrm{l}) \cdot \frac{dT_\mathrm{l}}{dt} &= G_\mathrm{ep}(T_\mathrm{es}) \cdot (T_\mathrm{es} - T_\mathrm{l}) && (7.3.1)\\
[c_\mathrm{e}(T_\mathrm{es}) + c_\mathrm{s}(T_\mathrm{es})] \cdot \frac{dT_\mathrm{es}}{dt} &= G_\mathrm{ep}(T_\mathrm{es}) \cdot (T_\mathrm{l} - T_\mathrm{es}) + S(t), && (7.3.2)
\end{aligned}
$$

with G_ep: electron-phonon coupling, T_l: lattice temperature, T_es: temperature of electrons and spins, c_l: lattice heat capacity, c_e: electron heat capacity, c_s: spin heat capacity, $S(t)$: source term (laser excitation). Figure 7.3.1(c) shows a schematic diagram of this modified TTM (s-TTM) and figure 7.3.1(d) visualizes the regular TTM for comparison. The only difference between the two models is that in the case of the s-TTM, the spin heat capacity is added to the electronic heat capacity. For this we used the combined heat capacity of electrons and spins provided by Ref. [217] (blue curve of Fig. 7.3.1(a)). The electron-phonon coupling parameter G_ep, shown in Fig. 7.3.1(b), as well as the heat capacity of the lattice (grey curve of Fig. 7.3.1(a)), were obtained using spin-resolved DFT calculations. The details of the calculations are described in Appendix A. For the comparison of the s-TTM to a regular TTM we also calculated the heat capacity of the electrons from the DFT calculations (orange curve of Fig. 7.3.1(a)). To compare the two models to the experimentally measured lattice response, we determined the absorbed energy densities based on the lattice temperature in the range 1.5-4 ps and the heat capacities. The arrival time of the laser pulse was determined from the exponential fits described earlier. Figure 7.3.2 presents the results for the s-TTM (blue curves) and the regular TTM (orange curves) for a range of fluences alongside experimental results (black dots). The regular TTM predicts a lattice response that is faster than the experimental results and is therefore inadequate for describing the dynamics of the system. In contrast, the s-TTM yields remarkable agreement with the experimental results, in particular since the lattice response in this model is determined by ab initio results and literature values, without any fit parameters. Clearly, the s-TTM describes the phonon dynamics much better than the regular TTM. This is an indication that a non-negligible amount of energy flows to the spin-system, in agreement with the results of Ref. [66]. This energy transfer leads to a significantly lower transient electronic temperature compared to the regular TTM (see Fig. 7.3.2(e)), which results in a slower electron-lattice-equilibration (see Equations 7.3.2,7.3.2). Note that in general, non-thermal electron and phonon distributions can also lead to a slow-down of the electron-lattice-equilibration. We found that for nickel, non-thermal distributions cannot explain our observations (see Appendix B for details). In

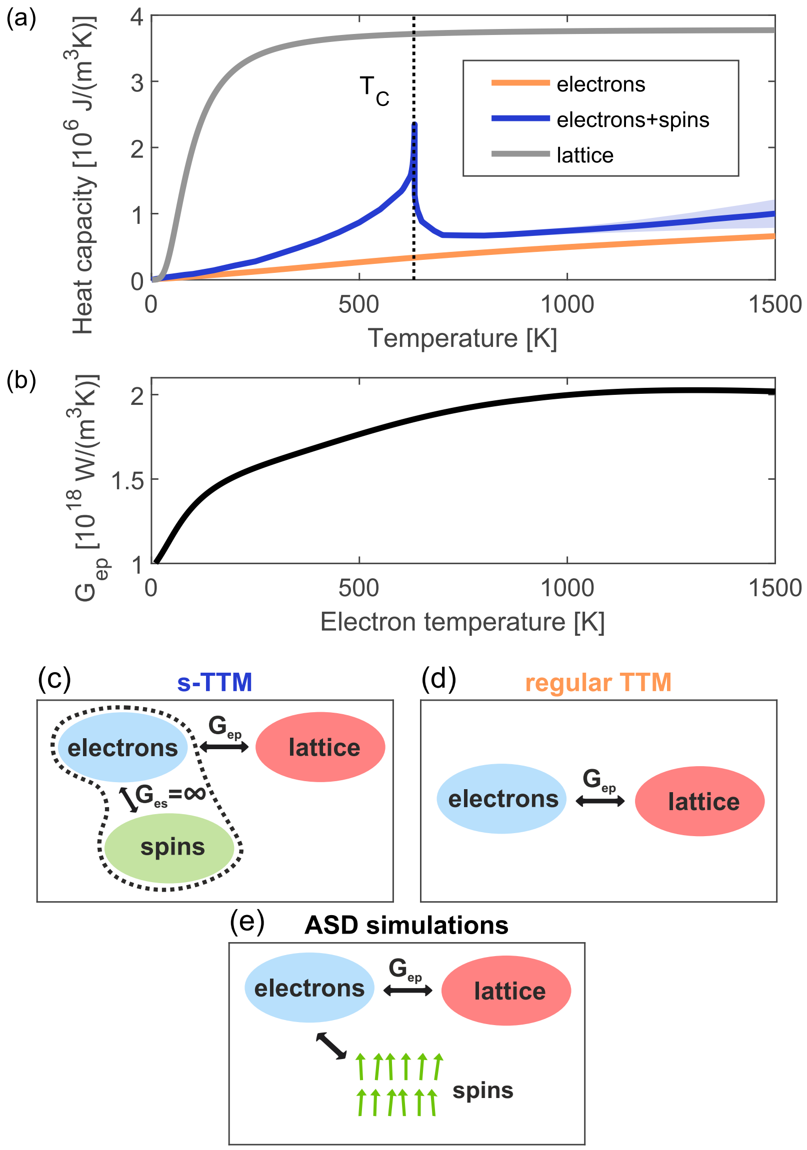

Figure 7.3.1: *Temperature-dependence of model parameters and schematic diagrams of the models. (a) Heat capacities of the electron (orange) and lattice subsystems (grey) as well as the combined heat capacity of electrons and spins (blue). Electronic and lattice heat capacities are calculated based on the spin-resolved DFT results. Since the magnetic contribution to the heat capacity cannot be calculated using DFT, we use the combined heat capacity of electrons and spins determined from experiments [217] for the s-TTM. The magnetic contribution peaks at the Curie temperature* T_c *(vertical dotted line). The light blue shaded area corresponds to the error estimate. (a) Electron-phonon coupling parameter* G_{ep} *as a function of electron temperature, obtained from the spin-resolved DFT calculations. The sum of majority and minority* G_{ep} *is shown. Panels (c), (d) and (e) are schematic diagrams of the s-TTM, the regular TTM and the ASD simulations, respectively (see text for details).*

conclusion, the s-TTM is able to capture the main features of the energy flow to and from magnetic degrees of freedom. It therefore provides a good description of the lattice response.

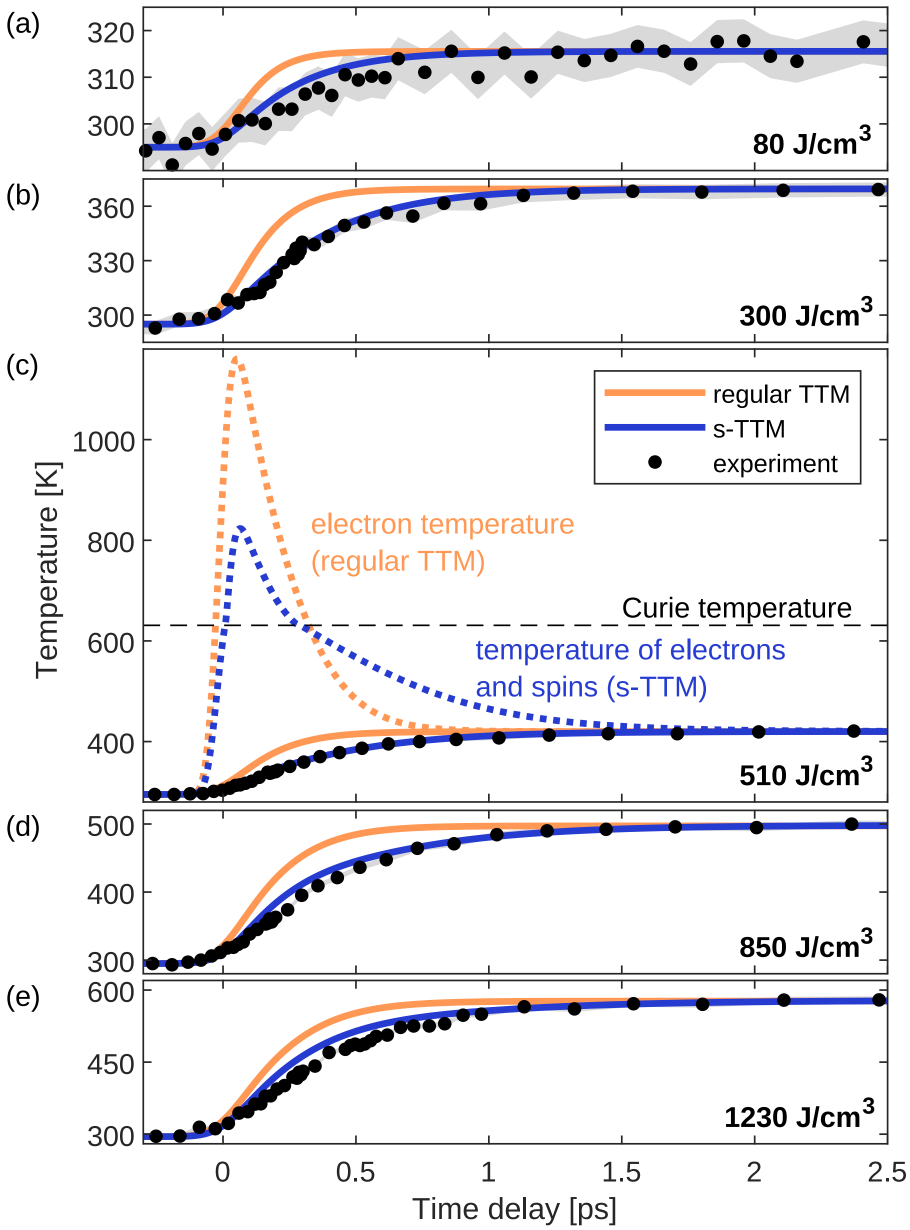

Figure 7.3.2: *Comparison of the experimental results with the regular two-temperature model (TTM) and the modified two-temperature model with infinitely strong electron-spin coupling (s-TTM). The lattice temperature predicted by the regular TTM (solid orange lines) and the s-TTM (solid blue lines) is displayed together with the experimental data for different energy densities (excitation wavelength: 2300 nm). Panel (c) also shows the evolution of the electronic temperatures for the two models (dashed lines). The grey areas represent the standard errors of the experimental data points. Both the TTM and the s-TTM results for the lattice temperature are convolved with a Gaussian (FWHM: 150fs) to account for the pulse duration of the electron pulse. Note that this is less than the convolution width for the single exponential fits of Fig. 7.2.2 because the pump pulse duration of ~80 fs is already included in the TTM and s-TTM. The displayed energy densities correspond to the absorbed energy densities of the s-TTM.*

However, a shortcoming of the s-TTM is that it implies quasi-instantaneous demagnetization dynamics, in disagreement with experimental results [14, 107]. To add a realistic description of the magnetization dynamics, an explicit treatment of the spin system is required, which will be discussed in the next subsection.

7.3.2 Atomistic spin dynamics simulations

Model and comparison with the experiment

In order to consistently describe the evolution of all three subsystems, we employ ASD simulations. These describe the spin system based on a classical Heisenberg model and the stochastic Landau-Lifshitz-Gilbert (s-LLG) equation. The evolution of electron and lattice temperature is based on the TTM with an additional coupling of the spin system to the electron system via the stochastic term of the s-LLG equation. A schematic diagram of the model is displayed in Fig. 7.3.1(e) and further details about the simulations are described in Appendix C. Commonly, ASD simulations disregard the energy cost of exciting the spin system since the electron system is considered as a heat bath that acts on the spins. However, in order to account for energy flow between the electron and spin system, the ASD simulations need to be energy-conserving. This was achieved following a similar approach as described in Ref. [106]. The energy $\mathcal{H}\{\mathbf{S}_i(t)\}$ of the spin system was monitored during each time step Δt of the ASD simulation and the spin energy change ΔE_s was calculated:

$$\Delta E_\mathrm{s} = \frac{1}{3}(\mathcal{H}\{\mathbf{S}_i(t+\Delta t)\} - \mathcal{H}\{\mathbf{S}_i(t)\}). \tag{7.3.3}$$

Here, $\mathbf{S}_i$ are the individual spins of the simulation and the factor $\frac{1}{3}$ is a correction factor that accounts for the quantized nature of the spins (see Appendix C for details). The energy change ΔE_s of the spin system was subtracted from the electron system, thus coupling the two systems in an energy-conserving way. We note that in our model direct spin-phonon coupling is not considered, which is a reasonable approximation due to the fast time scales of the demagnetization dynamics [14, 107] and the low magnetocrystalline anisotropy of nickel [240]. We therefore modify the TTM equation describing the evolution of the electronic temperature in the following way:

$$c_\mathrm{e}\frac{\Delta T_\mathrm{e}}{\Delta t} = G_\mathrm{ep}\,(T_\mathrm{l} - T_\mathrm{e}) + S(t) - \frac{\Delta E_\mathrm{s}}{\Delta t}. \tag{7.3.4}$$

Figure 7.3.3(a)-(e) compares the results of the ASD simulations (solid red lines) using this approach with our experiments (black dots). Similar to the s-TTM, the ASD simulations maintain the excellent agreement with the experimentally measured lattice dynamics, confirming the strong influence of the magnetization dynamics on the lattice dynamics. Note that also in this model, the electron-phonon coupling is not a fit parameter but stems from the spin-resolved DFT calculations. The main advantage of the ASD simulations is the improved description of the spin system and its magnetization dynamics compared to the s-TTM. This is shown in Fig. 7.3.3(f), which compares the magnetization dynamics from the ASD simulations with experimental results from Ref. [107]. Also for the other fluences, a much better description of the magnetization dynamics is obtained, as shown in figure 7.3.5(a). In addition to the magnetization dynamics, the ASD simulations also yield good agreement with previously reported time- and angle-resolved photoemission (tr-ARPES) measurements of the electronic temperature [66], shown in Fig. 7.3.3(g). Regarding the lattice dynamics, we find that for very high fluences (Fig. 7.3.3 (d) and (e)), the agreement of the ASD simulations with the experiments is less good. This can be due to pump-induced changes of the electronic band structure, which are not included in the model and become more pronounced at higher fluences. The results from DFT calculations describe the ground state properties. Hence, the thus obtained electronic band structure and the electron-phonon coupling best describe the weakly perturbed system as produced by low excitation fluences. In addition, the ASD simulations overestimate the spin heat capacity, in particular for high spin temperatures. This leads to an overestimation of the initial energy flow to the spins during demagnetization as well as the energy flow back from the spin system, especially for high fluences. In comparison to the s-TTM, the ASD simulations reach lower quantitative agreement with the high-fluence lattice dynamics. However, the *overall* agreement with the dynamics of all subsystems is significantly improved for all fluences. For low and moderate absorbed energy densities from 80 $\frac{\mathrm{J}}{\mathrm{cm}^3}$ to 540 $\frac{\mathrm{J}}{\mathrm{cm}^3}$, the ASD simulations yield excellent agreement with the lattice response. The comparison with the electronic, magnetic and lattice responses shows that beyond describing the lattice dynamics, the ASD simulations offer a consistent description of the dynamics of all three subsystems.

Energy flow dynamics

To highlight and discuss some of the key advantages of the ASD simulations and to gain further insights into the energy flow between the different subsystems, we now discuss the details of the temperature and energy dynamics. For this discussion, we also calculate a spin temperature (see Appendix C for details). Note that the spin system is not always in internal thermal equilibrium during the simulations, as will be discussed later. Figure 7.3.3(c) displays the temperature dynamics of electrons (blue), phonons (red) and spins (green) after the initial laser excitation for an absorbed energy density of 540 $\frac{\mathrm{J}}{\mathrm{cm}^3}$. The electron temperature increases rapidly when the laser pulse excites the sample. Contrary to the assumptions made for s-TTM, however, the spin temperature does not follow the electron temperature instantly. Instead, the spin temperature increase is slower and delayed due to the finite coupling between electrons and spins. After ~160 fs, the two subsystems have reached a similar temperature, and they cool down at similar rates while the lattice still heats up. Finally, thermal equilibrium is reached after ~ 2-2.5 ps. In addition to the temperatures, the ASD simulations also provide the energy dynamics of the different subsystems, shown in Fig. 7.3.4(a). After the initial laser excitation, the total additional energy in the system (solid black line) stays constant and energy is only transferred between subsystems. Initially, the electron system (solid blue line) absorbs all of the deposited energy. The rise of the electronic temperature initiates the demagnetization dynamics and energy immediately starts flowing to the spin system (solid green line). Here, we identify the key feature that is not captured by the regular TTM: Already shortly after excitation, the spin system contains more energy than the electron system, which leads to the significant slow-down of the lattice dynamics. The energy flow during demagnetization is schematically depicted in Fig. 7.3.4(b). In addition to the energy flow to the spin system, energy also flows to the lattice (solid red line), although at a lower rate. After ~150 fs, the energy flow to the spin system stops due to the lower electronic temperature. This initiates the remagnetization dynamics. Energy starts flowing back from the spin system to the electrons, which is visualized in Fig. 7.3.4(c). Energy also flows from the electrons to the lattice, such that in total, the electrons lose further energy, although at a much slower rate than during the demagnetization (see Fig. 7.3.4(a)). Note that there is no direct energy flow from the spins to the lattice in the model, but the net

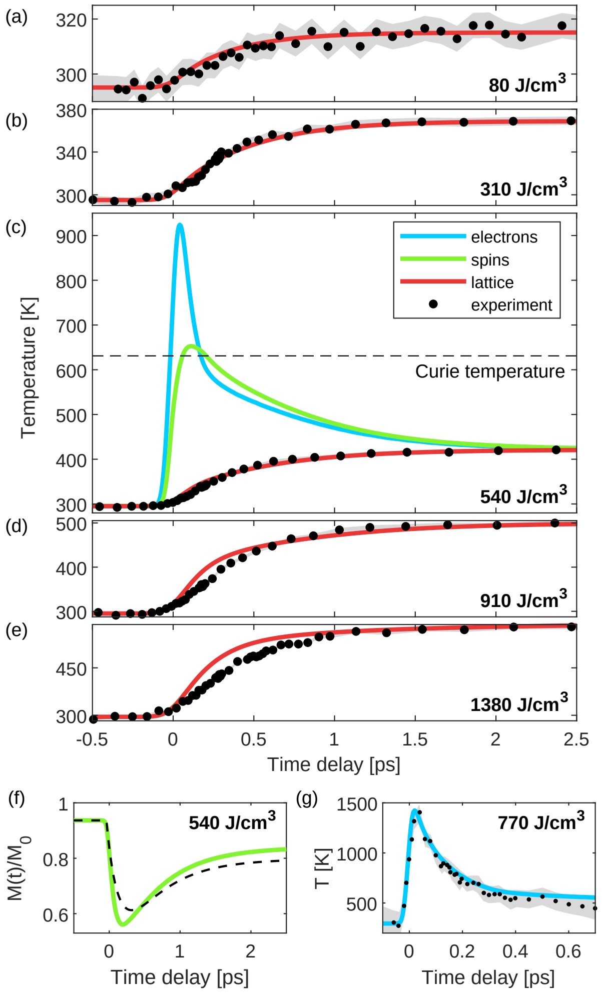

Figure 7.3.3: *Atomistic spin dynamics (ASD) simulations and comparison with the experiment. Panels (a)-(e) show the comparison between ASD simulations (solid red lines) and experiments (black dots) for different absorbed energy densities. The energy densities are slightly different compared to Fig. 7.3.2 due to the different spin heat capacity in the ASD simulations. In the simulations, the pump pulse has a FWHM of 80 fs. The results for the lattice temperature are convolved with a Gaussian (FWHM: 150 fs) to account for the pulse duration of the electron pulse. The electron-lattice interaction in the simulations is described based on spin-resolved DFT calculations, without fit parameters. Panel (c) additionally displays the evolution of the electronic (solid blue line) and the spin temperature (solid green line). Panel (f) displays the magnetization dynamics predicted by the ASD simulations (solid green line), normalized to the magnetization at $T_{\mathrm{s}} = 0$ K, as well as experimental results from Ref. [107] for the same absorbed energy density (dashed black line). Panel (g) compares the evolution of the electronic temperature in the ASD simulations (solid blue line) to experimental data from Ref. [66] (black dots). In this case, we assumed a shorter pump pulse duration in the simulations (FWHM: 30 fs). Note that the sample geometry (film thickness and substrate) was different in the measurements from Refs. [107, 66]. The grey shaded areas of Panels (a)-(e) represent the standard errors of the data points. The grey shaded area of Panel (g) represents the errors of the experimental data points from Ref. [66].*

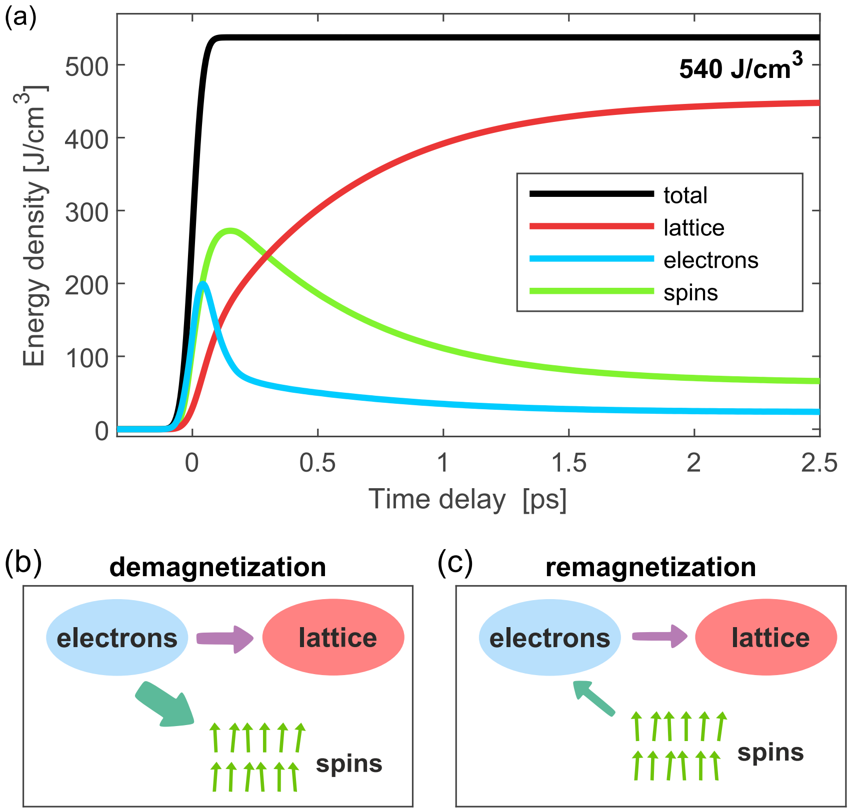

Figure 7.3.4: *Microscopic energy flow between electronic, magnetic and lattice degrees of freedom according to the atomistic spin dynamics (ASD) simulations. Panel (a) shows how the additional energy after laser excitation is distributed between the three different subsystems as a function of time. The black line corresponds to the total additional energy in the material, demonstrating that energy is conserved in the model. Panel (b) visualizes the energy flow during the demagnetization. There is a large energy flow from the electrons to the spin system and as well as energy flow from electrons to the lattice. Panel (c) shows the energy flow during remagnetization. Energy flows back from the spins to the electrons. In addition, energy flows from the electrons to the lattice, such that the electron as well as the spin energy decreases while the lattice energy increases.*

energy flow from spins to the lattice is indirect via the electrons. These processes continue until thermal equilibrium is established. Note that the experiments on the three different subsystems in Fig. 7.3.3 were performed under different experimental conditions. Therefore, the deviations of the experimental data from the simulations cannot be directly interpreted in terms of energy flow.

Non-thermal spin dynamics

Next, in order to gain further insights into the non-equilibrium behavior of the spin system, we analyze the ASD simulation results for the spin system in detail. The simulations provide the spin temperature, the spin energy as well as the magnetization simultaneously. By comparing these three quantities, further conclusions on the non-equilibrium spin system can be

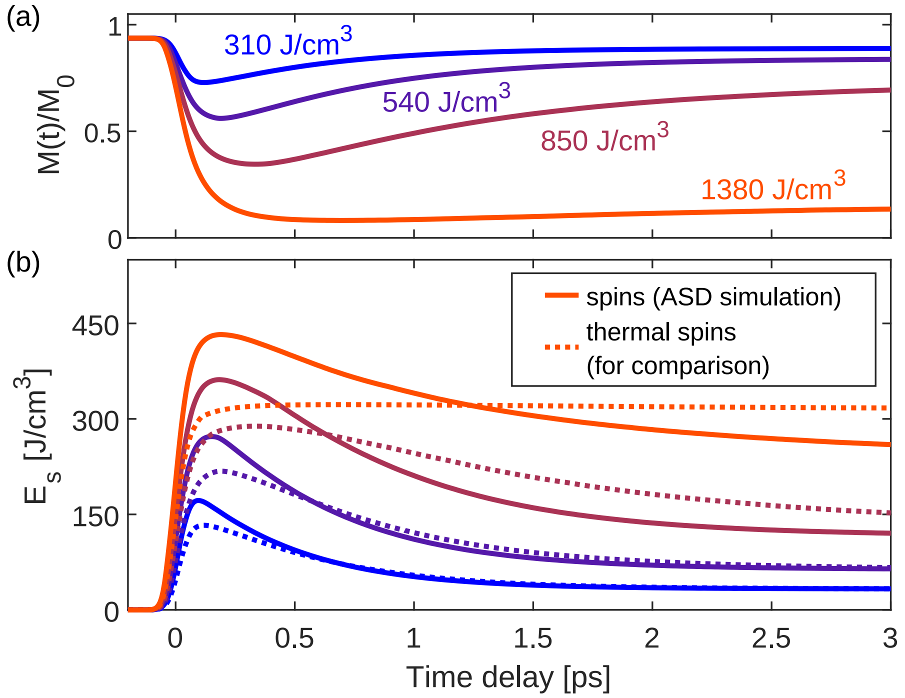

Figure 7.3.5: *Non-equilibrium spin dynamics. (a) Magnetization dynamics from the ASD simulations for several excitation densities of our experiments. (b) Energy content of the spin system as a function of pump-probe delay for several excitation densities (solid lines). For comparison, the dashed lines show the energy content of a hypothetical, thermalized spin system with the magnetization dynamics from the ASD simulations (shown in Panel (a)).*

drawn. First of all, note that despite the fact that the spin temperature in Fig. 7.3.3(c) rises above the Curie temperature, the system does not demagnetize completely, as displayed in Fig. 7.3.3(f). This demonstrates that on short time scales after laser excitation, the spin system is not in internal thermal equilibrium. To understand the characteristics of this transient non-thermal state, we analyze the magnetization and energy content of the spin system. The magnetization dynamics following laser excitation are displayed in Fig. 7.3.5(a) for several excitation densities. The corresponding additional spin energy content is shown in Fig. 7.3.5(b) (solid lines). We compare the evolution of these two quantities after laser excitation to the case in which the spin system is heated quasi-statically. The latter case is obtained from the ASD simulations by increasing the energy of the system in small steps and waiting for the system to reach equilibrium after each step (see Appendix C for details on heat capacities and statistics). By comparing the simulations of the laser-excited dynamics to the equilibrium relationships, we find that on short time scales after laser excitation, the ASD simulations predict a spin energy content that is higher than in equilibrium for the same magnetization. This is visualized by the dashed lines in Fig. 7.3.5(b), which represent the energy content of a hypothetical, thermalized spin system undergoing the magnetization dynamics predicted by the ASD simulations (shown in Fig. 7.3.5(a)). The comparison with the actual spin energy indicates that on short timescales, the spin system is in a transient non-thermal state with a large amount of high-energy spin excitations, in agreement with previous experimental results [66]. This behavior is analogous to non-thermal phonon distributions: In cases in which high-energy phonons couple strongly to the lattice, the atomic displacements can be relatively small compared to the lattice energy content on short time scales [241], because the equilibrium relationship between atomic displacements and lattice energy content is not applicable. Similarly, if the distribution of spin excitations differs from thermal equilibrium, the equilibrium relationship between magnetization and energy content of the spin system is not applicable. In the ASD simulations, the energy transfer from electrons to the spin system creates mostly high-energy spin excitations due to the localized nature of the electron-spin interaction. During the thermalization of the spin system, these excitations then decay into more delocalized spin waves with a larger magnetization reduction per energy. The lifetime of a spin wave mode can be estimated by $\tau \approx \frac{1}{2\alpha\omega}$ [242], where ω is the angular frequency of the spin wave and α is the Gilbert damping. In nickel, for the high-energy spin waves at the Brillouin zone boundary [243], this corresponds to a lifetime of ~ 70 fs. Consequently, the relationship between magnetization and spin energy relaxes towards the thermal relationship within a few hundred femtoseconds. On longer time scales, the behavior of the magnetization reverses: the magnetization recovery is delayed compared to the energy flow out of the spin system, particularly for high fluences. We find that if the magnetization is strongly reduced, the spin-system remains non-thermal for several picoseconds. This behavior is in agreement with previous ASD simulation results and was attributed to domain formation [197]. The comparison of the laser-induced dynamics to quasi-static heating highlights a main advantage of the ASD simulations: in contrast to temperature models, non-thermal states of the spin system can also be described, since the evolution of the spins is simulated directly. The non-equilibrium behavior of the spin system predicted by the ASD simulations results in good agreement of the model with the experimentally measured lattice dynamics as well as the magnetization dynamics. Consequently, using ASD simulations we have improved the theoretical description in two key aspects compared to the s-TTM: First, the magnetization dynamics are described realistically since we no longer assume infinite electron-spin coupling, which leads to instantaneous demagnetization. Second, we no longer use the equilibrium spin heat capacity to describe the spin system in this highly non-equilibrium scenario. Instead, we directly calculate the energy content of the spin system in the ASD simulations. These improvements allow for an excellent quantitative description of the experimentally measured lattice dynamics and provide a consistent model for the dynamics of the three subsystems after laser excitation. Unlike many previous demagnetization models, our approach has the advantage that the parameters for the ASD simulations stem either from ab-initio DFT calculations or are directly linked to measurable quantities, such as the Curie temperature. The avoidance of fit parameters, in combination with the comparison of the model to measurements of all subsystems, is the key to a consistent description of the laser-induced dynamics. The sole parameter that is only indirectly accessible through experiments is the Gilbert damping parameter α. Here, we use α=0.01, which yields good agreement with the lattice dynamics and is consistent with literature [244, 245]. We tested different values for α from 0.005 to 0.02, shown in Appendix C, and found good overall agreement to the experimental data, therefore showing the robustness of the model regarding variations of α. Since experimental results can always be influenced by transport or sample-specific effects, a more precise result for α could be obtained by measuring the dynamics of several subsystems on the same sample, ideally on a freestanding thin film. Furthermore, since α is a phenomenological constant that comprises several microscopic effects, additional accuracy could be gained by disentangling these microscopic effects in a future model.

7.4 Summary and conclusions

In this work, we combined direct experimental measurements of the lattice response with first-principles calculations of the electron-phonon interaction and atomistic spin dynamics (ASD) modelling in order to obtain a full picture of the dynamics in ferromagnetic nickel following laser excitation. The combination of theory and experiment enabled us to study the influence of the energy cost of demagnetization on the lattice dynamics. We found that energy flow to and from the spin system leads to a significant slow-down of the lattice dynamics. The spin system is the dominant heat sink in the initial few hundreds of femtoseconds. Consequently, it is paramount to include the energy flow to and from the spin system in any description of the laser-induced dynamics. In case only the lattice dynamics are of interest, a modified TTM employing electron-phonon coupling from first-principles calculations and incorporating infinitely strong electron-spin coupling (s-TTM) suffices. The agreement of the s-TTM with the measured lattice dynamics proved to be vastly superior to that of the regular TTM. A consistent description of the coupled energy flow between all three subsystems and of the magnetization dynamics is obtained with energy-conserving ASD simulations. Like the s-TTM, the ASD simulations are based on first-principles calculations, thus minimizing the use of fit parameters. The comparison with available experimental data for the electronic, lattice and spin dynamics shows that the ASD simulations achieve a quantitative description of all three subsystems. In the future, the precision of this comparison could be improved further by measuring the response of all three subsystems on identical samples. Both the s-TTM and the ASD simulations unambiguously demonstrate the strong influence of the magnetization dynamics on the lattice dynamics, highlighting the importance of considering their coupling in a full description of the material's response to laser excitation. In addition, the ASD simulations predict that shortly after excitation, the spin system is in a transient non-thermal state and absorbs more energy compared to thermal equilibrium. This finding is corroborated by the excellent agreement of the ASD simulations to the lattice, the electron and the magnetization dynamics. Therefore, our findings indicate that in order to describe both the microscopic energy flow and the magnetization dynamics accurately, an approach that considers non-thermal spin dynamics is necessary. We expect our findings to be valid for other magnetic metals as well, in particular for other itinerant $3d$ ferromagnets, but also for antiferromagnetic or ferrimagnetic metals. Furthermore, a quantitative description of the microscopic energy flow in ferromagnetic metals is valuable for the design of high-speed spintronic structures, since the functionality of magnetic heterostructures depends on their behavior in non-equilibrium states. This, in turn, is governed by the microscopic energy flow and magnetization dynamics within each component as well as interfacial coupling.

Appendix A: DFT calculations

The calculations of the electron-phonon energy transfer rates were performed using the DFT code ABINIT [246, 247, 248, 249, 250]. The norm-conserving electron-ion pseudopotential was generated using the FHI package [251] and is of GGA-PBE type [252]. 10 electrons were treated explicitly and 18 electrons were frozen in the core. The plane wave expansion of the electronic wavefunction had a cutoff of 50 Ha. 20 electronic bands were calculated. These bands are calculated with Fermi occupation featuring a smearing of 0.001 Ha. An unshifted k-point grid of 32 × 32 × 32 points was used. The experimental lattice constant of the fcc lattice of $d = 6.6594$ a_B (= 3.5240 $\mathring{A}$) was used. Figure 7.4.1(a) shows the result

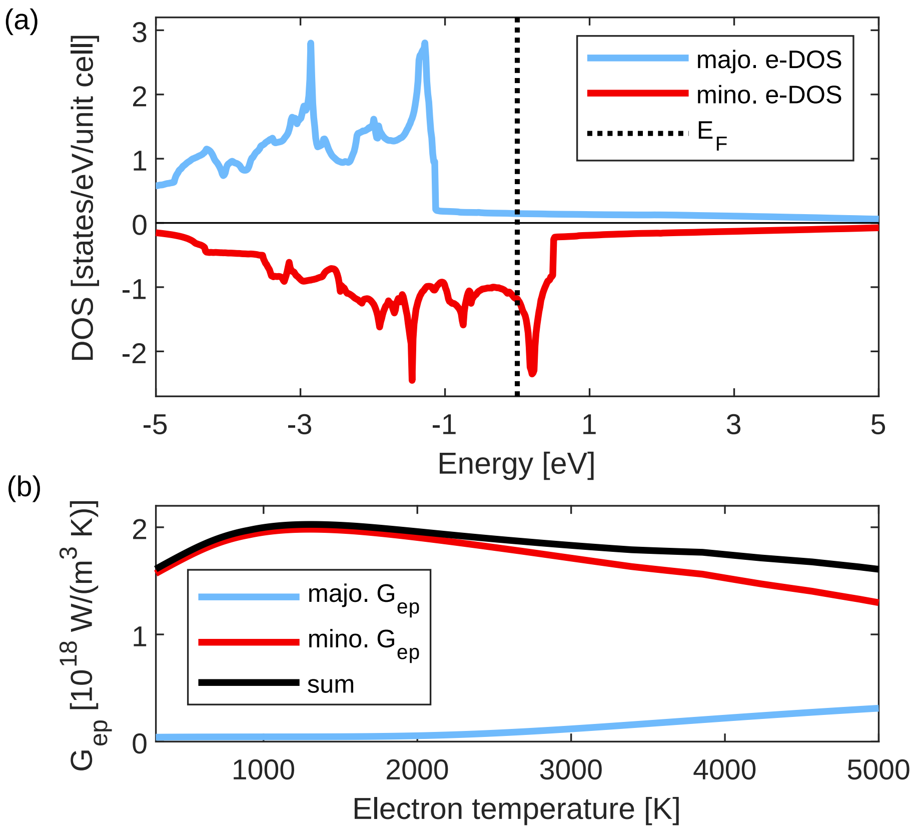

Figure 7.4.1: *Spin-polarized electronic density of states (DOS) and electron phonon coupling of nickel, calculated using spin-resolved DFT. (a) Electronic DOS. The Fermi level is marked with a dashed black line. (b) Electron-phonon-coupling parameter* G_{ep} *as a function of electron temperature. The majority* G_{ep} *(blue), the minority* G_{ep} *(red) and their sum (black) is displayed.*

for the spin-polarized electronic DOS. The DFT calculation predicts a magnetic moment of 0.815 μ_{B}, which is larger than the experimentally measured value of 0.616 μ_{B} [253]. This overestimation mainly affects the minority DOS at the Fermi level. We therefore tested its effects on our models by shifting the minority DOS to lower energies in several steps, until the maximum of the minority DOS coincides with the Fermi level. We then calculated TTM results based on these shifted DOS. Since the differences in the lattice responses are small, we conclude that the overestimation of the magnetic moment has no significant effect on our results. Regarding the phonons, the shape and energy range of the calculated phonon DOS (not shown) agree well with neutron scattering experiments [254]. The phonon DOS is used to calculate the lattice heat capacity, resulting in excellent agreement with experimental results [217]. To obtain the electron-phonon coupling G_{ep}, the spin-resolved electron-phonon matrix elements were computed as described in Ref. [255] for a $8 \times 8 \times 8$ grid of q-points. From the results, we extracted the Eliashberg functions (also phonon-branch resolved) for majority and minority electrons. The electron-phonon couplings as well as the electronic heat capacities were then calculated as in Ref. [241]. The result for the electron-phonon coupling is displayed in Fig. 7.4.1(b). In the calculation of the spin-resolved electron-phonon coupling and electronic heat capacities, we assume that the particle number is conserved within each spin type. In practice, for the electron temperatures reached in our experiments, the chemical potential shifts are small, and thus the differences between assuming two separate chemical potentials or assuming a common chemical potential are small. For the temperature models as well as the ASD simulations, we use the sum of majority and minority G_{ep} (black curve of figure 7.4.1(b)). Correspondingly, the electronic heat capacity used in the models is also the sum of minority and majority electronic heat capacity. The results of the DFT calculation are available on a data repository [256]. We note that our result for the electron-phonon coupling is significantly larger compared to results by Lin et al. [105], but similar to a spin-resolved calculation by Ritzmann et al. [215]. We also find significant differences compared to the values used in existing demagnetization models: In the original 3TM by Beaurepaire et al. [5], a much smaller value of $8 \cdot 10^{17}$ W/(m^{3}K) is used, resulting in a slower lattice response compared to our experiments. In the M3TM [14], the value for G_{ep} is $4.05 \cdot 10^{18}$ W/(m^{3}K), which differs from our result by more than a factor of 2. In addition, the heat capacities are different. In the μT model [196], the same G_{ep} of $1 \cdot 10^{18}$ W/(m^{3}K) is used for majority and minority carriers, whereas the G_{ep} from our ab initio calculations shows significant differences between majority and minority carriers.

Appendix B: The influence of non-thermal electron and phonon distributions

The TTM relies on the assumption that electrons and phonons are each in a thermal state, which is not necessary fulfilled shortly after laser excitation. For electrons, in metals, thermalization is typically rather efficient due to the large phase space for electron-electron scattering. In the case of nickel, there is experimental evidence for efficient electron-electron scattering [66]. In addition, to test if our measured lattice dynamics are influenced by non-thermal electrons, besides the experiments with 2300 nm, we also performed experiments with 800 nm and 480 nm excitation wavelength and compared the lattice dynamics. Figure 7.4.2(a) shows the time constants of a single exponential fit to the lattice temperature for these three wavelengths and different excitation densities. No dependence of the lattice dynamics on the wavelength is observed. From this, we conclude that electrons thermalize on timescales significantly faster than the timescales of electron-phonon equilibration. Otherwise, we would expect an influence of the photon energy on the lattice dynamics, since different initial states are excited and different electronic states have different lifetimes for electron-phonon scattering. Hence, we conclude that it is justified to assume a thermalized electron distribution in our models. On the other hand, for phonons, the assumption of a thermalized distribution is often more problematic [215, 241]. We investigated the influence of non-thermal phonon distributions on our observable, the MSD, using a non-linear lattice model (NLM) [241]. The three different phonon branches are treated as individual subsystems in order to account for energy redistribution between them. For this, we calculate the branch-projected phonon DOS and Eliashberg functions, shown in the inset of 7.4.2(b). We don't take into account direct phonon-phonon coupling, which means that the equilibration between the phonon branches is mediated by electron-phonon coupling only. The comparison between TTM and NLM is displayed in Fig. 7.4.2(b) and shows only small differences between the lattice temperatures predicted by the two models. In addition, a previously reported model predicts only minor deviations of the electronic temperature evolution compared to a TTM for nickel [215]. There are experimental observations of phonon thermalization processes in nickel [214], mostly observed in the range of 1-4 ps after laser excitation. Since we don't observe any significant MSD changes during this period (see

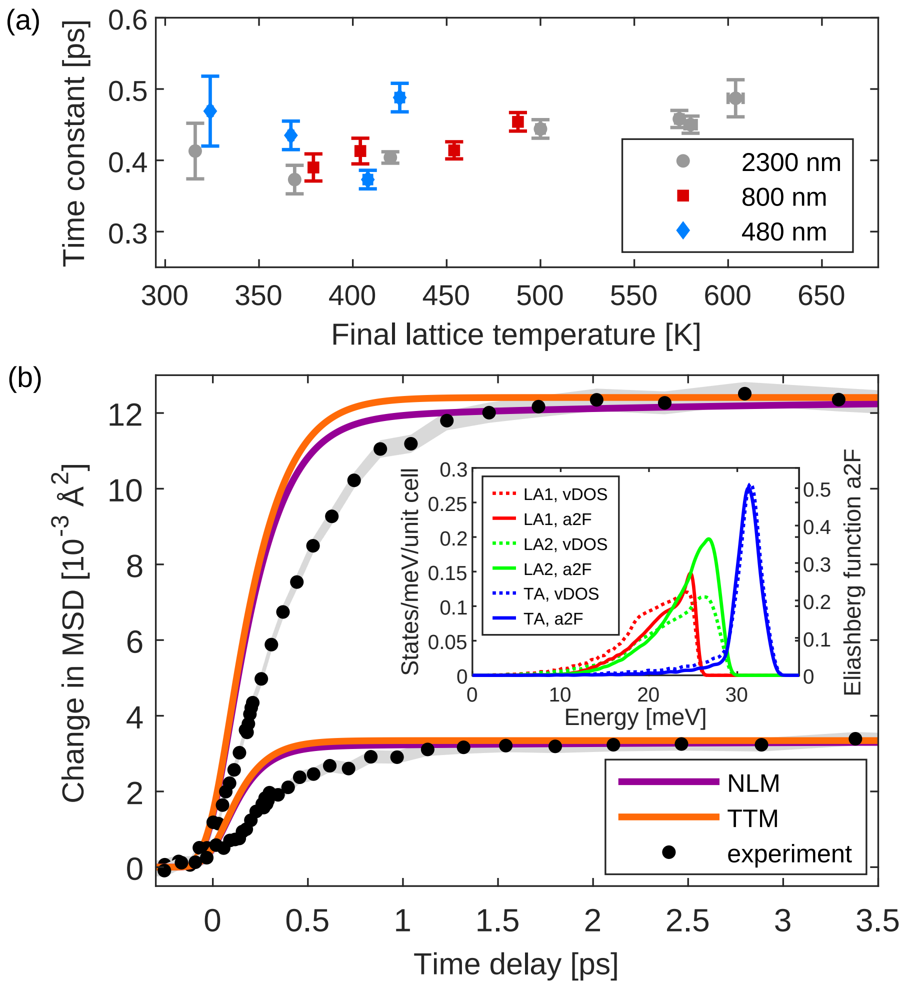

Figure 7.4.2: *Experimental and theoretical results regarding electron and phonon thermalization. (a) Time constants of electron-lattice equilibration for different excitation wavelengths, obtained by single-exponential fits of the experimental data. The grey dots are the same data as in the inset of 7.2.2, shown again for comparison. The error bars represent the standard errors from the single exponential fits. (b) Comparison of two-temperature model (TTM) results with non-thermal lattice model (NLM) results for two different fluences. Experimental data for 2300 nm excitation wavelength are also shown. The grey shaded areas represent the errors of the experimental data. The inset shows the Eliashberg function (solid lines, sum of majority and minority Eliashberg function) and the phonon DOS (dashed lines) projected onto the three phonon branches.*

figure 7.2.2), we conclude that the effect of these phonon thermalization processes on the MSD is small, and that the sub-picosecond dynamics that we observe correspond to electron-phonon equilibration. Based on these theoretical and experimental results, we conclude that in the case of nickel and for the purpose of describing energy flow between electrons and the lattice, a thermalized phonon population is a reasonable approximation.

Appendix C: Atomistic spin dynamics simulations

In the ASD simulations, the spin system is described using a classical Heisenberg Hamiltonian:

$$\mathcal{H} = -\sum_{i<j} J_{ij}\,\mathbf{S}_i \cdot \mathbf{S}_j - \sum_i d_z S_z^2. \tag{7.4.1}$$

Here $\mathbf{S}_i$ represents a unit vector describing the direction of the local magnetic moment at site i. Each spin $\mathbf{S}_i$, couples to its neighboring spins $\mathbf{S}_j$ via the exchange constant $J_{ij} = 2.986 \cdot 10^{-21}$ J. We use a simple cubic lattice structure with a spin volume of $V_\mathrm{s} = 10.94$ $\mathring{A}^3$. We tested different lattice structures and found that this has no significant effect on our results. To obtain the correct spin energy from Equation 7.4.1, a correction factor of 1/3 is necessary (see Equation 7.3.3). This accounts for the fact that the spins are quantized in reality ($s \approx 1/2$ for nickel), but described with the classical Heisenberg Hamiltonian ($s=\infty$). The relationship between the exchange constant J_{ij} and the Curie temperature T_c depends on the quantum number s. For a simple cubic system with only nearest neighbor interaction [257],

$$J = \frac{s^2}{s(s+1)} \cdot \frac{3k_\mathrm{B}}{T_\mathrm{c}}. \tag{7.4.2}$$

Consequently, to obtain a good description of both the Curie temperature and the energy content of a spin system with finite s, a factor of $\frac{s^2}{s(s+1)}$ ($\frac{1}{3}$ for $s = \frac{1}{2}$) needs to be considered. The second term of Equation 7.4.1 describes the on-site anisotropy with easy-axis along the z axis and a constant anisotropy energy, $d_z = 5 \cdot 10^{-24}$ J. The ASD-simulations are performed by solving the stochastic-Landau-Lifshitz-Gilbert equation (s-LLG) numerically using the Nvidia CUDA C-API [137, 72].

$$\frac{(1+\alpha^2)\mu_s}{\gamma}\frac{\partial \mathbf{S}_i}{\partial t} = -\left(\mathbf{S}_i \times \mathbf{H}_i\right) - \alpha\left(\mathbf{S}_i \times \left(\mathbf{S}_i \times \mathbf{H}_i\right)\right). \tag{7.4.3}$$

$\gamma = 1.76 \cdot 10^{11}$ is the gyromagnetic ratio and $\mathbf{H}_i$ is the effective field (see below). For the magnetic moment μ_s we use the literature value of 0.616 μ_B [253], which contains the spin as well as the (smaller) orbital contribution. The phenomenological Gilbert damping α determines the coupling strength of the spin system to the electron system and thus the energy transfer rate between these two subsystems. A Langevin thermostat is included, by adding a field-like stochastic term $\boldsymbol{\zeta}_i$ to the effective field $\mathbf{H}_i = \boldsymbol{\zeta}_i(t) - \frac{\partial \mathcal{H}}{\partial \mathbf{S}_i}$. The added noise term has white noise properties [97]:

$$\langle \boldsymbol{\zeta}_i(t) \rangle = 0 \quad \text{and} \quad \langle \boldsymbol{\zeta}_i(0)\boldsymbol{\zeta}_j(t) \rangle = 2\alpha k_\mathrm{B} T_\mathrm{el} \mu_s \delta_{ij}\delta(t)/\gamma. \tag{7.4.4}$$

The electron temperature T_el is therefore used to scale the noise and has a direct impact on the spin dynamics via the stochastic field $\boldsymbol{\zeta}(t)$ entering the s-LLG. The s-LLG is solved for system sizes of several million spins. These large systems yield minimal boundary effects and provides a large enough number of spins for calculating macroscopic parameters. While showing excellent qualitative agreement with experiments, due to their classical character ASD simulations are typically unable to quantitatively reproduce thermodynamic properties such as the heat capacity or the temperature-dependent equilibrium magnetization. To counteract this shortcoming, we make use of a rescaled temperature model [230]. A modified electron temperature T_sim, based on T_c and a material dependent factor $\beta = 2.322$ is used:

$$T_\mathrm{sim} = T_c \left(\frac{T_\mathrm{el}}{T_c}\right)^\beta. \tag{7.4.5}$$

This correction allows us to reproduce experimentally measured quantities such as the temperature-dependent equilibrium magnetization curve and the heat capacity (see figure 7.4.3(a) and (b)). For the temperature-dependent equilibrium magnetization (figure 7.4.3(b)) we obtain excellent agreement with experimental values. The spin heat capacity (figure 7.4.3(a)) is overestimated due to the classical nature of the spins in the ASD-simulations. The spin temperature in ASD simulations can be calculated through the instantaneous spin configuration following Ref. [258]:

$$T_s = \frac{\mu_{\mathrm{s}} \left\langle \sum_i |\mathbf{S}_i \times \mathbf{H}_i|^2 \right\rangle}{2k_{\mathrm{B}} \langle \sum_i \mathbf{S}_i \cdot \mathbf{H}_i \rangle}. \tag{7.4.6}$$

Here $\mathbf{S}_i$ and $\mathbf{H}_i$ represent the normalized spin variable and effective field at the lattice site i. The spin temperature in Equation (7.4.6) is defined as the ratio between the entropy and energy of spin degrees of freedom, $\mathbf{S}_i \times \mathbf{H}_i$ and $\mathbf{S}_i \cdot \mathbf{H}_i$, respectively. Note that despite this definition of a spin temperature, the spin system is not always in internal thermal equilibrium during the simulations. The values for the electronic heat capacity, lattice heat capacity and electron-phonon coupling are taken from the DFT calculations described earlier. The laser pulse is assumed to be Gaussian, with a FWHM of 80 fs and its peak intensity at $t = 0$. Figure 7.4.3(c)-(d) shows the ASD simulation results for different values of the Gilbert damping parameter α. Figure 7.4.3(c) displays the lattice temperature according to the ASD simulations alongside our experimental result while figure 7.4.3(d) shows the magnetization dynamics from the simulations together with experimental results from Ref. [107]. Figure 7.4.3(e) presents the evolution of the electronic temperature according to the ASD simulations.

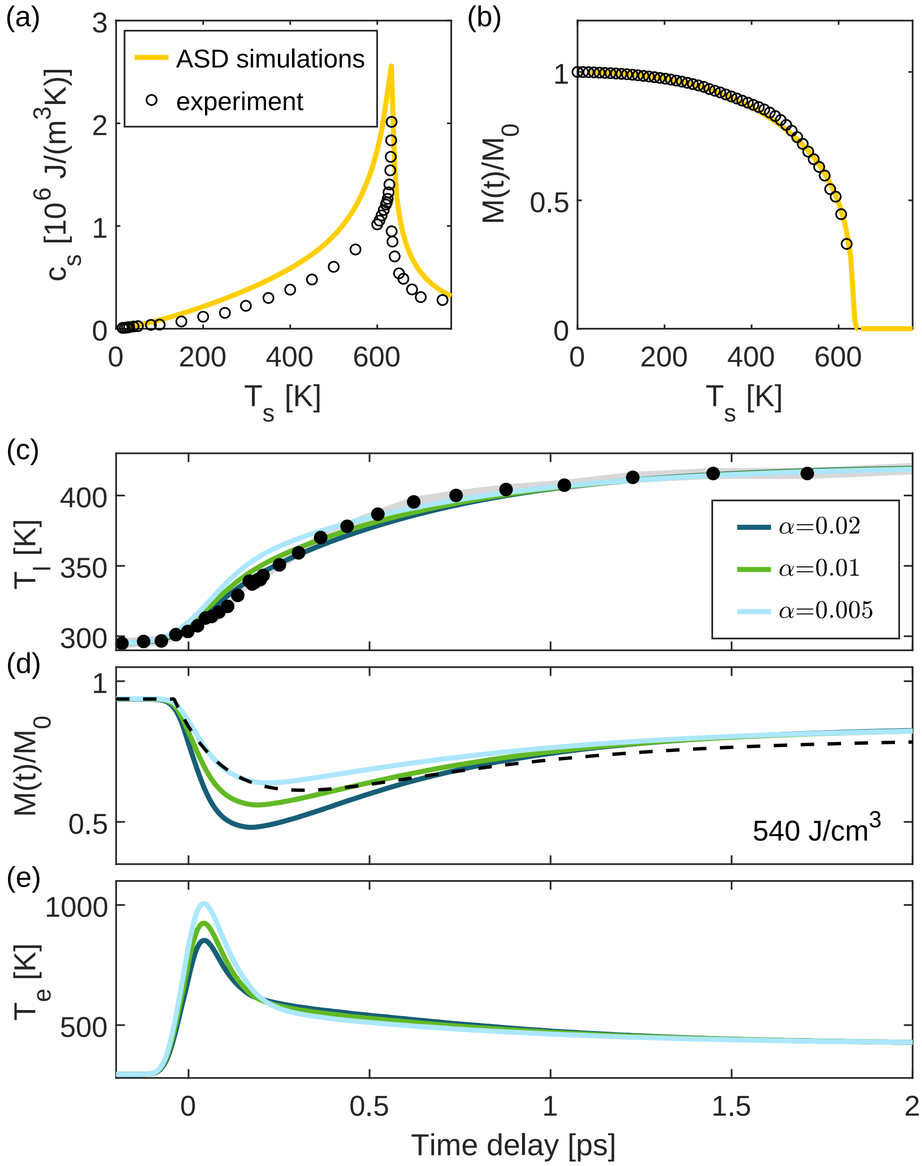

Figure 7.4.3: *Atomistic spin dynamics (ASD) simulation results for equilibrium and non-equilibrium conditions. (a) Comparison between experimentally measured equilibrium heat capacity (black circles) and the simulated equilibrium heat capacity (yellow line). The experimentally measured spin heat capacity corresponds to the heat capacity of electrons and spins [217] minus the electronic heat capacity from our DFT calculations. (b) Comparison between the experimentally measured magnetization curve as a function of temperature from Ref. [259] (black circles) to the simulation (yellow line). (c) Experimentally measured lattice dynamics (black dots) and ASD simulation results (solid lines) for different values of the Gilbert damping parameter* α*. The absorbed energy density is 540* $\frac{\mathrm{J}}{\mathrm{cm}^3}$*. The grey shaded area represents the errors of the experimental data. (d) Magnetization dynamics predicted by the ASD simulations for different values of* α *(solid lines). The dashed black line corresponds to the experimental magnetization dynamics for the same absorbed energy density of 540* $\frac{\mathrm{J}}{\mathrm{cm}^3}$ *from Ref. [107]. (e) Evolution of the electronic temperature for different values of* α *according to the ASD simulations. Note that in addition to* α*, the initial rise of the electronic temperature also depends on the pump pulse duration (here: 80 fs FWHM).*

Chapter 8

Intrinsic energy flow in laser-excited $3d$ ferromagnets

The results of this chapter have been published in

- D. Zahn, F. Jakobs, H. Seiler, T. A. Butcher, D. Engel, J. Vorberger, U. Atxitia, Y. W. Windsor, and R. Ernstorfer, Intrinsic energy flow in laser-excited $3d$ ferromagnets, *Physical Review Research* **4** p. 013104, (Feb 2022).

and the content of this chapter is in large parts identical with the published work.
Large parts of the theory and in particular all atomistic spin dynamics simulations have been performed as part of this thesis. All experiments were done by D. Zahn and coworkers from the Fritz-Haber-Institut. The density functional theory calculations have been performed by T. A. Butcher and J. Vorberger.

The published version can be found at `https://doi.org/10.1103/PhysRevResearch.4.013104`

8.1 Introduction

Ultrafast manipulation of magnetic order with light promises pathways to new applications in magnetic data storage and spintronics [175]. Femtosecond laser excitation can change magnetic order in various ways - for example, it can induce ultrafast demagnetization [5], switch the magnetization direction [6, 260], and induce spin reorientation [261]. The microscopic mechanisms governing the response of magnetic materials to laser excitation continue to be a topic of current research [14, 16, 55, 195, 202, 203, 66, 107, 213]. An important factor governing the response of a material to laser excitation is the intrinsic energy flow between electronic, magnetic, and lattice degrees of freedom. When Beaurepaire et al. discovered ultrafast demagnetization in Ni, they introduced a phenomenological three-temperature model (3TM) to describe the observed magnetization dynamics [5]. While the 3TM offers an intuitive explanation for the observed dynamics, recent studies suggest that it falls short of a full description of ultrafast demagnetization. In particular, there is experimental and theoretical evidence that the spin system is not in a thermal state on ultrafast timescales [66, 197, 207], suggesting that a more detailed description of the magnetic degrees of freedom is necessary. To obtain a full quantitative description of a material's response to laser excitation, any proposed model must be verified by comparison to experimental data of the responses of electronic, magnetic, and lattice degrees of freedom. The lattice plays a major role in the dynamics of $3d$ ferromagnets, since it drains energy from the electrons via electron-phonon coupling on similar timescales compared to the demagnetization, thus reducing the temperature of the electron system. On the other hand, lattice dynamics are also influenced by magnetization dynamics, even if the coupling is only indirect via the electron system. Our previous work on Ni demonstrated that energy flow into and out of the spin system leads to a significant slow-down of the lattice dynamics (see Chapter 7). This suggests that accounting for this energy flow is integral to any model quantitatively describing the responses of all three subsystems in $3d$ ferromagnets. Despite their significant role in the energy flow dynamics, the lattice dynamics of $3d$ ferromagnets are less studied compared to electron and spin dynamics [207, 14, 202, 203, 212, 262]. Time-resolved diffraction offers the most direct way to study lattice dynamics since it is only sensitive to the lattice. Hitherto, only two studies of the sub-picosecond lattice dynamics of Co or Fe with time-resolved diffraction exist [263, 264] and neither of them focuses on the lattice heating in the ferromagnet. Furthermore, literature values for the electron-phonon coupling parameter G_{ep} vary significantly, from 6×10^{17} to $4.05 \times 10^{18} \frac{W}{m^3K}$ for Co [265, 14, 215, 266] and from 7×10^{17} to $5.48 \times 10^{18} \frac{W}{m^3K}$ for Fe [267, 215, 268, 269, 270, 271]. In addition, there are several literature values for the electron-phonon coupling parameter λ, which is related to G_{ep} (see for example Ref. [105]), and also varies significantly [272, 273, 274, 255]. In ferromagnets, extracting the electron-phonon coupling solely from experiments is particularly challenging because three different subsystems contribute to the observed dynamics. Here, we measure the lattice dynamics of Co and Fe directly using femtosecond electron diffraction. Instead of extracting G_{ep} from experiments, we perform spin-resolved density functional theory (DFT) calculations, which yield G_{ep} as well as the heat capacities of the electrons and the lattice [241] (see Chapter 7). Based on the experimentally measured lattice dynamics and the DFT results, we study the intrinsic energy flow between electronic, magnetic, and lattice degrees of freedom. We employ energy-conserving atomistic spin dynamics (ASD) simulations [106] (see Chapter 7), a hybrid model which combines conventional ASD simulations with a description of the energy flow between all subsystems. By directly simulating the evolution of the spin system, ASD simulations have the advantage that they are not constrained to thermal descriptions of the spin system. Previously, we applied this approach to Ni with excellent agreement between theory and experiment (see Chapter 7). Here, we demonstrate that the same considerations hold also for Co and Fe, thus generalizing our approach to all three elemental $3d$ ferromagnets. To demonstrate the strong influence of the magnetization dynamics on the lattice dynamics, we compare results of the conventional two-temperature model (TTM), which does not consider the spin system, to results of the energy-conserving ASD simulations. With the latter, we obtain excellent agreement with the lattice dynamics of Co and Fe as well as a good description of the magnetization dynamics. This demonstrates that ASD simulations offer a consistent description of the laser-induced dynamics in all three elemental $3d$ ferromagnets. In Section 8.2, we describe the experiment and the data analysis. Section 8.3 presents both experimental results for the lattice dynamics as well as model results. Based on the ASD simulation results, in Section 8.4 we discuss the intrinsic energy flow between electrons, spins, and the lattice in detail. Section 8.5 summarizes the main findings.

8.2 Time-resolved diffraction experiment

The samples of our experiments are freestanding thin films of Co or Fe with a thickness of 20 nm, sandwiched between 5 nm-thick layers of silicon nitride. They were grown on a single crystal of NaCl by magnetron sputtering, resulting in polycrystalline films. Next, they were transferred onto a transmission electron microscopy (TEM) grid by floating the films on water. The samples were not subjected to a magnetic field before the experiment, i.e. different magnetic domains are likely present in the sample.

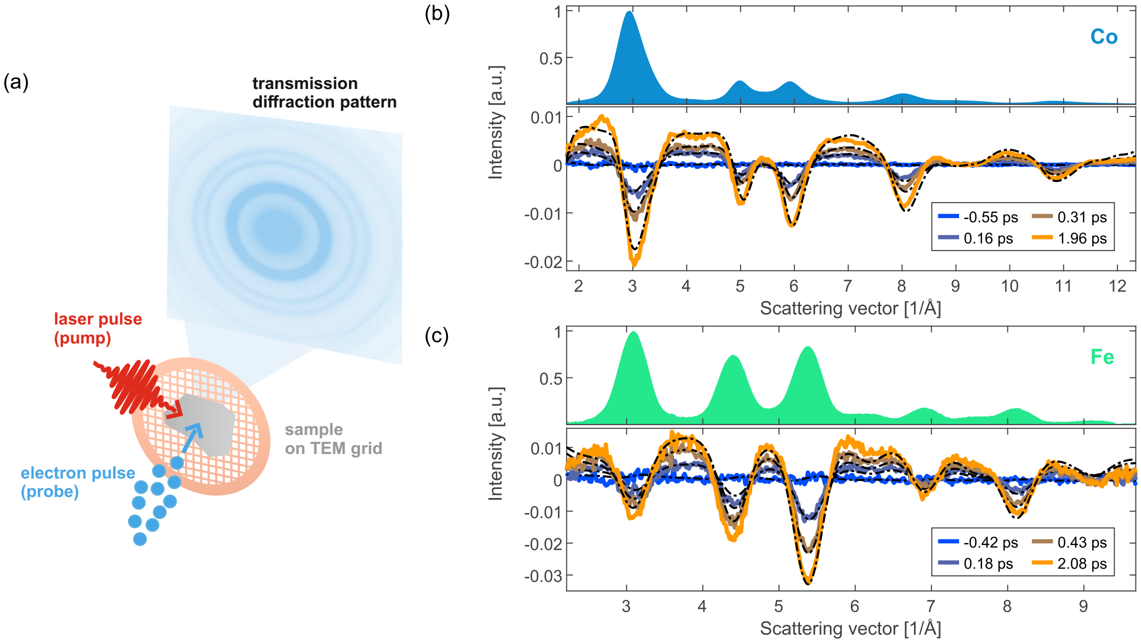

Figure 8.2.1: *The femtosecond electron diffraction experiment. (a) Schematic illustration of the measurement. The samples are thin, freestanding films on transmission electron microscopy (TEM) grids, which are excited by ultrashort laser pulses. The lattice response is probed using ultrashort electron pulses, which diffract off the sample. Diffraction patterns are recorded in transmission. In the case of polycrystalline samples such as the samples studied in this work, the diffraction patterns consist of rings. A diffraction pattern of our Co sample is shown. (b) Diffraction pattern of Co and time-resolved changes. The upper part shows the azimuthally averaged diffraction pattern (radial profile, RP) of Co. Here, the background-subtracted pattern is shown for illustrational purposes, however, note that in the analysis of the diffraction patterns, fits are performed to background and rings simultaneously. The lower part shows the differences of the RPs compared to the RP before laser excitation for several pump-probe delays (solid curves). The dashed black lines show the fit results of the global fitting routine described in Sec. 8.2 and in detail elsewhere [233]. (c) Same as (b), but for Fe.*

To directly access the lattice dynamics after laser excitation, we employ femtosecond electron diffraction, using the setup described in Ref. [68]. A schematic illustration of the experiment is presented in Fig. 8.2.1(a). In the electron diffraction experiment, the thin films are excited with an ultrashort laser pulse. The lattice response to laser excitation is probed using an ultrashort high-energy electron pulse. The electrons diffract off the sample and are recorded in transmission. The electron energy was 70 keV for the experiments on Co and 60 keV for the experiments on Fe. All experiments were performed at room temperature (295 K). Since the samples are polycrystalline, the diffraction patterns consist of Debye-Scherrer rings, as shown exemplarily in Fig. 8.2.1(a) for our Co sample. Our main observables are changes in the intensities of the diffraction rings following laser excitation. These are directly related to the change in atomic mean-squared displacement (MSD) [236]:

$$\frac{I(t)}{I_0} = \exp\{-\frac{1}{3}\, q^2\, \Delta\langle u^2\rangle\ \}. \tag{8.2.1}$$

Here, q is the scattering vector of the diffraction ring ($q = 4\pi \sin(\theta)/\lambda$), $\Delta\langle u^2\rangle = \langle u^2\rangle(t) - \langle u^2\rangle(t < 0)$ is the MSD change, $I(t)$ is the intensity as a function of pump-probe delay and I_0 is the intensity before laser excitation. To extract the MSD dynamics from the diffraction patterns, we employ a global two-step fitting routine [233]. In brief, the first step is a fit to the diffraction pattern before laser excitation. The fit function consists of a background function plus Lorentzians for the diffraction rings, all convolved with a Gaussian to account for the finite coherence of the electron beam. In the second step, the time-dependent changes are extracted. For this, we fix most parameters of the fit function and allow only changes of the lattice constant (i.e. expansion/contraction of the lattice), changes of the MSD, and changes of the background parameters. The lattice dynamics are extracted from the full diffraction pattern instead of individual diffraction rings, which increases the reliability of the results. Further information on the global fitting routine is available in Ref. [233].

8.3 Results

8.3.1 Experimental results for the lattice dynamics

Experiments were performed on Co and Fe for several excitation densities each. For every excitation density, several delay scans were recorded and the results were averaged before applying the two-step fitting routine. Examples for the resulting MSD dynamics of Co and Fe are presented in Fig 8.3.1(a) and (b), respectively. For the conversion of MSD to lattice temperature, we calculated the temperature-dependent Debye-Waller factors for Fe and Co based on the phonon density of states from DFT (see Appendix A). We performed fits to the experimental data using a single exponential function, convolved with a Gaussian of 250 fs (FWHM) to account for the time resolution. The time constant of the single exponential function, the amplitude, and the onset (time zero) were fit parameters and the fit range was from -0.5 to 4 ps. The results for the time constants are shown in Fig. 8.3.1(c) for different excitation densities. For Co, we find that the time constant increases with increasing excitation density. For Fe, no clear trend is observed.

8.3.2 Comparison of the experimental results to energy flow models

Two-temperature model

In the next step, our goal is to analyze the intrinsic energy flow between electronic, magnetic, and lattice degrees of freedom. For this, we compare our experimental data to models

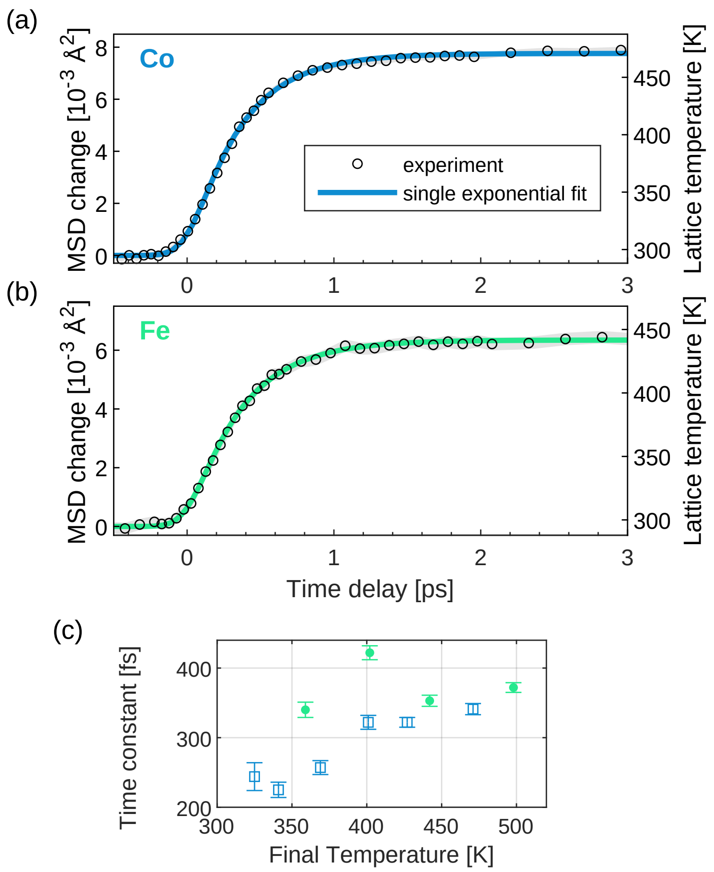

Figure 8.3.1: *Experimental results for the lattice dynamics and single exponential fits. (a) Evolution of the atomic mean-squared displacement (MSD) and corresponding lattice temperature for Co. (b) MSD evolution and corresponding lattice temperature for Fe. The solid lines in (a) and (b) are the results of fits of the experimental data with a single exponential function, convolved with a Gaussian (250 fs FWHM) to account for the time resolution of the experiment. The excitation wavelength was 2300 nm. (c) Fit results for the time constant of the single exponential function for different excitation densities, yielding different final lattice temperatures.*

for the energy flow. In order to minimize the number of free parameters in the models, we use spin-resolved DFT to obtain the (electron-temperature-dependent) electron-phonon coupling parameter as well as the electron and lattice heat capacities. The results for the heat capacities and the electron-phonon coupling parameters are presented in Fig. 8.3.2(a) and (b). All electronic heat capacity and G_{ep} curves presented in Fig. 8.3.2 are the sum of majority and minority carrier contributions. Details about the DFT calculations are described in Appendix A. Having obtained the input parameters for the models from DFT, we start with the conventional TTM [238, 239], which considers only the electronic and lattice degrees of freedom but disregards the spin system. The system is modeled as two heat baths, electrons and the lattice, which are coupled by the electron-phonon coupling parameter G_{ep}. The evolution of the electron temperature (T_e) and the lattice temperature

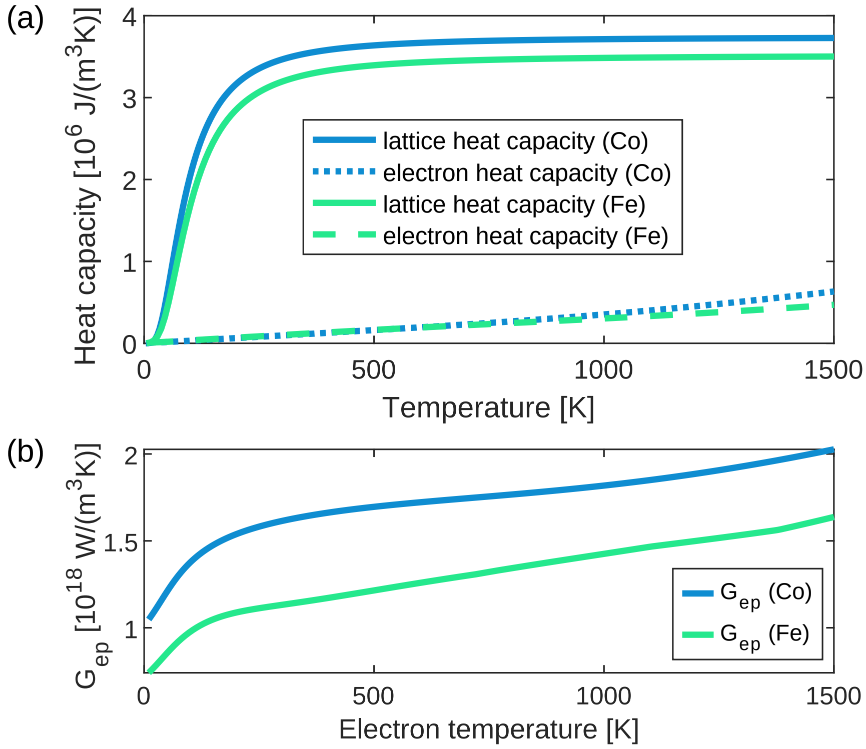

Figure 8.3.2: *Heat capacities, electron-phonon coupling parameters, and schematic illustrations of the employed energy-flow models. (a) Electronic (dashed curves) and lattice (solid curves) heat capacities, and (b) electron-phonon coupling parameters* G_{ep} *as a function of electron temperature calculated from spin-resolved DFT results.*

(T_l) is then described by two coupled differential equations:

$$c_{\mathrm{l}}(T_{\mathrm{l}}) \cdot \frac{dT_{\mathrm{l}}}{dt} = G_{\mathrm{ep}}(T_{\mathrm{e}})\,[T_{\mathrm{e}} - T_{\mathrm{l}}] \tag{8.3.1}$$

$$c_{\mathrm{e}}(T_{\mathrm{e}}) \cdot \frac{dT_{\mathrm{e}}}{dt} = G_{\mathrm{ep}}(T_{\mathrm{e}})\,[T_{\mathrm{l}} - T_{\mathrm{e}}] + P(t). \tag{8.3.2}$$

Here, c_{e} and c_{l} are the electronic and lattice heat capacities, and $P(t)$ is the source term, i.e. the energy input to the electronic system due to the laser excitation. The laser excitation is modeled as a Gaussian with a FWHM of 80 fs. Its maximum (time zero) is determined from the single exponential fits described earlier. The energy deposited by the laser is determined from the lattice temperature after electron-lattice equilibration (in the range from 1.5-4 ps after laser excitation) and the heat capacity (sum of electron and lattice contribution). Hence, there are no fit parameters in this TTM. The comparison between the TTM and the experimental results for the lattice dynamics is shown in Fig. 8.3.3 for both materials and several fluences each (dashed curves). We find that for both Fe and Co, the lattice temperature rise predicted by the TTM is faster compared to our experimental results. This finding agrees with previous results on Ni (see Chapter 7). A major source of this disagreement is the fact that the TTM does not consider magnetic degrees of freedom. Therefore, also the energy associated with magnetization dynamics is neglected. However, as we showed previously for the case of Ni, energy flow into and out of magnetic degrees of freedom has a profound influence on lattice dynamics (see Chapter 7). Hence, a model which takes the spin system into account is needed.

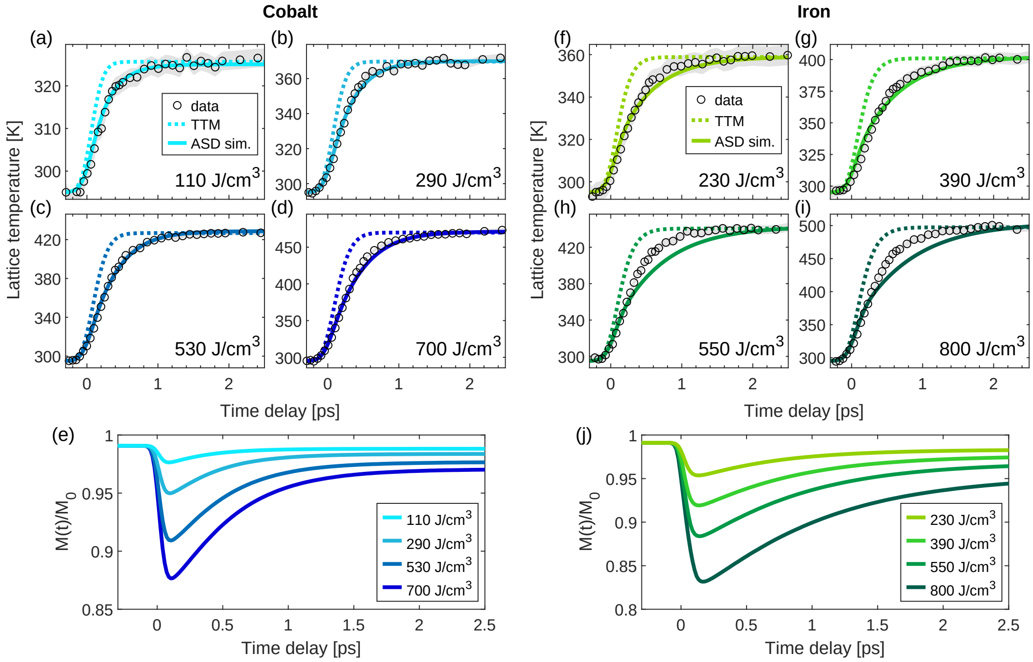

Figure 8.3.3: *Experimentally measured lattice dynamics and model predictions. (a)-(d) Lattice temperature as a function of pump-probe delay in Co for different absorbed energy densities. The experimental data are shown as black circles. The results of the two-temperature model (TTM) are shown as dashed curves and the results of the atomistic spin dynamics (ASD) simulations are shown as solid curves. The TTM and ASD results were convolved with a Gaussian with a FWHM of* $\sqrt{250^2 - 80^2}$*fs* $\approx$ *237fs, which accounts for the temporal broadening induced by the probe pulse (the effect of the pump pulse width is already included in the model itself). The grey shaded areas represent the standard errors of the experimental data, obtained from the fitting routine described in Section 8.2. The displayed energy densities correspond to the absorbed energy densities in the ASD simulations. (e) Magnetization dynamics of Co predicted by the ASD simulations. (f)-(i) Experimental results for the lattice temperature in Fe alongside results of the TTM and the ASD simulations. (j) Magnetization dynamics of Fe predicted by the ASD simulations.*

Atomistic spin dynamics simulations

In order to include the spin system in our model of the energy flow dynamics, we use energy-conserving ASD simulations, which simulate the dynamics of the spin system based on a Heisenberg model and the stochastic Landau-Lifshitz-Gilbert (s-LLG) equation. The coupling of electron and phonon system is described with a TTM based on the DFT results (see Fig. 8.3.2(a) and (b)), as in the previous subsection. Energy conservation is achieved by monitoring the energy content of the spin system and subtracting/adding the change in spin energy from/to the electron system at each time step of the simulation. The TTM equation for the electron temperature (Eq. 8.3.2) is thus modified as follows:

$$c_\mathrm{e}\frac{\Delta T_\mathrm{e}}{\Delta t} = G_\mathrm{ep}\left(T_\mathrm{l} - T_\mathrm{e}\right) + S(t) - \frac{\Delta E_\mathrm{s}}{\Delta t}. \tag{8.3.3}$$

Here ΔE_s corresponds to the change of spin energy in the time step Δt. It is calculated as follows:

$$\Delta E_\mathrm{s} = \frac{s^2}{s(s+1)}\left(\mathcal{H}\{\mathbf{S}_i(t+\Delta t)\} - \mathcal{H}\{\mathbf{S}_i(t)\}\right). \tag{8.3.4}$$

Here, the $\mathbf{S}_i$ are the individual spins of the ASD simulation and the factor $s^2/\left[s(s+1)\right]$ accounts for the quantized nature of the spins ($s \approx \frac{3}{2}$ for Co and $s \approx 2$ for Fe). Note that direct spin-lattice coupling is not included in the model. The fast demagnetization timescales in $3d$ ferromagnets suggest that the magnetization dynamics are dominated by electron-spin coupling. In nickel, spin-lattice coupling was estimated to be an order of magnitude smaller than other coupling constants [5]. More details about the energy-conserving ASD simulations are described in Chapter 7 and the material-specific simulation parameters for Co and Fe are stated in Appendix B. With this model, both the nonequilibrium spin dynamics as well as the energy flow between electrons, spins, and the lattice can be described. The coupling between electrons and spins in the ASD simulations is governed by the damping parameter α. It determines how fast the spins react to the stochastic field of the s-LLG equation, whose amplitude in turn depends on the electronic temperature. Here, we use $\alpha = 0.01$ for Co and $\alpha = 0.005$ for Fe, which yields a good description of the experimentally measured lattice dynamics at low excitation densities as well as realistic magnetization dynamics. These values are in good agreement with recent experimental results for α [275]. Fig. 8.3.3 presents the ASD simulation results for both Co and Fe. First, we focus on the results for Co, shown in Fig. 8.3.3(a)-(e). We find excellent agreement with the experimentally measured lattice dynamics for all excitation densities. Clearly, the agreement is much better than obtained with the TTM. This finding highlights the importance of considering energy flow into and out of magnetic degrees of freedom, in agreement with our previous results for Ni presented in Chapter 7. The ASD simulation results for the magnetization dynamics of Co are presented in Fig. 8.3.3(e). The general shape of the magnetization dynamics, in particular the pronounced drop and relatively fast recovery of the magnetization, agrees well with recent experimental results [266, 276]. Regarding the demagnetization dynamics in the first hundreds of femtoseconds, the ASD simulation results reach the minimal magnetization roughly 100-200 fs faster than in reported experiments [266, 276, 14]. This could be due to deviations of the electronic distribution from a Fermi-Dirac distribution at early times after laser excitation, and due to the phenomenological electron-spin coupling in the ASD simulations. In addition, the ASD simulations describe an idealized system without defects or surface effects and assume homogeneous excitation, which can also contribute to the observed discrepancies. Regarding the magnetization recovery, we observe good agreement with results from Ref. [266] while the recovery measured by Refs. [276, 14] is slower than the ASD simulation results. It should be noted that there is some spread in the experimental results for the magnetization dynamics, even when only thin films on non-metallic substrates are considered [276, 14, 266, 199, 23, 275]. On short timescales, the measured results can contain artifacts from state-filling effects when probing optically [277, 278]. On longer timescales, magnetization dynamics can be influenced by transport effects (of electrons and phonons out of the probed region), which depend on the sample geometry. Also other macroscopic sample properties may play a role in the magnetization response. A recent study found differences in the ultrafast response depending on the orientation of the magnetization relative to the crystal lattice [266]. In principle, both the demagnetization as well as the magnetization recovery contain valuable information on the coupling strength between electrons and spins. For example, reducing α in the ASD simulations leads to a slower demagnetization, but also to a less pronounced magnetization recovery because the spin system heats less (and thus absorbs less energy) during the time when the lattice is still cold. A more precise comparison of model results to the responses of all subsystems could be obtained by measuring the lattice, magnetization, and electron dynamics on identical samples. Next, we focus on the ASD simulation results for Fe, shown in Fig. 8.3.3(f)-(j). For low fluences, we obtain excellent agreement with the experimentally measured lattice dynamics, again corroborating the strong influence of the spin dynamics on the lattice dynamics. However, the quality of agreement is not as high as for Co. Specifically, for high fluences, the simulations predict lattice dynamics that are slower than the experimental observations. In the following, we discuss possible reasons for these deviations. In our ASD simulations, the strength of the electron-spin coupling described by the damping parameter α is constant. At higher excitation densities, however, the electron-spin coupling could react to the laser-induced changes of the electronic structure. Since Fe has the largest spin heat capacity of all three elemental $3d$ ferromagnets at room temperature in combination with a rather low electronic heat capacity, its lattice dynamics are most sensitive to energy flow into and out of the spin system. Therefore, it is plausible that deviations between ASD simulations and experiments performed at high fluences are larger for Fe compared to Ni or Co. Furthermore, transient nonthermal electron and phonon distributions could contribute to the observed lattice dynamics for both Fe and Co [215, 279]. Experimentally, we observed a small apparent shift in time zero by tens of fs for high excitation densities. This could be caused by electron thermalization, which is more efficient at high excitation densities and typically enhances energy transfer to the lattice [224]. Nonthermal distributions of electrons and phonons are not accounted for by our models and including them might change the optimal α towards lower values. In addition, direct spin-lattice coupling is not included in our model, as mentioned above. Even though we expect this coupling to be weak, it constitutes another channel for energy flow to the lattice and could enhance in particular the energy flow out of the spin system. Finally, DFT calculations are ground-state calculations. After laser excitation, band structure changes (for example a transient reduction of the exchange splitting) can occur [66], which lead to changes of the electronic heat capacity and the electron-phonon coupling, especially for higher fluences. Hence, ASD simulations are expected to be most accurate for low excitation densities in general, which we observed also for Ni (see Chapter 7). Nevertheless, for low and moderate fluences, our ASD simulations offer an excellent description of the laser-induced lattice dynamics for all three $3d$ ferromagnets. Regarding the magnetization dynamics of Fe, the ASD simulation results are presented in Fig. 8.3.3(j). The initial demagnetization rate agrees well with experimental results [276]. For the magnetization recovery, different results are reported in literature [276, 151, 207, 202, 278, 262, 275], from very little or no recovery [276, 278] to almost complete recovery [151] on few-picosecond timescales. Only thin films on non-metallic substrates are considered here, which are expected to have the least transport effects. Due to the large spread of literature results, as in the case of Co, a more precise comparison of the model to the results of all three subsystems would require measuring their responses on identical samples. Based on the available experimental data, we conclude that our simulations provide a realistic description of the magnetization dynamics. Energy-conserving ASD simulations thus offer a description that is consistent with the responses of the lattice and the magnetization, which is an important step towards a complete, consistent description of the laser-induced dynamics of $3d$ ferromagnets.

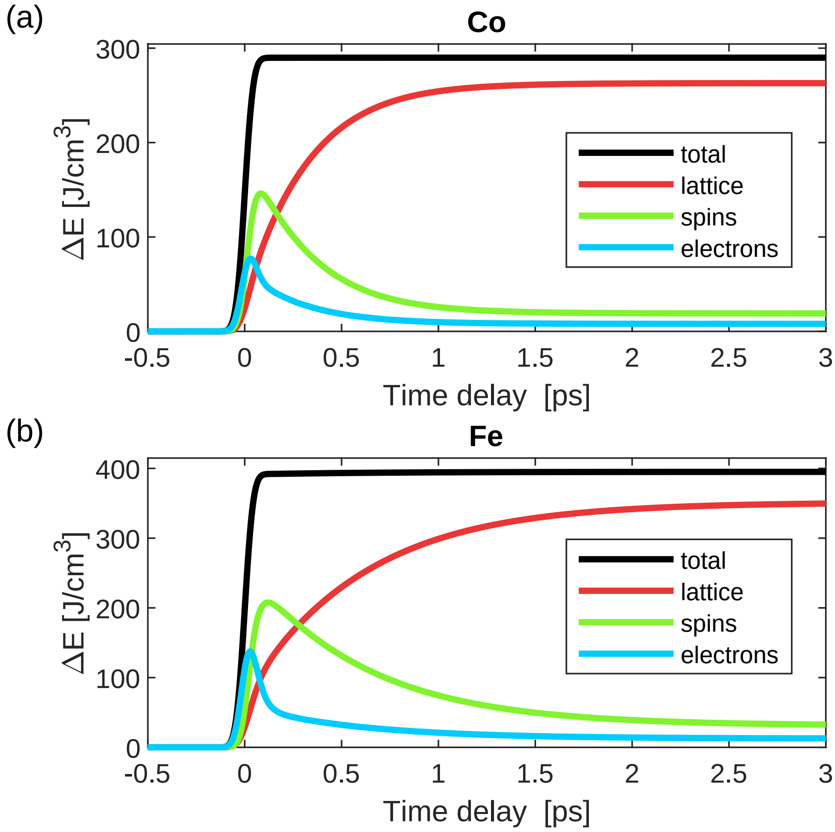

Figure 8.4.1: *Intrinsic energy flow between electrons, spins, and the lattice for (a) Co and (b) Fe. Here, results with the same excitation density as in Fig. 8.3.3(b) (Co) and Fig. 8.3.3(g) (Fe) are presented. The additional energy density ΔE in the system is displayed. After laser excitation, the total energy (black) stays constant and energy is redistributed between electronic (blue), magnetic (green), and lattice (red) degrees of freedom.*

8.4 Discussion

The good agreement of the ASD simulations with our experiments and the disagreement of the TTM show that energy flow into and out of the spin system has a significant impact on the lattice dynamics of Co and Fe. Based on the ASD simulation results, we are now able to analyze the intrinsic energy flow between electronic, magnetic, and lattice degrees of freedom in detail. The distribution of the absorbed energy between the three subsystems is presented in Fig. 8.4.1. After laser excitation, the total energy in the system stays constant, which is visualized by the black curve. From then on, energy is only redistributed between the different degrees of freedom. The laser pulse excites the electrons (blue curve), which initiates the energy flow from the electrons to the spin system (green curve). Already shortly after excitation, the spin system contains more of the additional energy than the electron system. Once spins and electrons have equilibrated and the electrons cool down further due to electron-phonon coupling, energy starts flowing back from the spin system to the electrons. In addition, energy also flows from the electrons to the lattice, such that in total, energy flows out of the electron system, although at a lower rate than during the demagnetization. Finally, thermal equilibrium is established after several picoseconds. Similar to our previous

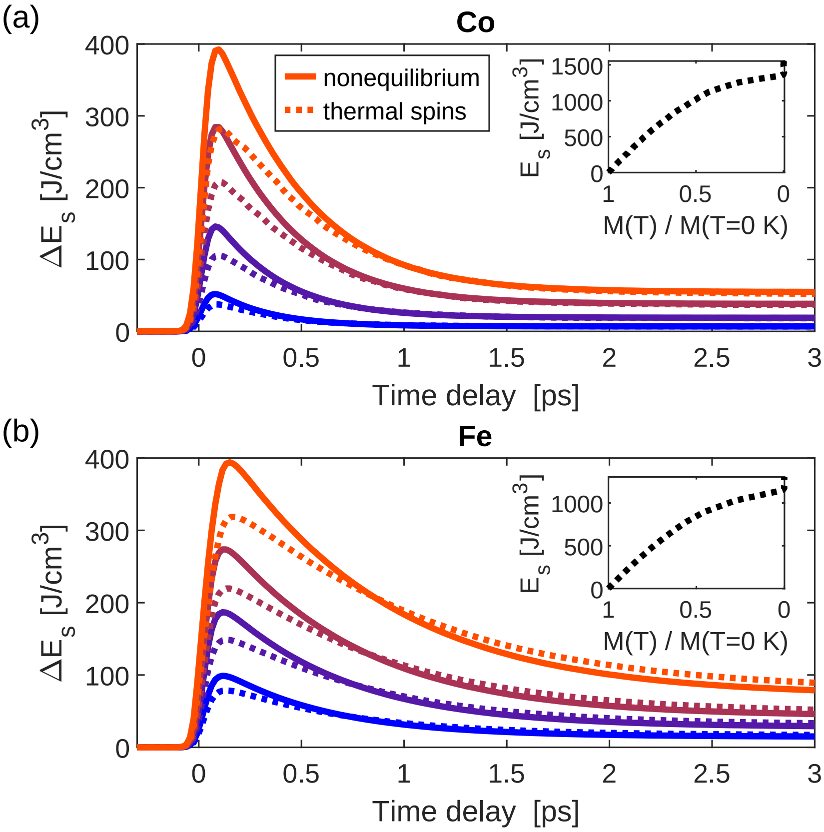

Figure 8.4.2: *Nonthermal spin dynamics for (a) Co and (b) Fe. The solid curves show the additional energy content of the spin system ΔE_s as a function of pump-probe delay for the same fluences as in Fig. 8.3.3. In contrast, the dashed curves show the additional spin energy content of a hypothetical, thermalized spin system with the magnetization dynamics from the ASD simulations, which was calculated using the equilibrium relationship between spin energy and magnetization. Differences between the solid and dashed curves indicate a nonthermal spin system. Note that the very small differences that persist on time scales larger than 3 ps are numerical artifacts, which could stem from the finite time steps in the nonequilibrium simulations or the larger α employed in the simulations of quasi-static heating. The insets show the equilibrium relationships between spin energy and magnetization.*

results for Ni, we find that also for Fe and Co, the ASD simulations predict a nonthermal spin system on short time scales after laser excitation. This is presented in Fig. 8.4.2. The additional spin energy in the system is shown as solid curves (the absorbed energy densities are the same as in Fig. 8.3.3). In addition, the dashed curves show how a thermalized spin system would behave. The thermalized case is based on the equilibrium properties of the spin system and the magnetization dynamics from the nonequilibrium simulation. We use the equilibrium relationships between magnetization and spin energy, shown in the insets of Fig. 8.4.2, to translate the magnetization dynamics from the simulations into spin energy dynamics. Comparing this result to the spin energy dynamics obtained directly from the simulations allows to identify deviations from thermal behavior: Whenever the two quantities do not coincide, the spin system is in a nonthermal state. On short time scales below ca.1̃ ps, dashed and solid curves differ, which indicates that the spin system is in a nonthermal state during this period. This nonthermal state is characterized by a relatively high spin energy content compared to the demagnetization amplitude, as the comparison between dashed and solid curves directly shows. This is analogous to our ASD simulation results for Ni and indicates that relatively many spin excitations with significant misalignment of neighboring spins are present compared to thermal equilibrium, which cost a lot of energy per magnetization reduction. The finding is corroborated by inspecting the simulated spin configuration at short time delays (see Appendix B), which exhibits disorder on small length scales, i.e. also between spins that are close to each other. For the fluences reached in our experiments, the spin system thermalizes within the first picosecond after laser excitation. In contrast, for Ni, we observed a prolonged nonthermal behavior for higher fluences. These differences between Fe, Co, and Ni are caused by their different Curie temperatures. Ni has a Curie temperature of only 631 K, while the Curie temperatures of Fe and Co are 1044 K and 1390 K, respectively [259]. As a consequence, for the same absorbed energy density, Ni demagnetizes much more than Fe or Co [276]. For stronger demagnetization of Fe or Co, a prolonged nonthermal behavior is observed as well, as shown exemplarily for Fe in Appendix B. The prolonged nonthermal behavior is found to be caused by domain formation during the remagnetization process, in agreement with previous results by Kazantseva et al. [197]. The ASD simulation results thus suggest that in particular for strong demagnetization, a thermal description of the spin system is not adequate to describe nonequilibrium dynamics of ferromagnets. In summary, according to the ASD simulations, two key aspects of ultrafast energy flow dynamics in ferromagnets are apparent: the slow-down of the lattice response caused by energy flow into and out of the spin system, and the nonthermal behavior of the spin system on short timescales. The first effect can be qualitatively reproduced with a simple 3TM as well (depending on the coupling constants, which are typically fit parameters). However, the second key aspect, the transient nonthermal excitation of the spin system, cannot be modeled with a 3TM. Therefore, we expect worse quantitative agreement of a 3TM with the ultrafast dynamics of all subsystems. Besides the ASD simulations presented here and the 3TM, another model describing the coupled energy flow dynamics of electrons, spins, and the lattice is the spin-lattice-electron dynamics (SLED) model by Ma et al. [218]. In contrast to our simulations, the SLED model employs the effective spin temperature [258] to calculate the energy flow dynamics. In order to investigate differences between the two descriptions, a comparison analogous to Fig. 8.4.2 can be made for the effective spin temperature. In our simulations, we find that on short timescales the energy content calculated using the effective spin temperature can differ from the energy of the spin system calculated using the spin Hamiltonian (see Eq. 8.3.4), in particular for iron and nickel and for high fluences. Such deviations from equilibrium relationships indicate a nonthermal behavior of the spin system, as discussed earlier. An additional difference between our model and the SLED model is that the latter includes direct spin-lattice coupling. For these two reasons, we expect qualitatively similar results for the energy flow dynamics, but quantitative differences between these two models.

8.5 Summary and conclusions

In this work, we investigated the ultrafast lattice dynamics of ferromagnetic Co and Fe using femtosecond electron diffraction. To model the intrinsic energy flow between electronic, magnetic, and lattice degrees of freedom, we combined spin-resolved DFT calculations of the electron-phonon coupling with energy-conserving ASD simulations. We found that for both

Co and Fe, the ultrafast spin dynamics have a profound impact on the lattice dynamics, slowing down the lattice heating due to energy transfer into and out of magnetic degrees of freedom. These findings generalize our previous results for Ni presented in Chapter 7, highlighting the prominent role of the spin system in the energy flow dynamics of all three elemental $3d$ ferromagnets. For a full description of the laser-induced dynamics, it is thus essential to take energy flow into and out of the spin system into account. This is achieved with energy-conserving ASD simulations, which simulate the spin dynamics while also accounting for the intrinsic energy flow between electrons, spins, and the lattice. For low and moderate fluences, the ASD simulations yielded excellent agreement with the measured lattice dynamics, as well as a good description of the magnetization dynamics for both Co and Fe. They are thus an important step towards a model for ultrafast demagnetization that is consistent with the responses of electronic, magnetic, and lattice degrees of freedom. Furthermore, we found that the ASD simulations predict a nonthermal spin system for both Co and Fe on short time scales after laser excitation. For high fluences, the nonthermal state of the spin system can last for several picoseconds, suggesting that particularly for strong excitations, a thermal description of the laser-induced spin dynamics is not sufficient. Our findings are also of relevance for other demagnetization models, since they enable the comparison to the experimental lattice dynamics for all three elemental $3d$ ferromagnets and highlight the importance of a consistent description of the energy flow dynamics. The combination of experiment and theory presented in this work can also be applied to gain insight into the ultrafast energy flow dynamics in other technologically relevant magnetic materials, e.g. magnetic oxides and layered van der Waals materials. In addition, the incorporation of the energy exchange of the spin system in the ASD simulations may prove to be invaluable for the explanation of the behavior of more complex materials and heterostructures in the future.

Appendix A: DFT calculations

The calculations of the electron-phonon energy transfer rates were performed using the DFT code ABINIT [246, 247, 248, 249, 250]. The optimized norm-conserving Vanderbilt pseudopotentials were generated using the method of Ref. [280] and are of generalized-gradient-approximation (GGA) Perdew-Burke-Ernzerhof (PBE) type [252]. 16 electrons were treated explicitly for Fe, and 17 electrons were explicitly taken into account for Co. The plane-wave expansion of the electronic wave function had a cutoff of 40 Ha for Fe and 50 Ha for Co. 22 electronic bands were calculated for Co and 15 for Fe. These bands were calculated with Fermi occupation featuring a smearing of 0.001 Ha. An unshifted k-point grid of $32 \times 32 \times 32$ points was used for both elements. The lattice constant for bcc Fe was set to 2.756 Å, which was obtained by relaxing the structure. For hcp Co, we used the experimental lattice constants $a = 2.5071$ Å and $c = 4.0695$ Å [281]. To obtain the electron-phonon coupling G_{ep}, the spin-resolved electron-phonon matrix elements were computed as described in Ref. [255] for a $8 \times 8 \times 8$ grid of q-points. From the results, we extracted the Eliashberg functions for majority and minority electrons. The electron-phonon couplings and the electronic heat capacities were then calculated as described in Ref. [241]. Following Chapter 7, we take chemical potential shifts into account and assume particle conservation within each spin type. Band shifts according to the Stoner model are not considered, since our description of magnetization dynamics with ASD simulations is based on the Heisenberg model. The results for the electronic densities of states (eDOS), the Eliashberg functions, and the electron-phonon couplings are presented in Fig. 8.5.1. The magnetic moments calculated from the spin resolved eDOS, 1.95 μ_B per atom for Co and $2.40\mu_\mathrm{B}$ per atom for Fe, are larger than the experimental results of $1.72\mu_\mathrm{B}$ and $2.22\mu_\mathrm{B}$ per atom [282]. Based on the phonon densities of states (vDOS), we also calculated the MSDs as a function of temperature, as described in Ref. [236]. To increase the accuracy of the calculation, we replaced the vDOS in the region below 5 meV by a fit with the function $f(x) = ax^2 + bx^3$. This ensures that the dominating term for very small phonon wavevectors is quadratic, which corresponds to the correct long-wavelength limit. The results were used to convert transient MSD changes to lattice temperatures (see Fig. 8.3.1(a) and (b)).

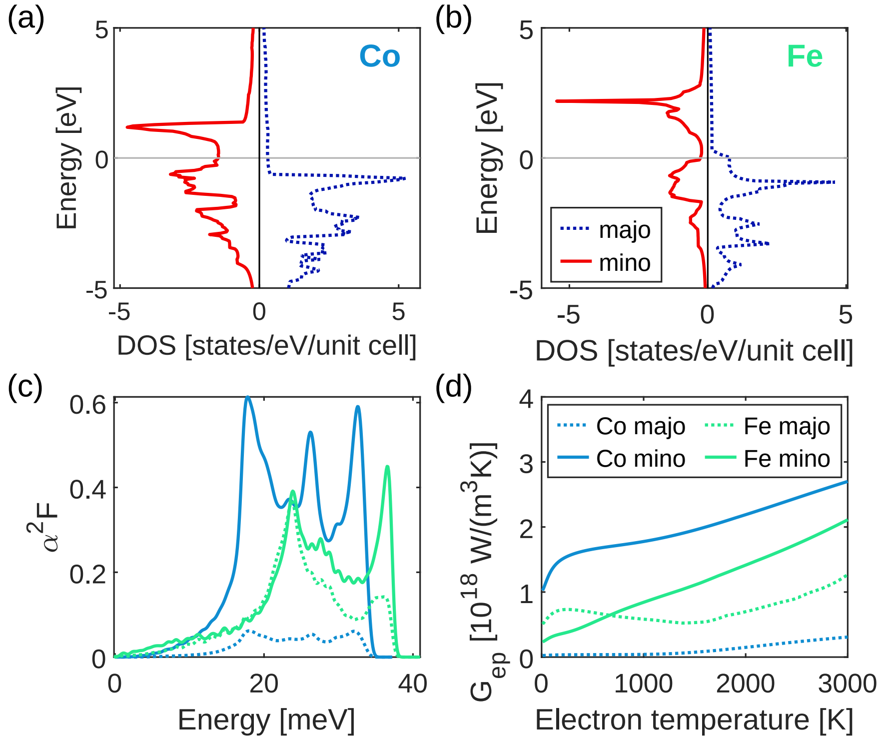

Figure 8.5.1: *Results of the spin-resolved DFT calculations. (a) Spin-split electronic density of states (eDOS) of Co. The position of the Fermi level is shown as a grey line. The majority (majo) DOS is shown in dashed blue and the minority (mino) DOS is shown in red. Note that hcp Co has two atoms per primitive unit cell. (b) Spin-split eDOS of Fe. (c) Majority and minority Eliashberg functions* α^2F *for Co (blue) and Fe (green). The dashed curves correspond to the majority Eliashberg functions and the solid curves represent the minority Eliashberg functions. (d) Majority and minority electron-phonon coupling parameter* G_ep *for Co and Fe.*

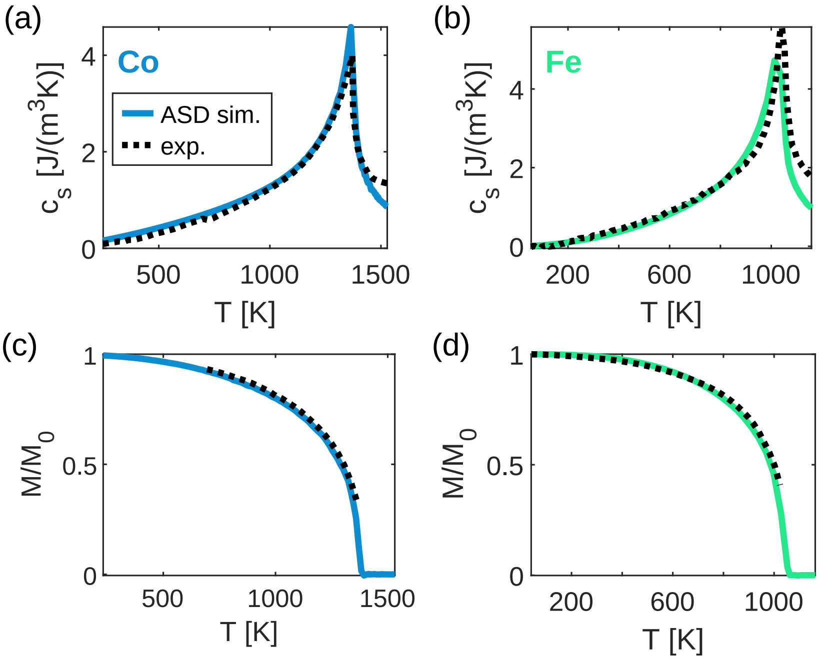

Figure 8.5.2: *ASD simulation results for equilibrium relationships and comparison to literature results. (a) Spin heat capacity of Co. The ASD simulation result (ASD sim.) is shown as a solid blue curve and the experimental result (exp.) is shown as a dashed black curve. The experimental result was obtained based on measurements of the total heat capacity from Ref. [283], which were dilation-corrected using the expansion coefficients from Ref. [284]. To obtain the spin heat capacity, the DFT results for the electronic and lattice contributions were subtracted. (b) Same as (a) but for Fe. (c) Magnetization as a function of temperature for Co. The solid curve shows the ASD simulation result. The dashed black curve is a literature result from Ref. [259]. The magnetization is normalized to its value at 0 K. (d) Same as (c), but for Fe.*

Appendix B: Atomistic spin dynamics simulations

Atomistic spin dynamics simulations use a classical Heisenberg spin model:

$$\mathcal{H} = -\sum_{i<j} J_{ij}\mathbf{S}_i \cdot \mathbf{S}_j - \sum_i d_z S_z^2. \tag{8.5.1}$$

with $\mathbf{S}_i$ representing a classical, normalized spin vector at site i. Each spin couples to its neighboring spin vectors $\mathbf{S}_j$ via the coupling constant J_{ij}. The second term of the Hamiltonian (Eq. 8.5.1) describes the on-site anisotropy with an easy-axis along the z-axis and constant anisotropy energy. All parameters are material-dependent and listed in Table 1. Except α, they are based on Ref. [83]. The simulations are performed on a simple cubic (sc) lattice. This has no significant effect on the energy flow or magnetization dynamics, which was verified directly by comparing simulations of body-centered cubic (bcc) and sc Fe. The reason is that for a given Curie temperature, the different number of neighbors in each case is compensated by a different value of J. Note that in contrast to the samples employed in the diffraction experiments, the ground state in the ASD simulations is a single-domain state. Due to the typical time and energy scales of domain wall dynamics, we don't expect

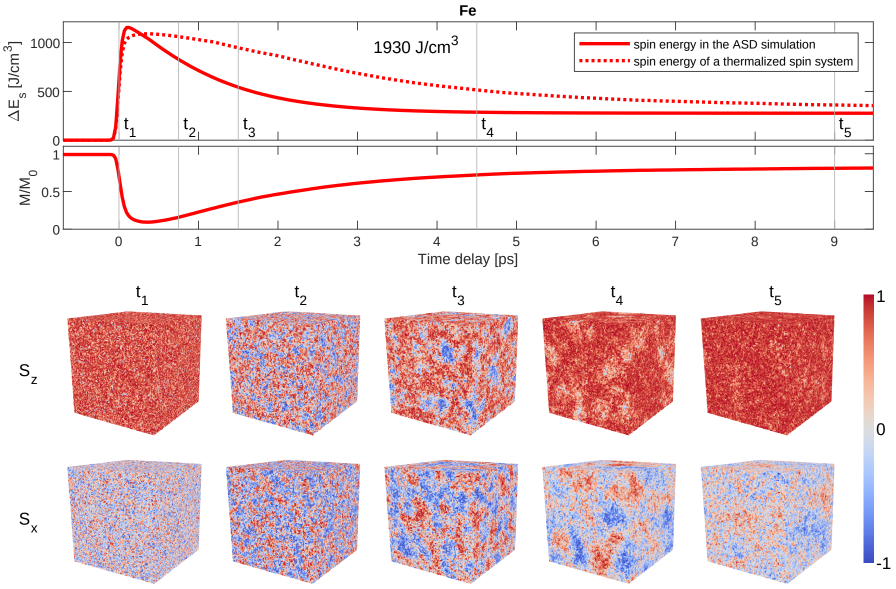

Figure 8.5.3: *Details about the spin configuration at selected time delays from an ASD simulation of Fe at a high excitation density. The upper panel shows the additional spin energy as a function of pump-probe delay (solid curve) for an absorbed energy density of* $1930\,J/cm^3$. *The dashed curve corresponds to the energy content of a thermalized spin system with the magnetization dynamics from the ASD simulations (shown directly below), analogous to Fig. 8.4.2. Note that for illustration purposes, we used a higher damping parameter of* $\alpha = 0.1$ *for the simulations shown here, and a spin system consisting of* $100 \times 100 \times 100$ *spins. Due to the relatively high fluence, the spin system exhibits a nonthermal behavior also on few-picosecond timescales. The lower part of the figure shows the spin configurations at different pump-probe delays. The spin components* S_x *and* S_z *are displayed, normalized to 1.* S_y *behaves analogously to* S_z *for symmetry reasons. Here, only the surface of the cube is visible. The inside of the cube displays an analogous behavior to the surface.*

Table 1: *ASD simulation parameters for Co and Fe.*

	Co		Units	Fe		Units
J	6.324	$\times 10^{-21}$	[J]	4.8	$\times 10^{-21}$	[J]
d_z	0.67	$\times 10^{-23}$	[J]	0.5	$\times 10^{-23}$	[J]
μ_s	1.72		[μ_B]	2.2		[μ_B]
α	0.01			0.005		

a significant influence of the domain structure on the intrinsic energy flow dynamics studied here. By solving the stochastic-Landau-Lifshitz-Gilbert (s-LLG) equation

$$\frac{(1+\alpha^2)\mu_s}{\gamma}\frac{\partial \mathbf{S}_i}{\partial t} = -\left(\mathbf{S}_i \times \mathbf{H}_i\right) - \alpha\left(\mathbf{S}_i \times \left(\mathbf{S}_i \times \mathbf{H}_i\right)\right) \tag{8.5.2}$$

numerically, the dynamics of the system are calculated [72]. Here $\gamma = 1.76 \cdot 10^{11} \frac{1}{Ts}$ refers to the gyromagnetic ratio and $\mathbf{H}_i$ describes the effective field derived via $\mathbf{H}_i = -\frac{\partial \mathcal{H}}{\partial \mathbf{S}_i}$. The material-dependent and phenomenological damping parameter α determines the coupling strength of the spin system to the electron system and thus the energy transfer rate between the two heat baths. In order to simulate the effects of finite temperatures, a Langevin thermostat is included by adding a field-like stochastic term $\boldsymbol{\zeta}_i$ to the effective field $\mathbf{H}_i = \boldsymbol{\zeta}_i(t) - \frac{\partial \mathcal{H}}{\partial \mathbf{S}_i}$. The added noise term has white noise properties [97]:

$$\langle \boldsymbol{\zeta}_i(t) \rangle = 0 \quad \text{and} \quad \langle \boldsymbol{\zeta}_i(0) \boldsymbol{\zeta}_j(t) \rangle = 2\alpha k_{\mathrm{B}} T_{\mathrm{el}} \mu_s \delta_{ij} \delta(t)/\gamma. \tag{8.5.3}$$

In order to better reproduce experimentally measured equilibrium properties such as magnetization and heat capacity, we make use of a rescaled temperature model, which utilizes a slightly modified electron temperature T_{sim} for the noise generation. In addition to the equilibrium properties, the rescaled temperature model also yields a better description of nonequilibrium dynamics [230]. Further details are available in Ref. [230] and Chapter 7. A major advantage of ASD simulations is that they are not limited to a thermal description of the spin system, since the spins are simulated directly. Fig. 8.5.3 shows the evolution of the spin energy content and a direct visualization of the simulated spin dynamics for a relatively high fluence of $1930 J/cm^3$. In addition, for illustration purposes, a simulation with a higher damping of $\alpha = 0.1$ is shown. A higher damping leads to a larger disorder of the spin system directly after excitation, however, the qualitative behavior displayed in Fig. 8.5.3 is also observed for lower values of the damping parameter at high fluences. The comparison of the simulated spin energy content (solid curve) to the energy content of a thermalized spin system with the simulated magnetization dynamics reveals that the spin system remains in a nonthermal state for several picoseconds. At short time delays, the nonthermal state is characterized by a relatively large spin energy content compared to the demagnetization amplitude. The behavior reverses on longer time scales. Further insights on these nonthermal states can be gained from the visualization of the spin dynamics. The instantaneous spin configuration is illustrated exemplarily for several delays after excitation. During and directly after excitation, e.g. at $t_1 = 0$ ps, there is significant short-range disorder in the spin system, i.e. significant misalignment between neighboring spins. According to the Heisenberg Hamiltonian, this comes with a significant energy cost and thus leads to the relatively large energy content of the spin system. On longer time scales, the magnetization recovers. However, for high fluences/strong demagnetization, domains form. This is already visible at $t_2 = 0.75$ ps. There are areas with significant magnetization in which the spins point predominantly in the x- or y-direction (note that in Fig. 8.5.3, each spin is normalized such that $S_x^2 + S_y^2 + S_z^2 = 1$). This behavior is similar to spin simulation results reported in Ref. [197]. Within a domain, spins are parallel. Therefore, the energy cost of this spin configuration is relatively low. Nevertheless, due to the different directions of the magnetization, the global magnetization is reduced. In the beginning, the domains are relatively small. As time progresses, the domains become larger (see $t_3 = 1.5$ ps and $t_4 = 4.5$ ps) and eventually disappear (see $t_5 = 9$ ps) as the spin system approaches thermal equilibrium. Note that for low fluences, domain formation as illustrated in Fig. 8.5.3 doesn't occur, since it requires significant initial disordering of the spin system. The initial nonthermal disorder of the spin system, visualized in Fig. 8.5.3 for t_1 and characterized by a large number of high-energy spin excitations, occurs for all fluences (see also Fig. 8.4.2).

Chapter 9

Summary and Outlook

In this thesis, laser-induced ultrafast demagnetization and switching dynamics have been studied by means of atomistic spin-dynamics simulations utilizing a semiclassical spin model. The dynamics of the model have been calculated numerically using the stochastic Landau-Lifshitz-Gilbert equation of motion. The obtained results have been compared with experimental measurements performed by collaborators from the University of California in Berkeley and at the Fritz-Haber Institute in Berlin, as well as with previously published data.

In Chapter 3, simulation results are presented on switching of various ferrimagnetic GdFeCo-alloys using a wide range of pulse durations. It was found that single pulse all-optical switching is possible for pulse durations over two orders of magnitude. However, the available parameter space in terms of energy and Gd concentrations shrinks for longer pulse durations. Furthermore, element-specific damping was found to be a key parameter for switching using longer pulse durations. The same underlying physics, based on atomistic spin-dynamics simulations, is able to describe switching within hundreds of femtoseconds as well as tens of picoseconds.
Furthermore, the simulation results have been compared to TR-MOKE measurements, yielding quantitative agreement for different pulse durations and over different alloy compositions when including local Gd-concentration inhomogeneities. Using an ideal set of parameters, switching durations of up to 14 ps could be achieved. The performed studies help to better understand the conditions necessary for electric pulse switching for possible technological applications, as these electric stimuli cannot be generated on a femtosecond scale.

In Chapter 4, results on the investigation of the Heusler alloy $\mathrm{Mn_2Ru_xGa}$, based on an atomistic spin model, which was developed within this thesis, are presented. The work consisted of two parts, where at first the material itself and its equilibrium properties were modeled based on various previously reported experimental measurements. The derived model is able to reproduce various key material properties, such as the Curie temperature, the magnetization curve or the Ru-concentration dependence of the magnetization-compensation temperature. In the second part the switching of $\mathrm{Mn_2Ru_xGa}$ was investigated using the previously derived material parameters. The model has been shown to be able to quantitatively reproduce the magnetization dynamics of single pulse toggle switching as measured by Banerjee *et al.* [1]. It was also demonstrated that, contrary to previous understanding coming from rare-earth transition metal alloys, toggle switching in $\mathrm{Mn_2Ru_xGa}$ is possible even when both Mn sublattices demagnetize at very similar rates.

However, right now theoretical modeling of Mn_2Ru_xGa still suffers from uncertainties on the material parameters. As described in Chapter 4, important parameters, such as the Curie temperature vary by up 50 %, which is not the case for GdFeCo. This makes it hard to model and understand this alloy completely. For further theoretical work and for an improved modeling more reliable parameters, determined in experiments or via ab-initio calculations, are needed.

After investigating the ferrimagnets GdFeCo and Mn_2Ru_xGa a general study of switching and magnetization dynamics in ferrimagnetic materials was performed. A general macroscopic theory for the magnetization dynamics of ferrimagnetic materials driven by femtosecond laser photo excitation was derived. The results are presented in Chapter 5. The theory reproduces all stages of the switching process observed in experiments. The developed model has been directly compared to atomistic spin-dynamics simulations for GdFeCo and for Mn_2Ru_xGa alloys utilizing the parameters derived in the previous chapter. It has been established that during the switching process the magnetization dynamics transits from a relativistic relaxation path to an exchange-dominated regime due to the strong enhancement of the exchange relaxation. Furthermore, it has been shown that switching occurs when the sublattice magnetization reaches a threshold value.

Chapter 6 focuses on the different magnetic responses of antiferromagnets and ferromagnets. In experiments it is difficult to systematically compare the magnetic response of the two magnetic orderings in the same system. Therefore, atomistic spin-dynamics simulations have been used, as they allow for the manipulation of the Heisenberg exchange by simply reversing the sign of the exchange while keeping all other material parameters unchanged. Furthermore, the previously developed macroscopic model for ferrimagnets was applied to antiferromagnets, as a special case of ferrimagnets. This yielded in an equation of motion for the antiferromagnetic magnetic order that predicted an intrinsic faster dynamics of antiferromagnets compared to ferromagnets. By means of atomistic spin-dynamics simulations it has been demonstrated that the ultrafast magnetic order dynamics in antiferromagnets is exchange-enhanced compared to ferromagnets with the same system parameters. Notably, the exchange enhancement strongly depends on the number of neighboring spins of the other sublattice to which a spin is coupled. For instance, a noticeable difference was found between the demagnetization speed of 2D antiferromagnets compared to a fcc antiferromagnet.
This finding raises the question of how the number of neighboring ferrimagnetic spins affects the ease of switching. The discovered demagnetization-speed differences in antiferromagnets suggest that the ability to switch a ferrimagnet also depends on the number of neighboring spins. In the future, atomistic spin-dynamics simulations could be used again to investigate this problem, as they allow for the simulation of materials with identical system parameters but with a different number of neighbors.

In the last two chapters, results are reported on spin-dynamics simulations of nickel, cobalt and iron utilizing ab-initio calculations of electron-phonon interactions. The resulting dynamics has been compared to experimental measurements of the lattice response in order to obtain a full picture of the dynamics in ferromagnetic nickel following laser excitation. It was found that the energy flow to and from the spin system leads to a significant slowdown of the lattice dynamics. The spin system is the dominant heat sink in the initial few hundreds of femtoseconds. Consequently, it is paramount to include the energy flow to and from the spin system in any description of the laser-induced dynamics. The comparison with available experimental data for the electronic, lattice and spin dynamics shows that

the atomistic spin-dynamics simulations achieve a quantitative description of all three subsystems. The study presents a consistent description of the coupled energy flow between all three subsystems and of the magnetization dynamics and represents an improvement on the three-temperature model used by Beaurepaire and Koopmans [5, 14].
In the future, the precision of this comparison could be improved further by measuring the response of all three subsystems on identical samples.

Publication List

- F. Jakobs, T. A. Ostler, C.-H. Lambert, Y. Yang, S. Salahuddin, R. B. Wilson, J. Gorchon, J. Bokor, and U. Atxitia, Unifying femtosecond and picosecond single-pulse magnetic switching in Gd-Fe-Co, *Physical Review B* **103**, p. 104422, (Mar 2021).
- F. Jakobs, and U. Atxitia, Atomistic spin model of single pulse toggle switching in $\mathrm{Mn_2Ru}_x\mathrm{Ga}$ Heusler alloys, *Applied Physics Letters* **120**, p. 172401, (Apr 2022).
- F. Jakobs, and U. Atxitia, Universal Criteria for Single Femtosecond Pulse Ultrafast Magnetization Switching in Ferrimagnets, *Physical Review Letters* **129**, p. 037203, (Jul 2022).
- F. Jakobs, and U. Atxitia, Bridging atomistic spin dynamics methods and phenomenological models of single-pulse ultrafast switching in ferrimagnets, *Physical Review B* **106**, p. 134414, (Oct 2022).
- F. Jakobs, and U. Atxitia, Exchange-enhancement of the ultrafast magnetic order dynamics in antiferromagnets, arXiv:2206.05783, (Jun 2022).
- D. Zahn, F. Jakobs, Y. W. Windsor, H. Seiler, T. Vasileiadis, T. A. Butcher, Y. Qi, D. Engel, U. Atxitia, J. Vorberger, and R. Ernstorfer, Lattice dynamics and ultrafast energy flow between electrons, spins, and phonons in a 3d ferromagnet, *Physical Review Research* **3**, p. 023032, (Apr 2021).
- D. Zahn, F. Jakobs, H. Seiler, T. A. Butcher, D. Engel, J. Vorberger, U. Atxitia, Y. W. Windsor, and R. Ernstorfer, Intrinsic energy flow in laser-excited $3d$ ferromagnets, *Physical Review Research* **4**, p. 013104, (Feb 2022).
- J. Zázvork, F. Jakobs, D. Heinze, N. Keil, S. Kromin, S. Jaiswal, K. Litzius, G. Jakob, P. Virnau, D. Pinna, K. Everschor-Sitte, L. Rózsa, A. Donges, U. Nowak, and M. Kläui, Thermal skyrmion diffusion used in a reshuffler device, *Nature Nanotechnology* **14**, p. 658-661, (Jul 2019).
- A. Donges, N. Grimm, F. Jakobs, S. Selzer, U. Ritzmann, U. Atxitia, and U. Nowak, Unveiling domain wall dynamics of ferrimagnets in thermal magnon currents: Competition of angular momentum transfer and entropic torque, *Physical Review Research* **2**, p. 013293, (Mar 2020).

Chapter 10

Appendix

A10.1 Bridging atomistic spin-dynamics methods and phenomenological models of ingle pulse ultrafast switching in ferrimagnets

The results of this chapter have been published in

- F. Jakobs, and U. Atxitia, Bridging atomistic spin dynamics methods and phenomenological models of single-pulse ultrafast switching in ferrimagnets, *Physical Review B* **106**, p. 134414, (Oct 2022).

and the content of this chapter is in large parts identical with the published work.
Since most of the concepts explored in this work have already been presented previously in chapter 2 and chapter 5 this work was moved to the appendix.

The published version can be found at `https://doi.org/10.1103/PhysRevB.106.134414`

A10.1.1 Introduction

Since its experimental discovery [24], the theoretical description of laser induced all-optical switching (AOS) of the magnetization in GdFeCo ferrimagnetic alloys has remained a challenge. Despite intense experimental and theoretical research in the field [24, 163, 6, 32, 126, 158, 20, 135, 116, 165, 127, 26], an established and unified picture of the process is still missing. Experimental findings are mostly compared or interpreted in terms of atomistic spin dynamics simulations [132, 128, 285, 41] (see chapter 3), multisublattice spin dynamics based on symmetry arguments [126, 118, 119], and based on the Landau-Lifshitz-Bloch equation [171, 286, 134]. The main goal of the present work is the revision, extension and merging of these approaches into a unified model.

Atomistic spin dynamics (ASD) models have been used before to quantitatively describe ultrafast dynamics in $3d$ transition metals (see chapter 7 and chapter 8) and $4f$ rare-earth ferromagnets [114, 109]. They have also been used in GdFeCo, to describe the equilibrium thermal properties [132], the thermal character of AOS [32], the so-called transient ferromagnetic-like state [6], the demonstration of spin-current-mediated rapid magnon localisation and coalescence [133] and the possibility of AOS using picosecond-long laser pulses (see chapter 3). Results from atomistic spin models also compare qualitatively well to an analytical theory based on the excitation of spin-wave exchange modes [135], provide insights for optimal electron, phonon and magnetic characteristics for low energy switching [287] and predict maximum repetition rate using two consecutive laser pulses [288]. More sophisticated, orbital-resolved atomistic models provide insights on the role of the intra-exchange coupling between $4f$ and $5d$ electrons in the dynamics of GdFeCo alloys[128]. Atomistic models can naturally describe switching in Gd/Fe multilayers composed of very thin layers [144, 33]. Recent observations [45, 1] of single pulse switching in $\mathrm{Mn_2Ru}_x\mathrm{Ga}$ alloys are also well-described by ASD methods (see chapter 5). Despite the demonstrated success in modeling AOS, ASD simulation results are cumbersome to interpret without an analytical model that unveils the role of the different processes and interactions during the switching process. This potential semi-analytical model has to capture most of the features of the ASD simulations. Semi-phenomenological models describing switching already exist. A macroscopic theory for the description of the dynamics and relaxation of the macroscopic (sublattice) magnetization of ferromagnets and antiferromagnets was developed originally by Baryakhtar [289, 116]. An extension of such phenomenology to ferrimagnets in the context of ultrafast spin dynamics was introduced in Ref. [126]. At the ultrafast scale, magnetization dynamics are dominated by atomic scale spin excitations, these spin dynamics are driven by dissipative processes which in ferrimagnets are two-fold, relativistic and exchange driven. Relativistic processes allow for exchange of angular momentum between the spins and lattice degree of freedom due to the presence of spin-orbit interaction connecting them. Exchange processes can arise due to transport of spin angular momentum – spin and magnon transport – which is the only mean to exchange angular momentum in ferromagnets. In multisublattice magnets another, different pathway opens, namely, local exchange of angular momentum. To account for such local exchange processes in ferrimagnets, the equation of motion for the magnetization dynamics proposed by Landau and Lifshitz [87] is enhanced by an exchange relaxation term [126, 119, 116, 290]. Within this macroscopic model, the exchange relaxation dominates the dynamics when the magnetic sublattices are driven into mutual non-equilibrium. Qualitative agreement to experiments in two-sublattice magnets has been demonstrated [119], such as AOS in ferrimagnetic GdFeCo using fs laser pulses [126] and ps laser pulses [131], AOS in Heusler semimetals $\mathrm{Mn_2Ru}_x\mathrm{Ga}$ [46], or element-specific demagnetization of ferromagnetic NiFe alloys [118]. Quantitative comparison of this model to neither experiments nor ASD simulations have been conducted so far. While the arguments behind such phenomenology are robust, the range of applicability and the validity of the model parameters could be questioned. For instance, the parameters defining the relativistic and exchange relaxation are assumed to be constant and of the same order. The magnetic free energy functional is calculated for near thermal equilibrium states. This implies a relatively strong coupling to the heat-bath, while switching conditions are supposedly fulfilled when exchange relaxation between sublattices dominates over the relaxation to the heat-bath. An alternative macroscopic model directly derived from an atomistic spin model has also been proposed. This model is based in the Landau-Lifshitz-Bloch (LLB) equation of motion [173, 291, 171, 292, 293]. The LLB model for two-sublattice magnets [171, 292] has been used in the context of AOS in GdFeCo, e.g. the element-specific demagnetization rates compare well to experiment, and it predicts that near the magnetic phase transition the otherwise slower Gd sublattice becomes faster than Fe [134], as recently observed [294]. The LLB model has been demonstrated to provide accurate analytical expressions for the temperature dependence of the relativistic relaxation parameter as well as for the non-equilibrium effective fields below and above the critical temperature [292]. Moreover, the LLB model also describes the transverse motion of the magnetization. This makes it the preferred model for computer simulations of heat-assisted magnetic recording [169] and realistic description of all-optical switching [295], and ultrafast spintronics, such as domain wall motion [296, 297] or skyrmion creation by ultrafast laser pulses [298]. So far the LLB model and Baryakhtar-like models have been considered as complementary approaches. Here, we merge them into one unified approach. In this work we address the issues discussed above by directly comparing both phenomenological models to ASD simulations. We do so since ASD simulations have been already quantitatively compared to experiments in literature. We find that quantitative comparison between ASD and both phenomenological models is partially possible for laser excitation producing small deviation from equilibrium. However, those models hardly reproduce magnetic switching using the same parameter values describing the relaxation of small perturbations. Here, based upon those phenomenological models, we propose a macroscopic model that compares precisely to the magnetization dynamics calculated using ASD simulations, including element-specific magnetization relaxation and switching. This model bridges atomistic spin dynamics based models and previously proposed phenomenological models. Notably, it provides a deeper understanding to the parameters entering the phenomenological models and sheds some light into the process of ultrafast switching in ferrimagnets. The work is broken down in the following way: in Sec. A10.1.2, we present the atomistic spin model for the calculation of the magnetic equilibrium properties and non-equilibrium dynamics. The equilibrium properties are compared to a mean field model. We then provide atomistic calculations of the ultrafast magnetization dynamics with input from the two temperature model. These results are the basis for the comparison to the phenomenological models presented in Sec. A10.1.3. Firstly, we present the Baryakhtar model and the Landau-Lifshitz-Bloch model. Secondly, we compare the ultrafast magnetization dynamics calculated with those models to the atomistic spin dynamics results. Finally, in Sec. A10.1.3 we present the unified phenomenological model, a hybrid model combining Baryakhtar and LLB models, and its comparison to atomistic spin dynamics.

A10.1.2 Atomistic Spin Model

Ferrimagnetic materials characterise by spontaneous magnetization as a resultant of two or more components of non-parallel magnetic moments [40]. Atomistic spin models based on the Heisenberg Hamiltonian can be considered one of the simplest microscopic models able to reproduce the equilibrium properties of ferrimagnets. The spin system energy due to only the exchange interactions can be described by an effective Heisenberg model:

$$\mathcal{H} = -\sum_{i\neq j} J_a \mathbf{S}_{a,i}\cdot\mathbf{S}_{a,j} - \sum_{i\neq j} J_b \mathbf{S}_{b,i}\cdot\mathbf{S}_{b,j} - \sum_{i\neq j} J_{ab}\mathbf{S}_{a,i}\cdot\mathbf{S}_{b,j} \tag{A10.1.1}$$

where $J_{a(b)(ab)}$ is the exchange constant between neighboring sites represented by two classical spin vectors $\mathbf{S}_i$ and $\mathbf{S}_j$ ($|\mathbf{S}| = 1$). Further, we include magnetic anisotropy terms to Eq. (A10.1.1) to set a preferential axis for the magnetization to switch about. However, since the anisotropy energy is relatively low in comparison to the exchange energy, at the picosecond time scale it plays a marginal role in the switching process. This makes for a simpler Hamiltonian and a more direct comparison to the phenomenological models. To model a ferrimagnet, one needs to consider two alternating sublattices of unequal and antiparallel moments, with three exchange coupling constants: ferromagnetic for each sublattice (J_a and J_b) and a third for the antiferromagnetic interaction between them, J_{ab}. For instance, GdFeCo alloys are composed of a transition metal FeCo and a Gd rare-earth sublattices. We

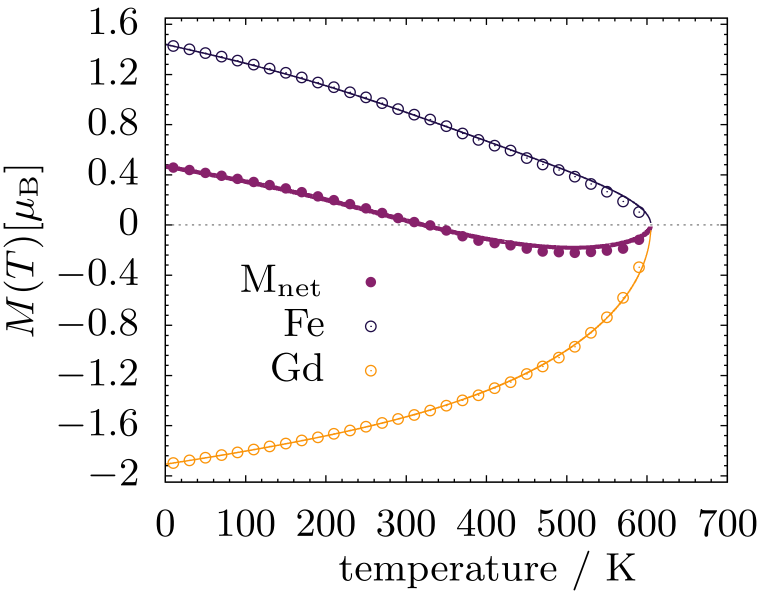

Figure A10.1.1: *Equilibrium magnetization of a GdFeCo alloy for Gd concentration,* $x_{\rm Gd} = 25\%$*. Element-specific normalized equilibrium magnetization and net equilibrium magnetization,* $M(T) = x_{\rm Gd}\mu_{\rm Gd}m_{\rm Gd} - x_{\rm Fe}\mu_{\rm Fe}m_{\rm Fe}$*, where* $\mu_{\rm Gd(Fe)}$ *is the atomic magnetic moment of Gd(Fe). Lines correspond to the mean-field approximation with renormalized exchange parameters. Symbols correspond to atomistic spin dynamics simulations.*

model the Fe and Co spins as only one magnetic sublattice, and we assume a common atomic magnetic moment of $\mu_{\rm FeCo} = 1.94\mu_{\rm B}$. In these alloys the rare-earth impurities add localised $4f$ spins to the system assumed to be, $\mu_{\rm Gd} = 7.6\mu_{\rm B}$. The amorphous nature of GdFeCo is modelled by using a simple cubic lattice model but with random placements of Gd moments within the lattice to the desired concentration. The applicability of the Heisenberg approximation relies on the stability of local moments under rotation and at high temperature where Stoner excitations are generally weak [229]. It is assumed that the electronic properties are temperature-independent in the range where the system is magnetically ordered.

Atomistic spin dynamics

Equilibrium and non-equilibrium element specific magnetic properties of a ferrimagnet are calculated using atomistic spin dynamics simulations which are based in the stochastic-Landau-Lifshitz-Gilbert equation (s-LLG) [72]

$$(1+\lambda_i^2)\mu_{s,i}\dot{\mathbf{S}}_i = -\gamma\mathbf{S}_i\times\left[\mathbf{H}_i - \lambda_i\ (\mathbf{S}_i\times\mathbf{H}_i)\right], \tag{A10.1.2}$$

where γ is the gyromagnetic ratio, and λ_i is the so-called phenomenological sublattice specific damping parameter. By including a Langevin thermostat the spin dynamics including statistical – equilibrium and non-equilibrium thermodynamic properties can be obtained. An effective field-like stochastic term $\boldsymbol{\zeta}_i$ is added to the effective field $\mathbf{H}_i = \boldsymbol{\zeta}_i(t) - \frac{\partial\mathcal{H}}{\partial\mathbf{S}_i}$, with white noise properties [97]: $\langle\boldsymbol{\zeta}_i(t)\rangle = 0$ and $\langle\boldsymbol{\zeta}_i(0)\boldsymbol{\zeta}_j(t)\rangle = 2\lambda_i k_{\rm B}T\mu_{s,i}\delta_{ij}\delta(t)/\gamma$. The variance of the Langevin noise is chosen such that the fluctuation-dissipation theorem is full filled.

Mean-field approximation

Exact analytical expressions for the $M(T)$ curve are cumbersome to derive due to the many body character of the problem. Here we resort the mean field approximation (MFA), already used in previous works [132, 135, 299]. We note that to be able to apply the MFA for the GdFeCo impurity model, and thus translation non-symmetric with respect to spin variables $\mathbf{S}_i$, we need to transform the Heisenberg Hamiltonian to a symmetric one. We use the spin analogy of the virtual crystal approximation (VCA) to transform the disordered lattice Hamiltonian $\mathcal{H}$ to a symmetric VCA Hamiltonian $\mathcal{H}_{\mathrm{VCA}}$. Within the VCA we evaluate the effective sublattice exchange parameters, given by the sum of the exchange interactions of a given spin at a site $\mathbf{r}_i$ of sublattice i with all other atoms of this sublattice. This involves weighting the exchange parameters by the relative composition, $x_i \equiv$ concentration species i [135],

$$J_i = \sum_{\mathbf{r}_i,\mathbf{r}'_i} J(\mathbf{r}_i,\mathbf{r}'_i) \underbrace{\equiv}_{\mathrm{VCA}} x_i J(\mathbf{r}_i,\mathbf{r}'_i) \quad \text{intrasublattice} \tag{A10.1.3}$$

whereas the intersublattice effective exchange reads

$$J_{ij} = \sum_{\mathbf{r}_i,\mathbf{r}'_j \notin A_i} J(\mathbf{r}_i,\mathbf{r}'_j) \underbrace{\equiv}_{\mathrm{VCA}} x_i J(\mathbf{r}_i,\mathbf{r}'_j) \quad \text{intersublattice} \tag{A10.1.4}$$

Thus the VCA Hamiltonian reads

$$\mathcal{H}_{\mathrm{VCA}} = \sum_{j\in A_i} J_i \mathbf{S}_i \cdot \mathbf{S}_j + \sum_{j\notin A_i} J_{ij} \mathbf{S}_i \cdot \mathbf{S}_j \tag{A10.1.5}$$

where A_i represent the magnetic sublattice of the spin $\mathbf{S}_i$. In the exchange approximation we define the MFA field as

$$\mu_a H_a^{\mathrm{MFA}} = z_a J_{aa} m_a + z_{ab} J_{ab} m_b \tag{A10.1.6}$$

The element-specific equilibrium magnetization is calculated via the self-consistent solution of $m_a = L(\beta\mu_a H_a^{\mathrm{MFA}})$ and $m_b = L(\beta\mu_b H_b^{\mathrm{MFA}})$. z_a and z_{ab} correspond to the number of first nearest neighbours of type a and b, respectively. It is well-known that the MFA overestimates the value of the critical temperature T_C. However, a very good agreement between ASD and MFA can be obtained by using a reduced value for the exchange parameters, even for multilattice magnets [299]. Figure A10.1.1 shows element-specific $M_a = x_a\mu_a m_a(T)$ using ASD simulations and renornalized MFA for $x_{\mathrm{Gd}} = 25\%$. Net magnetization is also shown in Fig. A10.1.1, which is defined as $M(T) = x_{\mathrm{Gd}}\mu_{\mathrm{Gd}}m_{\mathrm{Gd}} - x_{\mathrm{Fe}}\mu_{\mathrm{Fe}}m_{\mathrm{Fe}}$. The agreement between ASD and MFA is good enough for all the temperature regions. We observe the presence of compensation temperature T_{M} at room temperature for $x_{\mathrm{Gd}} = 25\%$ at which the thermally average magnetization of both sublattices are equal but opposite, so that the magnetization of the system is equal to zero $M(T_{\mathrm{M}}) = 0$. The mapping of the atomistic spin model and the corresponding mean-field approximation turns out to be necessary for a quantitative comparison to the phenomenological models, and thereby paramount for the unification of both pictures.

Two Temperature Model

Single pulse all-optical switching has been demonstrated to be a thermal process in ferrimagnetic GdFeCo alloys [32] and in $\mathrm{Mn_2Ru}_x\mathrm{Ga}$ Heusler semi-metals [45]. Ultrafast heating by optical or electric means are sufficient to achieve switching in specific GdFeCo alloys [35]. Although the minimum achievable duration of the electric pulses are limited to picoseconds, those are better suited for potential integration into applications. Laser pulses can be as short as only a few femtoseconds, which permits to excite the electron system in timescales of the order of the exchange interaction allowing for the investigation of fundamental physics governing switching. In this work, we center in excitation of the ferrimagnetic GdFeCo using femtosecond laser pulses. When a metallic ferrimagnetic thin film is subjected to a near infrared laser pulse, only the electrons are accessible by the photon electric field. Initially, the absorbed energy is barely transferred to the lattice and consequently the electron system heats up. The electron and phonon temperatures are decoupled for up to several picoseconds until the electron-phonon interaction equilibrates the two heat-baths. This phenomenology is well captured by the so-called two-temperature model (2TM) [102, 110] which can be written as two coupled differential equations:

$$C_{\mathrm{el}}\frac{\partial T_{\mathrm{el}}}{\partial t} = -g_{\mathrm{ep}}\left(T_{\mathrm{el}} - T_{\mathrm{ph}}\right) + P_l(t) \tag{A10.1.7}$$

$$C_{\mathrm{ph}}\frac{\partial T_{\mathrm{ph}}}{\partial t} = +g_{\mathrm{ep}}\left(T_{\mathrm{el}} - T_{\mathrm{ph}}\right). \tag{A10.1.8}$$

$C_{\mathrm{el}} = \gamma_{\mathrm{el}} T_{\mathrm{el}}$ where $\gamma_{\mathrm{el}} = 6 \times 10^2$ J/m^{3}K^2, and $C_{\mathrm{ph}} = 3.8 \times 10^6$ J/m^{3}K represent the specific heat of the electron- and phonon system. The electron-phonon coupling is taken temperature independent, $G_{\mathrm{ep}} = 7 \times 10^{17}$ J/m^{3}K. Here, $P(t)$ is a Gaussian shaped pulse with a duration of 55 fs. The exact values of the parameters entering the TTM in GdFeCo are still unknown. The values we use here are close to the commonly used, e.g. Refs. [135, 32] (also see chapter 5).

Ultrafast magnetization dynamics using ASD

Element-specific magnetization dynamics induced by a femtosecond laser pulse are calculated by combining the atomistic s-LLG equation for the spin dynamics (Eq. (A10.1.2)) and the 2TM for the electron temperature (Eq. (A10.1.7)). The electron system acts as heat-bath for the atomic spins. We consider a lattice with $N = 50 \times 50 \times 50$ spins, and damping parameters, $\lambda_{\mathrm{Gd}} = 0.01 = \lambda_{\mathrm{Fe}}$. Figure (A10.1.2) shows, for $t < 0$, the dynamics of the element-specific magnetization from an initial saturated state ($T = 0$ K), towards thermal equilibrium with the heat-bath which is set to $T = 300$ K. The relaxation dynamics of Fe sublattice is faster than those of the Gd sublattice. This comes out naturally as the element-specific dissipation of angular momentum scales as $\dot{m}_z \sim \gamma\lambda/\mu_s$, in Gd ($\mu_{\mathrm{Gd}} = 7.6\mu_{\mathrm{B}}$) is slower than in Fe sublattice ($\mu_{\mathrm{Gd}} = 1.94\mu_{\mathrm{B}}$). Once the magnetic system is in thermal equilibrium with the heat-bath, we apply the laser pulse, $t > 0$, which introduces energy into the electron system and induces ultrafast magnetization dynamics. To illustrate the switching and no switching dynamics we consider two limiting cases, dynamics induced by low laser power, P_0, and large laser power, $2P_0$. The electron temperature increases up and above the Curie temperature in time scales of a few hundreds of femtoseconds Fig. (A10.1.2) (a). This reflects in the magnetic system as a fast demagnetization of both Fe and Gd sublattices. For relatively low laser power, P_0, the magnetization of both sublattices reduces while the electron temperature remains relatively high. Once the electron temperature reduces and equalizes to the lattice temperature, they can be considered to be in a new, thermal quasi-equilibrium. The magnetization recovers to the thermal state given by the heat-bath temperature, which is higher than initially ($T = 300$ K). This is why the final magnetization value is smaller

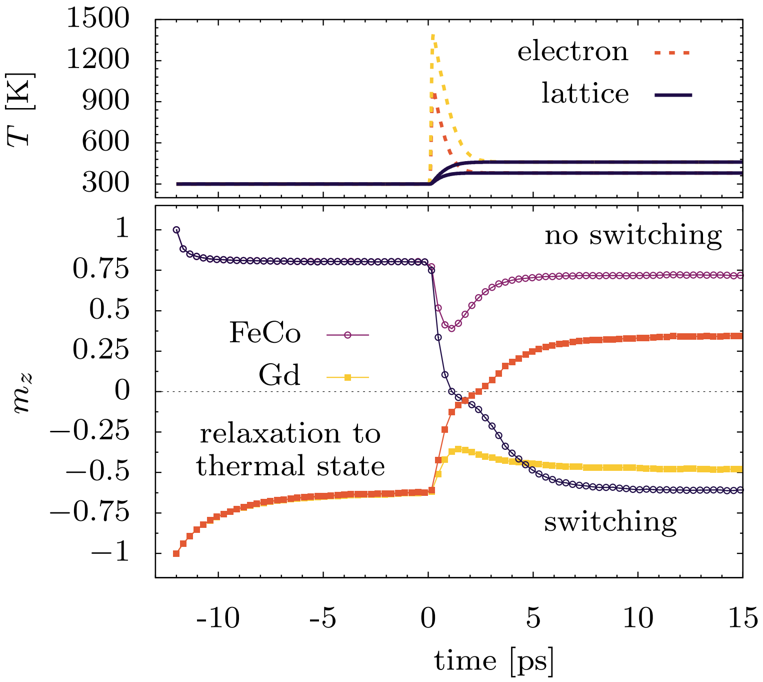

Figure A10.1.2: *(a) Electron and lattice temperature dynamics for two laser pulse power values, P_0 and $2P_0$. Both electron and lattice temperature are kept constant, $T = 300K$, for $t < 0$. At $t = 0$ a laser pulse is applied and the dynamics of the electron and lattice temperature heat up. The dynamics of those temperatures are theoretically described by the two-temperature model. (b) Element-specific magnetization dynamics induced by the heat profile at (a). The dynamics are calculated using atomistic spin dynamics methods. For lower laser powers P_0, the magnetization of both sublattices demagnetize rapidly and remagnetize towards the new equilibrium. For laser power $2P_0$, the magnetization of both sublattices demagnetizes and switches. After switching they relax towards the thermal equilibrium state. GdFeCo alloys with $x_{\mathrm{Gd}} = 25\%$ are calculated.*

than the initial one. For higher laser powers, $2P_0$, the magnetization of both sublattices reduces quickly. The Fe sublattice faster than the Gd one. Once the magnetization of the Fe sublattice hits zero, instead of remaining demagnetized, the magnetization starts to develop toward the opposite direction, while the magnetization of the Gd sublattice is still in the process of demagnetization. During a couple of picoseconds, both sublattice magnetization are aligned along the same direction, similar to a ferromagnet. Consequently, this non-equilibrium state has been named the transient ferromagnetic-like state [6]. One can observe in Fig. (A10.1.2) (b) that the demagnetization rates of both sublattices slow down when the Fe magnetization crosses zero. This change reveals the set in of a process driving the magnetization dynamics different to the one driving the initial demagnetization. It has been argued that at this point direct exchange of angular momentum between sublattices dominates over processes of relativistic origin, which in turn dissipate angular momentum into the heat-bath. Interestingly, soon after switching, both sublattice magnetization rapidly relax to equilibrium indicating that relaxation into the heat-bath dominates the dynamics.

A10.1.3 Phenomenological models

Differently to ASD simulations, phenomenological models describe the element-specific magnetization dynamics by solving two coupled equations of motion, one for each sublattice. In this work we aim at finding a phenomenological model that describes the same element-specific magnetization dynamics as those coming out from the ASD simulations (Fig. A10.1.2). The starting point is the comparison of the ASD simulations to well-known phenomenological models. We show that those models are unable to describe in a satisfactory way the different element-specific magnetization dynamics studied in the previous section and summarized in Fig. A10.1.2.

Baryakhtar model

The simplest model to describe element-specific magnetization dynamics and switching in ferrimagnets was proposed by Mentink and co-workers [126]. Longitudinal spin dynamics was derived from Onsager's relations

$$\frac{\mu_a}{\gamma_a}\frac{dm_a}{dt} = \alpha_a^{\mathrm{B}}\mu_a H_a + \alpha_e^{\mathrm{B}}(\mu_a H_a - \mu_b H_b) \tag{A10.1.9}$$

$$\frac{\mu_b}{\gamma_b}\frac{dm_b}{dt} = \alpha_b^{\mathrm{B}}\mu_b H_b + \alpha_e^{\mathrm{B}}(\mu_b H_b - \mu_a H_a) \tag{A10.1.10}$$

here, $\alpha_{a,b}^{\mathrm{B}}$ stands for the relaxation parameter of relativistic origin, which dissipates angular momentum out of the spin system, and α_e^{B} stands for the exchange relaxation parameter and describes the rate of dissipation of angular momentum between sublattices. By construction exchange relaxation conserves the total angular momentum. We emphasize here the difference in the notation between the atomic relaxation parameter, λ, describing the dissipation of the atomic spins in ASD simulations and the macrospin relaxation parameter, α, describing the dissipation of the whole magnetic sample. Within this model, the values for $\alpha_{a,b}^{\mathrm{B}}$ and α_e^{B} are unknown but used as fitting parameters when compared to experiments. The internal effective field $H_{a(b)}$, acting on sublattice $a(b)$ are derived from a non-equilibrium mean-field approximation,

$$\mu_a H_a = -\beta^{-1}L^{-1}(m_a) + \mu_a H_a^{\mathrm{MFA}} \tag{A10.1.11}$$

where, $L^{-1}(x)$ is the inverse Langevin function, $\beta = 1/k_B T$, where T represents the temperature of the heat-bath to which the spin system is coupled to. At equilibrium, the effective field is $H_a = 0$, as $m_a = L(\beta\mu_a H_a^{\mathrm{MFA}})$. The same arguments apply for sublattice b. It turns out that by solving Eqs. (A10.1.9) and (A10.1.10) together with the 2TM, described in Eqs. (A10.1.7) and (A10.1.8), one obtains similar ultrafast magnetization dynamics as those using ASD simulations (Fig. (A10.1.2)). Element-specific demagnetization [118] and switching dynamics [119] based on this approach have been discussed thoroughly before. On those works, the values for the relaxation parameters, relativistic and exchange, are taken constant and of the same order, $\alpha_{\mathrm{Fe}}^{\mathrm{B}} \approx \alpha_{\mathrm{Gd}}^{\mathrm{B}} \approx \alpha_e^{\mathrm{B}}$. We note that here α_a^{B} defines the rate of change of angular momentum $(m\mu/\gamma)$. It differs from the definition of intrinsic damping parameters in ASD, which are related to the rate of change of the magnetization (m). Similarly to ASD methods though, within the Baryakhtar model the observed fast dynamics of the Fe sublattice is related to a smaller value of atomic magnetic moment. The switching process within the Baryakhtar-like model is explained in the following manner. Since the

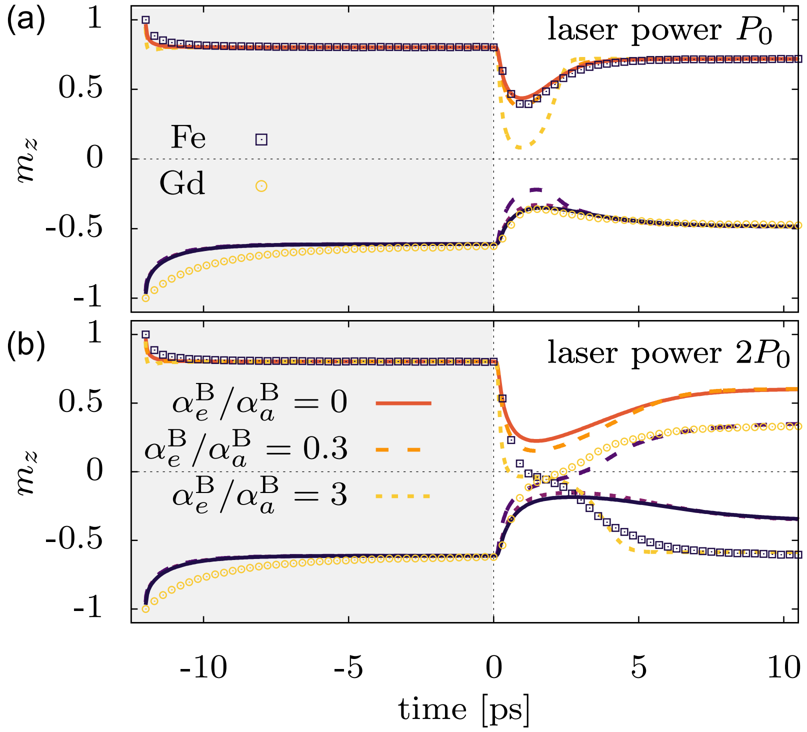

Figure A10.1.3: *Element-specific magnetization dynamics of GdFeCo calculated using atomistic spin dynamics (symbols) and macroscopic Baryakhtar-like equation (solid lines) for two laser pulse power values, (a) P_0 and (b) $2P_0$. Both electron and lattice temperature are kept constant, $T = 300$ K, for $t < 0$. At $t = 0$ a laser pulse is applied. In the Baryakhtar-like model the relativistic relaxation parameters α_a^B have a value different to the Gilbert damping in ASD simulations, $(\gamma/\mu_{\rm Fe})\alpha_{\rm Fe}^B = 0.005$ and $(\gamma/\mu_{\rm Gd})\alpha_{\rm Gd}^B = 0.01$. The exchange relaxation parameter is varied, $\alpha_e^B/\alpha_{\rm Fe}^B = 0, 0.3$ and 3. The relaxation to thermal state ($t < 0$) is only well described for the Fe sublattice. (a) For P_0, the laser induced dynamics is well described by $\alpha_e^B/\alpha_{\rm Fe}^B = 0.1$. (b) For $2P_0$ the demagnetization phase of both sublattices is relatively well described in comparison to ASD simulations. Switching is also possible, here one instance, for a value $\alpha_e^B/\alpha_{\rm Fe}^B = 3$.*

Fe sublattice reacts faster than Gd to heating it is expected to remain closer to thermal equilibrium with the heat-bath. This translates into a smaller non-equilibrium effective field acting on Fe than in Gd, $H_{\rm Fe} \ll H_{\rm Gd}$, during the action of the laser pulse. For strong enough pulses, the Fe magnetization rapidly reduces, $m_{\rm Fe} \approx 0$, still $H_{\rm Fe}$ is small in comparison to $H_{\rm Gd}$, in a way that the dynamics of Fe can be fairly approximated by $\dot{m}_{\rm Fe} \approx \alpha_e^B H_{\rm Gd}$. This drives the magnetization of Fe towards the opposite direction. The field, $H_{\rm Gd}$ is defined by the energy of the system, $H_{\rm Gd}^{\rm MFA}$ (Eq. (A10.1.6)) and α_e^B from the coupling between the Gd and the Fe sublattices. After switching, $H_{\rm Fe} \approx H_{\rm Gd}$ and relativistic relaxation processes dominate the dynamics and drive magnetization to complete the switching. The question here is to what extent the non-equilibrium fields as given by Eq. (A10.1.11) are accurate, and how are the relaxation parameters related to atomic damping parameters in ASD. So far the connection between the relaxation parameters in the ASD and Baryakhtar-like model is unknown. In ASD simulations shown in Fig. A10.1.2 we have used $\lambda_{\rm Fe} = \lambda_{\rm Gd} = 0.01$ as atomistic relaxation parameter. One would expect that the relaxation parameters in the atomistic and macroscopic models are related as $\lambda_a \approx \alpha_a^B(\gamma_a/\mu_a)$. In an attempt to find this correspondence, we directly compare results from ASD simulations and Baryakhtar-like models for different values of α_a^{B} and α_e^{B} in Eqs. (A10.1.9) and (A10.1.10). We numerically solve Eqs. (A10.1.9),(A10.1.10), and (A10.1.11) coupled to the 2TM with exactly the same parameters as for the ASD simulations. After exploring the results of the Baryakhtar model for a range of values for α_a^{B} and α_e, we find that for some values the agreement is good, as one observes in Fig. A10.1.3, however, it is not possible to find a good match for all scenarios. In order to illustrate this, we first focus on the dynamics induced by the laser pulse with power P_0 (Fig. (A10.1.3)(a)). We find a good match for the laser induced magnetization dynamics ($t > 0$ for $(\gamma/\mu_{\mathrm{Fe}})\alpha_{\mathrm{Fe}} = 0.005$ and $(\gamma/\mu_{\mathrm{Gd}})\alpha_{\mathrm{Gd}} = 0.01$, and for values of exchange relaxation of up to $\alpha_e^{\mathrm{B}}/\alpha_{\mathrm{Fe}}^{\mathrm{B}} = 0.3$. For values $\alpha_e^{\mathrm{B}}/\alpha_{\mathrm{Fe}}^{\mathrm{B}} < 0.3$, thermal relaxation ($t < 0$) of the Fe is also well described, however the relaxation of the Gd sublattice is significantly faster. For larger values of the exchange relaxation $\alpha_e^{\mathrm{B}}/\alpha_{\mathrm{Fe}}^{\mathrm{B}} = 3$, the dynamics of both sublatttices are substantially speed up and strongly disagree with ASD simulations. For larger laser pulse power $2P_0$ the magnetization switches using ASD simulations. We keep the same values for the relaxation parameters in Baryakhtar-like model as for P_0, and compare to the ASD simulations. For small values of α_e^{B} (Fig. (A10.1.3)(b)), differently to the P_0 case (Fig. (A10.1.3)(a)), the dynamics described by the Baryakhtar-like model is not only slower than those of ASD simulations but it hardly reproduces magnetization switching. In order to reproduce switching, we need to use larger values of the exchange relaxation parameter, $\alpha_e^{\mathrm{B}}/\alpha_{\mathrm{Fe}}^{\mathrm{B}} = 3$. These findings are in agreement with previous works using Baryakhtar-like model where switching was reproduced for comparable values of α_e^{B}. However, as we have discussed before, for those values of α_e^{B}, thermal relaxation dynamics ($t < 0$) is much faster than in ASD simulations. This brings us to the question of how much understanding about switching can we gain by using this bare Baryakhtar-like model, are we missing something?

The Landau-Lifshitz-Bloch model

Since the Baryakhtar-like model is based on symmetry arguments, the macroscopic magnetization dynamics coming out from ASD simulations should also be described by that model with adequate expression for the relaxation parameters and non-equilibrium effective fields. The magnetization dynamics coming out from ASD simulations is well described by the LLB equation of motion.

$$\frac{dm_a}{dt} = \Gamma_{\parallel,a}\left(m_a - m_{0,a}\right), \tag{A10.1.12}$$

where

$$\Gamma_{\parallel,a} = 2\lambda_a \frac{\gamma}{\mu_a} k_B T \frac{1}{\xi_a} \frac{L(\xi_a)}{L'(\xi_a)}, \tag{A10.1.13}$$

with $\xi_a = \beta\mu_a H_a^{\mathrm{MFA}}$, where H_a^{MFA} is given in Eq. (A10.1.6), and $m_{0,a} = L(\xi_a)$. The same equation applies to the second sublattice b. Here, the relaxation rate $\Gamma_{\parallel,a}$ depends non-linearly on the non-equilibrium sublattice magnetization, $m_{a(b)}$, through the parameter ξ_a. We note that Eq. (A10.1.12) can be expanded around equilibrium for small perturbations of the magnetization. By doing so, the relaxation rates and effective fields are expressed in terms of equilibrium properties such as equilibrium magnetization and zero-field susceptibilities [171]. In the present work, however, we use the version in Eq. (A10.1.12). Direct comparison between ASD simulations and the LLB model of element-specific magnetization dynamics is possible and with relatively good agreement. Importantly, since the LLB model is derived directly from the ASD microscopic model, the damping parameters, $\lambda_{a(b)}$ in Eqs. (A10.1.13) and (A10.1.2) stand for the same physics, the rate of angular momentum dissipation of

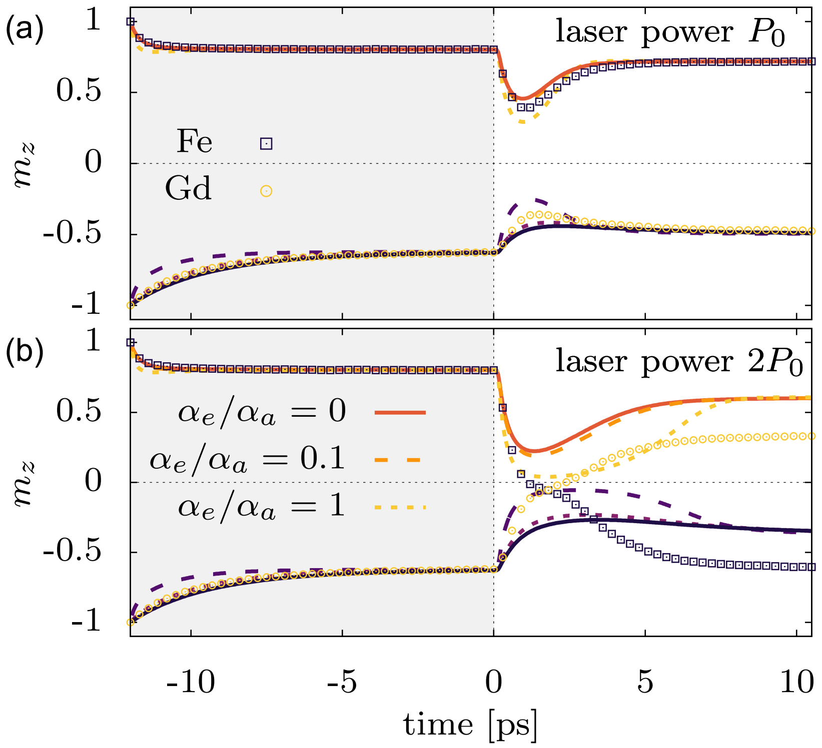

Figure A10.1.4: *Element-specific magnetization dynamics of GdFeCo calculated using atomistic spin dynamics (symbols) and macroscopic LLB equation (solid lines) for two laser pulse power values, (a) P_0 and (b) $2P_0$. For $t < 0$, electron and lattice temperature are $T = 300K$, and at $t = 0$ a laser pulse is applied. The exchange relaxation parameter is varied, $\alpha_e/\alpha_a = 0, 0.1$ and 1, where $\alpha_a = 0.01$, and a =FeCo or Gd. The initial relaxation dynamics is well described by $\alpha_e/\alpha_a = 0$. (a) For laser power P_0, the element-specific dynamics is well-described for $\alpha_e/\alpha_a = 0.1$. (a) For $\alpha_e/\alpha_a = 1$, exchange relaxation dominates and the element-specific dynamics are similar. (b) For laser power $2P_0$, the switching dynamics is not described by the LLB model.*

the atomic spins. Differently to the Baraykhtar model where $\alpha^{\mathrm{B}}_{a(b)}$ is taken as a fitting parameter, within the LLB model the value of $\lambda_{a(b)}$ in Eq. (A10.1.13) is the same as in the ASD simulations. A key difference between the Baryakhtar-like model and the LLB model is that in the latter an exchange relaxation term is missing. In order to find a meeting point between these phenomenological models, we rewrite Eq. (A10.1.12) in terms of a damping term multiplied by an effective field,

$$\frac{dm_a}{dt} = \frac{2\lambda_a L(\xi_a)}{\xi_a}\frac{\gamma}{\mu_a}\frac{m_a - m_{0,a}}{\beta L'(\xi_a)} = \gamma\alpha_a H_a, \tag{A10.1.14}$$

where

$$\alpha_a = 2\lambda_a \frac{L(\xi_a)}{\xi_a}. \tag{A10.1.15}$$

Differently to Baryakhtar-like model, in the LLB model, the relaxation parameter strongly depends on temperature and non-equilibrium sublattice magnetization through the thermal field, $\xi_a = \beta\mu_a H^{\mathrm{MFA}}_a$. At the same time, the non-equilibrium fields $\mu_a H_a$ within the LLB and Baryakhtar-like models differ. The effective field in the LLB model is defined as

$$\mu_a H_a = \frac{(m_a - m_{0,a})}{\beta L'(\xi_a)}. \tag{A10.1.16}$$

Equation (A10.1.16) provides a microscopic description of the effective field driving the magnetization dynamics in ferrimagnets, based on the Heisenberg spin model (Eq. (A10.1.1)). Under the assumption of small perturbations around the equilibrium both, LLB and Baryakhtar-like effective fields, simplify to Landau-like expressions [119]. Equation (A10.1.14) describes with a very good degree of accuracy the relaxation of the angular momentum via dissipation to the heat-bath, which corresponds to the relativistic term in Eqs. (A10.1.9) and (A10.1.10). Previously, it has been found that ASD simulations compare well to Eq. (A10.1.14) for coupling parameters of around $\lambda_a \approx 0.1 - 1$ [171, 292]. These values can be considered to correspond to the intermediate-to-high coupling regime. Direct comparison between ASD simulations and experiments of single pulse switching in GdFeCo has suggested values of $\lambda_{\mathrm{Fe}} \approx 0.06$ and $\lambda_{\mathrm{Gd}} \approx 0.01$ (see chapter 3). In the context of the present work we find that Eq. (A10.1.14) describes relatively well the thermal relaxation dynamics in direct comparison to ASD simulations (Fig. (A10.1.4)). In order to account for the exchange relaxation in the LLB model, we follow the Baryakhtar-like model ((A10.1.9) and (A10.1.10)), and add an exchange relaxation term to Eq. (A10.1.14),

$$\frac{\mathrm{d}m_a}{\mathrm{d}t} = \gamma\alpha_a H_a + \gamma\frac{\alpha_e}{\mu_a}(\mu_a H_a - \mu_b H_b) \tag{A10.1.17}$$

where α_e is a phenomenological exchange relaxation parameter to be determined by comparison to ASD dynamics. The inclusion of the exchange relaxation (second term in r.h.s) in the LLB improves the agreement to ASD simulations. With this addition, the LLB model describes well thermal relaxation for small values of the ratio α_e/α_a as demonstrated in Fig. A10.1.4. For large values of α_e the LLB model is unable to describe thermal relaxation dynamics ($t < 0$ in Fig. A10.1.4(a) and (b)). For laser power P_0 (Fig. A10.1.4(a) ($t > 0$)) the magnetization dynamics is slightly slower using the LLB model than those gained by ASD simulations for $\alpha_e/\alpha_a = 0$. For $\alpha_e/\alpha_a = 0.1$, the agreement is even better than without exchange relaxation. The agreement vanishes when the exchange relaxation is increased to $\alpha_e/\alpha_a = 1$. Critically, when the laser power is increased from P_0 to $2P_0$, for which ASD simulations show ultrafast switching, the LLB model only shows demagnetization-remagnetization of both sublattices. We find some agreement on the demagnetization time scales when a quite large exchange relaxation is used, $\alpha_e/\alpha_a = 1$. These dynamics are similar to those observed using the Baryakhtar-like model for intermediate values of the exchange relaxation parameter (Fig. (A10.1.3)). It has been demonstrated previously that by including the transverse components of the equation of motion, switching is possible via a precessional path when a canting between the magnetization of each sublattice exists [286]. Here, we restrict to purely longitudinal switching within the LLB model.

Unified phenomenological model

So far we have constructed a phenomenological model based on the LLB and Baryakhtar-like models, the dynamics is given by Eq. (A10.1.17), the effective field by Eq. (A10.1.16) and the relativistic relaxation parameter Eq. (A10.1.15). We still need an expression for the exchange relaxation parameter. We construct this expression starting with single species ferromagnets, where sublattices a and b represent the same spin lattice, hence exchange of angular momentum is non-local. Therefore, $\mu_a H_a - \mu_b H_b = \mu_a H_{\rm ex} a_0^2 \Delta m_a$, with a_0 representing the lattice constant. Hence, the rate of non-local angular momentum transfer reads $\Gamma_{\rm ex}^{\rm non-loc.} = \alpha_{\rm ex}(\mu_a H_a - \mu_b H_b) = \alpha_a (A/M_a(T))\Delta m_a$, where A is the so-called micromagnetic exchange stiffness [172]. $M_a(T) = (\mu_a/\upsilon_a) m_a$ is the magnetization density at temperature T, where υ_a is the unit cell volume. Therefore, we find that $\alpha_{\rm ex} = \alpha_a/(z m_a)$, where z is the number of nearest neighbors. By considering that the exchange relaxation rate should conserve the symmetry under the exchange of lattice index, $\alpha_{ex}(M_1, M_2) = \alpha_{ex}(M_2, M_1)$, we find that

$$\alpha_{\rm ex} = \frac{1}{2}\left(\frac{\alpha_a}{z_{ab} m_a} + \frac{\alpha_b}{z_{ba} m_b}\right). \tag{A10.1.18}$$

This expression is the extension of the non-local exchange relaxation in ferromagnets to local exchange relaxation in ferrimagnets. This explicit expression for the exchange relaxation parameter in Eq. (A10.1.18) completes our unified model, which bridges the atomistic spin dynamics model and the Baryakhtar and LLB macroscopic models. The previously discussed phenomenological models have introduced the relaxation parameters at a purely phenomenological level (Baryakhtar) or missed to include the exchange relaxation (LLB). Contrary to this, our unified model overcomes this shortcoming, by providing expressions for the relativistic and exchange relaxation parameters as a function of the sublattice specific atomic relaxation parameter, $\lambda_{a(b)}$ through Eqs. (A10.1.15) and (A10.1.18), and normalized magnetization $m_{a(b)}$. We note that in our unified model, the values of the relaxation parameters are given by the system parameters and do not depend on the power of the laser fluence. For all laser fluences, the expressions and values are exactly the same, however, due to the their dependence of the system temperature and element-specific magnetization, upon photoexcitation with laser pulse, the values of the relaxation parameters will change dynamically. For large laser powers, the exchange relaxation parameter becomes of the same order or even larger than the relativistic relaxation parameter. In the previous phenomenological models the exchange relaxation constant needed to have a large value in order to describe switching. By contrast, in order to describe low laser power dynamics, the exchange relaxation constant needed to have a relatively small value ($\alpha_{\rm ex}/\alpha_{a(b)} \ll 1$) (Fig. A10.1.3). The expression for the exchange relaxation parameter that we propose in Eq. (A10.1.18) captures this behaviour naturally. Figure A10.1.5 shows the equilibrium value of the relativistic exchange parameters ($\alpha_{\rm Fe}$ and $\alpha_{\rm Gd}$) and the exchange relaxation parameter ($\alpha_{\rm ex}$) as a function of temperature. For the sake of simplicity, the values are those corresponding to the thermal equilibrium. The element-specific relativistic relaxation parameters scale with the value of $\lambda_{a(b)}$ as given in Eq. (A10.1.15) and depend almost linearly with temperature, with a maximum at the Curie temperature of $2\lambda_{a(b)}/3$. By contrast, the exchange relaxation shows a drastically different behaviour. At low temperatures, assuming $\alpha_a = \alpha_b$, one gets $\alpha_{\rm ex} \approx \alpha_a/z$. By contrast, for relatively high temperatures, close to T_c, where $m_{a(b)} \to 0$, $\alpha_{\rm ex}$ scales as $\alpha_{\rm ex} \sim 1/m_a$. Therefore, even at equilibrium, close to the critical temperature, the relaxation dynamics is dominated by exchange relaxation processes. At non-equilibrium situations, the exchange relaxation can become larger than the relativistic relaxation by driving one of the sublattice magnetization to zero, in principle without the need of approaching the critical temperature. We conduct a direct comparison between the proposed unified and atomistic spin dynamics simulations. The system parameters are exactly the same as those used in the previous sections, when ASD simulations were compared to Baryakhtar and LLB models. The damping parameter is the same for both sublattices, $\lambda_{a(b)} = 0.01$ and we use the same laser powers. We find that the agreement between our unified phenomenological model and ASD simulations is excellent, see Fig. (A10.1.6)(a) and (b). Figure A10.1.6(a) shows that for $t < 0$, the sublattice magnetization relaxation towards thermal equilibrium

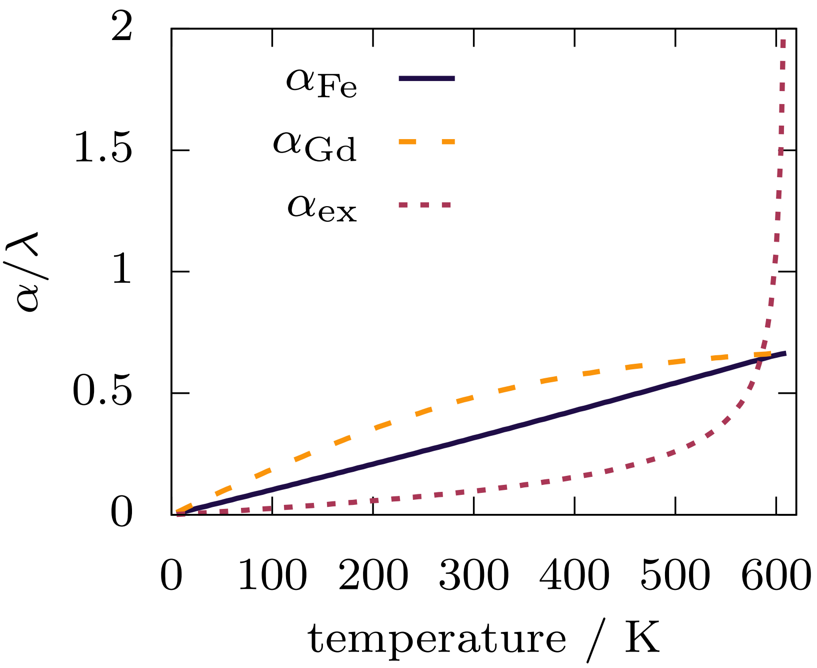

Figure A10.1.5: *Thermal equilibrium value of the relativistic exchange parameters* α_{Fe} *and* α_{Gd} *and the exchange relaxation parameter* α_{ex} *as a function of temperature.*

value is described with a high level of accuracy by our model. For $t > 0$ and a relatively low laser power P_0, the agreement is also excellent for the demagnetization and remagnetization dynamics. Figure A10.1.6(b) shows the comparison between the unified model and ASD simulations of the switching dynamics. We conclude that Eq. (A10.1.17) for the sublattice magnetization dynamics together with the Eq. (A10.1.16) for the effective field and Eqs. (A10.1.15) and (A10.1.18) for the relaxation parameters, unify the Barayakhtar and the LLB phenomenological models for single-pulse all-optical switching in ferrimagnets. Our unified model compares well to ASD simulations for realistic system parameters. For some limiting cases, our model is unable to reproduce ASD simulations. For example, ASD simulations of an isolated ferrimagnet, e.g. no coupling to the heat-bath, are impossible to reproduce by our model [128]. This type of sublattice magnetization relaxation has been named *non-dissipative relaxation* since there is no net dissipation into an external bath. All three phenomenological models discussed in this work; Baryakhtar, LLB and our unified model are based on the assumption that the spin system is coupled to a heat-bath and they are near thermal equilibrium. Non-dissipative relaxation processes could play a role in the exchange relaxation for very low damping values, both non-realistic and of little interest for ultrafast toggle switching. Nevertheless, we emphasize that the agreement between our model and ASD simulations demonstrates that the potential contribution of internal exchange of angular momentum and energy is minimal for the damping values considered here ($\lambda = 0.01$).

A10.1.4 Discussion and conclusion

The macroscopic model presented in this work solves some open questions in the field of ultrafast magnetization dynamics in ferrimagnets. For example, it answers the question of

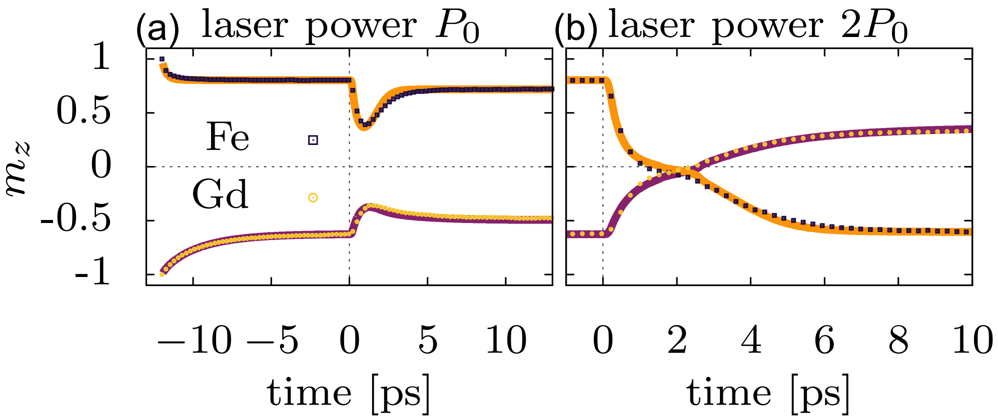

Figure A10.1.6: *Element-specific magnetization dynamics of GdFeCo calculated using atomistic spin dynamics (symbols) and the unified phenomenological model derived here, following Eq.* (A10.1.17) *(solid lines) for two laser pulse power values, (a) P_0 and (b) $2P_0$. Both electron and lattice temperature are kept constant, $T = 300$ K, for $t < 0$. At $t = 0$ a laser pulse is applied, the same as in figure* (A10.1.2). *GdFeCo alloys with $x_{\rm Gd} = 25\%$ are calculated.*

the range of applicability and the validity of the parameters of the Barayakhtar and LLB phenomenological models. In the one hand, within our model, the relativistic relaxation parameters (α_a) are element-specific and strongly depend on both the temperature and the non-equilibrium sublattice magnetization. The temperature and magnetization dependence of the relativistic relaxation parameters are well described by the LLB model. In the other hand, the exchange relaxation parameter ($\alpha_{\rm ex}$) is cast in terms of the element specific relativistic relaxation parameters and sublattice magnetization. We have demonstrated that in order to reproduce the ASD simulations results, the relaxation parameters in the Barayakhtar model have to be both temperature and magnetization dependent. The explicit expression of the exchange relaxation parameter is the main result of the present work since it allows us to unify the Barayakhtar and LLB models. While for the Barayakhtar model α_e is unconnected to α_a, within our proposed model they are proportional to each other, $\alpha_e \sim \alpha_a/m_a$. This relation is the key to bridge both ASD simulations and Barayakhtar and LLB models together. Additionally, we have also demonstrated the validity of the non-equilibrium effective fields given in Eq. (A10.1.16) as derived in the LLB model instead of the Barayakhtar model. Single-pulse switching in ferrimagnets has been described before by the Baryakhtar model. A necessary condition for switching is that the system transits from the relativistic relaxation regime to the so-called exchange-dominated relaxation regime. Although details of switching in such a regime have been already discussed in detail [126, 119], so far it has remained unknown how this transition could be described theoretically. Our model resolves this question. When the system is at equilibrium or weakly excited, the exchange-relaxation parameter fulfills, $\alpha_e \ll \alpha_a$. For strong excitation, such that the magnetic order of one sublattice reduces significantly, close to zero $m_a \to 0$, the exchange relaxation will dominate the dynamics since $\alpha_e \sim \alpha_a/m_a \gg \alpha_a$. From our model, one can derive universal criteria for switching in ferrimagnets, including GdFeCo and $\mathrm{Mn_2Ru_xGa}$ (see chapter 5). The provided understanding is paramount for further research on material engineering, for example, to find alternative material classes showing all-optical switching. Notably, our model predicts that the exchange relaxation term is enhanced as the number of neighbours reduces. This dependence suggests that magnetic systems of lower dimension, e.g. 2D magnets [189], could show a faster, more efficient switching than bulk materials. Further, the extension of our model to the micromagnetic level will allow to optimize switching conditions. The use of micromagnetic computational solvers permits for a realistic description of ultrafast AOS processes in ferrimagnetic alloys, such as helicity-independent and helicity-dependent AOS, where multidomain states and thermal gradients play an important role in the process [295]. To summarize, in the present work we have presented a unified model for single-pulse all-optical switching in ferrimagnets. Our model merges and improves previous semi-phenomenological models, the Landau-Lifshitz-Bloch model and Barayakhtar-like models. To verify the accuracy of the proposed model, we directly compare the laser induced magnetization dynamics to atomistic spin dynamics computer simulations. Differently to previous models, our model has the advantage that it can be directly compared to ASD simulations. Further, we have established the connection between ASD and macroscopic equations of motion. Importantly, we provide here the stepping stone for the construction of a micromagnetic model valid for ferrimagnets including exchange relaxation between sublattices. This is paramount for a robust construction of a multiscale scheme of the switching process in which not only local magnetization dynamics is described but also magnetic domain nucleation and motion under strong non-equilibrium. Multiscale-based micromagnetic models will allow for the description of realistic sample sizes and describe recent spintronics phenomena using laser pulses, e.g. magnetic skyrmion creation/deletion with fs laser pulses, or domain-wall motion under dynamics thermal gradients.

Acknowledgments

Finally, I would like to thank all those who supported me during my work on this thesis.

In particular, I want to express my deep gratitude to my thesis supervisor Unai Atxitia for his constant willingness to help me with all major and minor problems that came up during the work of this thesis, for the countless constructive discussions and his constant support and immense patience.

I would also like to thank Professor Piet Brouwer for being the second supervisor of this thesis and for providing the necessary infrastructure for this work, from the desk to the access to the computing cluster, as well as for his valuable feedback towards the end of this thesis.

I also want to thank all members of *TRR 227 - Ultrafast Spin Dynamics -* for the friendly and inspiring atmosphere during numerous meetings, events, seminars and lectures, constituting an excellent research environment. In particular, I would like to thank Britta Anstötz and Christian Frischkorn for the organization of the said events and for always being available for the needs of us PhD students.

I express my thanks as well to all co-workers that made this work possible, in particular Jon Gorchon for his experiments on GdFeCo and for the opportunity to work on this project, Tom Ostler for his contributions to the GdFeCo work and many helpful discussions on different projects, and Daniela Zahn for her experiments on the phonon dynamics in transition metals and the collaboration in these projects.

I also express my thanks to David Reiß for sharing an office over our entire PhD time, the cheerful working atmosphere and all discussions we had together. Furthermore, I thank him, Jan Böhnke and Adam Chaou for proof-reading my thesis and giving valuable feedback.

At last, I would like to thank the working groups Brouwer, von Oppen and Reuther for the time we spent together and for the good working atmosphere.

Bibliography

[1] C. Banerjee, K. Rode, G. Atcheson, S. Lenne, P. Stamenov, J. M. D. Coey, and J. Besbas, “Ultrafast double pulse all-optical reswitching of a ferrimagnet,” *Physical Review Letters*, vol. 126, p. 177202, Apr 2021.

[2] IDC and Statista, “Volume of data/information created, captured, copied, and consumed worldwide from 2010 to 2020, with forecasts from 2021 to 2025 (in zettabytes).,” 2021. Accessed: October 2022.

[3] L. Pan and D. B. Bogy, “Heat-assisted magnetic recording,” *Nature Photonics*, vol. 3, pp. 189–190, Apr 2009.

[4] B. C. Stipe, T. C. Strand, C. C. Poon, H. Balamane, T. D. Boone, J. A. Katine, J.-L. Li, V. Rawat, H. Nemoto, A. Hirotsune, O. Hellwig, R. Ruiz, E. Dobisz, D. S. Kercher, N. Robertson, T. R. Albrecht, and B. D. Terris, “Magnetic recording at 1.5 pb m-2 using an integrated plasmonic antenna,” *Nature Photonics*, vol. 4, pp. 484–488, Jul 2010.

[5] E. Beaurepaire, J.-C. Merle, A. Daunois, and J.-Y. Bigot, “Ultrafast spin dynamics in ferromagnetic nickel,” *Phys. Rev. Lett.*, vol. 76, pp. 4250–4253, May 1996.

[6] I. Radu, K. Vahaplar, C. Stamm, T. Kachel, N. Pontius, H. A. Dürr, T. A. Ostler, J. Barker, R. F. L. Evans, R. W. Chantrell, A. Tsukamoto, A. Itoh, A. Kirilyuk, T. Rasing, and A. V. Kimel, “Transient ferromagnetic-like state mediating ultrafast reversal of antiferromagnetically coupled spins,” *Nature*, vol. 472, pp. 205–208, Apr 2011.

[7] M. Agranat, S. Ashitkov, A. Granovskii, and G. Rukman, “Interaction of picosecond laser pulses with the electron, spin, and phonon subsystems of nickel,” *Sov. Phys. JETP*, vol. 59, pp. 804–806, 1984.

[8] A. Vaterlaus, T. Beutler, D. Guarisco, M. Lutz, and F. Meier, “Spin-lattice relaxation in ferromagnets studied by time-resolved spin-polarized photoemission,” *Phys. Rev. B*, vol. 46, pp. 5280–5286, Sep 1992.

[9] W. Hubner and K. H. Bennemann, “Simple theory for spin-lattice relaxation in metallic rare-earth ferromagnets,” *Phys. Rev. B*, vol. 53, pp. 3422–3427, Feb 1996.

[10] J. Hohlfeld, E. Matthias, R. Knorren, and K. H. Bennemann, “Nonequilibrium magnetization dynamics of nickel,” *Phys. Rev. Lett.*, vol. 78, pp. 4861–4864, Jun 1997.

[11] A. Scholl, L. Baumgarten, R. Jacquemin, and W. Eberhardt, “Ultrafast spin dynamics of ferromagnetic thin films observed by fs spin-resolved two-photon photoemission,” *Phys. Rev. Lett.*, vol. 79, pp. 5146–5149, Dec 1997.

[12] J. Güdde, U. Conrad, V. Jähnke, J. Hohlfeld, and E. Matthias, "Magnetization dynamics of ni and co films on cu(001) and of bulk nickel surfaces," *Phys. Rev. B*, vol. 59, pp. R6608–R6611, Mar 1999.

[13] H.-S. Rhie, H. A. Dürr, and W. Eberhardt, "Femtosecond electron and spin dynamics in Ni/W(110) films," *Phys. Rev. Lett.*, vol. 90, p. 247201, Jun 2003.

[14] B. Koopmans, G. Malinowski, F. Dalla Longa, D. Steiauf, M. Fähnle, T. Roth, M. Cinchetti, and M. Aeschlimann, "Explaining the paradoxical diversity of ultrafast laser-induced demagnetization," *Nature Materials*, vol. 9, pp. 259–265, Mar 2010.

[15] K. Carva, M. Battiato, and P. M. Oppeneer, "Ab initio investigation of the elliott-yafet electron-phonon mechanism in laser-induced ultrafast demagnetization," *Phys. Rev. Lett.*, vol. 107, p. 207201, Nov 2011.

[16] M. Battiato, K. Carva, and P. M. Oppeneer, "Superdiffusive spin transport as a mechanism of ultrafast demagnetization," *Phys. Rev. Lett.*, vol. 105, p. 027203, Jul 2010.

[17] M. Battiato, K. Carva, and P. M. Oppeneer, "Theory of laser-induced ultrafast superdiffusive spin transport in layered heterostructures," *Phys. Rev. B*, vol. 86, p. 024404, Jul 2012.

[18] D. Rudolf, C. La-O-Vorakiat, M. Battiato, R. Adam, J. M. Shaw, E. Turgut, P. Maldonado, S. Mathias, P. Grychtol, H. T. Nembach, T. J. Silva, M. Aeschlimann, H. C. Kapteyn, M. M. Murnane, C. M. Schneider, and P. M. Oppeneer, "Ultrafast magnetization enhancement in metallic multilayers driven by superdiffusive spin current," *Nature Communications*, vol. 3, p. 1037, Sep 2012.

[19] E. Turgut, C. La-o vorakiat, J. M. Shaw, P. Grychtol, H. T. Nembach, D. Rudolf, R. Adam, M. Aeschlimann, C. M. Schneider, T. J. Silva, M. M. Murnane, H. C. Kapteyn, and S. Mathias, "Controlling the competition between optically induced ultrafast spin-flip scattering and spin transport in magnetic multilayers," *Phys. Rev. Lett.*, vol. 110, p. 197201, May 2013.

[20] C. E. Graves, A. H. Reid, T. Wang, B. Wu, S. de Jong, K. Vahaplar, I. Radu, D. P. Bernstein, M. Messerschmidt, L. Müller, R. Coffee, M. Bionta, S. W. Epp, R. Hartmann, N. Kimmel, G. Hauser, A. Hartmann, P. Holl, H. Gorke, J. H. Mentink, A. Tsukamoto, A. Fognini, J. J. Turner, W. F. Schlotter, D. Rolles, H. Soltau, L. Strüder, Y. Acremann, A. V. Kimel, A. Kirilyuk, T. Rasing, J. Stöhr, A. O. Scherz, and H. A. Dürr, "Nanoscale spin reversal by non-local angular momentum transfer following ultrafast laser excitation in ferrimagnetic gdfeco," *Nature Materials*, vol. 12, pp. 293–298, Apr 2013.

[21] N. Moisan, G. Malinowski, J. Mauchain, M. Hehn, B. Vodungbo, J. Lüning, S. Mangin, E. E. Fullerton, and A. Thiaville, "Investigating the role of superdiffusive currents in laser induced demagnetization of ferromagnets with nanoscale magnetic domains," *Scientific Reports*, vol. 4, p. 4658, Apr 2014.

[22] V. Shokeen, M. Sanchez Piaia, J.-Y. Bigot, T. Müller, P. Elliott, J. K. Dewhurst, S. Sharma, and E. K. U. Gross, "Spin flips versus spin transport in nonthermal electrons excited by ultrashort optical pulses in transition metals," *Phys. Rev. Lett.*, vol. 119, p. 107203, Sep 2017.

[23] E. Turgut, D. Zusin, D. Legut, K. Carva, R. Knut, J. M. Shaw, C. Chen, Z. Tao, H. T. Nembach, T. J. Silva, S. Mathias, M. Aeschlimann, P. M. Oppeneer, H. C. Kapteyn, M. M. Murnane, and P. Grychtol, "Stoner versus heisenberg: Ultrafast exchange reduction and magnon generation during laser-induced demagnetization," *Phys. Rev. B*, vol. 94, p. 220408, Dec 2016.

[24] C. D. Stanciu, F. Hansteen, A. V. Kimel, A. Kirilyuk, A. Tsukamoto, A. Itoh, and T. Rasing, "All-optical magnetic recording with circularly polarized light," *Phys. Rev. Lett.*, vol. 99, p. 047601, Jul 2007.

[25] A. Hassdenteufel, B. Hebler, C. Schubert, A. Liebig, M. Teich, M. Helm, M. Aeschlimann, M. Albrecht, and R. Bratschitsch, "Thermally assisted all-optical helicity dependent magnetic switching in amorphous $\mathrm{Fe}_{100-x}\mathrm{Tb}_x$ alloy films," *Advanced Materials*, vol. 25, no. 22, pp. 3122–3128, 2013.

[26] S. Mangin, M. Gottwald, C.-H. Lambert, D. Steil, V. Uhlíř, L. Pang, M. Hehn, S. Alebrand, M. Cinchetti, G. Malinowski, Y. Fainman, M. Aeschlimann, and E. E. Fullerton, "Engineered materials for all-optical helicity-dependent magnetic switching," *Nature Materials*, vol. 13, pp. 286–292, Mar 2014.

[27] R. John, M. Berritta, D. Hinzke, C. Müller, T. Santos, H. Ulrichs, P. Nieves, J. Walowski, R. Mondal, O. Chubykalo-Fesenko, J. McCord, P. M. Oppeneer, U. Nowak, and M. Münzenberg, "Magnetisation switching of fept nanoparticle recording medium by femtosecond laser pulses," *Scientific Reports*, vol. 7, p. 4114, Jun 2017.

[28] C.-H. Lambert, S. Mangin, B. S. D. C. S. Varaprasad, Y. K. Takahashi, M. Hehn, M. Cinchetti, G. Malinowski, K. Hono, Y. Fainman, M. Aeschlimann, and E. E. Fullerton, "All-optical control of ferromagnetic thin films and nanostructures," *Science*, vol. 345, no. 6202, pp. 1337–1340, 2014.

[29] P. S. Pershan, J. P. van der Ziel, and L. D. Malmstrom, "Theoretical discussion of the inverse faraday effect, raman scattering, and related phenomena," *Phys. Rev.*, vol. 143, pp. 574–583, Mar 1966.

[30] A. V. Kimel, A. Kirilyuk, P. A. Usachev, R. V. Pisarev, A. M. Balbashov, and T. Rasing, "Ultrafast non-thermal control of magnetization by instantaneous photomagnetic pulses," *Nature*, vol. 435, pp. 655–657, Jun 2005.

[31] D. Popova, A. Bringer, and S. Blügel, "Theory of the inverse faraday effect in view of ultrafast magnetization experiments," *Phys. Rev. B*, vol. 84, p. 214421, Dec 2011.

[32] T. A. Ostler, J. Barker, R. F. L. Evans, R. W. Chantrell, U. Atxitia, O. Chubykalo-Fesenko, S. El Moussaoui, L. Le Guyader, E. Mengotti, L. J. Heyderman, F. Nolting, A. Tsukamoto, A. Itoh, D. Afanasiev, B. A. Ivanov, A. M. Kalashnikova, K. Vahaplar, J. Mentink, A. Kirilyuk, T. Rasing, and A. V. Kimel, "Ultrafast heating as a sufficient stimulus for magnetization reversal in a ferrimagnet," *Nature Communications*, vol. 3, p. 666, Feb 2012.

[33] S. Gerlach, L. Oroszlany, D. Hinzke, S. Sievering, S. Wienholdt, L. Szunyogh, and U. Nowak, "Modeling ultrafast all-optical switching in synthetic ferrimagnets," *Phys. Rev. B*, vol. 95, p. 224435, Jun 2017.

[34] R. B. Wilson, J. Gorchon, Y. Yang, C.-H. Lambert, S. Salahuddin, and J. Bokor, “Ultrafast magnetic switching of gdfeco with electronic heat currents,” *Phys. Rev. B*, vol. 95, p. 180409, May 2017.

[35] Y. Yang, R. B. Wilson, J. Gorchon, C.-H. Lambert, S. Salahuddin, and J. Bokor, “Ultrafast magnetization reversal by picosecond electrical pulses,” *Science Advances*, vol. 3, no. 11, p. e1603117, 2017.

[36] J. Gorchon, R. B. Wilson, Y. Yang, A. Pattabi, J. Y. Chen, L. He, J. P. Wang, M. Li, and J. Bokor, “Role of electron and phonon temperatures in the helicity-independent all-optical switching of gdfeco,” *Phys. Rev. B*, vol. 94, p. 184406, Nov 2016.

[37] D. Steil, S. Alebrand, A. Hassdenteufel, M. Cinchetti, and M. Aeschlimann, “All-optical magnetization recording by tailoring optical excitation parameters,” *Phys. Rev. B*, vol. 84, p. 224408, Dec 2011.

[38] A. V. Kimel and M. Li, “Writing magnetic memory with ultrashort light pulses,” *Nature Reviews Materials*, vol. 4, pp. 189–200, Mar 2019.

[39] A. El-Ghazaly, J. Gorchon, R. B. Wilson, A. Pattabi, and J. Bokor, “Progress towards ultrafast spintronics applications,” *Journal of Magnetism and Magnetic Materials*, vol. 502, p. 166478, 2020.

[40] J. Barker and U. Atxitia, “A review of modelling in ferrimagnetic spintronics,” *Journal of the Physical Society of Japan*, vol. 90, no. 8, p. 081001, 2021.

[41] A. Ceballos, A. Pattabi, A. El-Ghazaly, S. Ruta, C. P. Simon, R. F. L. Evans, T. Ostler, R. W. Chantrell, E. Kennedy, M. Scott, J. Bokor, and F. Hellman, “Role of element-specific damping in ultrafast, helicity-independent, all-optical switching dynamics in amorphous (gd,tb)co thin films,” *Phys. Rev. B*, vol. 103, p. 024438, Jan 2021.

[42] W. Zhang, J. X. Lin, T. X. Huang, G. Malinowski, M. Hehn, Y. Xu, S. Mangin, and W. Zhao, “Role of spin-lattice coupling in ultrafast demagnetization and all optical helicity-independent single-shot switching in $\mathrm{gd}_{1-x-y}\mathrm{tb}_y\mathrm{co}_x$ alloys,” *Phys. Rev. B*, vol. 105, p. 054410, Feb 2022.

[43] L. Avilés-Félix, A. Olivier, G. Li, C. S. Davies, L. Álvaro-Gómez, M. Rubio-Roy, S. Auffret, A. Kirilyuk, A. V. Kimel, T. Rasing, L. D. Buda-Prejbeanu, R. C. Sousa, B. Dieny, and I. L. Prejbeanu, “Single-shot all-optical switching of magnetization in tb/co multilayer-based electrodes,” *Scientific Reports*, vol. 10, p. 5211, Mar 2020.

[44] M. L. M. Lalieu, M. J. G. Peeters, S. R. R. Haenen, R. Lavrijsen, and B. Koopmans, “Deterministic all-optical switching of synthetic ferrimagnets using single femtosecond laser pulses,” *Phys. Rev. B*, vol. 96, p. 220411, Dec 2017.

[45] C. Banerjee, N. Teichert, K. E. Siewierska, Z. Gercsi, G. Y. P. Atcheson, P. Stamenov, K. Rode, J. M. D. Coey, and J. Besbas, “Single pulse all-optical toggle switching of magnetization without gadolinium in the ferrimagnet $\mathrm{mn}_2\mathrm{ru}_x\mathrm{ga}$,” *Nature Communications*, vol. 11, p. 4444, Sep 2020.

[46] C. S. Davies, G. Bonfiglio, K. Rode, J. Besbas, C. Banerjee, P. Stamenov, J. M. D. Coey, A. V. Kimel, and A. Kirilyuk, “Exchange-driven all-optical magnetic switching in compensated $3d$ ferrimagnets,” *Phys. Rev. Research*, vol. 2, p. 032044, Aug 2020.

[47] A. R. Khorsand, M. Savoini, A. Kirilyuk, A. V. Kimel, A. Tsukamoto, A. Itoh, and T. Rasing, "Element-specific probing of ultrafast spin dynamics in multisublattice magnets with visible light," *Phys. Rev. Lett.*, vol. 110, p. 107205, Mar 2013.

[48] C. Y. You and S. C. Shin, "Derivation of simplified analytic formulae for magneto-optical kerr effects," *Applied Physics Letters*, vol. 69, no. 9, pp. 1315–1317, 1996.

[49] T. Kampfrath, R. G. Ulbrich, F. Leuenberger, M. Münzenberg, B. Sass, and W. Felsch, "Ultrafast magneto-optical response of iron thin films," *Phys. Rev. B*, vol. 65, p. 104429, Feb 2002.

[50] J.-Y. Chen, J. Zhu, D. Zhang, D. M. Lattery, M. Li, J.-P. Wang, and X. Wang, "Time-resolved magneto-optical kerr effect of magnetic thin films for ultrafast thermal characterization," *The Journal of Physical Chemistry Letters*, vol. 7, pp. 2328–2332, Jul 2016.

[51] A. Y. Elezzabi, M. R. Freeman, and M. Johnson, "Direct measurement of the conduction electron spin-lattice relaxation time t_1 in gold," *Phys. Rev. Lett.*, vol. 77, pp. 3220–3223, Oct 1996.

[52] W. K. Hiebert, A. Stankiewicz, and M. R. Freeman, "Direct observation of magnetic relaxation in a small permalloy disk by time-resolved scanning kerr microscopy," *Phys. Rev. Lett.*, vol. 79, pp. 1134–1137, Aug 1997.

[53] J. Stöhr, "X-ray magnetic circular dichroism spectroscopy of transition metal thin films," *Journal of Electron Spectroscopy and Related Phenomena*, vol. 75, pp. 253–272, 1995. Future Perspectives for Electron Spectroscopy with Synchrotron Radiation.

[54] F. Radu, R. Abrudan, I. Radu, D. Schmitz, and H. Zabel, "Perpendicular exchange bias in ferrimagnetic spin valves," *Nature Communications*, vol. 3, p. 715, Mar 2012.

[55] A. Eschenlohr, M. Battiato, P. Maldonado, N. Pontius, T. Kachel, K. Holldack, R. Mitzner, A. Föhlisch, P. M. Oppeneer, and C. Stamm, "Ultrafast spin transport as key to femtosecond demagnetization," *Nature Materials*, vol. 12, pp. 332–336, Apr 2013.

[56] N. Bergeard, V. López-Flores, V. Halté, M. Hehn, C. Stamm, N. Pontius, E. Beaurepaire, and C. Boeglin, "Ultrafast angular momentum transfer in multisublattice ferrimagnets," *Nature Communications*, vol. 5, p. 3466, Mar 2014.

[57] G. van der Laan and A. I. Figueroa, "X-ray magnetic circular dichroism—a versatile tool to study magnetism," *Coordination Chemistry Reviews*, vol. 277-278, pp. 95–129, 2014. Following Chemical Structures using Synchrotron Radiation.

[58] J. Stöhr, "Exploring the microscopic origin of magnetic anisotropies with x-ray magnetic circular dichroism (xmcd) spectroscopy," *Journal of Magnetism and Magnetic Materials*, vol. 200, no. 1, pp. 470–497, 1999.

[59] J. Vogel, M. Sacchi, F. Sirotti, and G. Rossi, "X-ray dichroism of dy overlayers on a magnetic substrate," *Applied Surface Science*, vol. 65-66, pp. 170–174, 1993.

[60] M. M. Schwickert, G. Y. Guo, M. A. Tomaz, W. L. O'Brien, and G. R. Harp, "X-ray magnetic linear dichroism in absorption at the l edge of metallic co, fe, cr, and v," *Phys. Rev. B*, vol. 58, pp. R4289–R4292, Aug 1998.

[61] J. B. Kortright and S.-K. Kim, “Resonant magneto-optical properties of fe near its $2p$ levels: Measurement and applications,” *Phys. Rev. B*, vol. 62, pp. 12216–12228, Nov 2000.

[62] J. Stöhr, A. Scholl, T. J. Regan, S. Anders, J. Lüning, M. R. Scheinfein, H. A. Padmore, and R. L. White, “Images of the antiferromagnetic structure of a nio(100) surface by means of x-ray magnetic linear dichroism spectromicroscopy,” *Phys. Rev. Lett.*, vol. 83, pp. 1862–1865, Aug 1999.

[63] C. Luo, H. Ryll, C. H. Back, and F. Radu, “X-ray magnetic linear dichroism as a probe for non-collinear magnetic state in ferrimagnetic single layer exchange bias systems,” *Scientific Reports*, vol. 9, p. 18169, Dec 2019.

[64] J. Kuneš, P. Oppeneer, S. Valencia, D. Abramsohn, H.-C. Mertins, W. Gudat, M. Hecker, and C. Schneider, “Understanding the xmld and its magnetocrystalline anisotropy at the l2,3-edges of 3d transition metals,” *Journal of Magnetism and Magnetic Materials*, vol. 272-276, pp. 2146–2147, 2004. Proceedings of the International Conference on Magnetism (ICM 2003).

[65] G. van der Laan, “Magnetic linear x-ray dichroism as a probe of the magnetocrystalline anisotropy,” *Phys. Rev. Lett.*, vol. 82, pp. 640–643, Jan 1999.

[66] P. Tengdin, W. You, C. Chen, X. Shi, D. Zusin, Y. Zhang, C. Gentry, A. Blonsky, M. Keller, P. M. Oppeneer, H. C. Kapteyn, Z. Tao, and M. M. Murnane, “Critical behavior within 20 fs drives the out-of-equilibrium laser-induced magnetic phase transition in nickel,” *Science Advances*, vol. 4, no. 3, p. eaap9744, 2018.

[67] A. Damascelli, Z. Hussain, and Z.-X. Shen, “Angle-resolved photoemission studies of the cuprate superconductors,” *Rev. Mod. Phys.*, vol. 75, pp. 473–541, Apr 2003.

[68] L. Waldecker, R. Bertoni, and R. Ernstorfer, “Compact femtosecond electron diffractometer with 100 kev electron bunches approaching the single-electron pulse duration limit,” *Journal of Applied Physics*, vol. 117, no. 4, p. 044903, 2015.

[69] D. Zahn, F. Jakobs, H. Seiler, T. A. Butcher, D. Engel, J. Vorberger, U. Atxitia, Y. W. Windsor, and R. Ernstorfer, “Intrinsic energy flow in laser-excited $3d$ ferromagnets,” *Phys. Rev. Research*, vol. 4, p. 013104, Feb 2022.

[70] O. Eriksson, A. Bergman, L. Bergqvist, and J. Hellsvik, *Atomistic Spin Dynamics: Foundations and Applications.* Oxford University Press, 02 2017.

[71] P. W. Atkins and R. S. Friedman, *Molecular Quantum Mechanics.* Oxford University Press, 2010.

[72] U. Nowak, *Classical Spin Models - Handbook of Magnetsim and Advanced Magnetic Materials.* John Wiley and Sons, Ltd,, 2007.

[73] P. Hohenberg and W. Kohn, “Inhomogeneous electron gas,” *Phys. Rev.*, vol. 136, pp. B864–B871, Nov 1964.

[74] W. Kohn and L. J. Sham, “Self-consistent equations including exchange and correlation effects,” *Phys. Rev.*, vol. 140, pp. A1133–A1138, Nov 1965.

[75] L. Hedin, “New method for calculating the one-particle green’s function with application to the electron-gas problem,” *Phys. Rev.*, vol. 139, pp. A796–A823, Aug 1965.

[76] L. Hedin and B. I. Lundqvist, “Explicit local exchange-correlation potentials,” *Journal of Physics C: Solid State Physics*, vol. 4, pp. 2064–2083, oct 1971.

[77] V. Moruzzi, J. Janak, and A. Williams, “Iv - electron and state densities,” in *Calculated Electronic Properties of Metals* (V. Moruzzi, J. Janak, and A. Williams, eds.), pp. 30–159, Pergamon, 1978.

[78] A. I. Liechtenstein, M. I. Katsnelson, and V. A. Gubanov, “Exchange interactions and spin-wave stiffness in ferromagnetic metals,” *Journal of Physics F: Metal Physics*, vol. 14, pp. L125–L128, jul 1984.

[79] A. Liechtenstein, M. Katsnelson, V. Antropov, and V. Gubanov, “Local spin density functional approach to the theory of exchange interactions in ferromagnetic metals and alloys,” *Journal of Magnetism and Magnetic Materials*, vol. 67, no. 1, pp. 65–74, 1987.

[80] M. Stamenova, J. Simoni, and S. Sanvito, “Role of spin-orbit interaction in the ultrafast demagnetization of small iron clusters,” *Phys. Rev. B*, vol. 94, p. 014423, Jul 2016.

[81] W. Heisenberg, “Zur Theorie des Ferromagnetismus,” *Zeitschrift für Physik*, vol. 49, pp. 619–636, Sep 1928.

[82] N. M. N. Ashcroft, *Solid State Physics.* Cengage Learning, Jan 1976.

[83] R. F. L. Evans, W. J. Fan, P. Chureemart, T. A. Ostler, M. O. A. Ellis, and R. W. Chantrell, “Atomistic spin model simulations of magnetic nanomaterials,” *Journal of Physics: Condensed Matter*, vol. 26, p. 103202, feb 2014.

[84] D. A. Garanin, “Self-consistent gaussian approximation for classical spin systems: Thermodynamics,” *Phys. Rev. B*, vol. 53, pp. 11593–11605, May 1996.

[85] L. Rózsa, K. Palotás, A. Deák, E. Simon, R. Yanes, L. Udvardi, L. Szunyogh, and U. Nowak, “Formation and stability of metastable skyrmionic spin structures with various topologies in an ultrathin film,” *Phys. Rev. B*, vol. 95, p. 094423, Mar 2017.

[86] P. Ehrenfest, “Bemerkung über die angenäherte Gültigkeit der klassischen Mechanik innerhalb der Quantenmechanik,” *Zeitschrift fur Physik*, vol. 45, pp. 455–457, July 1927.

[87] L. Landau and E. Lifshitz, “On the theory of the dispersion of magnetic permeability in ferromagnetic bodies,” *Phys. Z. Sowjetunion*, vol. 8, pp. 153–164, 1935.

[88] T. L. Gilbert, “A lagrangian formulation of the gyromagnetic equation of the magnetization field,” *Physical Review D*, vol. 100, p. 1243, 1955.

[89] A. Amikam, *Introduction to the Theory of Ferromagnetism.* Oxford University Press, 2008.

[90] V. Kamberský, “On the landau–lifshitz relaxation in ferromagnetic metals,” *Canadian Journal of Physics*, vol. 48, no. 24, pp. 2906–2911, 1970.

[91] V. Kamberský, “On ferromagnetic resonance damping in metals,” *Czechoslovak Journal of Physics B*, vol. 26, pp. 1366–1383, Dec 1976.

[92] J. Kuneš and V. Kamberský, "First-principles investigation of the damping of fast magnetization precession in ferromagnetic $3d$ metals," *Phys. Rev. B*, vol. 65, p. 212411, Jun 2002.

[93] A. Brataas, Y. Tserkovnyak, and G. E. W. Bauer, "Scattering theory of gilbert damping," *Phys. Rev. Lett.*, vol. 101, p. 037207, Jul 2008.

[94] A. A. Starikov, P. J. Kelly, A. Brataas, Y. Tserkovnyak, and G. E. W. Bauer, "Unified first-principles study of gilbert damping, spin-flip diffusion, and resistivity in transition metal alloys," *Phys. Rev. Lett.*, vol. 105, p. 236601, Dec 2010.

[95] S. Mankovsky, D. Ködderitzsch, G. Woltersdorf, and H. Ebert, "First-principles calculation of the gilbert damping parameter via the linear response formalism with application to magnetic transition metals and alloys," *Phys. Rev. B*, vol. 87, p. 014430, Jan 2013.

[96] W. F. Brown, "Thermal fluctuations of a single-domain particle," *Phys. Rev.*, vol. 130, pp. 1677–1686, Jun 1963.

[97] U. Atxitia, O. Chubykalo-Fesenko, R. W. Chantrell, U. Nowak, and A. Rebei, "Ultrafast spin dynamics: The effect of colored noise," *Phys. Rev. Lett.*, vol. 102, p. 057203, Feb 2009.

[98] "*CUDA C Best Practice Guide.* english. version 11.7." `https://docs.nvidia.com/cuda/pdf/CUDA_C_Best_Practices_Guide.pdf`. Accessed: September 2022.

[99] A. Donges, *Computer Simulations of Ultrafast Magnetic Phenomena.* PhD thesis, Universität Konstanz, Konstanz, 2018.

[100] "*CUDA Toolkit Documentation - cuRAND* english. version 11.7." `https://docs.nvidia.com/cuda/curand/index.html`. Accessed: September 2022.

[101] J. L. García-Palacios and F. J. Lázaro, "Langevin-dynamics study of the dynamical properties of small magnetic particles," *Phys. Rev. B*, vol. 58, pp. 14937–14958, Dec 1998.

[102] M. Kaganov, I. Lifshitz, and L. Tanatarov, "Relaxation between electrons and crystalline lattices," *Sov. Phys. JETP*, vol. 4, p. 173, 1957.

[103] P. Debye, "Zur Theorie der spezifischen Wärmen," *Annalen der Physik*, vol. 344, no. 14, pp. 789–839, 1912.

[104] A. Einstein, "Die Plancksche Theorie der Strahlung und die Theorie der spezifischen Wärme," *Annalen der Physik*, vol. 327, no. 1, pp. 180–190, 1907.

[105] Z. Lin, L. V. Zhigilei, and V. Celli, "Electron-phonon coupling and electron heat capacity of metals under conditions of strong electron-phonon nonequilibrium," *Phys. Rev. B*, vol. 77, p. 075133, Feb 2008.

[106] S. Wienholdt, *Modeling of Laser-Induced Ultrafast Spin Dynamics in Magnetically Ordered Materials.* PhD thesis, Universität Konstanz, 2015.

[107] W. You, P. Tengdin, C. Chen, X. Shi, D. Zusin, Y. Zhang, C. Gentry, A. Blonsky, M. Keller, P. M. Oppeneer, H. Kapteyn, Z. Tao, and M. Murnane, "Revealing the nature of the ultrafast magnetic phase transition in ni by correlating extreme ultraviolet magneto-optic and photoemission spectroscopies," *Phys. Rev. Lett.*, vol. 121, p. 077204, Aug 2018.

[108] H. Warlimont and W. Martienssen, *Springer Handbook of Materials Datam.* Springer, 2018.

[109] B. Frietsch, A. Donges, R. Carley, M. Teichmann, J. Bowlan, K. Döbrich, K. Carva, D. Legut, P. M. Oppeneer, U. Nowak, and M. Weinelt, "The role of ultrafast magnon generation in the magnetization dynamics of rare-earth metals," *Science Advances*, vol. 6, no. 39, p. eabb1601, 2020.

[110] J. Chen, D. Tzou, and J. Beraun, "A semiclassical two-temperature model for ultrafast laser heating," *International Journal of Heat and Mass Transfer*, vol. 49, no. 1, pp. 307–316, 2006.

[111] E. Carpene, "Ultrafast laser irradiation of metals: Beyond the two-temperature model," *Phys. Rev. B*, vol. 74, p. 024301, Jul 2006.

[112] P. Maldonado, K. Carva, M. Flammer, and P. M. Oppeneer, "Theory of out-of-equilibrium ultrafast relaxation dynamics in metals," *Phys. Rev. B*, vol. 96, p. 174439, Nov 2017.

[113] U. Ritzmann, P. M. Oppeneer, and P. Maldonado, "Theory of out-of-equilibrium electron and phonon dynamics in metals after femtosecond laser excitation," *Phys. Rev. B*, vol. 102, p. 214305, Dec 2020.

[114] B. Frietsch, J. Bowlan, R. Carley, M. Teichmann, S. Wienholdt, D. Hinzke, U. Nowak, K. Carva, P. M. Oppeneer, and M. Weinelt, "Disparate ultrafast dynamics of itinerant and localized magnetic moments in gadolinium metal," *Nature Communications*, vol. 6, p. 8262, Sep 2015.

[115] X. Wang, S. Nie, J. Li, R. Clinite, J. E. Clark, and J. Cao, "Temperature dependence of electron-phonon thermalization and its correlation to ultrafast magnetism," *Phys. Rev. B*, vol. 81, p. 220301, Jun 2010.

[116] V. G. Bar'yakhtar, V. I. Butrim, and B. A. Ivanov, "Exchange relaxation as a mechanism of the ultrafast reorientation of spins in a two-sublattice ferrimagnet," *JETP Letters*, vol. 98, pp. 289–293, Nov 2013.

[117] Y. M. Gufan, A. S. Prokhorov, and E. G. Rudashevskii, "Closed-form description of the magnetization and of the resonant frequencies of antiferromagnets in a magnetic field.," *Sov. Phys. JETP*, vol. 50, p. 1156, 1979.

[118] I. Radu, C. Stamm, A. Eschenlohr, F. Radu, R. Abrudan, K. Vahaplar, T. Kachel, N. Pontius, R. Mitzner, K. Holldack, A. Föhlisch, T. A. Ostler, J. H. Mentink, R. F. L. Evans, R. W. Chantrell, A. Tsukamoto, A. Itoh, A. Kirilyuk, A. V. Kimel, and T. Rasing, "Ultrafast and distinct spin dynamics in magnetic alloys," *SPIN*, vol. 05, no. 03, p. 1550004, 2015.

[119] J. H. Mentink, "Manipulating magnetism by ultrafast control of the exchange interaction," *Journal of Physics: Condensed Matter*, vol. 29, p. 453001, oct 2017.

[120] R. Mishra, J. Yu, X. Qiu, M. Motapothula, T. Venkatesan, and H. Yang, "Anomalous current-induced spin torques in ferrimagnets near compensation," *Phys. Rev. Lett.*, vol. 118, p. 167201, Apr 2017.

[121] J. Yu, D. Bang, R. Mishra, R. Ramaswamy, J. H. Oh, H. J. Park, Y. Jeong, P. Van Thach, D.-K. Lee, G. Go, S. W. Lee, Y. Wang, S. Shi, X. Qiu, H. Awano, K. J. Lee, and H. Yang, "Long spin coherence length and bulk-like spin–orbit torque in ferrimagnetic multilayers," *Nature Materials*, vol. 18, Jan 2019.

[122] K. Cai, Z. Zhu, J. M. Lee, R. Mishra, L. Ren, S. D. Pollard, P. He, G. Liang, K. L. Teo, and H. Yang, "Ultrafast and energy-efficient spin–orbit torque switching in compensated ferrimagnets," *Nature Electronics*, vol. 3, pp. 37–42, Jan 2020.

[123] K.-J. Kim, S. K. Kim, Y. Hirata, S.-H. Oh, T. Tono, D.-H. Kim, T. Okuno, W. S. Ham, S. Kim, G. Go, Y. Tserkovnyak, A. Tsukamoto, T. Moriyama, K.-J. Lee, and T. Ono, "Fast domain wall motion in the vicinity of the angular momentum compensation temperature of?ferrimagnets," *Nature Materials*, vol. 16, no. 12, pp. 1187–1192, 2017.

[124] L. Caretta, M. Mann, F. Büttner, K. Ueda, B. Pfau, C. M. Günther, P. Hessing, A. Churikova, C. Klose, M. Schneider, D. Engel, C. Marcus, D. Bono, K. Bagschik, S. Eisebitt, and G. S. D. Beach, "Fast current-driven domain walls and small skyrmions in a compensated ferrimagnet," *Nature Nanotechnology*, vol. 13, no. 12, pp. 1154–1160, 2018.

[125] A. Donges, N. Grimm, F. Jakobs, S. Selzer, U. Ritzmann, U. Atxitia, and U. Nowak, "Unveiling domain wall dynamics of ferrimagnets in thermal magnon currents: Competition of angular momentum transfer and entropic torque," *Phys. Rev. Research*, vol. 2, p. 013293, Mar 2020.

[126] J. H. Mentink, J. Hellsvik, D. V. Afanasiev, B. A. Ivanov, A. Kirilyuk, A. V. Kimel, O. Eriksson, M. I. Katsnelson, and T. Rasing, "Ultrafast spin dynamics in multisublattice magnets," *Physical Review Letters*, vol. 108, p. 057202, 1 2012.

[127] A. J. Schellekens and B. Koopmans, "Microscopic model for ultrafast magnetization dynamics of multisublattice magnets," *Phys. Rev. B*, vol. 87, p. 020407, Jan 2013.

[128] S. Wienholdt, D. Hinzke, K. Carva, P. M. Oppeneer, and U. Nowak, "Orbital-resolved spin model for thermal magnetization switching in rare-earth-based ferrimagnets," *Physical Review B*, vol. 88, p. 020406, 7 2013.

[129] A. M. Kalashnikova and V. I. Kozub, "Exchange scattering as the driving force for ultrafast all-optical and bias-controlled reversal in ferrimagnetic metallic structures," *Phys. Rev. B*, vol. 93, p. 054424, Feb 2016.

[130] V. N. Gridnev, "Ferromagneticlike states and all-optical magnetization switching in ferrimagnets," *Phys. Rev. B*, vol. 98, p. 014427, Jul 2018.

[131] C. S. Davies, T. Janssen, J. H. Mentink, A. Tsukamoto, A. V. Kimel, A. van der Meer, A. Stupakiewicz, and A. Kirilyuk, "Pathways for single-shot all-optical switching of magnetization in ferrimagnets," *Phys. Rev. Applied*, vol. 13, p. 024064, Feb 2020.

[132] T. A. Ostler, R. F. L. Evans, R. W. Chantrell, U. Atxitia, O. Chubykalo-Fesenko, I. Radu, R. Abrudan, F. Radu, A. Tsukamoto, A. Itoh, A. Kirilyuk, T. Rasing, and

A. Kimel, “Crystallographically amorphous ferrimagnetic alloys: Comparing a localized atomistic spin model with experiments,” *Phys. Rev. B*, vol. 84, p. 024407, Jul 2011.

[133] E. Iacocca, T.-M. M. Liu, A. H. Reid, Z. Fu, S. Ruta, P. W. Granitzka, E. Jal, S. Bonetti, A. X. Gray, C. E. Graves, R. Kukreja, Z. Chen, D. J. Higley, T. Chase, L. Le Guyader, K. Hirsch, H. Ohldag, W. F. Schlotter, G. L. Dakovski, G. Coslovich, M. C. Hoffmann, S. Carron, A. Tsukamoto, A. Kirilyuk, A. V. Kimel, T. Rasing, J. Stöhr, R. F. L. Evans, T. Ostler, R. W. Chantrell, M. A. Hoefer, T. J. Silva, and H. A. Dürr, “Spin-current-mediated rapid magnon localisation and coalescence after ultrafast optical pumping of ferrimagnetic alloys.,” *Nature Communications*, vol. 10, no. 1, p. 1756, 2019.

[134] U. Atxitia, J. Barker, R. W. Chantrell, and O. Chubykalo-Fesenko, “Controlling the polarity of the transient ferromagneticlike state in ferrimagnets,” *Phys. Rev. B*, vol. 89, p. 224421, Jun 2014.

[135] J. Barker, U. Atxitia, T. A. Ostler, O. Hovorka, R. W. Chantrell, O. Chubykalo-Fesenko, and R. W. Chantrell, “Two-magnon bound state causes ultrafast thermally induced magnetisation switching.,” *Scientific reports*, vol. 3, p. 3262, jan 2013.

[136] J. Gorchon, C.-H. Lambert, Y. Yang, A. Pattabi, R. B. Wilson, S. Salahuddin, and J. Bokor, “Single shot ultrafast all optical magnetization switching of ferromagnetic co/pt multilayers,” *Applied Physics Letters*, vol. 111, no. 4, p. 042401, 2017.

[137] J. Nickolls, I. Buck, M. Garland, and K. Skadron, “Scalable parallel programming with cuda,” *Queue*, vol. 6, p. 40–53, Mar. 2008.

[138] A. Ceballos, A. Pattabi, A. El-Ghazaly, S. Ruta, C. P. Simon, R. F. L. Evans, T. Ostler, R. W. Chantrell, E. Kennedy, M. Scott, J. Bokor, and F. Hellman, “Role of element-specific damping on the ultrafast, helicity-independent all-optical switching dynamics in amorphous (gd,tb)co thin films,” 2019.

[139] I. Radu, G. Woltersdorf, M. Kiessling, A. Melnikov, U. Bovensiepen, J.-U. Thiele, and C. H. Back, “Laser-induced magnetization dynamics of lanthanide-doped permalloy thin films,” *Phys. Rev. Lett.*, vol. 102, p. 117201, Mar 2009.

[140] A. Rebei and J. Hohlfeld, “Origin of increase of damping in transition metals with rare-earth-metal impurities,” *Phys. Rev. Lett.*, vol. 97, p. 117601, Sep 2006.

[141] D.-H. Kim, T. Okuno, S. K. Kim, S.-H. Oh, T. Nishimura, Y. Hirata, Y. Futakawa, H. Yoshikawa, A. Tsukamoto, Y. Tserkovnyak, Y. Shiota, T. Moriyama, K.-J. Kim, K.-J. Lee, and T. Ono, “Low magnetic damping of ferrimagnetic gdfeco alloys,” *Phys. Rev. Lett.*, vol. 122, p. 127203, Mar 2019.

[142] M. L. M. Lalieu, R. Lavrijsen, and B. Koopmans, “Integrating all-optical switching with spintronics,” *Nature Communications*, vol. 10, Oct 2019.

[143] R. F. L. Evans, T. a. Ostler, R. W. Chantrell, I. Radu, and T. Rasing, “Ultrafast thermally induced magnetic switching in synthetic ferrimagnets,” *Applied Physics Letters*, vol. 104, p. 082410, 2 2014.

[144] C. Xu, T. A. Ostler, and R. W. Chantrell, “Thermally induced magnetization switching in gd/fe multilayers,” *Phys. Rev. B*, vol. 93, p. 054302, Feb 2016.

[145] T.-M. Liu, T. Wang, A. H. Reid, M. Savoini, X. Wu, B. Koene, P. Granitzka, C. E. Graves, D. J. Higley, Z. Chen, G. Razinskas, M. Hantschmann, A. Scherz, J. Stöhr, A. Tsukamoto, B. Hecht, A. V. Kimel, A. Kirilyuk, T. Rasing, and H. A. Dürr, "Nanoscale confinement of all-optical magnetic switching in TbFeCo - competition with nanoscale heterogeneity," *Nano Letters*, vol. 15, no. 10, pp. 6862–6868, 2015.

[146] S. Lenne, A. Lau, Y. C. Jha, G. Atcheson, R. E. Troncoso, A. Brataas, J. Coey, P. Stamenov, and R. K., "Giant spin-orbit torque in a single ferrimagnetic metal layer," *Preprint at https://arxiv.org*, 2019.

[147] G. Bonfiglio, K. Rode, K. Siewerska, J. Besbas, G. Y. P. Atcheson, P. Stamenov, J. M. D. Coey, A. V. Kimel, T. Rasing, and A. Kirilyuk, "Magnetization dynamics of the compensated ferrimagnet $\mathrm{Mn_2Ru_xGa}$," *Physical Review B*, vol. 100, p. 104438, sep 2019.

[148] G. Bonfiglio, K. Rode, G. Y. P. Atcheson, P. Stamenov, J. M. D. Coey, A. V. Kimel, T. Rasing, and A. Kirilyuk, "Sub-picosecond exchange–relaxation in the compensated ferrimagnet mn2ru x ga," *Journal of Physics: Condensed Matter*, vol. 33, p. 135804, jan 2021.

[149] C. Fowley, K. Rode, Y.-C. Lau, N. Thiyagarajah, D. Betto, K. Borisov, G. Atcheson, E. Kampert, Z. Wang, Y. Yuan, S. Zhou, J. Lindner, P. Stamenov, J. M. D. Coey, and A. M. Deac, "Magnetocrystalline anisotropy and exchange probed by high-field anomalous Hall effect in fully compensated half-metallic $\mathrm{Mn_2Ru_xGa}$ thin films," *Physical Review B*, vol. 98, p. 220406, Dec 2018.

[150] D. Betto, N. Thiyagarajah, Y.-C. Lau, C. Piamonteze, M.-A. Arrio, P. Stamenov, J. M. D. Coey, and K. Rode, "Site-specific magnetism of half-metallic $\mathrm{Mn_2Ru_xGa}$ thin films determined by x-ray absorption spectroscopy," *Physical Review B*, vol. 91, p. 094410, Mar 2015.

[151] G. P. Zhang, R. Meadows, A. Tamayo, Y. H. Bai, and T. F. George, "An attempt to simulate laser-induced all-optical spin switching in a crystalline ferrimagnet," *AIP Advances*, vol. 10, p. 125323, dec 2020.

[152] H. Kurt, K. Rode, P. Stamenov, M. Venkatesan, Y.-C. Lau, E. Fonda, and J. M. D. Coey, "Cubic $\mathrm{Mn_2Ga}$ thin films: crossing the spin gap with Ruthenium," *Physical Review Letters*, vol. 112, p. 027201, Jan 2014.

[153] L. Yang, B. Liu, F. Meng, H. Liu, H. Luo, E. Liu, W. Wang, and G. Wu, "Magnetic properties of Heusler alloy $\mathrm{Mn_2RuGe}$ and $\mathrm{Mn_2RuGa}$ ribbons," *Journal of Magnetism and Magnetic Materials*, vol. 379, pp. 1–5, 2015.

[154] I. Galanakis, K. Özdoğan, E. Şaşıoğlu, and S. Blügel, "Effect of disorder on the magnetic properties of cubic $\mathrm{Mn_2Ru_xGa}$ compounds: A first-principles study," *Journal of Applied Physics*, vol. 116, p. 33903, jul 2014.

[155] J. S. Smart and J. H. Van Vleck, "Effective field theories of magnetism," *Physics Today*, vol. 19, no. 8, pp. 77–78, 1966.

[156] N. Thiyagarajah, Y.-C. Lau, D. Betto, K. Borisov, J. M. D. Coey, P. Stamenov, and K. Rode, "Giant spontaneous Hall effect in zero-moment $\mathrm{Mn_2Ru_xGa}$," *Applied Physics Letters*, vol. 106, no. 12, p. 122402, 2015.

[157] A. Mekonnen, A. R. Khorsand, M. Cormier, A. V. Kimel, A. Kirilyuk, A. Hrabec, L. Ranno, A. Tsukamoto, A. Itoh, and T. Rasing, “Role of the inter-sublattice exchange coupling in short-laser-pulse-induced demagnetization dynamics of GdCo and GdCoFe alloys,” *Physical Review B*, vol. 87, p. 180406, May 2013.

[158] L. Le Guyader, S. El Moussaoui, M. Buzzi, R. V. Chopdekar, L. J. Heyderman, a. Tsukamoto, A. Itoh, A. Kirilyuk, T. Rasing, A. V. Kimel, and F. Nolting, “Demonstration of laser induced magnetization reversal in GdFeCo nanostructures,” *Applied Physics Letters*, vol. 101, no. 2, p. 022410, 2012.

[159] M. S. El Hadri, P. Pirro, C.-H. Lambert, S. Petit-Watelot, Y. Quessab, M. Hehn, F. Montaigne, G. Malinowski, and S. Mangin, “Two types of all-optical magnetization switching mechanisms using femtosecond laser pulses,” *Phys. Rev. B*, vol. 94, p. 064412, Aug 2016.

[160] J.-Y. Chen, L. He, J.-P. Wang, and M. Li, “All-Optical Switching of Magnetic Tunnel Junctions with Single Subpicosecond Laser Pulses,” *Physical Review Applied*, vol. 7, p. 21001, feb 2017.

[161] D. O. Ignatyeva, C. S. Davies, D. A. Sylgacheva, A. Tsukamoto, H. Yoshikawa, P. O. Kapralov, A. Kirilyuk, V. I. Belotelov, and A. V. Kimel, “Plasmonic layer-selective all-optical switching of magnetization with nanometer resolution,” *Nature Communications*, vol. 10, no. 1, p. 4786, 2019.

[162] Y. L. W. van Hees, P. van de Meugheuvel, B. Koopmans, and R. Lavrijsen, “Deterministic all-optical magnetization writing facilitated by non-local transfer of spin angular momentum,” *Nature Communications*, vol. 11, no. 1, p. 3835, 2020.

[163] K. Vahaplar, A. Kalashnikova, A. V. Kimel, D. Hinzke, U. Nowak, R. Chantrell, A. Tsukamoto, A. Itoh, A. Kirilyuk, and T. Rasing, “Ultrafast Path for Optical Magnetization Reversal via a Strongly Nonequilibrium State,” *Physical Review Letters*, vol. 103, p. 117201, sep 2009.

[164] A. Baral and H. C. Schneider, “Magnetic switching dynamics due to ultrafast exchange scattering: A model study,” *Physical Review B*, vol. 91, p. 100402, mar 2015.

[165] V. N. Gridnev, “Ultrafast heating-induced magnetization switching in ferrimagnets,” *Journal of Physics: Condensed Matter*, vol. 28, no. 47, p. 476007, 2016.

[166] G. P. Zhang, T. Latta, Z. Babyak, Y. H. Bai, and T. F. George, “All-optical spin switching: A new frontier in femtomagnetism — A short review and a simple theory,” *Modern Physics Letters B*, vol. 30, p. 16300052, aug 2016.

[167] V. N. Krivoruchko, “Longitudinal spin dynamics in ferrimagnets: Multiple spin wave nature of longitudinal spin excitations,” *Physical Review B*, vol. 94, p. 54434, aug 2016.

[168] M. Beens, M. L. M. Lalieu, A. J. M. Deenen, R. A. Duine, and B. Koopmans, “Comparing all-optical switching in synthetic-ferrimagnetic multilayers and alloys,” *Physical Review B*, vol. 100, p. 220409, dec 2019.

[169] C. Vogler, C. Abert, F. Bruckner, and D. Suess, “Stochastic ferrimagnetic Landau-Lifshitz-Bloch equation for finite magnetic structures,” *Physical Review B*, vol. 100, p. 054401, aug 2019.

[170] K. Carva, P. Baláž, and I. Radu, "Chapter 2 - Laser-Induced Ultrafast Magnetic Phenomena," in *Handbook of Magnetic Materials* (E. B. T. H. o. M. M. Brück, ed.), vol. 26, pp. 291–463, Elsevier, 2017.

[171] U. Atxitia, P. Nieves, and O. Chubykalo-Fesenko, "Landau-lifshitz-bloch equation for ferrimagnetic materials," *Phys. Rev. B*, vol. 86, p. 104414, Sep 2012.

[172] U. Atxitia, D. Hinzke, O. Chubykalo-Fesenko, U. Nowak, H. Kachkachi, O. N. Mryasov, R. F. Evans, and R. W. Chantrell, "Multiscale modeling of magnetic materials: Temperature dependence of the exchange stiffness," *Phys. Rev. B*, vol. 82, p. 134440, Oct 2010.

[173] D. A. Garanin, "Fokker-planck and landau-lifshitz-bloch equations for classical ferromagnets," *Physical Review B*, vol. 55, pp. 3050–3057, 2 1997.

[174] J.-W. Liao, P. Vallobra, L. O'Brien, U. Atxitia, V. Raposo, D. Petit, T. Vemulkar, G. Malinowski, M. Hehn, E. Martínez, S. Mangin, and R. Cowburn, "Controlling All-Optical Helicity-Dependent Switching in Engineered Rare-Earth Free Synthetic Ferrimagnets," *Advanced Science*, vol. 6, no. 24, 2019.

[175] A. Kirilyuk, A. V. Kimel, and T. Rasing, "Ultrafast optical manipulation of magnetic order," *Reviews of Modern Physics*, vol. 82, pp. 2731–2784, Sep 2010.

[176] K. Carva, M. Battiato, D. Legut, and P. M. Oppeneer, "Ab initio theory of electron-phonon mediated ultrafast spin relaxation of laser-excited hot electrons in transition-metal ferromagnets," *Physical Review B*, vol. 87, p. 184425, May 2013.

[177] A. V. Kimel, A. Kirilyuk, A. Tsvetkov, R. V. Pisarev, and T. Rasing, "Laser-induced ultrafast spin reorientation in the antiferromagnet TmFeO3," *Nature*, vol. 429, no. 6994, pp. 850–853, 2004.

[178] P. Wadley, B. Howells, J. Železný, C. Andrews, V. Hills, R. P. Campion, V. Novák, K. Olejník, F. Maccherozzi, S. S. Dhesi, S. Y. Martin, T. Wagner, J. Wunderlich, F. Freimuth, Y. Mokrousov, J. Kuneš, J. S. Chauhan, M. J. Grzybowski, A. W. Rushforth, K. W. Edmonds, B. L. Gallagher, and T. Jungwirth, "Electrical switching of an antiferromagnet," *Science*, vol. 351, pp. 587 LP – 590, feb 2016.

[179] V. Baltz, A. Manchon, M. Tsoi, T. Moriyama, T. Ono, and Y. Tserkovnyak, "Antiferromagnetic spintronics," *Reviews of Modern Physics*, vol. 90, p. 15005, feb 2018.

[180] T. Jungwirth, X. Marti, P. Wadley, and J. Wunderlich, "Antiferromagnetic spintronics," *Nature Nanotechnology*, vol. 11, no. 3, pp. 231–241, 2016.

[181] K. Olejník, T. Seifert, Z. Kašpar, V. Novák, P. Wadley, R. P. Campion, M. Baumgartner, P. Gambardella, P. Němec, J. Wunderlich, J. Sinova, P. Kužel, M. Müller, T. Kampfrath, and T. Jungwirth, "Terahertz electrical writing speed in an antiferromagnetic memory," *Science Advances*, vol. 4, p. eaar3566, mar 2018.

[182] L. Rózsa, S. Selzer, T. Birk, U. Atxitia, and U. Nowak, "Reduced thermal stability of antiferromagnetic nanostructures," *Phys. Rev. B*, vol. 100, p. 064422, Aug 2019.

[183] Z. Kašpar, M. Surýnek, J. Zubáč, F. Krizek, V. Novák, R. P. Campion, M. S. Wörnle, P. Gambardella, X. Marti, P. Němec, K. W. Edmonds, S. Reimers, O. J. Amin,

F. Maccherozzi, S. S. Dhesi, P. Wadley, J. Wunderlich, K. Olejník, and T. Jungwirth, “Quenching of an antiferromagnet into high resistivity states using electrical or ultrashort optical pulses,” *Nature Electronics*, 2020.

[184] C. Kittel, “Theory of antiferromagnetic resonance,” *Physial Review*, vol. 82, pp. 565–565, May 1951.

[185] T. Kampfrath, A. Sell, G. Klatt, A. Pashkin, S. Mährlein, T. Dekorsy, M. Wolf, M. Fiebig, A. Leitenstorfer, and R. Huber, “Coherent terahertz control of antiferromagnetic spin waves,” *Nature Photonics*, vol. 5, no. 1, pp. 31–34, 2011.

[186] M. Fiebig, N. P. Duong, T. Satoh, B. B. Van Aken, K. Miyano, Y. Tomioka, and Y. Tokura, “Ultrafast magnetization dynamics of antiferromagnetic compounds,” *Journal of Physics D: Applied Physics*, vol. 41, no. 16, p. 164005, 2008.

[187] N. Thielemann-Kühn, D. Schick, N. Pontius, C. Trabant, R. Mitzner, K. Holldack, H. Zabel, A. Föhlisch, and C. Schüßler-Langeheine, “Ultrafast and Energy-Efficient Quenching of Spin Order: Antiferromagnetism Beats Ferromagnetism,” *Physical Review Letters*, vol. 119, p. 197202, nov 2017.

[188] U. Atxitia and O. Chubykalo-Fesenko, “Ultrafast magnetization dynamics rates within the Landau-Lifshitz-Bloch model,” *Physical Review B*, vol. 84, p. 144414, oct 2011.

[189] Q. H. Wang, A. Bedoya-Pinto, M. Blei, A. H. Dismukes, A. Hamo, S. Jenkins, M. Koperski, Y. Liu, Q.-C. Sun, E. J. Telford, H. H. Kim, M. Augustin, U. Vool, J.-X. Yin, L. H. Li, A. Falin, C. R. Dean, F. Casanova, R. F. L. Evans, M. Chshiev, A. Mishchenko, C. Petrovic, R. He, L. Zhao, A. W. Tsen, B. D. Gerardot, M. Brotons-Gisbert, Z. Guguchia, X. Roy, S. Tongay, Z. Wang, M. Z. Hasan, J. Wrachtrup, A. Yacoby, A. Fert, S. Parkin, K. S. Novoselov, P. Dai, L. Balicas, and E. J. G. Santos, “The magnetic genome of two-dimensional van der waals materials,” *ACS Nano*, 2022. PMID: 35442017.

[190] V. Barthem, C. Colin, H. Mayaffre, M.-H. Julien, and D. Givord, “Revealing the properties of mn 2 au for antiferromagnetic spintronics,” *Nat. Commun.*, vol. 4, no. 1, p. 2892, 2013.

[191] P. E. Roy, R. M. Otxoa, and J. Wunderlich, “Robust picosecond writing of a layered antiferromagnet by staggered spin-orbit fields,” *Phys. Rev. B*, vol. 94, no. 1, p. 014439, 2016.

[192] M. Meinert, D. Graulich, and T. Matalla-Wagner, “Electrical switching of antiferromagnetic mn2au and the role of thermal activation,” *Phys. Rev. Appl.*, vol. 9, no. 6, p. 064040, 2018.

[193] R. Jedynak, “Approximation of the inverse langevin function revisited,” *Rheologica Acta*, vol. 54, pp. 29–39, Jan. 2015.

[194] A. N. Nguessong, T. Beda, and F. Peyraut, “A new based error approach to approximate the inverse langevin function,” *Rheologica Acta*, vol. 53, pp. 585–591, Aug. 2014.

[195] W. Töws and G. M. Pastor, “Many-body theory of ultrafast demagnetization and angular momentum transfer in ferromagnetic transition metals,” *Phys. Rev. Lett.*, vol. 115, p. 217204, Nov 2015.

[196] B. Y. Mueller and B. Rethfeld, "Thermodynamic μt model of ultrafast magnetization dynamics," *Phys. Rev. B*, vol. 90, p. 144420, 2014.

[197] N. Kazantseva, U. Nowak, R. W. Chantrell, J. Hohlfeld, and A. Rebei, "Slow recovery of the magnetisation after a sub-picosecond heat pulse," *EPL*, vol. 81, no. 2, p. 27004, 2007.

[198] T. Balashov, A. F. Takács, M. Däne, A. Ernst, P. Bruno, and W. Wulfhekel, "Inelastic electron-magnon interaction and spin transfer torque," *Phys. Rev. B*, vol. 78, p. 174404, 2008.

[199] M. Krauß, T. Roth, S. Alebrand, D. Steil, M. Cinchetti, M. Aeschlimann, and H. C. Schneider, "Ultrafast demagnetization of ferromagnetic transition metals: The role of the coulomb interaction," *Phys. Rev. B*, vol. 80, p. 180407(R), 2009.

[200] A. B. Schmidt, M. Pickel, M. Donath, P. Buczek, A. Ernst, V. P. Zhukov, P. M. Echenique, L. M. Sandratskii, E. V. Chulkov, and M. Weinelt, "Ultrafast magnon generation in an fe film on cu(100)," *Phys. Rev. Lett.*, vol. 105, p. 197401, Nov 2010.

[201] U. Atxitia, O. Chubykalo-Fesenko, J. Walowski, A. Mann, and M. Münzenberg, "Evidence for thermal mechanisms in laser-induced femtosecond spin dynamics," *Phys. Rev. B*, vol. 81, p. 174401, 2010.

[202] E. Carpene, H. Hedayat, F. Boschini, and C. Dallera, "Ultrafast demagnetization of metals: Collapsed exchange versus collective excitations," *Phys. Rev. B*, vol. 91, p. 174414, May 2015.

[203] S. Eich, M. Plötzing, M. Rollinger, S. Emmerich, R. Adam, C. Chen, H. C. Kapteyn, M. M. Murnane, L. Plucinski, D. Steil, B. Stadtmüller, M. Cinchetti, M. Aeschlimann, C. M. Schneider, and S. Mathias, "Band structure evolution during the ultrafast ferromagnetic-paramagnetic phase transition in cobalt," *Sci. Adv.*, vol. 3, no. 3, p. e1602094, 2017.

[204] Z. Chen and L.-W. Wang, "Role of initial magnetic disorder: A time-dependent ab initio study of ultrafast demagnetization mechanisms," *Sci. Adv.*, vol. 5, no. 6, p. eaau8000, 2019.

[205] M. Cinchetti, M. Sánchez Albaneda, D. Hoffmann, T. Roth, J.-P. Wüstenberg, M. Krauß, O. Andreyev, H. C. Schneider, M. Bauer, and M. Aeschlimann, "Spin-flip processes and ultrafast magnetization dynamics in co: Unifying the microscopic and macroscopic view of femtosecond magnetism," *Phys. Rev. Lett.*, vol. 97, p. 177201, Oct 2006.

[206] F. Dalla Longa, J. T. Kohlhepp, W. J. M. de Jonge, and B. Koopmans, "Influence of photon angular momentum on ultrafast demagnetization in nickel," *Phys. Rev. B*, vol. 75, p. 224431, 2007.

[207] E. Carpene, E. Mancini, C. Dallera, M. Brenna, E. Puppin, and S. De Silvestri, "Dynamics of electron-magnon interaction and ultrafast demagnetization in thin iron films," *Phys. Rev. B*, vol. 78, p. 174422, Nov 2008.

[208] T. Roth, A. J. Schellekens, S. Alebrand, O. Schmitt, D. Steil, B. Koopmans, M. Cinchetti, and M. Aeschlimann, "Temperature dependence of laser-induced demagnetization in ni: A key for identifying the underlying mechanism," *Phys. Rev. X*, vol. 2, p. 021006, 2012.

[209] C. La-O-Vorakiat, E. Turgut, C. A. Teale, H. C. Kapteyn, M. M. Murnane, S. Mathias, M. Aeschlimann, C. M. Schneider, J. M. Shaw, H. T. Nembach, and T. J. Silva, "Ultrafast demagnetization measurements using extreme ultraviolet light: Comparison of electronic and magnetic contributions," *Phys. Rev. X*, vol. 2, p. 011005, 2012.

[210] C. Stamm, T. Kachel, N. Pontius, R. Mitzner, T. Quast, K. Holldack, S. Khan, C. Lupulescu, E. F. Aziz, M. Wietstruk, H. A. Dürr, and W. Eberhardt, "Femtosecond modification of electron localization and transfer of angular momentum in nickel," *Nat. Mater.*, vol. 6, pp. 740–743, 2007.

[211] T. Kachel, N. Pontius, C. Stamm, M. Wietstruk, E. F. Aziz, H. A. Dürr, W. Eberhardt, and F. M. F. de Groot, "Transient electronic and magnetic structures of nickel heated by ultrafast laser pulses," *Phys. Rev. B*, vol. 80, p. 092404, 2009.

[212] R. Gort, K. Bühlmann, S. Däster, G. Salvatella, N. Hartmann, Y. Zemp, S. Holenstein, C. Stieger, A. Fognini, T. U. Michlmayr, T. Bähler, A. Vaterlaus, and Y. Acremann, "Early stages of ultrafast spin dynamics in a $3d$ ferromagnet," *Phys. Rev. Lett.*, vol. 121, p. 087206, 2018.

[213] C. Dornes, Y. Acremann, M. Savoini, M. Kubli, M. J. Neugebauer, E. Abreu, L. Huber, G. Lantz, C. A. F. Vaz, H. Lemke, E. M. Bothschafter, M. Porer, V. Esposito, L. Rettig, M. Buzzi, A. Alberca, Y. W. Windsor, P. Beaud, U. Staub, D. Zhu, S. Song, J. M. Glownia, and S. L. Johnson, "The ultrafast einstein-de haas effect," *Nature*, vol. 565, no. 7738, pp. 209–212, 2019.

[214] P. Maldonado, T. Chase, A. H. Reid, X. Shen, R. K. Li, K. Carva, T. Payer, M. Horn von Hoegen, K. Sokolowski-Tinten, X. J. Wang, P. M. Oppeneer, and H. A. Dürr, "Tracking the ultrafast nonequilibrium energy flow between electronic and lattice degrees of freedom in crystalline nickel," *Phys. Rev. B*, vol. 101, p. 100302(R), 2020.

[215] U. Ritzmann, P. M. Oppeneer, and P. Maldonado, "Theory of out-of-equilibrium electron and phonon dynamics in metals after femtosecond laser excitation," *Phys. Rev. B*, vol. 102, p. 214305, Dec 2020.

[216] X. Wang, S. Nie, J. Li, R. Clinite, M. Wartenbe, M. Martin, W. Liang, and J. Cao, "Electronic grüneisen parameter and thermal expansion in ferromagnetic transition metal," *Appl. Phys. Lett.*, vol. 92, p. 121918, 2008.

[217] P. J. Meschter, J. W. Wright, C. R. Brooks, and T. G. Kollie, "Physical contributions to the heat capacity of nickel," *J. Phys. Chem. Solids*, vol. 42, no. 9, pp. 861–871, 1981.

[218] P.-W. Ma, S. L. Dudarev, and C. H. Woo, "Spin-lattice-electron dynamics simulations of magnetic materials," *Phys. Rev. B*, vol. 85, p. 184301, 2012.

[219] A. Manchon, Q. Li, L. Xu, and S. Zhang, "Theory of laser-induced demagnetization at high temperatures," *Phys. Rev. B*, vol. 85, p. 064408, 2012.

[220] S. S. Wellershoff, J. Gudde, J. Hohlfeld, J. G. Muller, and E. Matthias, "Role of electron-phonon coupling in femtosecond laser damage of metals," *Appl. Phys. A*, vol. 69, no. 1, pp. S99–S107, 1999.

[221] T. Saito, O. Matsuda, and O. B. Wright, "Picosecond acoustic phonon pulse generation in nickel and chromium," *Phys. Rev. B*, vol. 67, p. 205421, 2003.

[222] A. P. Caffrey, P. E. Hopkins, J. M. Klopf, and P. M. Norris, "Thin film non-noble transition metal thermophysical properties," *Microscale Thermophys. Eng.*, vol. 9, no. 4, pp. 365–377, 2005.

[223] P. E. Hopkins, J. M. Klopf, and P. M. Norris, "Influence of interband transitions on electron-phonon coupling measurements in ni films," *Appl. Opt.*, vol. 46, no. 11, pp. 2076–2083, 2007.

[224] B. Y. Mueller and B. Rethfeld, "Relaxation dynamics in laser-excited metals under nonequilibrium conditions," *Phys. Rev. B*, vol. 87, p. 035139, Jan 2013.

[225] M. Dvornik, A. Vansteenkiste, and B. Van Waeyenberge, "Thermodynamically self-consistent non-stochastic micromagnetic model for the ferromagnetic state," *Appl. Phys. Lett.*, vol. 105, no. 16, p. 162411, 2014.

[226] A. I. H. Persson, A. Jarnac, X. Wang, H. Enquist, A. Jurgilaitis, and J. Larsson, "Studies of electron diffusion in photo-excited ni using time-resolved x-ray diffraction," *Appl. Phys. Lett.*, vol. 109, no. 20, p. 203115, 2016.

[227] M. van Kampen, J. T. Kohlhepp, W. J. M. de Jonge, B. Koopmans, and R. Coehoorn, "Sub-picosecond electron and phonon dynamics in nickel," *J. Phys. Condens. Matter*, vol. 17, no. 43, p. 6823, 2005.

[228] U. Atxitia, O. Chubykalo-Fesenko, N. Kazantseva, D. Hinzke, U. Nowak, and R. W. Chantrell, "Micromagnetic modeling of laser-induced magnetization dynamics using the landau-lifshitz-bloch equation," *Appl. Phys. Lett.*, vol. 91, p. 232507, Dec. 2007.

[229] R. Chimata, A. Bergman, L. Bergqvist, B. Sanyal, and O. Eriksson, "Microscopic Model for Ultrafast Remagnetization Dynamics," *Physical Review Letters*, vol. 109, p. 157201, oct 2012.

[230] R. F. L. Evans, U. Atxitia, and R. W. Chantrell, "Quantitative simulation of temperature-dependent magnetization dynamics and equilibrium properties of elemental ferromagnets," *Phys. Rev. B*, vol. 91, p. 144425, 2015.

[231] J. Kimling, J. Kimling, R. B. Wilson, B. Hebler, M. Albrecht, and D. G. Cahill, "Ultrafast demagnetization of fept: Cu thin films and the role of magnetic heat capacity," *Phys. Rev. B*, vol. 90, p. 224408, Dec 2014.

[232] J. R. Dwyer, R. E. Jordan, C. T. Hebeisen, M. Harb, R. Ernstorfer, T. Dartigalongue, and R. J. D. Miller, "Experimental basics for femtosecond electron diffraction studies," *J. Mod. Opt.*, vol. 54, no. 7, pp. 923–942, 2007.

[233] D. Zahn, H. Seiler, Y. W. Windsor, and R. Ernstorfer, "Ultrafast lattice dynamics and electron–phonon coupling in platinum extracted with a global fitting approach for time-resolved polycrystalline diffraction data," *Struct. Dyn.*, vol. 8, no. 6, p. 064301, 2021.

[234] M. Ligges, I. Rajkovic, P. Zhou, O. Posth, C. Hassel, G. Dumpich, and D. von der Linde, "Observation of ultrafast lattice heating using time resolved electron diffraction," *Appl. Phys. Lett.*, vol. 94, no. 10, p. 101910, 2009.

[235] A. Nakamura, T. Shimojima, M. Nakano, Y. Iwasa, and K. Ishizaka, "Electron and lattice dynamics of transition metal thin films observed by ultrafast electron diffraction and transient optical measurements," *Struct. Dyn.*, vol. 3, no. 6, p. 064501, 2016.

[236] L. Peng, S. Dudarev, and M. Whelan, *High Energy Electron Diffraction and Microscopy.* Oxford Science Publications, 2011.

[237] D. Zahn, Y. W. Windsor, H. Seiler, T. Vasileiadis, T. A. Butcher, Y. Qi, D. Engel, J. Vorberger, and R. Ernstorfer, "Femtosecond electron diffraction data of nickel." [Data set]. Zenodo. `http://doi.org/10.5281/zenodo.4575398`, 2021.

[238] S. I. Anisimov, B. L. Kapeliovich, and T. L. Perelman, "Electron emission from metal surfaces exposed to ultrashort laser pulses," *J. Exp. Theor. Phys.*, vol. 66, pp. 776–781, Aug. 1974.

[239] P. B. Allen, "Theory of thermal relaxation of electrons in metals," *Phys. Rev. Lett.*, vol. 59, pp. 1460–1463, 1987.

[240] M. Müller, H. Harada, and H. Warlimont, "Magnetic materials," in *Handbook of Materials Data* (H. Warlimont and W. Martienssen, eds.), Springer Nature, 2018.

[241] L. Waldecker, R. Bertoni, R. Ernstorfer, and J. Vorberger, "Electron-phonon coupling and energy flow in a simple metal beyond the two-temperature approximation," *Phys. Rev. X*, vol. 6, p. 021003, Apr 2016.

[242] A. G. Gurevich and G. A. Melkov, *Magnetization Oscillations and Waves.* CRC Press, 1996.

[243] M. Niesert, *Ab initio Calculations of Spin-Wave Excitation Spectra from Time-Dependent Density-Functional Theory.* Forschungszentrum Jülich, 2011.

[244] H. Ebert, S. Mankovsky, D. Ködderitzsch, and P. J. Kelly, "Ab initio calculation of the gilbert damping parameter via the linear response formalism," *Phys. Rev. Lett.*, vol. 107, p. 066603, Aug 2011.

[245] A. Widom, C. Vittoria, and S. D. Yoon, "Gilbert ferromagnetic damping theory and the fluctuation-dissipation theorem," *Journal of Applied Physics*, vol. 108, no. 7, p. 073924, 2010.

[246] X. Gonze, "First-principles responses of solids to atomic displacements and homogeneous electric fields: Implementation of a conjugate-gradient algorithm," *Phys. Rev. B*, vol. 55, pp. 10337–10354, April 1997.

[247] X. Gonze and C. Lee, "Dynamical matrices, born effective charges, dielectric permittivity tensors, and interatomic force constants from density-functional perturbation theory," *Phys. Rev. B*, vol. 55, no. 16, pp. 10355–10368, 1997.

[248] X. Gonze, B. Amadon, P.-M. Anglade, J.-M. Beuken, F. Bottin, P. Boulanger, F. Bruneval, D. Caliste, R. Caracas, M. Côté, T. Deutsch, L. Genovese, P. Ghosez, M. Giantomassi, S. Goedecker, D. Hamann, P. Hermet, F. Jollet, G. Jomard, S. Leroux, M. Mancini, S. Mazevet, M. Oliveira, G. Onida, Y. Pouillon, T. Rangel, G.-M. Rignanese, D. Sangalli, R. Shaltaf, M. Torrent, M. Verstraete, G. Zerah, and J. Zwanziger, "ABINIT: First-principles approach to material and nanosystem properties," *Comput. Phys. Commun.*, vol. 180, no. 12, pp. 2582–2615, 2009.

[249] X. Gonze, F. Jollet, F. Abreu Araujo, D. Adams, B. Amadon, T. Applencourt, C. Audouze, J.-M. Beuken, J. Bieder, A. Bokhanchuk, E. Bousquet, F. Bruneval, D. Caliste, M. Côté, F. Dahm, F. Da Pieve, M. Delaveau, M. Di Gennaro, B. Dorado, C. Espejo, G. Geneste, L. Genovese, A. Gerossier, M. Giantomassi, Y. Gillet, D. Hamann, L. He, G. Jomard, J. Laflamme Janssen, S. Le Roux, A. Levitt, A. Lherbier, F. Liu, I. Lukačević, A. Martin, C. Martins, M. Oliveira, S. Poncé, Y. Pouillon, T. Rangel, G.-M. Rignanese, A. Romero, B. Rousseau, O. Rubel, A. Shukri, M. Stankovski, M. Torrent, M. Van Setten, B. Van Troeye, M. Verstraete, D. Waroquiers, J. Wiktor, B. Xu, A. Zhou, and J. Zwanziger, "Recent developments in the ABINIT software package," *Comput. Phys. Commun.*, vol. 205, pp. 106–131, August 2016.

[250] F. Bottin, S. Leroux, A. Knyazev, and G. Zérah, "Large-scale ab initio calculations based on three levels of parallelization," *Comput. Mater. Sci.*, vol. 42, no. 2, pp. 329–336, 2008.

[251] M. Fuchs and M. Scheffler, "Ab initio pseudopotentials for electronic structure calculations of poly-atomic systems using density-functional theory," *Comput. Phys. Commun.*, vol. 119, no. 1, pp. 67–98, 1999.

[252] J. P. Perdew, K. Burke, and M. Ernzerhof, "Generalized gradient approximation made simple," *Phys. Rev. Lett.*, vol. 77, p. 3865, 1996.

[253] H. Danan, A. Herr, and A. J. P. Meyer, "New determinations of the saturation magnetization of nickel and iron," *J. Appl. Phys.*, vol. 39, no. 2, pp. 669–670, 1968.

[254] M. Kresch, O. Delaire, R. Stevens, J. Y. Y. Lin, and B. Fultz, "Neutron scattering measurements of phonons in nickel at elevated temperatures," *Phys. Rev. B*, vol. 75, p. 104301, 2007.

[255] M. J. Verstraete, "Ab initio calculation of spin-dependent electron–phonon coupling in iron and cobalt," *J. Phys. Condens. Matter*, vol. 13, no. 25, p. 136001, 2013.

[256] D. Zahn, F. Jakobs, W. Windsor, H. Seiler, T. Vasileiadis, T. A. Butcher, Y. Qi, D. Engel, U. Atxitia, J. Vorberger, and R. Ernstorfer, "Data for: Lattice dynamics and ultrafast energy flow between electrons, spins, and phonons in a 3d ferromagnet." [Data set]. Rodare. `http://doi.org/10.14278/rodare.501`, 2020.

[257] R. M. White, *Quantum Theory of Magnetism.* Springer, 3rd edition ed., 2007.

[258] P.-W. Ma, S. L. Dudarev, A. A. Semenov, and C. H. Woo, "Temperature for a dynamic spin ensemble," *Phys. Rev. E*, vol. 82, p. 031111, 2010.

[259] J. Crangle and G. M. Goodman, "The magnetization of pure iron and nickel," *Proc. R. Soc. Lond. A*, vol. 321, no. 1547, pp. 477–491, 1971.

[260] A. Stupakiewicz, C. S. Davies, K. Szerenos, D. Afanasiev, K. S. Rabinovich, A. V. Boris, A. Caviglia, A. V. Kimel, and A. Kirilyuk, "Ultrafast phononic switching of magnetization," *Nat. Phys.*, vol. 17, no. 4, pp. 489–492, 2021.

[261] D. Afanasiev, J. R. Hortensius, B. A. Ivanov, A. Sasani, E. Bousquet, Y. M. Blanter, R. V. Mikhaylovskiy, A. V. Kimel, and A. D. Caviglia, "Ultrafast control of magnetic interactions via light-driven phonons," *Nat. Mater.*, vol. 20, no. 5, pp. 607–611, 2021.

[262] K. Bühlmann, R. Gort, G. Salvatella, S. Däster, A. Fognini, T. Bähler, C. Dornes, C. A. F. Vaz, A. Vaterlaus, and Y. Acremann, "Ultrafast demagnetization in iron: Separating effects by their nonlinearity," *Struct. Dyn.*, vol. 5, no. 4, p. 044502, 2018.

[263] D. Durham, K. Siddiqui, F. Ji, J. G. Navarro, P. Musumeci, R. Kaindl, A. Minor, and D. Filippetto, "Relativistic ultrafast electron diffraction of nanomaterials," *Microsc. Microanal.*, vol. 26, no. S2, p. 676–677, 2020.

[264] N. Rothenbach, M. E. Gruner, K. Ollefs, C. Schmitz-Antoniak, S. Salamon, P. Zhou, R. Li, M. Mo, S. Park, X. Shen, S. Weathersby, J. Yang, X. J. Wang, R. Pentcheva, H. Wende, U. Bovensiepen, K. Sokolowski-Tinten, and A. Eschenlohr, "Microscopic nonequilibrium energy transfer dynamics in a photoexcited metal/insulator heterostructure," *Phys. Rev. B*, vol. 100, p. 174301, Nov 2019.

[265] J.-Y. Bigot, M. Vomir, L. Andrade, and E. Beaurepaire, "Ultrafast magnetization dynamics in ferromagnetic cobalt: The role of the anisotropy," *Chem. Phys.*, vol. 318, no. 1, pp. 137–146, 2005.

[266] V. Unikandanunni, R. Medapalli, E. E. Fullerton, K. Carva, P. M. Oppeneer, and S. Bonetti, "Anisotropic ultrafast spin dynamics in epitaxial cobalt," *Appl. Phys. Lett.*, vol. 118, no. 23, p. 232404, 2021.

[267] Z. Lin, L. V. Zhigilei, and V. Celli, "Electron-phonon coupling and electron heat capacity in metals at high electron temperatures." retrieved from `https://faculty.virginia.edu/CompMat/electron-phonon-coupling/` (following the approach of Z. Lin, L. V. Zhigilei, and V. Celli, Phys. Rev. B 77, 075133, 2008).

[268] N. Medvedev and I. Milov, "Electron-phonon coupling in metals at high electronic temperatures," *Phys. Rev. B*, vol. 102, p. 064302, Aug 2020.

[269] K. P. Migdal, N. A. Inogamov, Y. V. Petrov, and V. V. Zhakhovsky, "Two-temperature equations of state for d-band metals irradiated by femtosecond laser pulses," 2017.

[270] Y. V. Petrov, N. A. Inogamov, and K. P. Migdal, "Thermal conductivity and the electron-ion heat transfer coefficient in condensed media with a strongly excited electron subsystem," *JETP Letters*, vol. 97, no. 1, pp. 20–27, 2013.

[271] T. Ogitsu, A. Fernandez-Pañella, S. Hamel, A. A. Correa, D. Prendergast, C. D. Pemmaraju, and Y. Ping, "Ab initio modeling of nonequilibrium electron-ion dynamics of iron in the warm dense matter regime," *Phys. Rev. B*, vol. 97, p. 214203, Jun 2018.

[272] D. A. Papaconstantopoulos, *Handbook of the Band Structure of Elemental Solids*. Springer, Boston, MA, 2 ed., 2015.

[273] P. B. Allen, "Empirical electron-phonon λ values from resistivity of cubic metallic elements," *Phys. Rev. B*, vol. 36, pp. 2920–2923, Aug 1987.

[274] T. Jarlborg and M. Peter, "Electronic structure, magnetism and Curie temperatures in Fe, Co and Ni," *J. Magn. Magn. Mater.*, vol. 42, no. 1, pp. 89–99, 1984.

[275] R. Mohan, V. H. Ortiz, L. Vuong, S. Coh, and R. B. Wilson, "Electron-phonon scattering governs both ultrafast and precessional magnetization dynamics in Co-Fe alloys," 2021.

[276] M. Borchert, C. von Korff Schmising, D. Schick, D. Engel, S. Sharma, S. Shallcross, and S. Eisebitt, “Uncovering the role of the density of states in controlling ultrafast spin dynamics,” 2020.

[277] B. Koopmans, M. van Kampen, J. T. Kohlhepp, and W. J. M. de Jonge, “Ultrafast magneto-optics in nickel: Magnetism or optics?,” *Phys. Rev. Lett.*, vol. 85, pp. 844–847, Jul 2000.

[278] I. Razdolski, A. Alekhin, U. Martens, D. Diesing, M.Münzenberg, u. Bovensiepen, and A. Melnikov, “Analysis of the time-resolved magneto-optical Kerr effect for ultrafast magnetization dynamics in ferromagnetic thin films,” *J. Phys.: Condens. Matter*, vol. 29, no. 17, p. 174002, 2017.

[279] R. B. Wilson and S. Coh, “Parametric dependence of hot electron relaxation timescales on electron-electron and electron-phonon interaction strengths,” *Commun. Phys.*, vol. 3, no. 1, p. 179, 2020.

[280] D. R. Hamann, “Optimized norm-conserving Vanderbilt pseudopotentials,” *Phys. Rev. B*, vol. 88, p. 085117, Aug 2013.

[281] F. Vincent and M. Figlarz, “Quelques précisions sur les paramètres cristallins et l’intensité des raies Debye-Scherrer du cobalt cubique et du cobalt hexagonal,” *C. R. Hebd. Séances Acad. Sci. C*, vol. 264, pp. 1270–1273, 1967.

[282] C. Kittel, *Introduction to Solid State Physics.* John Wiley & Sons, 8 ed., 2005.

[283] K. Thurnay, “Thermal properties of transition metals,” tech. rep., Karlsruher Institut für Technologie, 1998. 32.21.02; LK 01.

[284] D. R. Lide, ed., *CRC Handbook of Chemistry and Physics.* CRC Press, 84 ed., 2003.

[285] R. Chimata, L. Isaeva, K. Kádas, A. Bergman, B. Sanyal, J. H. Mentink, M. I. Katsnelson, T. Rasing, A. Kirilyuk, A. Kimel, O. Eriksson, and M. Pereiro, “All-thermal switching of amorphous Gd-Fe alloys: Analysis of structural properties and magnetization dynamics,” *Physical Review B*, vol. 92, no. 9, p. 094411, 2015.

[286] U. Atxitia, T. A. Ostler, J. Barker, R. F. L. Evans, R. W. Chantrell, and O. Chubykalo-Fesenko, “Ultrafast dynamical path for the switching of a ferrimagnet after femtosecond heating,” *Physical Review B*, vol. 87, p. 224417, jun 2013.

[287] U. Atxitia, T. A. Ostler, R. W. Chantrell, and O. Chubykalo-Fesenko, “Optimal electron, phonon, and magnetic characteristics for low energy thermally induced magnetization switching,” *Applied Physics Letters*, vol. 107, no. 19, p. 192402, 2015.

[288] U. Atxitia and T. A. Ostler, “Ultrafast double magnetization switching in GdFeCo with two picosecond-delayed femtosecond pump pulses,” *Applied Physics Letters*, vol. 113, p. 62402, aug 2018.

[289] V. G. Baryakhtar and A. G. Danilevich, “The phenomenological theory of magnetization relaxation (review article),” *Low Temperature Physics*, vol. 39, no. 12, pp. 993–1007, 2013.

[290] A. Kamra, R. E. Troncoso, W. Belzig, and A. Brataas, “Gilbert damping phenomenology for two-sublattice magnets,” *Phys. Rev. B*, vol. 98, p. 184402, Nov 2018.

[291] O. Chubykalo-Fesenko, U. Nowak, R. W. Chantrell, and D. Garanin, "Dynamic approach for micromagnetics close to the Curie temperature," *Physical Review B*, vol. 74, p. 094436, sep 2006.

[292] P. Nieves, D. Serantes, U. Atxitia, and O. Chubykalo-Fesenko, "Quantum Landau-Lifshitz-Bloch equation and its comparison with the classical case," *Physical Review B*, vol. 90, p. 104428, sep 2014.

[293] U. Atxitia, D. Hinzke, and U. Nowak, "Fundamentals and applications of the Landau–Lifshitz–Bloch equation," *Journal of Physics D: Applied Physics*, vol. 50, no. 3, p. 33003, 2016.

[294] M. Hennecke, I. Radu, R. Abrudan, T. Kachel, K. Holldack, R. Mitzner, A. Tsukamoto, and S. Eisebitt, "Angular Momentum Flow During Ultrafast Demagnetization of a Ferrimagnet," *Physical Review Letters*, vol. 122, p. 157202, apr 2019.

[295] V. Raposo, F. García-Sánchez, U. Atxitia, and E. Martínez, "Realistic micromagnetic description of all-optical ultrafast switching processes in ferrimagnetic alloys," *Phys. Rev. B*, vol. 105, p. 104432, Mar 2022.

[296] F. Schlickeiser, U. Ritzmann, D. Hinzke, and U. Nowak, "Role of Entropy in Domain Wall Motion in Thermal Gradients," *Physical Review Letters*, vol. 113, p. 097201, aug 2014.

[297] S. Moretti, V. Raposo, E. Martinez, and L. Lopez-Diaz, "Domain wall motion by localized temperature gradients," *Physical Review B*, vol. 95, p. 064419, feb 2017.

[298] S. Lepadatu, "Emergence of transient domain wall skyrmions after ultrafast demagnetization," *Physical Review B*, vol. 102, p. 94402, sep 2020.

[299] D. Hinzke, U. Atxitia, K. Carva, P. Nieves, O. Chubykalo-Fesenko, P. M. Oppeneer, and U. Nowak, "Multiscale modeling of ultrafast element-specific magnetization dynamics of ferromagnetic alloys," *Physical Review B*, vol. 92, p. 054412, aug 2015.